Dynamical Measurements with Quartz Resonators

Dissertation zur Erlangung des Grades
Doktor der Naturwissenschaften
am Fachbereich Chemie und Pharmazie
der Johannes Gutenberg-Universität
in Mainz

Alexander Thomas Laschitsch

geb. in Weingarten/Württemberg

Mainz 1999

Day of Oral Exam: January, 14th 2000

Information is not knowledge
Knowledge is not wisdom
Wisdom is not truth
Truth is not Beauty
Beauty is not love
Love is not music
Music is the BEST...
(Voice of Mary's Vision)
in: Joe's Garage, Act III,
Scene 16: Packard Goose
(FZ, 1979)

Contents

1 Introduction **9**

2 Quartz Crystal Resonators (QCR) **13**

2.1 Historical Remarks 13

2.2 The Quartz Crystal 14

2.3 Piezoelectricity 16

2.3.1 Thickness Shear Modes 17

2.3.2 Applications of Quartz Crystal Resonators 17

3 Surface Forces **20**

3.1 van-der-Waals Forces 20

3.2 Surface and Interfacial Energy 23

3.3 The Derjaguin Approximation 25

3.4 Contact of Elastic Solids 26

3.4.1 The Hertz Theory 26

3.4.2 The Johnson-Kendall-Roberts Theory (JKR) 27

3.4.3 The Derjaguin–Muller–Toporov Theory (DMT) 28

4 Friction **29**

4.1 Classical Description 29

4.2 Nanotribology 31

4.2.1 Stick-Slip Motion 33

4.3 Lubrication 38

4.3.1 Different Lubrication Regimes 38

4.4 Instruments of Nanotribology 40

4.4.1 Atomic Force Microscope (AFM) 41

4.4.2 Surface Forces Apparatus (SFA) 44

4.4.3 Quartz Crystal Microbalance (QCM) 46

5 Development of a Setup to Measure Friction Based on Quartz Crystal Resonators **48**

5.1 Background and Requirements 48

5.2 Piezo Stage — Nanopositioning 49

5.2.1 Capacitive Sensors 51

5.3 Piezo translational stage PT 30 - Sample positioning 52

5.4 Force Transducer 52

5.4.1 Calibration - Spring Constant 54

5.4.2 Capacitive Measurement 58

5.5 Mechanical Stability 58

5.5.1 Mechanical Connections 58

5.5.2 Mechanical Vibrations 58

5.5.3 Sample Holder 59
5.5.4 Quartz Resonators 60
5.6 Data Acquisition 62
5.6.1 HP Network Analyzer — Passive Measurements in the Frequency Domain 64
5.6.2 Analysis of the Resonance Curves 65
5.6.3 Data Acquisition in the Time Domain 67
5.7 Control via Software 68
5.7.1 Programs and Units 68
5.8 The Opposing, Curved Surface 70
5.8.1 Different Spherical Surfaces 70

6 Characterization of the Setup 73

6.1 Data Treatment 73
6.1.1 Plotting Conventions 73
6.2 Data Noise and Resolution 74
6.2.1 Frequency and Bandwidth 76
6.2.2 Normal Force 76
6.3 Typical Data for a Gold–Gold Contact 77
6.4 Smooth, Low-Energy Surfaces 79
6.5 Dependence on Overtone Order 80
6.6 Nonlinearities 83
6.6.1 Drive Level Dependence 84

6.6.2 Anharmonic Sidebands 84
6.6.3 Fourier Amplitudes from Time Domain Experiments 86
6.6.4 Nonlinearities of the Unloaded Quartz Resonator 88
6.6.5 Bending of a Circular Quartz Plate 89
6.6.6 Pressure Dependence of Resonance Frequencies 89
6.7 Quartz Crystals for Tribological Investigations 92
6.7.1 Linear Modeling 92
6.7.2 Equivalent Circuits – Mechanical Impedances 96
6.7.3 Modeling of the Frequency Behavior 96
6.7.4 Oscillation Amplitude and Surface Velocity for Different Overtones 100
6.7.5 Calculation of Rheological Parameters 102
6.8 Experimental Problems 107
6.8.1 Amplitude Distribution and Energy Trapping 107
6.8.2 Long-Range Normal Force Drift and its Correction 108
6.8.3 Distortion of Resonances 113
6.8.4 Varying the Approach Speed 115

7 Friction Properties of Perfluoropolyether Coated Amorphous Carbon Surfaces 119

7.1 Introduction 119
7.1.1 Materials and Sample Preparation 120
7.1.2 Properties of Thin PFPE Films and Interaction with Amorphous Carbon Substrates 123
7.1.3 Experimental Conditions 127

7.2 Effect of Varying Thickness of the Lubricant Layer . . . 129
7.2.1 CH_x Substrate . . . 129
7.2.2 CN_x Substrate . . . 130
7.3 Attraction and Adhesion . . . 132

8 Discussion of Results on PFPE Films 134

8.1 Introduction . . . 134
8.2 Variations in Friction with Lubricant Thickness . . . 135
8.3 Attractive Forces . . . 138
8.3.1 Force Steps and Attractive Minima . . . 138
8.3.2 Calculated van der Waals Forces . . . 141
8.3.3 Estimation of Laplace Pressure . . . 144
8.4 Miscellaneous . . . 146
8.4.1 Shear Viscosity of the Lubricant Layers . . . 146
8.4.2 Dissipated Power . . . 149
8.4.3 Stability of the Lubricant Layers . . . 151
8.4.4 Differing Data Quality between CH_x and CN_x . . . 152
8.4.5 Friction Surface Profiles . . . 152

9 Solvent–Induced Glass Transition in Thin Polymer Brushes 157

9.1 Introduction . . . 157
9.2 Theoretical Background . . . 159
9.3 Materials . . . 163
9.4 Experimental and Data Analysis . . . 164

9.5 Results and Discussion . . . 170
9.5.1 Influence of Pumping Speed . . . 170
9.5.2 Influence of Thickness . . . 173
9.5.3 Influence of History . . . 175
9.6 Conclusions . . . 179

10 Conclusions **180**

10.1 Summary . . . 180
10.1.1 Friction Experiments . . . 180
10.1.2 Osmotic Glass Transition in Thin Films . . . 182
10.2 Perspectives . . . 183
10.2.1 Electrical Measurements . . . 183
10.2.2 Measurement of Interfacial Distance . . . 183
10.2.3 Dielectric Measurements . . . 183
10.2.4 Measurement of Contact Area . . . 184
10.3 Measurements in Vacuum or in a Liquid . . . 184
10.4 Surface Preparation . . . 185
10.4.1 Spheres . . . 185

Bibliography **186**

Chapter 1

Introduction

The bulk behavior of polymers has been investigated extensively since the discovery of their (commercial) value in many applications during the 1940s. Thus, nowadays the relation between molecular structure and macroscopic behavior is fairly well understood. Polymers constitute a class of designable materials because the materials' properties can be tuned via their molecular structure. Further, blending of several compounds can lead to new materials.
Miniaturization is a general trend being utilized in many applied disciplines such as the microelectronics and computer industry, as well as medicine and biology. The concentration of a device's functionality in a much smaller volume is an enabling technology. The micro-fabrication of compounds is a common goal and research efforts are on-going towards further miniaturization down to the nano-scale. Consequently, the manipulation and characterization of materials must deal with single monolayers of atoms or molecules. However, on these scales the materials often show differing behavior than in the bulk. This is due to geometrical confinements, lower dimensionality, interactions with the substrate (which for bulk films is negligible), and the nanoscale-surface structures. In this work we focus on the dynamic behavior of ultra-thin polymeric films on solid substrates.

Polymers exhibit a rather different macroscopic behavior than inorganic materials. One important reason for this is their molecular structure: As opposed to crystalline materials where single atoms form lattices with a defined long-range order, an (amorphous) polymer consists of long chain molecules (a typical length can be a several thousand segments).

Thus, the motions of a single segment are constrained by its bonds in the chain and again by the chain–chain–interactions. This already implies that not only the short–range atomic interactions are important for the macroscopic properties but also longer–ranging interactions that are mediated along and among the chains. The glass transition of an amorphous polymer is a typical example for such a cooperative phenomenon [Jae86]. Although it has also been investigated since the start of polymer science there is still a lively discussion aiming to explain this behavior on a molecular basis. During recent years research in this field has turned towards the investigation of thin films: The confinement of a polymer to a solid surface can decisively influence its dynamical properties. In particular, the glass transition of the polymer is quite a useful probe for the changes of the dynamical behavior caused by the confinement.

In this work the main tool for investigations were based on quartz crystal resonators (QCRs). They are unique because one is able to probe high-frequency (MHz-range) mechanical behavior of materials. There is no other method that provides a similar access to rheological material properties in this regime. If the temperature–frequency superposition principle is applied it can be seen that the quartzes probe the dynamical behavior at temperatures 40 K below the experimental temperature. This means that many of the molecules cannot follow the excitation and, hence, appear "frozen" on this time-scale.

In this work, QCRs are used in two different applications:

1. Firstly, they serve as a very sensitive balance to monitor small amounts of organic solvent penetrating a polymer brush matrix [LBH$^+$99]. By the take-up of solvent an amorphous polymer matrix is plasticized, i.e., its glass transition can be induced by controlled sorption of the latter. The aim of this study can be subdivided into several steps:

   (a) The solvent–induced glass transition must be identified and related to the temperature induced glass transition.

   (b) Polymer brushes with high grafting-densities have a conformation quite different from adsorbed layers. It has to be demonstrated that they obey a similar sorption (and, thus, glass transition) behavior.

   (c) Theoretical models for the sorption behavior like the Flory theory can be applied to check whether the sorption in thin films obeys the same laws as in the

bulk.

(d) The influence of confinement can be probed by varying the film thickness and investigating the changes in the solvent-induced glass transition.

2. A new approach for investigations of friction on a molecular level ("nanotribology") was realized on the basis of QCRs [LJ99]. Historically, the friction phenomenon has been treated in quite a pragmatic way: Its description was based on macroscopic phenomenological observations and the easiest method to avoid friction was to "simply lubricate the sliding interface" [Dow79]. However, with the advent of machines that are able to probe the dissipative forces on a molecular scale it became clear that classical tribological laws would have to be changed — or at least modified — to describe "nanotribology" [Per98]. Application problems during the past one or two decades have also caused an increased interest in this field [Gra99]. For example, the computer industry lubricates hard-disk surfaces to protect them from wear and damage if crashes with the reading head occur. Because of the need to miniaturize the distance between disk and head the protective lubricant layers become as thin as single monolayers of molecules [JMM+96]. However, particularly in this regime many lubricants tend to solidify [BIL95, DG96] because of the geometrical constraints and the extreme conditions in hard-disk drives (spinning velocities of several thousand revolutions per minute (RPM) are common). Investigations concerning interfacial surface and friction forces on the molecular scale have so far been carried out using primarily two methods: The Surface Forces Apparatus (SFA) and the Atomic Force Microscope (AFM). However, especially for the conditions in disk–drives, the results from SFA and AFM have only a qualitative value because both methods are limited to comparatively low speeds ($v \leq 1$ mm/s) and frequencies ($f \leq 100$ Hz). Here, the quartz resonator can close a gap. For bulk rheology [Sch93, ALST97, Kan90] and for the characterization of thin films [Joh99, WSJ97, KW88] it is already an established rheological method. In this work we follow the same high-frequency approach for friction measurements. In principle, many experimental and theoretical concepts could be transferred from AFM and SFA setups and measurements. We report about the following topics:

(a) Chapter 4 gives an overview about the current knowledge of friction, tribol-

ogy and lubrication with emphasis on topics that are relevant for the quartz method. It includes a description of the main methods that have been used for nanotribological investigations, the AFM and the SFA.

(b) Chapter 5 gives a comprehensive survey of the developed setup.

(c) Chapter 6 summarizes results from test measurements which show that the measurement of friction is possible with quartz resonators. Characteristic data sets are analyzed and a model for the qualitative description is developed.

(d) Finally, in Chapters 7 and 8 measurements on molecular lubricants are presented. In order to test the potential of the quartz setup the film thickness was systematically varied in the sub-monolayer range to exactly adjust the "friction coefficient". The second goal of this study was to find out whether — under the high frequency stress exerted by QCRs — the perfluoropolyether lubricant layers can still "do their job", i.e., whether they are still in a liquid state.

Both parts of the work deal with the dynamical behavior of polymers at interfaces and, in particular, with its change when being confined to ultrathin films. The swelling experiments probe this behavior indirectly by detecting the changes in the glass transition when the film thickness decreases. The friction experiments, however, directly probe the high-frequency behavior of confined lubricant films. The presented approaches differ considerably but in the end both try to clarify the change of the dynamical behavior when polymers are confined to ultrathin films on solid substrates.

Chapter 2

Quartz Crystal Resonators (QCR)

2.1 Historical Remarks

In India and Ceylon the mysterious behavior of Turmalin-crystals had been known for a long time. In 1703, Dutch navigators first brought Turmalin to Europe and called it Ceylon magnet: If put into hot ashes the turmalins attracted ash particles on one side whereas repelled them on the opposite side. Aepinus called this effect pyro-electricity in 1756. In 1877, Lord Kelvin found a relation between pyro- and piezo-electricity, and in 1880 the Curie brothers discovered that mechanical deformation generated electrical charges and named this piezo-effect ("piezo" (Gr.) = "I press"). For the following 30 years the piezo-effect was still considered a little side-aspect in science until crystal physics "was founded" by the appearance of the "Lehrbuch der Kristallphysik" by W. Voigt. Another development which promoted the use of quartz resonators was the first generation of electrical oscillators by Meißner in 1913. From the 1920s on, Quartz Crystal Resonators have been in use in the strongly developing field of electronics. They are mainly utilized as frequency control elements in oscillator circuits. One of the unique properties of the quartz crystal is that it is simultaneously a mechanical resonator and an electro-mechanical transducer.

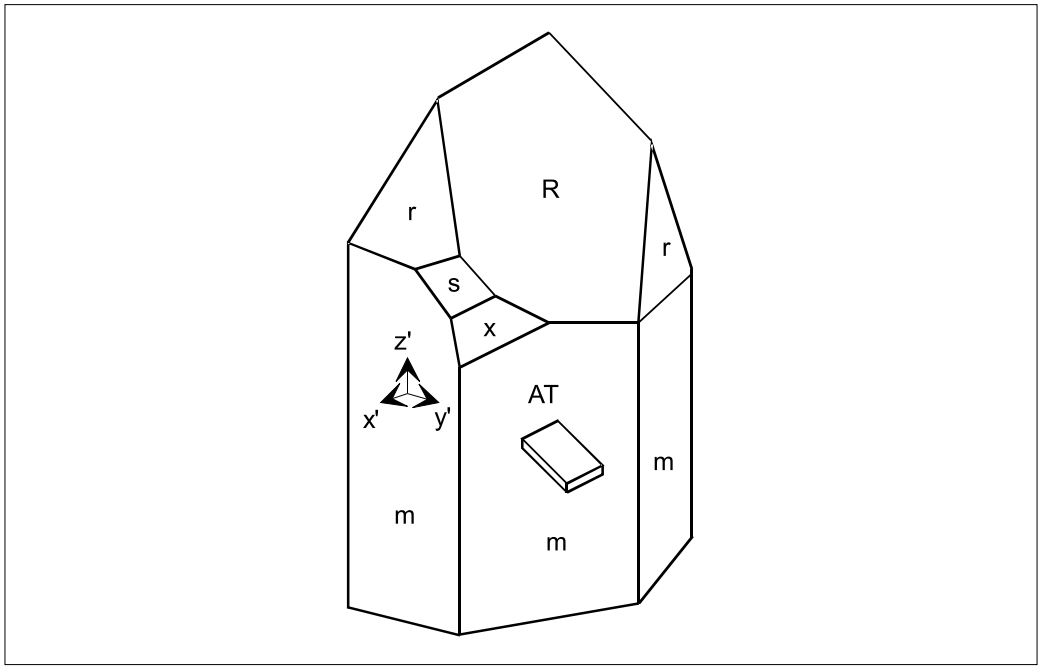

Figure 2.1: Left-handed quartz crystal (adapted from [Bot82]) showing the 35.25°–inclined AT–cut plane. R–faces are called major, r the minor rhomb faces. The s and x faces are very rare, but when occurring enable one to distinguish between right and left quartz.

2.2 The Quartz Crystal

Quartz is a crystalline form of SiO_2 with a density of 2649 kgm^{-3} and a melting temperature of 1750 °C. It is technically important because of its piezo-electric, mechanical and thermal properties. Figure 2.1 shows an idealized left–handed quartz crystal. It is a hexagonal prism with six cap faces at each end. The prism faces are called m-faces whereas the cap faces are designated R and r for major and minor rhomb surfaces, respectively. The z-axis of α–quartz has a three-fold symmetry (point class D_3) without an inversion center which is a vital requirement for the occurrence of piezoelectricity. Perpendicular to the z-axis there are three axes with two-fold symmetry which span an angle of 120°. The dipole moments given by the lattice structure compensate at equilibrium, but not in the deformed state.

Above 573 °C, which is called the Curie temperature, SiO_2 exists as β–quartz, which has a hexagonal instead of a trigonal structure. When a crystal of β–quartz is cooled through the Curie temperature to become α–quartz, very large thermal stresses occur and the

crystal often shatters. Even if it does not break, the crystal usually becomes electrically twinned [Bot82].

The anisotropy of the lattice structure induces anisotropy of several macroscopic physical parameters, e.g., elastic modulus, thermal and electrical conductivity, coefficient of thermal expansion, dielectric constants, piezoelectric constants, optical indices of refraction, and the velocities of propagation of longitudinal (sound) and shear waves. Effective values given in Table 2.1 are those matrix components that are applicable for the movement of AT-cut quartz. AT stands for a special cut of the quartz crystal (35.25° inclined relative to the z-axis). This crystal cut mainly exhibits shear oscillations. "T" stands for "temperature–compensated": The temperature dependence of the resonance frequency of quartz resonators is generally a third-order polynomial (cubic). For the AT- and BT-cuts first and second order contributions vanish, thus, the temperature dependence around the reference temperature (usually room temperature) is negligible.

The resonance frequency of the thickness shear resonator is determined by its thickness h_q: For the first harmonic it is simply half the wavelength ($\lambda/2$) that "fits into the plate". Therefore, the resonance frequency f_0 is given by:

$$f_0 = \frac{c_\mathrm{t}}{\lambda} = \frac{c_\mathrm{t}}{2h_\mathrm{q}} = \frac{\sqrt{G_\mathrm{q}/\rho_\mathrm{q}}}{2h_\mathrm{q}} = \frac{N_\mathrm{AT}}{h_\mathrm{q}}\ [\mathrm{mm}] \tag{2.1}$$

with c_t the transversal velocity of sound. For an explanation of the variables and respective values see Table 2.1. Knowing the thickness h_q of the quartz plate (in mm) the resonance frequency can easily be calculated using the frequency constant N_AT. The even harmonics usually cannot be excited because the shear induced polarization averages to zero, whereas this is possible for the odd ones at the frequencies $f_\mathrm{n} \approx n \cdot f_0$ with n = 1,3,5...

The plane of polarization of light being passed through the quartz crystal along its z-axis is rotated by 15° to 45° for each millimeter of quartz traversed. The crystal is said to be right-hand if the plane of polarization is rotated clockwise as seen towards the source of light. Most natural quartzes are optically twinned, i.e., consist partially of left- and right-handed quartz. This should be avoided in technical quartzes.

Table 2.1: Effective physical properties of AT-cut crystalline quartz.

density (ρ_q)	2649 kgm^{-3}
eff. shear modulus (G_q)	$2.957 \cdot 10^{10}$ Nm^{-2}
eff. piezoelectric constant (e)	$9.5 \cdot 10^{-2}$ Cm^{-2}
eff. dielectric constant (ϵ_q)	$40.3 \cdot 10^{-12}$ Fm^{-1}
piezoelectric coefficient ($d = e/G_q$)	$3.21 \cdot 10^{-12}$ mV^{-1}
frequency constant (N_{AT})	1660 kHz mm

2.3 Piezoelectricity

Generally speaking, a material is called piezo-electric if mechanical deformation leads to an electrical polarization (piezo-effect). Conversely, an applied electrical field deforms the piezoid (inverse piezo-effect). An important requirement for the occurrence of piezo-electricity is the lack of a point of inversion in the crystal symmetry. Crystals with an inversion center do not show piezo-electricity but are also mechanically deformable by application of an electrical field. This effect is called electro-striction and is several orders of magnitude weaker than piezo-electricity. Electro-striction is of second order in the applied field, that is, it depends on E^2.

The piezo-effect is described by the following tensor relationship (Voigt-notation, cf. [Bot82]):

$$\vec{D} = (e_{\alpha\beta})(x_\beta) + (\epsilon_{ik})\epsilon_0\vec{E} \tag{2.2}$$

with $\vec{D}$ the mechanical deformation. The first term of eq. 2.2 describes the influence of the mechanical deformation tensor (x_β), the second term the effect of an externally–applied electrical field $\vec{E}$. The constants $(e_{\alpha\beta})$ are the piezo-electric moduli, (ϵ_{ik}) is the dielectric tensor, and ϵ_0 the dielectric constant of vacuum. For α-quartz the matrix of the moduli has only two independent components (e_{11}, e_{14}). Because of their piezo-electric effect, quartzes are electro-mechanical transducers. On the other hand, they are also mechanical resonators with high quality factors ($Q \approx 10^5$).

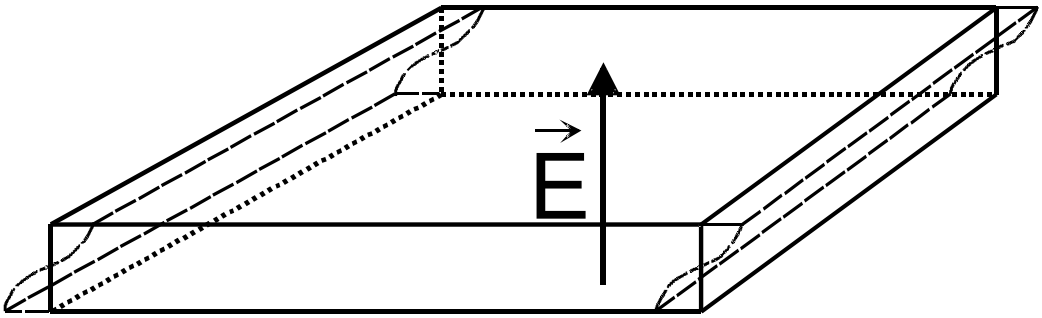

Figure 2.2: Shear deformation of an (oscillating) rectangular AT-cut quartz plate. The electrical field $\vec{E}$ is applied perpendicular to the quartz surfaces.

2.3.1 Thickness Shear Modes

Ideally, an AT-cut quartz oscillates exhibiting a pure shear motion of the surfaces (cf. Figure 2.2). The surfaces move parallel with respect to each other and the thickness of the plate does not change, i.e., there is no normal component.

2.3.2 Applications of Quartz Crystal Resonators

In resonance, both the amplitude of motion and the electrical conductance show a maximum. Measuring the conductance as a function of frequency therefore provides a means to electrically determine the acoustic resonance. Figure 2.3 shows the resonance curves (Lorentzians) of an unloaded and loaded quartz resonator. The complex frequency is defined by:

$$f^* = f + i\Gamma \tag{2.3}$$

with f the resonance frequency and 2Γ the bandwidth of the resonance at half maximum. The resonance frequency is a measure of the elastic properties of the quartz (and anything on its surface), whereas the bandwidth reflects dissipative phenomena occurring at the quartz surface. Therefore, an increase in bandwidth was expected for the friction experiment, but the increase of resonance frequency was not.

Only in the friction experiment do we observe a frequency *increase* (cf. Chapter 6), for all other known applications the frequency shift is usually negative (added mass to a

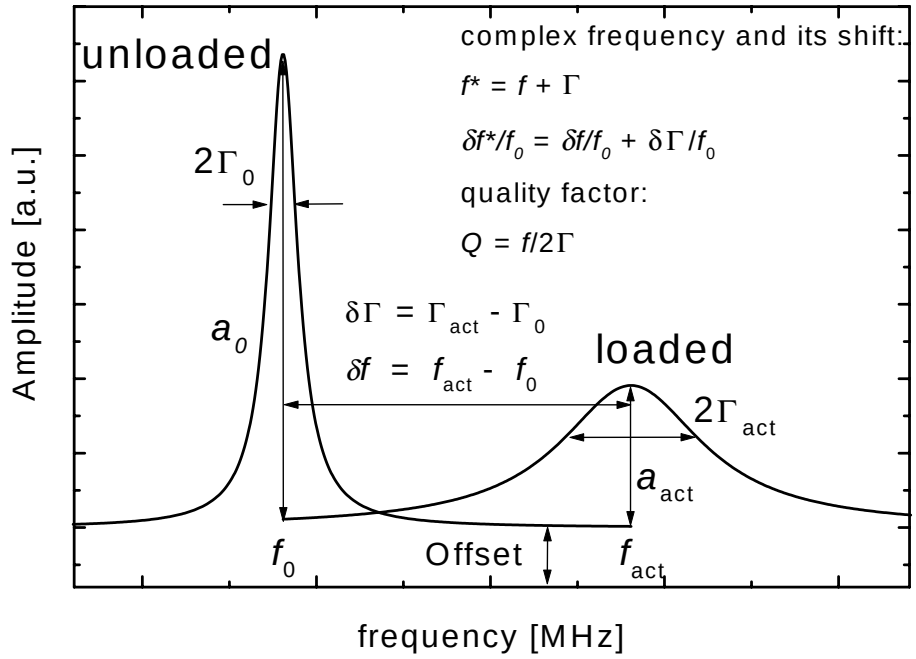

Figure 2.3: Typical resonance curves (Lorentzians) for a quartz crystal resonator that is unloaded and loaded (friction experiment). Also shown are the resonance parameters that completely characterize a change in resonance properties. f: resonance frequency; 2Γ: resonance bandwidth; a: Lorentzian amplitude. The indices distinguish the unloaded (0) and loaded (act) parameters.

resonator). The simple analogy of a spring(k)–mass(m) system illustrates this principle: Its resonance frequency is written as: $\omega = \sqrt{k/m}$. Since no mass can be withdrawn from the resonator, it is believed that the increase of the frequency is due to the increased stiffness of the quartz–sphere system, a phenomenon that will be discussed in more detail in Chapter 6.7.3.

Quartz crystal microbalance. For the final part of the work presented in this Dissertation the quartz resonators were only used as highly precise balances with sub-monolayer resolution. For thin films adhering to the quartz surface the Sauerbrey equation is valid [Sau57, Sau59]:

$$\delta m \approx -\frac{Z_{\mathrm{q}}}{2f_0}\frac{\delta f_{\mathrm{n}}}{f_{\mathrm{n}}} \tag{2.4}$$

with δm the mass coverage per unit area; $Z_{\mathrm{q}} = 8.8 \cdot 10^6$ kg/m^{2}s the acoustic impedance, and δf_{n} the frequency shift with respect to the unloaded frequency f_{n} of the n^{th} harmonic.

Detectable changes in the normalized frequency shift of the resonance are on the order of $\delta f_{\mathrm{n}}/f_{\mathrm{n}} \approx 10^{-7}$ or below (see Chapter 6.2). This corresponds to a minimum detectable film thickness of 1 Å. As such, this method deserves the name "Quartz Crystal Nanobalance".

It is also possible to determine viscoelastic properties of the films adjacent to the quartz surface from the combined evaluation of resonance frequency and bandwidth. However, this was not the focus of the present work. We do not give a presentation of that field but refer to appropriate literature: [Joh91, Joh99, Kan97, KM93, RKK90, WSJ97, Wol98, ALST97, Sch93].

Chapter 3

Surface Forces

In the last few decades research on surface forces has been growing immensely. This development was partly driven by applications. Modern electronic products, for example, require miniaturization and hence a control of the surface structuring down to the micrometer or even the nanometer range. Manipulations at these small length scales require a profound knowledge of the interactions of single molecules as well as of macroscopic surfaces.

Our research was focused on ultrathin polymeric films on top of smooth surfaces. Some surface force models and laws will be applied to evaluate and discuss the experimental results. Therefore, in this chapter an overview is given of how surface phenomena can be described in terms of thermodynamical and molecular parameters. The description of van-der-Waals forces is briefly reviewed and related to macroscopic surface forces. The Derjaguin approximation relates the forces between curved surfaces to the energies between — otherwise identical — flat surfaces. Finally, models for the deformation and area of the contact between two macroscopic bodies are summarized.

3.1 van-der-Waals Forces

Long-range interactions between macroscopic particles are governed by electrostatic, steric, and van-der-Waals forces. At shorter distances (below 1 to 3 nm) solvation (structural) forces also come into play [Isr92c].

Origin of van-der-Waals forces. The term "van-der-Waals forces" subsumes different kinds of polarization interactions between molecules, namely the Keesom, Debye, and London attractions. For non-retarded interactions (at small separations) their distance dependence scales as r^{-6}. The Keesom interaction can be understood within the framework of classical electrostatics (permanent dipole-dipole interaction), the Debye energy finds a classical explanation in an attractive interaction, where a permanent dipole induces a polarization in a polarizable molecule. The London dispersion energy, however, can only be understood within the framework of quantum mechanics. The static dipole moment in Debye theory is replaced by a fluctuating one, which polarizes neighboring molecules. The London interaction occurs between all atoms and molecules, including neutral ones. At a specific distance from each other interacting molecules can oscillate out of phase. This is known as retardation: the force decays more rapidly for larger surface separations (10-100 nm)[IT72] and is then proportional to r^{-7}.

Lifshitz theory. This continuum theory between macroscopic objects expresses the dispersion forces as a function of distance in terms of bulk properties of the materials such as dielectric constants ϵ and refractive indices n. In Chapter 8 we will refer to values obtained from such calculations [Ber97].

The Hamaker constant. The interaction between two atoms is described by the atom-atom pair potential w:

$$w = -\frac{C}{r^6} \tag{3.1}$$

where C is the atom-dependent coefficient. The Hamaker constant is defined as

$$A_{\mathrm{H}} = \pi^2 C \rho_1 \rho_2 \tag{3.2}$$

with ρ_{i} the number of atoms per unit volume. The distance dependence of the force laws between macroscopic bodies varies with their geometries. The most prominent examples are the plane–plane, the crossed–cylinders (e.g., in a surface forces apparatus), and the

sphere–plane geometry. The respective interaction energies are:

$$W_{\mathrm{p-p}} = -\frac{A_{\mathrm{H}}}{12\pi D^2} \tag{3.3}$$

$$W_{\mathrm{cyl}} = -\frac{A_{\mathrm{H}}\sqrt{R_1 R_2}}{6D} \tag{3.4}$$

$$W_{\mathrm{sp-pl}} = -\frac{A_{\mathrm{H}} R}{6D} \tag{3.5}$$

with D the surface separation and R_1, R_2 the radii of the contacting spheres. For $R_1 = R_2$ the crossed-cylinders interaction equals that of a sphere–plane contact. This force–distance law is used in data treatment of the Surface Forces Apparatus, and also in our sphere–plane setup (cf. Chapter 8). The theoretical calculations for surface forces are mostly carried out for the plane–plane geometry. To transform these to the force laws for curved surfaces one can use the Derjaguin approximation (cf. Chapter 3.3).

Combining relations. In many cases the van-der-Waals interactions between surfaces of the same material are known. However, in the experiment we approach two different materials. If the separate values are known, combining relations for the Hamaker constants help to estimate the combined value:

$$A_{132} \approx \pm\sqrt{A_{131}A_{232}} \qquad\qquad A_{12} \approx \sqrt{A_{11}A_{22}} \tag{3.6}$$

where A_{12} is the Hamaker constant for material 1 interacting with material 2 across vacuum, and A_{132} the one for interaction across medium 3. Another useful expression is

$$A_{131} \approx A_{313} \approx A_{11} + A_{33} - 2A_{13} \approx (\sqrt{A_{11}} - \sqrt{A_{33}})^2 \tag{3.7}$$

Combination of both gives:

$$A_{132} \approx (\sqrt{A_{11}} - \sqrt{A_{33}})(\sqrt{A_{22}} - \sqrt{A_{33}}) \tag{3.8}$$

Relation between surface energy and Hamaker constant. There is also a relation between the (macroscopic) surface energy γ and the (microscopic) Hamaker constant:

$$\gamma \approx \frac{A_{\mathrm{H}}}{24\pi(0.165\ \mathrm{nm})^2} \qquad\qquad \Rightarrow\ A_{\mathrm{H}} \approx 2.1 \times 10^{-21}\ \gamma \tag{3.9}$$

where γ is in mJ/m^2 and A_{H} is in Joules.

3.2 Surface and Interfacial Energy

Surface energy. In order to separate bodies initially in contact, mechanical work must be expended to overcome the adhesive forces. This work is done to create 'new' surface area and the energy required to do this is defined as the surface free energy:

$$\Delta G = -2\gamma = -W \tag{3.10}$$

where G is the thermodynamic free energy, γ is the surface free energy per unit area and W is the work needed in this process.

Interfacial energy. If two flat surfaces of material A, each of unit area, are initially separated by a liquid B and then brought into adhesive contact, the following expression gives the (negative) free energy change:

$$\Delta W = -2\gamma_{\mathrm{AB}} \tag{3.11}$$

The factor 2 arises because the two initially separated surfaces of unit area have merged. Hence two unit areas of the interface A-B have been eliminated. If two like bodies "cohere" we speak of the work of cohesion W^c, while for two unlike bodies we refer to work of adhesion W^a. Concerning two different surfaces 1 and 2 in contact the Dupré equation is valid [Isr92c]:

$$\gamma_{12} = \frac{1}{2}(W_{11} + W_{22}) - W_{12} = \gamma_1 + \gamma_2 - W_{12} \tag{3.12}$$

W_{12} is the work of adhesion. $\gamma_{\mathrm{i}} = \frac{1}{2}W_{\mathrm{ii}}$ are the surface energies of bodies i.
Common units are $[\gamma] = \mathrm{mJ/m^2} = \mathrm{mN/m} = \mathrm{erg/cm^2} = \mathrm{dyn/cm}$.

Surface energies can vary considerably between different materials. Most metals have high energy surfaces ($\gamma > 1000$ mN/m) and most polymers and ceramic materials have low energy surfaces ($\gamma < 100$ mN/m). One method to determine surface energies experimentally is to measure the contact angle θ of a water droplet and the respective surface. However, this technique can only be applied for surfaces with energies lower than the

surface tension of water $\gamma_{H_2O} = 72.8$ mN/m. The surface energy can be calculated via Young's equation:

$$\gamma_{SL} + \gamma_L \cos\theta_0 = \gamma_S \tag{3.13}$$

where γ_{SL} is the interfacial energy between solid and liquid, γ_S and γ_L are the surface energy of the solid and the liquid, respectively. For the determination of the surface energy γ_S of a solid one has to know the interfacial energy γ_{SL}. The use of combining relations can help to calculate the interfacial energy:

$$\gamma_{SL} = \gamma_S + \gamma_L - 2\sqrt{\gamma_S \gamma_L} = (\sqrt{\gamma_S} - \sqrt{\gamma_L})^2 \tag{3.14}$$

These combining relations are also valid for Hamaker constants (cf. Chapter 3.1).

Polar and dispersive components. Water is a highly polar liquid. Contact angle measurements carried out with non-polar liquids (e.g., hydrocarbons) produce results significantly different from those obtained with water. On a phenomenological basis the surface energy has been divided into a "polar" and a "dispersive" (originating from London "dispersion" forces) component [OW69]:

$$\gamma = \gamma^d + \gamma^p \tag{3.15}$$

where γ is the total surface energy, γ^d is the dispersive component and γ^p the polar component. The solid–liquid interfacial energy is then given by [OW69]:

$$\gamma_{SL} = \gamma_S + \gamma_L - 2\sqrt{\gamma_S^d \gamma_L^d} - 2\sqrt{\gamma_S^p \gamma_L^p} \tag{3.16}$$

If dispersive interactions are dominating this reduces to:

$$\gamma_{SL} = \gamma_S + \gamma_L - 2\sqrt{\gamma_S^d \gamma_L^d} \tag{3.17}$$

Combination rules are useful to calculate interfacial energies from measured values of the surface energies of the individual components (Chapter 8).

3.3 The Derjaguin Approximation

The interfacial energy is a property of a flat surface in contact with another medium. However, the surfaces used in many experiments are curved because of exact approach on the nanometer-scale is easier to perform. Consequently, it is necessary to calculate the forces occurring between curved surfaces. A very helpful relation in this context is the Derjaguin approximation which relates the force between two spheres $F_{\text{curved}}(D)$ to the energy per unit area W(D) of two flat surfaces at the same separation D [Der34]:

$$F_{\text{curved}}(D) \approx \int_D^\infty 2\pi \left(\frac{R_1 R_2}{R_1 + R_2}\right) f(Z) dZ = 2\pi \left(\frac{R_1 R_2}{R_1 + R_2}\right) W(D) \tag{3.18}$$

where $f(Z)$ is the normal force per unit area between the flat surfaces. The only restriction is that the separation D of the surfaces has to be much smaller than the radii of the spheres R_1 and R_2. For the case of a sphere of radius R in close proximity to a flat surface ($R_1 \ll R_2$), equation 3.18 reduces to:

$$\frac{F_{\text{curved}}(D)}{R} = 2\pi E_f(D) = 2\pi \int_D^\infty F_{\text{flat}}(D) dD \tag{3.19}$$

Experimental data are displayed in terms of the interaction energy per unit area $W(D)$, rather than the normal forces, in order to facilitate comparison of results obtained with different setups and sample geometries. Also, the energy is directly related to the relevant physical property, the surface energy γ.

Modification of force law for layer systems. The non-retarded van-der-Waals force between two flat surfaces 1 and 1' separated by a distance D with adsorbed layers 2 and 2' of thickness T and T' interacting across medium 3 is given by the approximate expression [Isr72]:

$$F_{\text{flat}}(D) = \frac{1}{6\pi}\left[\frac{A_{232'}}{D^3} - \frac{\sqrt{A_{121}A_{32'3}}}{(D+T)^3} - \frac{\sqrt{A_{1'2'1'}A_{323}}}{(D+T')^3} + \frac{\sqrt{A_{1'2'1'}A_{121}}}{(D+T+T')^3}\right] \tag{3.20}$$

When applying the Derjaguin approximation 3.19 to 3.20 we obtain:

$$\frac{F_{\text{curved}}(D)}{R} = \frac{1}{6}\left[\frac{A_{232'}}{D^2} - \frac{\sqrt{A_{121}A_{32'3}}}{(D+T)^2} - \frac{\sqrt{A_{1'2'1'}A_{323}}}{(D+T')^2} + \frac{\sqrt{A_{1'2'1'}A_{121}}}{(D+T+T')^2}\right] \tag{3.21}$$

For the estimation of the occurring normal forces we distinguish between short- and long-range behavior:

- At small separations, i.e., for $D \ll (T + T')$ equation 3.21 becomes:

$$\frac{F_c}{R} = \frac{A_{2'32}}{6D^2} \tag{3.22}$$

- while at large separations, for $D \gg (T + T')$, one obtains

$$\frac{F_c}{R} = \frac{A_{1'31}}{6D^2} \tag{3.23}$$

For very small separations the forces between the surface layers on top of the substrates become dominant, whereas for large separations the underlying properties of the substrate dominate the van-der-Waals interaction.

3.4 Contact of Elastic Solids

3.4.1 The Hertz Theory

Hertz (1896)[Her81] was the first to investigate the shape of the contact area of smooth surfaces when two elastic bodies are in contact. He demonstrated that the size and shape of the contact zone depend on the elastic deformation of the bodies. His calculation of the contact radius r_c of two spheres of radius R_1 and R_2 pressed together under a load L gives the following result:

$$r_c^3 = \frac{3}{4}(K_1 + K_2)\frac{R_1 R_2}{R_1 + R_2}L \tag{3.24}$$

where K_1 and K_2 are elastic constants of the material of each sphere: $K_i = (1 - \nu_i^2)/E_i$ where ν_i is the Poisson ratio and E_i the Young's modulus of material i. For a contact between a sphere and a flat surface ($R_2 \to \infty$), assuming that both bodies have the same elastic constant K, one obtains:

$$r_c^3 = \frac{R}{K}L \tag{3.25}$$

3.4.2 The Johnson-Kendall-Roberts Theory (JKR)

Using smooth rubber and glass spheres Roberts (1968) and Kendall (1969) noted that at small loads, contact areas were significantly larger than those predicted by Hertz and that, in particular, they were still finite for zero load and even for loads below zero. This resulted in the Johnson–Kendall–Roberts (JKR) theory for elastic point contacts, where adhesive forces acting between the two solids are taken into account. From their calculations they obtain [JKR71]:

$$r_c^3 = \frac{R}{K}(L + 3\pi W_{12}R + \sqrt{6\pi W_{12}RL + (3\pi W_{12}R)^2}) \tag{3.26}$$

where the surface energy $W_{12} = 2\gamma_{SV}$ (γ_{SV} is the interfacial energy). For $\gamma = 0$ this reverts to the simple Hertz equation $r_c^3 = RL/K$. At zero applied load the contact radius is finite and given by:

$$r_0^3 = \frac{6\pi R^2 W_{12}}{K} \tag{3.27}$$

The JKR equation 3.26 shows that for small negative loads, i.e., forces pulling the surfaces apart, there is still adhesion up to a "pull-off" force:

$$F_{po} = -3\pi R\gamma_{SV} \tag{3.28}$$

and the separation occurs abruptly when the contact radius has fallen to $r_{po} = 0.63r_0$. The pressure distribution within the contact circle is not uniform. In particular, the pressure in the center spot is a factor 1.5 larger than the average pressure [Mau92]. One main problem of JKR theory becomes obvious when calculating this stress distribution: The JKR theory would predict an infinite stress at the edge of the contact area.

The basic assumption for JKR theory is that the surfaces are elastically deformed by the adhesive forces. This is valid for liquids and soft materials, as for example polymers above their glass transition temperature T_g.

3.4.3 The Derjaguin–Muller–Toporov Theory (DMT)

For contacts between hard solids it is appropriate to assume that the surfaces do not deform due to the adhesive forces and the shape of the contact area remains Hertzian. DMT theory [DMT75] takes adhesive forces into account. The result for the contact radius under zero load strongly resembles the JKR result. However, the contact area is smaller because there is no deformation.

$$r_0^3 = \frac{2\pi R^2 W_{12}}{K} = \frac{1}{3} r_{\mathrm{JKR}}^3 \tag{3.29}$$

Moreover, the pull-out force, $F_{\mathrm{po}} = 2\pi R W_{12}$, is reached at $r_{\mathrm{c}} = 0$. The resulting pressures are zero at the edges of the contact zone, but not continuous inside.

A more realistic situation is often in-between those described by JKR- and DMT-theory. These describe the limits of very soft solids and hard solids, respectively.

Chapter 4

Friction

4.1 Classical Description

Amontons' law. In the early experiments by Leonardo da Vinci, Amontons, and Newton [Dow79] it was found that the (friction) force F_p needed to slide a body across a surface was directly proportional to the normal force F_N (usually exerted by the load $L = m \cdot g$ of the body with mass m). The friction coefficient μ is defined as the ratio of lateral to normal force:

$$\mu = F_\mathrm{p}/F_\mathrm{N} = \text{constant} \tag{4.1}$$

and adopts values between 0 and 1. Implicitly, Amontons' law contains two more assumptions, which are that the friction force does not depend on

- the contact area A between the macroscopic bodies
- the sliding velocity v.

From an intuitive point of view both assumptions are not evident.

Bowden and Tabor. Bowden and Tabor [BT73] presented a microscopic explanation of Amontons' law. They assume that — because of surface roughness — the effective contact area is much smaller than the apparent macroscopic one ($A_{\text{eff}} \ll A$). In equilibrium the normal force can be expressed by:

$$F_{\text{N}} = p_{\text{y}} \cdot A_{\text{eff}} \tag{4.2}$$

where p_{y} is the yield strength of the material. The friction force can be written as:

$$F_{\text{p}} = \sigma_{\text{c}} \cdot A_{\text{eff}} \tag{4.3}$$

where σ_{c} is the critical shear stress at the interface. The friction coefficient can thus be solely expressed in materials properties:

$$\mu = \frac{\sigma_{\text{c}}}{p_{\text{y}}} \tag{4.4}$$

This theory, however, appeared to be inconsistent with the Hertz theory (cf. Chapter 3.4, p. 26) which predicted that the contact area should vary as $F_{\text{N}}^{2/3}$.

Area of real contact. According to Bowden and Tabor the friction force equals the critical shear stress integrated over the area A_{eff} of real contact. The latter is usually much smaller than the apparent area of contact A because of surface roughness. Depending on the lateral length-scale, "micro"- and "nano"-scale junctions can be distinguished. They differ significantly in their behavior.

Static and kinetic friction. For non-lubricated interfaces the force needed to initiate sliding is larger than the force needed to keep it sliding, that is, the static friction force is greater than the kinetic one $F_{\text{s}} > F_{\text{k}}$. The same distinction applies to the static and the kinetic friction coefficients μ_{s} and μ_{k}. The surfaces remain "pinned" to each other until some critical shear force is reached. At this point the surfaces begin to slide past each other either smoothly or in jerks ("stick-slip").

4.2 Nanotribology

Adhesion-controlled friction. Particularly in the case of adhering surfaces, Amontons' law does not adequately describe the friction behavior with load because of the finite frictional force measured at zero and even negative applied loads [YCI93b]. The standard coefficient of friction in this case, as defined in equation 4.1, would vary enormously with the applied load, which renders it rather meaningless. In an effort to reconcile these results with the traditional picture of a single, constant coefficient of friction for a given system, the following friction law

$$F_{\mathrm{p}} = F_{\mathrm{p},0} + \mu F_{\mathrm{N}} = \sigma_{\mathrm{c}} A_{\mathrm{eff}} + \mu F_{\mathrm{N}} \tag{4.5}$$

has been used to describe the results, where $F_{\mathrm{p},0} = \mu L_0$ is the friction force at zero load [YCI93b]. Such friction is often termed 'adhesion-controlled' because of the finite friction at zero load, and yet equation 4.5 also conforms to some extent to Amontons' law, merging with it at high loads. We may also note that for 'adhesion-controlled' friction, the friction coefficient μ is given by $\mu = dF_{\mathrm{p}}/dF_{\mathrm{N}}$, which contrasts with 'load-controlled' friction, equation 4.1, where $\mu = F_{\mathrm{p}}/F_{\mathrm{N}}$.
Simultaneous adhesion, friction, and molecular contact area measurements have been made, both of unlubricated mica surfaces and mica surfaces coated with surfactant monolayers [Isr92a, Isr92b]. In all cases it was found that

1. the contact area varied with load as predicted by the JKR theory (cf. Chapter 3.4, [JKR71]),
2. the JKR adhesion energy is the same as the thermodynamic surface energy,
3. at low pressures the friction force is proportional to the contact area but not to the applied load, and
4. the results are essentially independent of sliding velocity (for $v < 10\mu$m/sec).

Adhesion contribution to the friction force. The friction force contains a contribution from adhesion and from the externally applied load [ICY94]:

$$F_{\mathrm{p}} = C_1 A + C_2 F_{\mathrm{L}} = \mu(\frac{4\gamma}{D} + F_{\mathrm{L}}) \tag{4.6}$$

where A is the contact area; F_{L} the force exerted by the external load; γ is the surface energy; and D the surface separation at rest. The constant C_1 is directly proportional to the surface energy γ and $C_2 = \mu$. The first term is the intrinsic adhesion contribution. For surfaces that are not atomically flat equation 4.6 reduces to Amontons' law.

Adhesion hysteresis and friction. While equation 4.6 relates the adhesion energy to the friction force, more elaborate models yield the conclusion that the adhesion *hysteresis* between surface energies measured during approach and retraction ($\Delta\gamma = \gamma_{\mathrm{A}} - \gamma_{\mathrm{R}}$) is the quantity of interest. According to this, the lateral force is:

$$F_{\mathrm{p}} = \frac{A \times \Delta\gamma}{D_0} = \frac{\pi r_{\mathrm{c}}^2}{D_0}(\gamma_{\mathrm{R}} - \gamma_{\mathrm{A}}) \tag{4.7}$$

where r_{c} is the contact radius. The critical shear stress is then:

$$S_{\mathrm{c}} = \frac{F_{\mathrm{p}}}{A} = \frac{\Delta\gamma}{D_0} \tag{4.8}$$

This strong statement could be confirmed experimentally [CHI91].

Cobblestone model. The cobblestone model [Tab82, HIGM89, ICY94] describes successfully the interfacial and boundary friction of two crystalline solids. It is not unlike the old interlocking asperity models of friction [Dow79], except that it is applied at the molecular level, where the external load is augmented by attractive intermolecular forces.

Figure 4.1 shows a sketch of the situation: As the upper surface is moved laterally by Δd it has to be lifted by ΔD before it can slide across the lower surface. On impact, some fraction ϵ of the kinetic energy is transferred to the lower surface. The cobblestone model rationalizes the notion that friction should be caused by adhesion hysteresis.

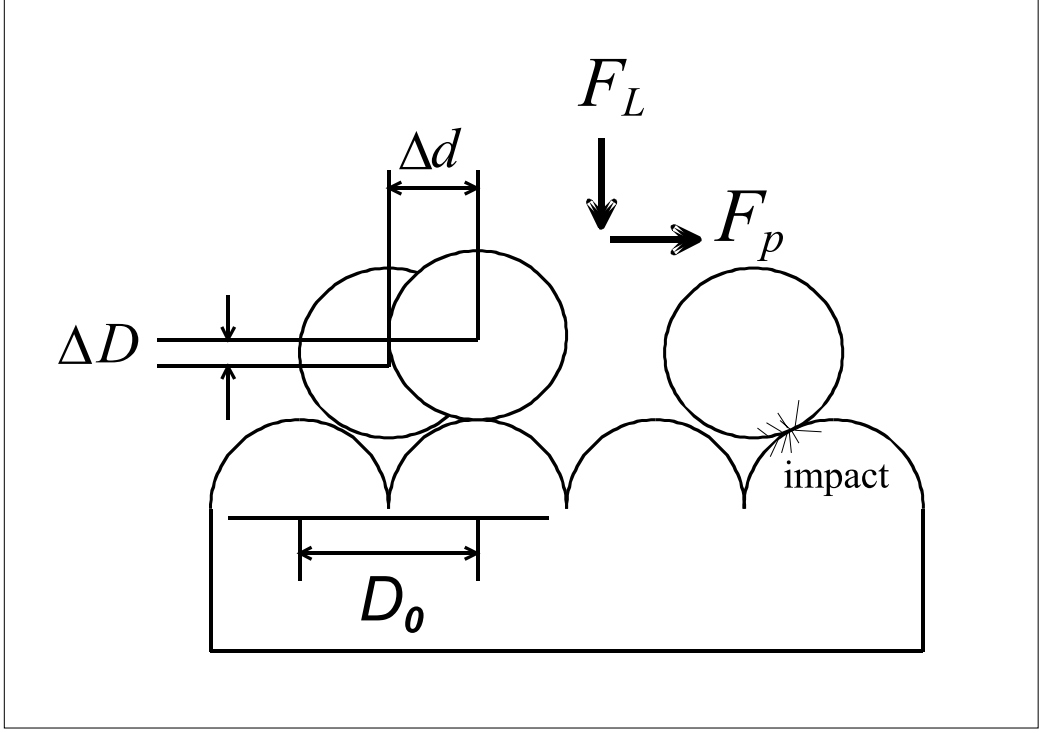

Figure 4.1: The cobblestone model illustrates the interfacial sliding of two molecular flat surfaces past one another. F_{L} is the load and F_{p} the lateral force (adapted from [ICY94]).

4.2.1 Stick-Slip Motion

When applying a linearly increasing lateral force to move a body that rests on a (rough) surface, it does not commence sliding immediately but holds its position until the static friction force F_{s} is overcome. At the point where this happens, it suddenly slips until the "next" potential minimum where the surfaces interlock again. Stick-slip is a wide-spread phenomenon causing, for example, the vibration of strings on instruments, squeaking doors and earthquakes.

Figure 4.2 shows a typical stick-slip curve. The height of the force spikes depends on the mechanical properties of the measuring system. There are several more detailed models for stick-slip friction that include the effects of molecular or asperity size, sliding velocity, various relaxation times, previous history, and other system parameters.

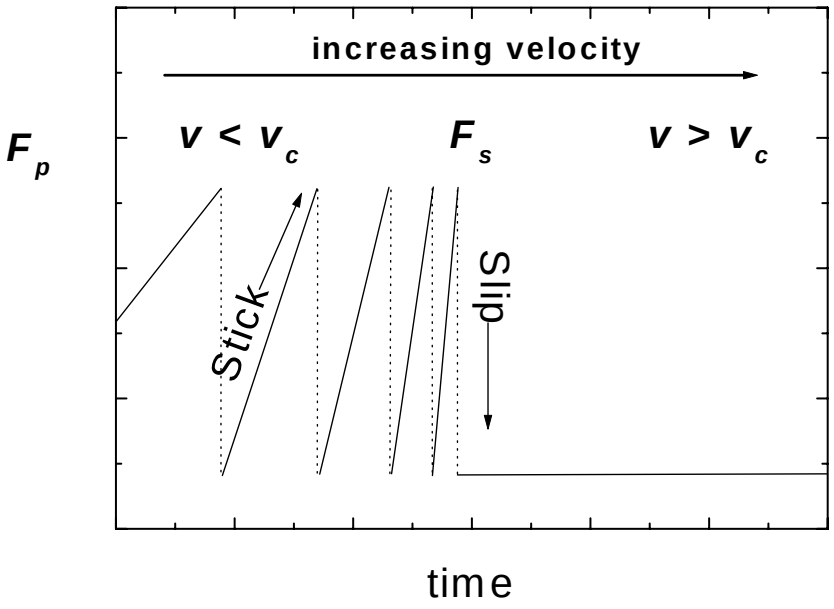

Figure 4.2: Typical stick-slip motion: The lateral force increases linearly (stick) until slip occurs. The sticking time depends on the velocity of the slider, the height of the stiction spikes remains the same and depends on the static friction force F_s. When the slider is moved at a speed faster than the critical velocity ($v > v_\mathrm{c}$) steady sliding is observed (adapted from [Per98]) .

Non-lubricated Surfaces

Surface topology (roughness) model. As the slider climbs an asperity on the substrate, a resisting force is encountered. Once the peak is reached, the slider will slide down rapidly into the valley, resulting in a slip. The measured friction trace vs. time will show regular or irregular stick-slip 'spikes' depending on whether the surface corrugations themselves are regular or not. The controlling factors of this type of stick-slip are the topology of the surface, and the elastic and inertial properties of the sliding surfaces which determine the rate of slip. Topological stick-slip is observed in the sliding of macroscopically rough surfaces, as well as in Friction Force Microscopy (FFM) experiments where the intermittent motion of the AFM-tip is a measure of the molecular-scale roughness of the surface [MMEC87].

Distance-dependent model. This model involves a characteristic distance, D_c, and a characteristic time, τ_c, required for two asperities to increase their adhesion strength after coming into contact. It suggests that two macroscopic surfaces adhere through their microscopic asperities of characteristic length, D_c. During shearing, each surface must first creep a distance D_c — the size of the contacting junctions — after which the surfaces continue to slide but with a lower (kinetic) friction force F_k than the original (static) value F_s. Once the surfaces have moved the characteristic distance, D_c, the friction rapidly drops from the static to the kinetic value. This type of friction has been observed mainly in dry (unlubricated) systems such as paper-on-paper [BHP94].

Lubricated Surfaces

Velocity-dependent model. In contrast to the above models, which apply to non-lubricated, solid-on-solid contacts, surfaces with thin liquid films in between exhibit different stick-slip mechanisms. One of the simplest models is a pure velocity–dependent friction law. In this case there is a high static friction force F_s, when the surfaces are at rest because the film has become solid-like. Once the shearing force exceeds this value, the surfaces slide with a lower kinetic friction force F_k, because the film is now in a molten,

liquid-like state. Stick-slip sliding proceeds as the film passes successive freezing-melting cycles [Rob91, TR90].

Critical velocity. In general, the stick-slip behavior disappears above some critical velocity v_c (cf. Figure 4.2), where the motion continues smoothly in the liquid-like state. This critical velocity is found to be well-described by an equation based on a phase transition model, i.e., that the interfacial film undergoes solid-liquid transitions during sliding and stick-slip. The critical velocity can be written as [YCI93b]:

$$v_c \approx \frac{F_s - F_k}{5k\tau_0} \tag{4.9}$$

with k the spring constant of the lateral slider system; and τ_0 the characteristic nucleation or freezing time of the film. Typical values of the critical velocity for molecular films are in the range of a few μm/s. In the case of polymers one can imagine that the characteristic time τ_c, that could also be called a "reaction time" to the exterior disturbance, is closely related to relaxation times of the polymer chains that actually dominate the rheological behavior of the polymeric film and, hence, also determine the shear viscosity.

Tribological phase diagram. Both friction and adhesion hysteresis vary nonlinearly with temperature. Often they pass a maximum at a certain temperature T_0. The temperature dependence of these dissipative forces can therefore be displayed in a schematic phase diagram. From experiments it is known that with varying parameters (cf. Figure 4.3) the bell-shaped curve can be shifted along the temperature axis. All these effects are also highly correlated with one another.

Another possibility to vary the rheological properties of the lubricating composites is to change their chemical structure. Examples would be the chain length variation of thiols, or the molecular weight variation of perfluoropolyether lubricants.

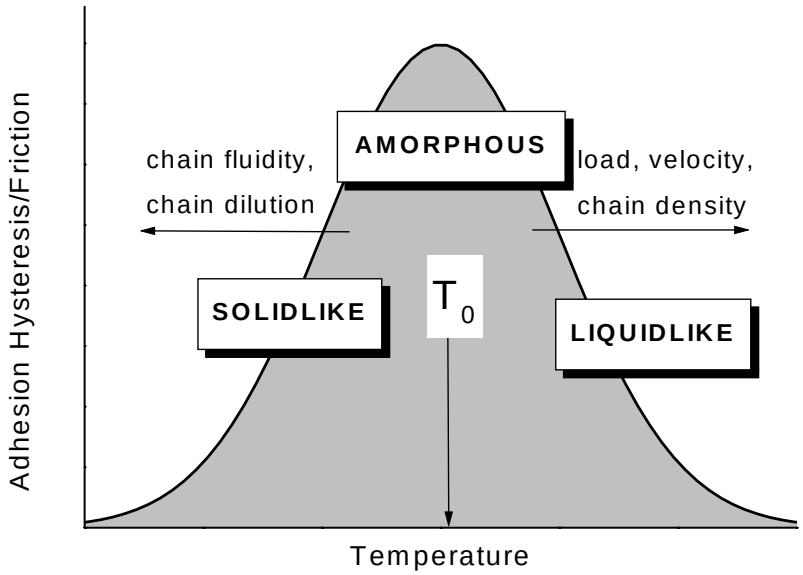

Figure 4.3: Friction phase diagram for the trends observed in boundary layer friction (adapted from [YCI93b]).

4.3 Lubrication

There are mainly two reasons why friction in applications should be minimized:
a) Kinetic energy of the moving bodies is dissipated into thermal energy and therefore "lost" for the original purpose of moving them.
b) The surfaces in sliding contact are destroyed. This is called "wear".
It has always been a goal to reduce interfacial friction by the application of lubricants. They "work" because of their particular physical properties, that is, their fluid behavior in the interfacial situation. They prevent the direct contact of the sliding surfaces by keeping them at a constant distance, determined by the lubricant layer thickness. Hence, the surface asperities do not touch. Instead of a solid-contact stick-slip behavior the lubrication promotes a viscosity-dominated sliding of the surfaces. Thus, the influencing molecular parameters are shifted from the phonon generation (friction) and rupture of atomic bonds (wear) in crystal lattices to the relaxation of polymer chains. In macroscopic terms these are described by the visco-elastic properties of the lubricant. They can be different from the bulk because of the geometric confinement. As usual, they depend on temperature, frequency (sliding velocity) and the interaction with the coated surfaces.

4.3.1 Different Lubrication Regimes

Experiments have shown that as a liquid film becomes progressively thinner, its physical properties change, first quantitatively and then qualitatively [vAG90b, HG92, Gra91]. The quantitative changes are manifested by an increased viscosity, non-Newtonian flow behavior, and the replacement of normal-melting by a glass transition. But the film still remains recognizable as a liquid. For even thinner films, the properties change qualitatively: First-order phase transitions can now occur to solid or liquid-crystalline phases [GMIH90, TR90, YCI93b, YI93], whose properties can no longer be characterized in terms of bulk or continuum liquid properties such as viscosity. These films now exhibit yield points and their molecular diffusion and relaxation times can be 10 orders of magnitude longer than in the bulk liquid or even in films that are just slightly thicker [Isr92c]. Thus, there are mainly three tribological regimes that can be distinguished and categorized by the properties of the lubricant layers.

Bulk Regime

In the bulk regime the lubricant films are thicker than 10 molecular diameters. Compared to the radius of gyration R_g of the polymers involved this is very thick, i.e., no effects of a confined geometry come into play and the interaction with the substrate is of negligible importance for their viscoelastic properties. The dynamic behavior is dominated by a Newtonian viscosity, short relaxation times, and the absence of a glass transition or a yield point.

Boundary Lubrication

In this case, the films are molecularly thin, i.e. consist of less than four monolayers of the lubricant molecules. This can often be achieved by applying high normal pressures and/or low shear rates. In this regime a rather rich phenomenology in-between fluid–like and solid–like behavior is found: It is possible to observe liquid-solid phase transitions, new liquid-crystalline states or an ordering that is induced by the surface structure of the underlying substrate. Here, tribological properties of the now solid-like lubricant film dominate the scenario: Flow does not occur until the yield point or the critical shear stress of the film is reached. Common lubricants are liquids. They have to wet the entire surface and should not become squeezed out if the surfaces are pressed against each other. Another important requirement is that the lubricating film maintains its liquid properties, i.e., high mobility, and does not solidify in a confined geometry. Water layers that condense from vapor between the surfaces because of capillary condensation (cf. Chapter 8.3.3, p. 144) can also act as lubricants. Actually, a single monolayer of water (2.5 Å) reduces the coefficient of friction between mica surfaces by an order of magnitude from $\mu_{\mathrm{dry}} = 0.3$ to $\mu_{\mathrm{H_2O}} = 0.03$ (which is remarkably close to the macroscopic friction of ice). For measurements characterizing dry surfaces this is not desirable but can only be avoided by performing measurements in (a) a liquid or (b) vacuum.

Intermediate Regime

For liquid films in the thickness range between 4 and 10 molecular diameters, their properties can already be significantly different from the bulk behavior. They still behave

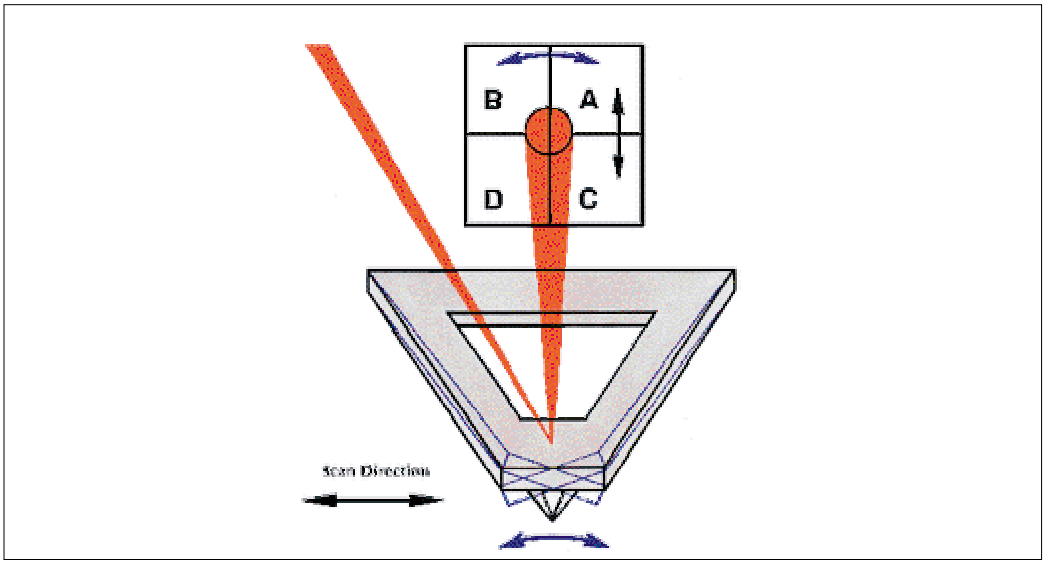

Figure 4.4: AFM principle: A laser beam is reflected off the cantilever towards a 4-segment diode.

---

like fluids, i.e. do not undergo a phase transition into a solid or liquid-crystalline phase but usually exhibit an increased viscosity as compared to the bulk. This regime has been studied by Granick and co-workers [vAG90a, Gra91, HG92] using a modified Surface Forces Apparatus for friction measurements. They found that liquid films become non-Newtonian in the 25 to 50 Å regime. For all liquids studied so far, the viscosity in this regime scales with $\eta = \dot{\gamma}^{-2/3}$, with $\dot{\gamma}$ the shear rate. This effect is called shear thinning.

4.4 Instruments of Nanotribology

There have been several recent developments of techniques that allow researchers to determine atomic and molecular forces between surfaces. In the following a short description is given of the most important, currently used devices. Emphasis will be placed on those issues that are relevant to our setup and experiments.

4.4.1 Atomic Force Microscope (AFM)

The atomic force microscope [BQG86, PBH90, Wie94] consists of a cantilever (length $l = 100 - 200$ μm) with a sharp tip at its end (radius $R = 10 - 100$ nm). When brought very close to the surface under investigation the interaction force between the tip and the surface induce a deflection z of the cantilever (cf. Figure 4.4). This deflection causes a laser beam reflecting off the cantilever to deflect by an angle of roughly $2z/l$ (optical-lever technique) [AHM$^+$89, MA88]. The deflected beam hits a 4-segment photodiode. Because of the optical cantilever, the deflection of the laser beam at the photodiode is roughly 1000 times the deflection of the cantilever [PBH90].

For topological measurements with the AFM it is sufficient to regard the difference between the top (A+B) and the bottom part (C+D) of the diode because only the vertical deflection of the cantilever is of interest.

Normal Forces and Force–Distance Curves

The vertical deviation (top(A+B)– bottom(C+D) signal) is a direct measure of the normal forces acting between tip and surface, and they can be monitored in a force–distance plot (Figure 4.5). The sample is moved in the z-direction using a piezoelectric tube. Far from contact one finds a straight base line. As soon as the interaction is strong enough to bend the cantilever, the reflected light beam is deviated from its central position on the detector. When the attractive force gradient exceeds the spring constant of the cantilever ($\partial F/\partial D > k$, with k the spring constant of the cantilever) an instability occurs and the cantilever jumps into contact. The height of the jump depends on the attractive force F_{attr}. Upon retraction the tip adheres to the sample. Usually, there is a hysteresis between approach and retraction which is contributed to the adhesion between tip and surface. The height of the "jump–out–of–contact" is determined by the adhesion force F_{adh} between the surfaces. Common frequencies for these approach-retraction cycles are $f \approx 1$ Hz.

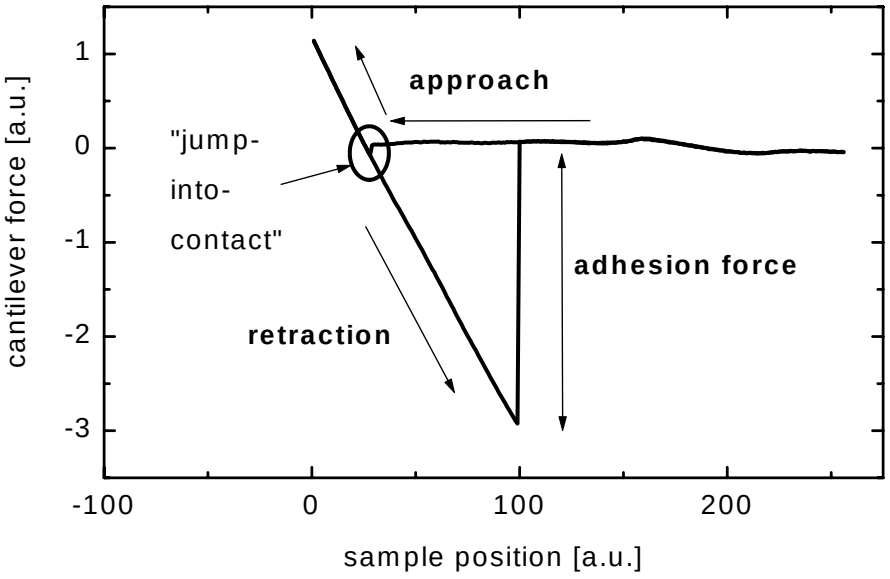

Figure 4.5: Typical force–distance curve obtained on a CN_x surface coated with a 6 Å lubricant layer. Upon retraction the adhesion force determines the height of the force step.

Scanning the Surface

For topological imaging the sample is moved in the x-y directions by a piezo tube while the tip remains at rest. The normal forces change during scanning, and so does the detected laser signal. The difference between the photocurrents of the upper and the lower detectors is fed into the controller of the piezo tube as a feedback signal. For measurements in constant force mode this signal is to be held constant. The image is generated by adjusting the piezo voltage such that the normal force is constant.

Friction Force Microscopy (FFM)

To be able to monitor the friction forces between the tip and a surface one has to scan the surface in contact mode. The measurement is carried out in the same way as in topological imaging (contact-mode) and can be performed at the same time. However, a different signal is regarded: Whereas topology uses the top(A+B)–bottom(C+D) signal, the friction image is constructed from the diagonal difference (A+C)–(B+D) signal which

is a measure of the horizontal bending and the lateral buckling of the cantilever. It is directly proportional to the lateral forces between the tip and the sliding sample. This gives a unique possibility of imaging the nanotribological landscape of an investigated area. Common scanning frequencies range from 1–100 Hz. The area can vary from several square microns down to a square of 1×1 nm (atomic resolution).

Limitations of FFM

Scanning speed. Typical scan speeds (sliding speed of the tip) for AFM and FFM measurements range from several tens of nm/s up to several μm/s which represents an upper limit for atomic resolution [BSS+93]. In most applied cases friction becomes important at speeds of several m/s.

Spring constant of the cantilever. Theoretical calculations of the spring constant of triangular cantilevers are difficult due to their complicated geometry. On the other hand, for rectangular levers, not only the vertical deflection, but also the horizontal one can be calculated accurately if the elastic constants and the geometry of the cantilever are known. However, exact determination of the latter is not easy and for most measurements too costly. Another possibility is the experimental determination of the spring constant from calibration of the response of a cantilever to lateral forces [OCS96] or the cantilevers' thermal noise.

Tip properties. The AFM tips are manufactured as sharp as possible to allow measurements with atomic resolution. Typically, the tip radius ranges from 10 to 100 nm. This has several consequences:

- Wear

  The contact area is very small, $A_c = \pi r_c^2 \approx 10^{-12} - 10^{-14}$ m^2. Therefore, the pressure exerted within the contact area is quite high ($p = F_N/A_c \approx 10$ nN$/A_c \approx 10^4 - 10^6$ Pa). Friction measurements have to be carried out in contact mode and are particularly interesting for varying (and increasing) normal forces. This leads to

an increased wear of the surfaces, and one has to make sure that the measurement itself does not change the tip nor the surface.

- Penetration of (soft) surfaces

  Soft surfaces often cannot bear the pressure exerted by an AFM tip. Therefore, a contact measurement, where a finite normal load is applied, easily destroys the surface under investigation. Also, the tip can penetrate the (often molecularly thin) layer and just images the (tribological) properties of the underlying substrate.

- Pollution of the tip

  The forces that act while scanning the surface can remove the sample molecules from the substrate (uncovering). First, the observed properties change from the ones of the sample to those of the substrate. Secondly, the tip is polluted with the samples molecules and hence the surface energy of the tip changes which again alters interactions between tip and sample. This may also be the intention: by functionalizing the tip of an AFM it is possible to tune the interactions with the substrate (Chemical Force Microscopy, [NVL97]).

4.4.2 Surface Forces Apparatus (SFA)

Normal Force Measurements

The aim in developing the SFA (Tabor, Winterton, Israelachvili) was to measure forces between surfaces or particles in air or a liquid. With this setup it is possible to perform measurements of forces (both attractive and repulsive) over a range of six orders of magnitude. Using the SFA, Israelachvili et al. were able to investigate the molecular origin of a wide range of forces acting between macroscopic surfaces such as van der Waals, electrostatic, and structural (oscillatory) forces [IT72, IA78].
Figure 4.6 shows a sketch of one type of Surface Forces Apparatus with a liquid cell (Mark II). Its heart are two cylindrical lenses that can be moved with respect to one another. Their surfaces are covered by thin mica sheets which after cleaving (thickness $\approx 1-3\ \mu$m) are atomically flat. The distance between the surfaces can be determined to within $\approx$ 1 Å by multiple beam interferometry [Isr87].

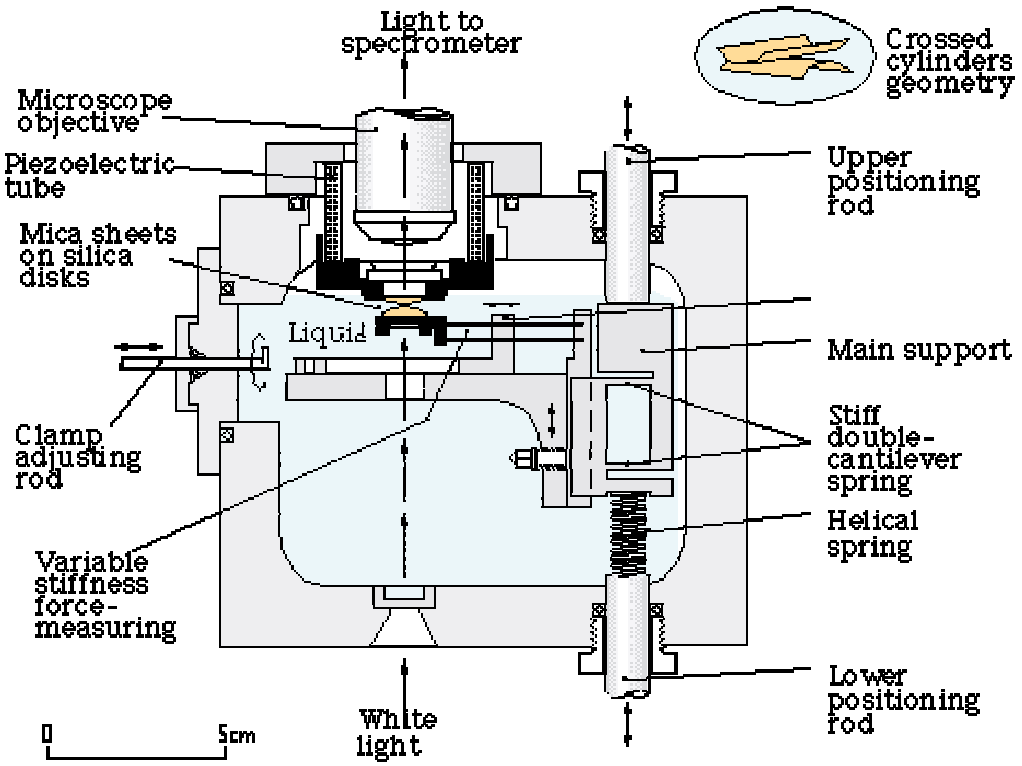

Figure 4.6: Surface Forces Apparatus Mark II (adapted from [Isr99]).

The lower surface is connected to a double cantilever spring. The deflection x of that spring is directly proportional to the force F acting between the surfaces with its spring constant k as a constant factor ($F = k \cdot x$). The force measured between the cylindrical surfaces can be related to the energy between two flat surfaces. The surfaces are approached slowly and the changing normal force is monitored. The advantages of the SFA are

(i) an atomically flat contact area in the range of several square microns (up to $30 \times 30 \mu m^2$)

(ii) the normal as well as the lateral forces can be measured directly (as opposed to the AFM/FFM)

(iii) the distance and the contact area and radius of curvature of the interacting region between the two surfaces can be measured directly.

The surfaces can also be held at a fixed vertical position and then be slid past each other at a fixed normal load. A very typical behavior observed in this regime is a stick-slip movement of the surfaces: Up to a certain applied lateral force the surfaces stick together because of their adhesion. Once this static friction force is overcome the surfaces start to slide. This leads to a decrease in the lateral force until the stick condition is fulfilled again. Typical speeds for these measurements are 1 μm/s.

4.4.3 Quartz Crystal Microbalance (QCM)

The fundamental driving mechanisms and physical properties of the quartz crystal microbalance will be explained in Chapter 6.7 (p. 92). Here we concentrate on the description of "nanotribological" experiments using quartz crystal resonators carried out by J. Krim and coworkers [KSC91, DK96a, DK96b]. They used AT-cut quartz crystals that exhibited pure shear oscillations at resonance frequencies of $f = 5$ MHz and 8 MHz, amplitudes of $A \approx 1$ nm, quality factors of $Q = 10^5$ and surface velocities of typically $v = 1$ cm/s. The electrodes were evaporated onto the quartz crystal in ultra high vacuum (UHV) and consisted of either smooth gold or rougher silver layers ([DK96a, DK96b]). In UHV at 77.4 K, monolayers of a non-polar neutral noble gas (Kr [KSC91], Xe [KC91]) were condensed on top of the electrodes. Since the binding derived only from van-der-Waals forces it was very weak (0.2 nN). If the quartz surface oscillated the inertial mass of the adsorbed monolayers led to their slippage. The inertia was extremely weak and was not able to move the adsorbate layers over the lateral barriers of the bonding potential. In actuality the potential surface was slightly tilted and this resulted in a reduced lateral diffusion barrier in the direction of the lateral forces and induced a slow thermally activated creep of the adsorbate layer in direction of the external lateral force, F_p. The drift velocity was proportional to the driving force. The quartz oscillation was driven by a conventional Pierce oscillator circuit [HH80] and the frequency and damping of the quartz resonance was determined from the free decay of a driven oscillation after switching it off. The adsorbed film produced shifts in both frequency and amplitude of vibration, which were simultaneously recorded as a function of pressure. After gas-phase corrections a charac-

teristic slip time (τ) was obtained from the relation $\delta(Q^{-1}) = 4\pi\tau\delta f$ [KW88]. It was assumed that the frictional force was directly proportional to the sliding speed (Stokes' law). Apart from a liquid-solid transition during condensation the authors discovered the following:

1. The solid phase exhibited more slippage on the smooth gold substrate than the liquid phase did. Solid films slid more easily on smooth gold than liquid films, while the reverse was true for rough silver substrates.

2. The rougher silver samples exhibited larger frequency shifts because monolayer coverings of these substrates with higher surface area required more particles.

3. The slip time was clearly dependent on the substrate velocity which indicated a nonlinear friction law.

More recent work of J. Krim describes the combination of a scanning tunneling microscope (STM) with a QCM [KDD93]. Here, the authors followed the frequency and amplitude of the quartz oscillation during water adsorption in vacuum. Besides the increase of these parameters with increasing vapor pressure, they observed an increased damping and frequency if a STM tip was engaged onto the quartz surface. The conclusions of the authors are vague when they claim that "a certain stiffness or solid-like quality develops in the film held between the tip and the substrate" [KDD93]. This effect could be similar to the one described in our work (cf. Chapter 6.7.3, p. 97) although the contact area for a STM tip is much smaller. In preliminary experiments an AFM tip was pressed onto a quartz surface, however, changes in the quartz signal were not observable. We accredited this to the fact that the interacting surface area was too small (contact radius $r_c \approx 10 - 100$ nm) compared to the actively oscillating quartz surface ($r_q \approx 2.5$ mm)(cf. Chapter 6.7.3).

Chapter 5

Development of a Setup to Measure Friction Based on Quartz Crystal Resonators

5.1 Background and Requirements

The use of quartz resonators for tribological measurements bridges the gap between the existing methods for nanotribological investigations, namely the Surface Forces Apparatus (SFA) and the Friction Force Microscope (FFM), and the friction phenomena in everyday life.

1. Both the SFA and the FFM work at frequencies of up to 100 Hz — typical frequencies for measurements are more likely to be in the 1 Hz range. An exception are oscillating tip experiments at kHz- and MHz frequencies [RSHA97, SBRA97, Stu98]. Quartz resonators cover 1–2 decades in the MHz range.

2. Closely connected to the scanning frequency is the scanning speed (relative speed between tip and substrate) that can be reached. For both the SFA and the AFM the maximum speed is 1 mm/s. Typical experimental speeds are in the range of several tens of nanometers up to several micrometers per second. The sliding speeds

in macroscopic machines, on the other hand, are closer to 1 m/s. Surface speeds of quartz crystal resonators reach that range.

Despite the limitations of the SFA and FFM, many concepts developed in this field can be adopted for the development of our experimental setup. In this work we transfer these known guidelines to the quartz resonator method. Further, we will compare results from our method with those from literature, most of them being obtained with either SFA or FFM.
The basic concept in our method is to approach a surface to a quartz crystal resonator and record the changes in frequency and bandwidth of the resonator.

Figure 5.1 shows a sketch of the quartz resonator setup. A macroscopic sphere adheres magnetically to the end of a normal force transducer that is moved in steps of 1 Å perpendicular to the quartz surface. The quartz crystal resonator performs shear oscillations and exerts a lateral force F_{p}.

5.2 Piezo Stage — Nanopositioning

For the fine approach of the surfaces a commercial available flexure stage (PZT) (P–732.ZC) manufactured by Physics Instruments (PI, Waldbronn, Germany) was implemented. The stage was able to travel 12 μm in the z-direction with a resolution better than 1 nm. The straightness of travel was better than 2 arcsec with a settling time of 1–2 ms. This was achieved by the use of three independent low voltage (100 V) piezo actuators mounted concentrically spanning an angle of 120°. Their operation is based on the piezoelectric effect (cf. Chapter 2.3). Hysteresis arises from polarization effects and molecular friction inside the actuators. The absolute position of a PZT depends on its "voltage history" and on the distance actually moved [HA97]. The linearity of the PZT expansion is typically on the order of 5%, and can be improved if operated in the range of 20% to 80% of its maximum voltage (24–96 V, $2.4 - 9.6$ μm). The life-time of a piezo stack increases the lower the applied voltage×time product. As a consequence the piezo was mainly driven in the range from 2.5 to 4 μm (travel range: $-2 - +12$ μm) and the voltage was released after completion of the experiments.

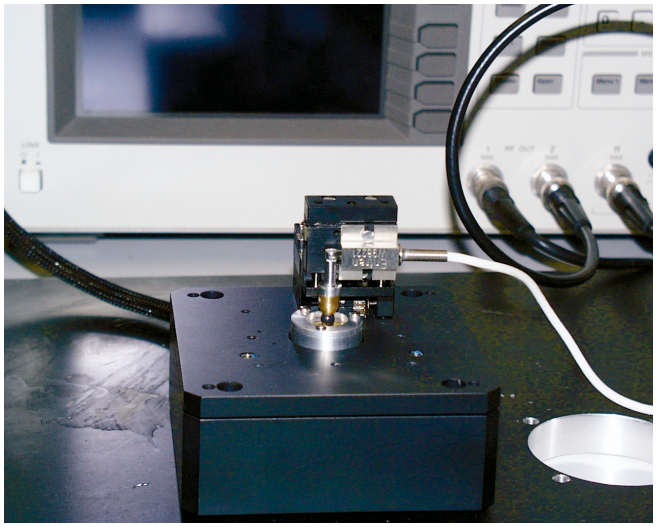

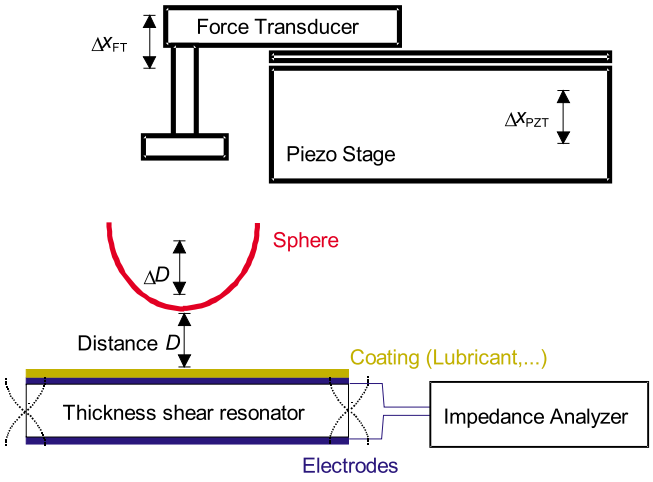

Figure 5.1: Photo and sketch of the quartz resonator setup for friction measurements.

5.2.1 Capacitive Sensors

To circumvent hysteresis, non-linearity, and drifts of the piezo actuators, a closed-loop feedback control was used: An air-capacitor consisted of a probe and a target plate with an active area of $A = 16.6$ mm^2 and a nominal range of 15 μm. Its capacitance depended on the separation of the plates ($C = \epsilon\epsilon_0 \times A/d$) and was compared to an internal reference capacitor of $C = 10$ pF. Changes of the distance D between the two plates caused a change in capacitance and the resulting signal was related to the deviation from the nominal distance D_0 where the capacitance of the sensor equals the one of the internal reference capacitor. The output voltage is related to the plate separation by $U_{\text{out}} = 10\ \text{V} \times (D/D_0 - 1)$. At closest approach, $D = 7.5$ μm, the monitor signal drops to -5 V, whereas at the maximum separation, $D = 22.5$ μm, it reaches $+5$ V. Its resolution is limited by electronic noise in the signal processing electronics (noise density 1.15 $\mu\text{V}/\sqrt{\text{Hz}}$). The specifications of the capacitor are summarized in Table 5.1.

Table 5.1: Technical specifications of the capacitive sensors.

Parameter	typical	maximum	units
Noise (f =100 Hz)	1.2	1.75	pm/$\sqrt{\text{Hz}}$
linearity	0.05	0.1	percent
expansion (thickness)	180	220	nm/°C
air pressure		0.013	nm/hPa
humid partial pressure		-1.7	pm/hPa
temperature		0.042	nm/°C

Compared to effects from common variations of temperature (± 1 °C) and relative humidity ($\pm 10\%$) the fluctuations induced by electronic noise and non-linearity were negligible. An E-802.50 Position Control Circuit (PCC, PI, Germany) was used to compare the control voltage input and the sensor reference signal in order to generate the amplifier control signal. Mechanical resonances were suppressed by notch filters. The E-515 interface module (Physics Instruments) contains an IEEE-488 card and can be directly controlled from a computer using a simple command language. Manual control is also possible but does not achieve the high positioning accuracy of the digital control (0.1 nm according to man-

ufacturer's specification). The PZT stage contains low voltage piezo stacks (LVPZT). The power is supplied by an amplifier module (E-503.00) with three channels providing $P^{max} = 6$ W maximum output power (max. output current $I^{max} = 60$ mA) for each channel. The output voltage can range from $-20 - +120$ V which corresponds to a positioning range from $-2 - +12$ μm. The nonlinearity is less than 0.5%.

5.3 Piezo translational stage PT 30 - Sample positioning

Since the PZT stage can only travel 12 μm, the sample has to be positioned within 12 μm from the quartz surface before commencing the measurement. This coarse-positioning was performed with a 3-axial PT30 translation stage (OWIS, Staufen, Germany): A small piezo is driven by voltage pulses to literally "hammer" the table to the next position, contracting to its original length after every pulse. The force of the hammering pulse is adjusted such that it just overcomes the frictional force of the table-track that holds the platform in place. The advantages compared to other piezo-crawlers are:

- Very small dimensions ($30 \times 55 \times 30$ mm) that cannot be achieved with conventional stages driven by mechanical micrometer screws
- Low weight (< 200 g)
- Large travel (5 mm along each axis) combined with high positioning accuracy (600 nm/step)
- No electrical currents when at rest
- Absolutely drift-free

5.4 Force Transducer

A sketch of the force transducer and its mounting is shown in Figure 5.2. The force transducer (ELG-H20, ENTRAN, France) was based on a strain gauge that is glued onto

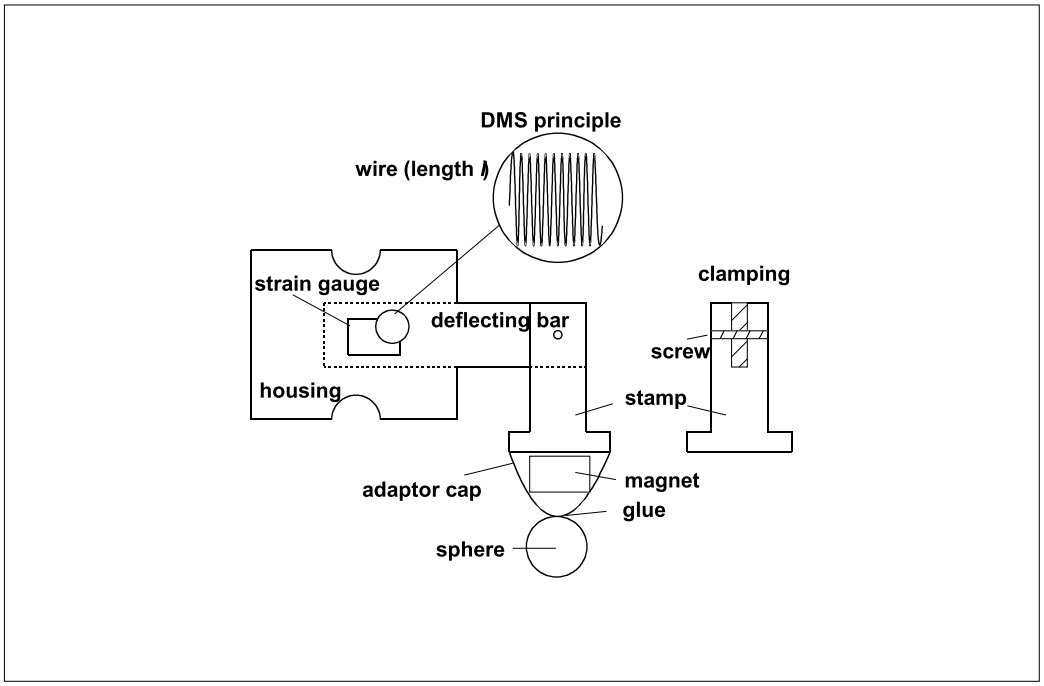

Figure 5.2: Sketch of the force transducer. A zoom onto the strain gauge shows its working principle. The Si_3N_4 sphere is glued onto a brass adaptor. A permanent magnet provides a drift-free and "easy-to-change" holding on the stamp. The clamping of the stamp provides a fixed orientation.

a small metal bar (material, $1\times3\times5$ mm^3). The deflection of the bar caused by application of a force perpendicular to its long axis was determined from the change in resistance of the strain gauge (DMS). The strain gauge was a folded wire with length l and resistance $R = \rho \cdot l$. When the bar was deflected the total change in length of the wire Δl causes a change in resistance ΔR.

The gram-force range was $\pm$20 g ($F = \pm 0.2$ N), the overrange limit $10\times$ full scale = 200 g (2 N). The nominal full-scale output was FSO = $\pm$100 mV. Combined non-linearity and hysteresis was $\pm 0.5\%$ FSO = 10^{-3} N. These force ranges appear too high for the occurring interfacial forces estimated to be in the μN range [Isr92c]. However, when the sphere comes into contact, differential measurements suffice for the purpose of this work. Although the absolute accuracy was only a mN, the differential sensitivity can be as good as 100 nN (cf. Chapter 6.2.2, p. 76), which was well in the range of interest.

5.4.1 Calibration - Spring Constant

The calibration of the force transducer was carried out with weights in the range from 1 mg – 5 g. Figure 5.3A shows the relationship between voltage and load, which was linear in the gram range as well as in the mg-range. The offset voltage was $U_0 = (0.986 \pm 0.001)$ V, and the slope $\partial U/\partial m = (0.305 \pm 0.006 \cdot 10^{-7})$ V/g. Figure 5.3B shows the voltage–deflection relationship, which was measured by defined bending of the force transducer using the piezo stage to perform this deflection. For approach we obtained a slope of $\partial U/\partial x = (-0.268 \pm 3.7 \cdot 10^{-5})$ V/μm, for retraction $\partial U/\partial x = (-0.276 \pm 1.37 \cdot 10^{-4})$ V/μm. For retraction a hysteresis was found (Figure 5.3C): After a previous maximum deflection of $x_{\max} = 7000$ nm ($\hat{=}$ 6.6 g) the force transducer remained deflected by $x_{\text{hyst}} = 352$ nm. The ratio was $x_{\text{hyst}}/x_{\max} \approx 2\%$. However, we consider this as a maximum value because hysteresis was not linear and increases strongly with the degree of previous deformation $x_{\max}$.

The spring constant k was calculated using:

$$k = \partial F/\partial x \quad = \quad g \cdot \partial m/\partial x = g \cdot \partial m/\partial U \cdot \partial U/\partial x$$

$$
\begin{aligned}
&= 9.81\ \mathrm{m/s^2} \cdot 3.28 \cdot 10^{-3}\ \mathrm{kg/V} \cdot 0.268 \cdot 10^{6}\ \mathrm{V/m} \\
&= (8620 \pm 260)\ \mathrm{N/m} \qquad (5.1)
\end{aligned}
$$

The high-weight regime in Figure 5.3A shows a strictly linear response, which was expected. In the low weight regime (< 20 mg) it was not possible to measure exact values because of two effects:

- **Mechanical drift** caused by load: Before the voltage reached a stable value we observe a unidirectional drift to a higher apparent weight. Probably, the deformation was subject to hysteresis.
- **Hysteresis**: The zero weight value shifted to higher voltages after loading it with heavier weights (> 1 g) and did not recover completely. Figure 5.3C illustrates this behavior: Shown are the voltage readings after removal of the load indicated on the x-axis. This indicates a permanent deformation of the bar which takes longer to recover than the time-scale of the experiment (≈ 1 min).

This hysteresis was also observed during our experiments. Approach–retraction curves, that usually give a useful insight into adhesion hysteresis, often had this offset on the x-scale, apart from the offset originating from thermal drift.

Estimation of deflection caused by the interfacial forces

When two surfaces approach each other the forces interacting between them at small separations cause the force transducer to deflect. Since the force was continuously monitored this deflection can be calculated at any point because we know the spring constant k. The x-scale in measurements shown in Chapters 6 and 7 is the travel of the PZT-stage. For a determination of the distance between the surfaces we will have to take into account ([IA78]) that if the base of the force transducer moves by an amount Δx_{PZT} (> 0 for expansion and < 0 for contraction) then the difference in measured force is:

$$\Delta F = k \Delta D \qquad (5.2)$$

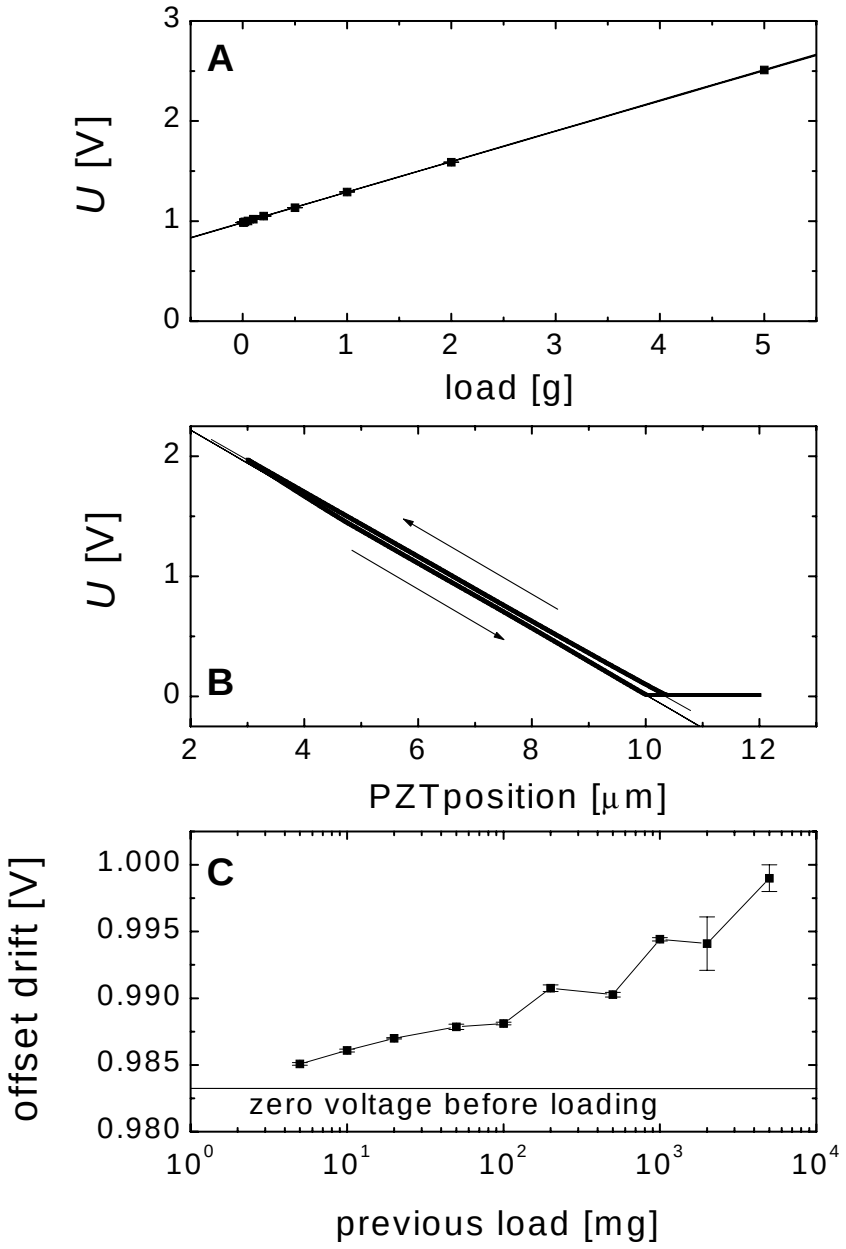

Figure 5.3: Calibrations of the force transducer: (A): Voltage–Load relationship. (B): Voltage–Distance relationship. (C): Hysteresis after loading. The offset voltage before loading was $U_{\text{off}} = 0.983$ V.

The change in distance ΔD (< 0 for approach and > 0 for retraction) between the surfaces when the piezo expands or contracts by a distance Δx_{PZT} is:

$$\underbrace{\Delta D}_{<0} = \underbrace{-\Delta x_{\mathrm{PZT}}}_{<0} + \underbrace{\frac{\Delta F}{k}}_{<0} \tag{5.3}$$

where ΔF is the change in measured normal force. If we also take into account the bending of the quartz plate (cf. Chapter 6.6.5, p. 89) the resulting spring constant of the system k_{s} is composed of both, the spring constant of the force transducer $k_{\mathrm{FT}} = 8620$ N/m and the quartz plate $k_{\mathrm{q}}(10\ \mathrm{MHz}) = 1.5 \cdot 10^4$ N/m:

$$k_{\mathrm{s}} = (k_{\mathrm{q}}^{-1} + k_{\mathrm{FT}}^{-1})^{-1} \approx (5500 \pm 260)\ \mathrm{N/m} \tag{5.4}$$

Jump into contact. The quartz surface is fixed whereas the spherical surface is suspended from a spring of stiffness k_{FT} (force transducer). At equilibrium, equation 5.2 is satisfied. For $\partial F/\partial D < k_{\mathrm{FT}}$ the equilibrium is stable, whereas if $\partial F/\partial D > k_{\mathrm{FT}}$ it is unstable. Thus, there exist certain instability regions in which no forces may be measured, bounded by $\partial F/\partial D = k_{\mathrm{FT}}$.

Example: van der Waals forces. If an attractive van der Waals force between the surfaces is assumed one can write for approach and retraction:

$$\begin{aligned} \Delta F = &\ \frac{\partial F}{\partial D} \cdot \Delta D = +\frac{AR}{3D^3} \cdot \Delta D \\ \Rightarrow\ \Delta D = &\ \Delta x_{\mathrm{PZT}} + \frac{\Delta F}{k} = \Delta x_{\mathrm{PZT}} + \frac{AR\Delta D}{3kD^3} \end{aligned} \tag{5.5}$$

Thus, the deflection Δx of the force transducer induced by the attractive surface forces F_{attr} can be estimated.

The distance D at which a jump into contact of the surfaces occurs due to van der Waals forces is:

$$D = \sqrt[3]{\frac{AR}{3k}} \tag{5.6}$$

5.4.2 Capacitive Measurement

An optical determination of the distance between quartz surface and the surface of the sphere is not possible because there is no access for a light beam. However, a capacitive measurement could enable us to determine the interfacial distance: One plate of the capacitor is the ground electrode of the quartz resonator, the other one is a spherical surface that only has to be coated with gold and electrically contacted. We did this in experiments with optical lenses; their size allowed an electrical contact outside of the quartz area which was not possible for the smaller Si_3N_4 spheres that we used later on. By applying an oscillating voltage in the kHz–regime the electrical reactance $X = 1/\omega C$ of the capacitor can be measured. The capacitance increases with decreasing surface distance and an electrical short circuit occurs when the surfaces start touching.

5.5 Mechanical Stability

5.5.1 Mechanical Connections

In order to resolve small distances down to 1 Å it is necessary to avoid all possible sources of thermal and mechanical drift. The latter is generated mainly by "loose" connections that relax under load or external forces. As with an SFA, the entire setup has to be built as stiff and compact as possible.

5.5.2 Mechanical Vibrations

To avoid the transfer of environmental high frequency oscillations onto the setup it is placed on a heavy marble plate settled on YTONG-stones. This kind of support is established for optical as well as for AFM measurements. The piezo stage is tightly mounted onto a heavy base plate ($400 \times 400 \times 10$ mm^3, stainless steel, 10 kg). The translational stage (PT30) is mounted on top of it using an aluminum adapter piece to fit the holes in both tables. The force transducer is mounted onto the z-axis plate of the PT 30 translational stage in order to achieve parallel orientation of the force transducer and the quartz surface.

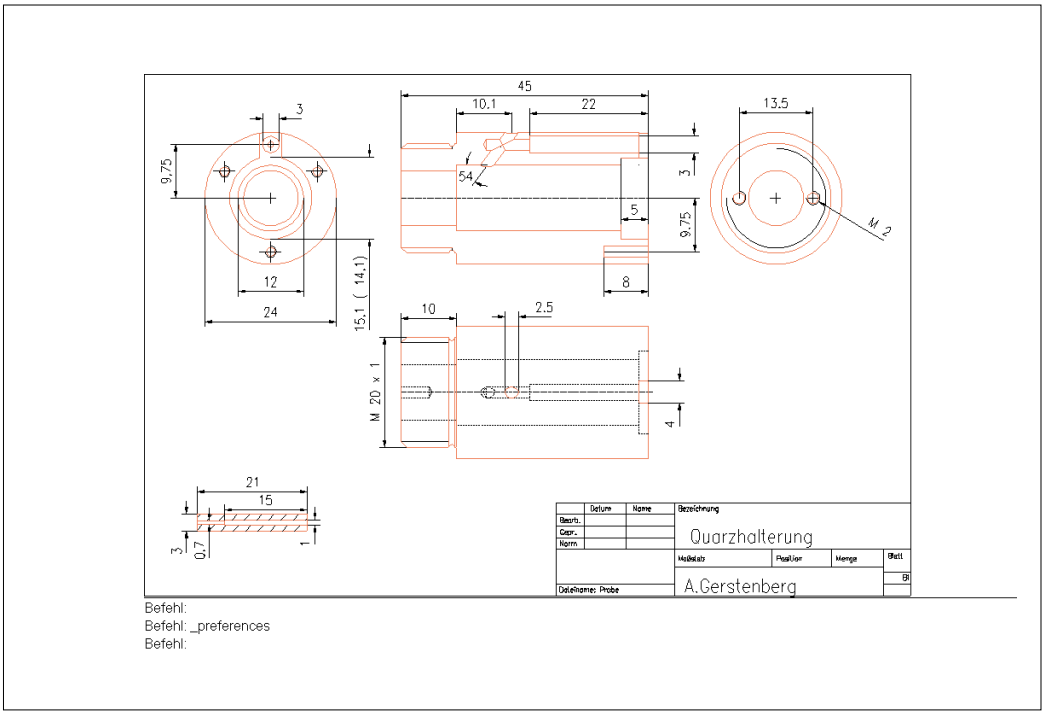

Figure 5.4: Engineering drawing of the quartz holder constructed by the machine shop of the MPI-P (©A. Gerstenberg).

5.5.3 Sample Holder

The holder for the quartz resonators has to fulfill several requirements:

- The quartz resonator must be positioned parallel to the base plate and held fixed with less than 1 μm clearance. Even if normal forces are applied these should not be able to push the plate out of its original position. On the other hand, the quartz plate must not be broken by the tight mounting.
- The resonance properties should remain the same as without a holder, e.g., a pre-deformation of the quartz that would induce internal stresses should be avoided. In particular, the oscillator damping (parameter: resonance bandwidth) should not increase because a high quality factor Q is crucial for the achievement of the high accuracy in frequency determination (cf. Chapter 5.6.2, p. 65).
- The oscillating part of the quartz should be freely accessible from above to enable

the approach of another surface.

- The electrical contact of the electrodes must be very stable to ensure the possibility of data acquisition at all stages of deformation of the quartz plate.

A holder that fulfills all these requirements was constructed with the help of the machine shop and the electronics department of the Max-Planck-Institute for Polymer Research in Mainz. Figure 5.4 shows a drawing of the quartz holder. The quartz lies in the top rim (diameter 14.1 mm) of the holder with the (smaller) "hot" electrode facing "into" the holder and, thus, establishing the electrical contact via a thin gold flag. The base part is threaded and is used to screw it into the fitting hole in the base plate. At the bottom a BNC–Adaptor is mounted for electrical contact with the Network Analyzer. The larger ground electrode covers the entire quartz and is contacted automatically when the cover is mounted (cf. Figure 5.5, p. 61).

5.5.4 Quartz Resonators

Geometries. Throughout this work only AT-cut quartzes were used. They were received from Quarz-Technik (QT Daun, Germany). Three types of geometries have been used:

- 4 MHz without facets: diameter 14 mm, thickness 0.4 mm, Quality-factors $Q = 10^4 - 10^5$.
- 4 MHz with facets: diameter 14 mm, thickness 0.4 mm. To avoid the occurrence of parasitic resonance modes close to the shear resonance mode, and to increase the quality factor a facet is grinded at the edge (cf. Chapter 6.15, p. 108, [Sau64b]).
- 10 MHz without facets: diameter 14 mm, thickness 0.18 mm, $Q = 5 \cdot 10^4 - 10^6$.

The geometry of all quartzes was plane-plane (both surfaces are parallel planes) and the blanks were polished.

Electrodes. Quartz blanks were first cleaned by a) ultrasonic bath in a 2% Hellmanex-water solution, b) 10-15 times rinsing with Milli-Q water, c) ultrasonic bath in ethanol, d) plasma-cleaning in a 90% Argon/10% Oxygen plasma at a power of P = 200 W.

After this, AFM images were taken at random samples. The results did not vary significantly between the different quartzes nor batches. An average root-mean-square (rms) roughness of $\sigma_{\text{rms}} = 10$ nm or below was observed. However, there were 100–150 nm deep holes (diameter $\approx 1\mu$m) scattered over the entire quartz surface. These holes were also reported by other users of similar blanks [Bun99]. This surface structure could not be removed nor covered by any of the applied coating procedures utilized during this work. After the cleaning procedure a 2.5 nm adhesive layer of chromium was evaporated onto the cleaned quartz blanks (vacuum: $p < 5 \cdot 10^{-6}$ bar). This was followed by the evaporation of the 100 nm-thick gold electrodes. Figure 5.5 shows the geometry of the electrodes.

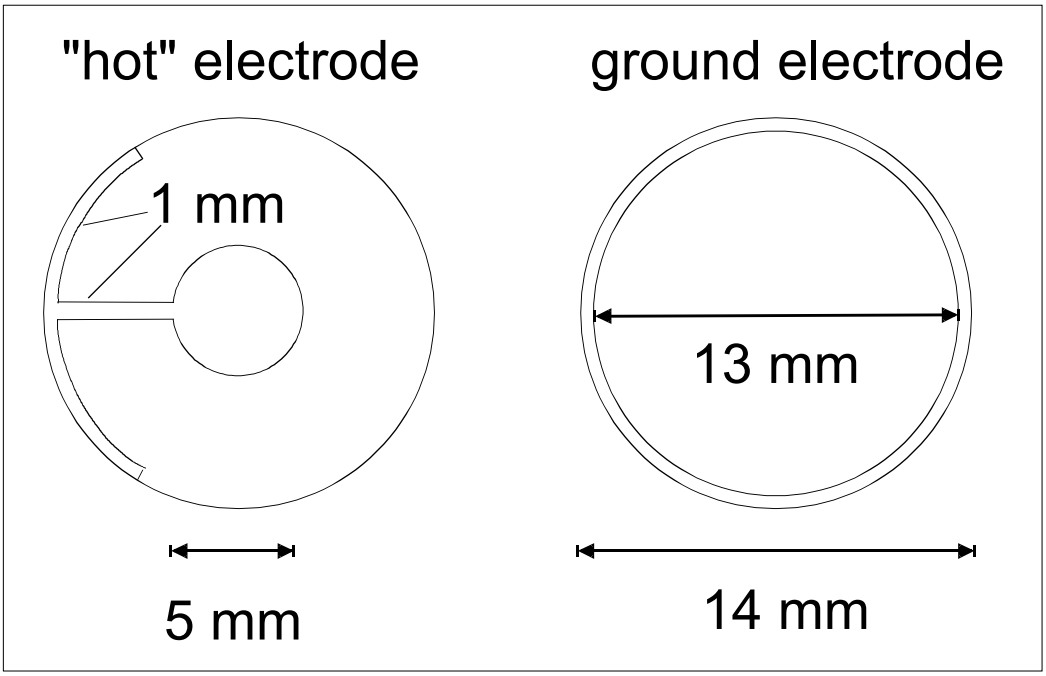

Figure 5.5: Shape of the evaporated electrodes.

The ground electrode had a diameter of 13 mm, thus, almost completely covered the 14 mm-diam quartz blank. This electrode was covered with the materials under investigation and was electrically grounded during experiments. No mirror charges will be induced if a charged surface approaches it. The 5 mm-diam small electrode was usually

not covered with other layers. It was "hot", that is, connected to the signal-carrying line from the Network Analyzer. Due to energy-trapping the shear oscillation is confined to an area of around the electrode: Outside this area the oscillating amplitude decays exponentially [Sau64a]. During friction experiments it is mounted face-down such that no electrical disturbances can intersperse from the surrounding media.

The surface roughness of the gold electrodes was also checked using AFM. Usual rms roughness is approximately $\sigma_{\mathrm{rms}} = 3$ nm after the evaporation procedure (cf. Figure 5.6A). However, it was possible to "smooth" the gold layers by annealing the substrates. Annealing procedures used to obtain atomically flat Au(111)-terraces (temperature T = 600 °C, exposure time t = 1 min) cannot be used for our purpose because of two reasons: If the quartz crystal would be exposed to a higher temperature than its Curie temperature ($T = 573$ °C) it would change its lattice structure and lose its shear resonator properties (cf. Chapter 2.2, p. 14, [Bot82]). Secondly, the rms roughness over a larger range even *increases* with this method because the gold terraces grow out of the substrate plane. By annealing the quartzes at T = 200–300 °C overnight it was possible to reduce rms-surface roughness down to $\sigma_{\mathrm{rms}} = 0.7$ nm (cf. Figure 5.6B). Now, reference frequencies for the first ten harmonics of every quartz were taken. For glass-transition experiments (Chapter 9) five spots on the electrode were measured with Null-ellipsometry [AB87] as a reference for the later determination of polymer layer thickness.

5.6 Data Acquisition

The quartz crystals are mechanical resonators with high resonance qualities ($Q \approx 10^5$). Another specific advantage is that due to their piezo-electricity the mechanical oscillation can be excited via an electrical signal applied to their surface. No additional electromechanical transducer is required for the transformation from electrical to mechanical oscillation and vice versa.

The quartz resonances can be probed either in the frequency or in the time domain (cf. Figure 5.7). Frequency spectra can be transformed mathematically into the time domain by Fourier transformation and vice versa. Signal acquisition for both domains is principally different and will be explained in the following. Both measurements have

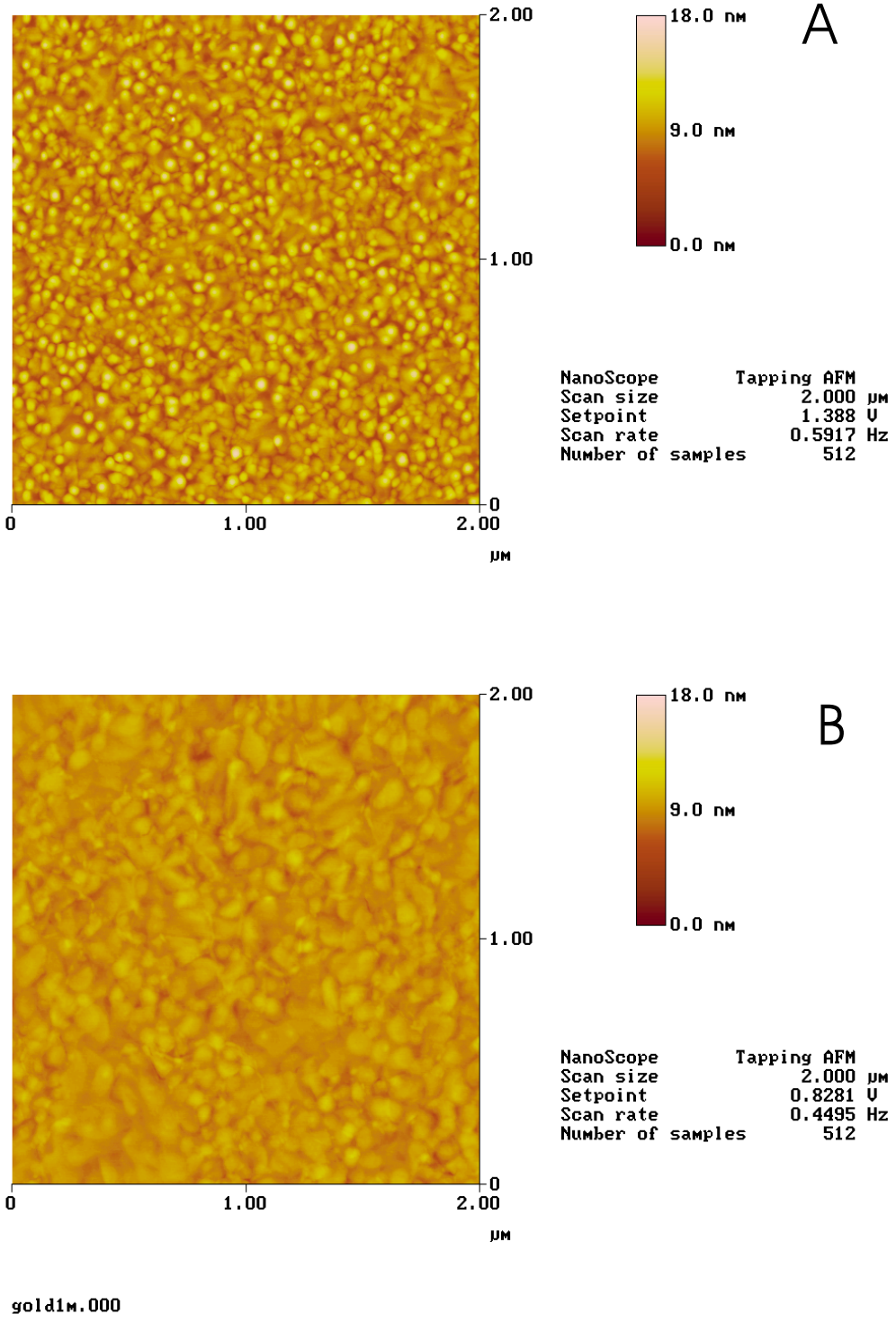

Figure 5.6: AFM-images of a gold electrode (A) *before* and (B) *after* annealing. (A) The surface structure on the micrometer scale is granular. The rms surface roughness is $\sigma_{\text{rms}} = 3.3$ nm. (B) The grains in (A) became flat and have "spread out". The rms roughness is now $\sigma_{\text{rms}} = 0.7$ nm.

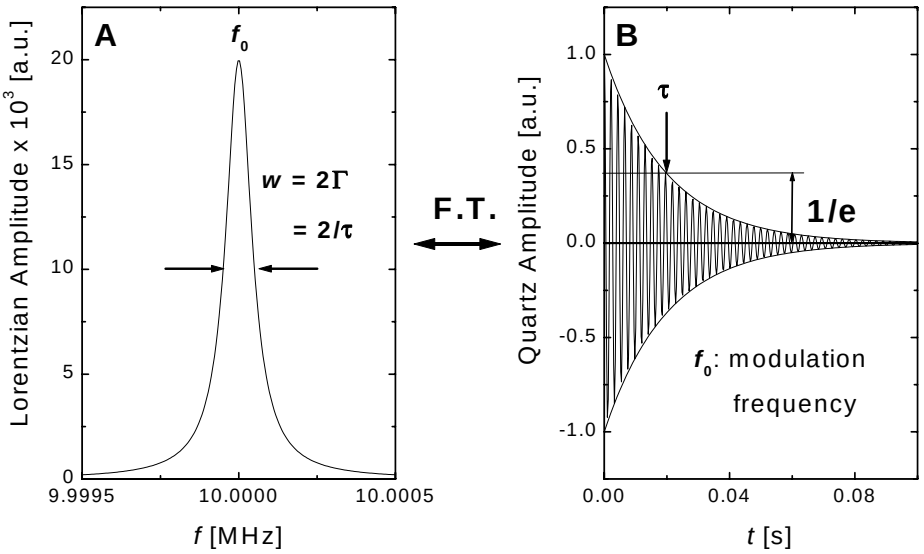

Figure 5.7: Quartz signals in the frequency (A) and the time domain (B). Fourier transform (F.T.) of the Lorentz curve in (A) provides the exponentially–decaying function in (B). w is the half-height-full-width of the resonance curve, $\Gamma = w/2 = \tau^{-1}$ is the damping constant. For unloaded quartz resonators the characteristic time is typically $\tau \approx 20$ ms.

---

specific advantages and disadvantages for our measurements.

5.6.1 HP Network Analyzer — Passive Measurements in the Frequency Domain

A Network Analyzer (NWA) HP 5100A (Hewlett-Packard) was used to measure the resonance curves of the quartz resonators in the frequency domain.

The principle of measurement is based on reflectometry. The NWA sends an electrical signal through a cable which is shunted at its end with the resonator. For practical reasons a π-network adaptor is situated in-between the cable and the quartz. The NWA corrects for the π-network and the user may ignore it. The reflection coefficient $r = (1 - Z^*)/(1 + Z^*)$ directly depends on the electrical impedance of the shunt resistance, the quartz resonator. In our measurements we recorded and fitted the conductance G and

the susceptance B of the complex admittance Y^*, which is the reciprocal of the complex impedance Z^*.

$$\begin{aligned} \text{impedance:} \quad & Z^* = R + iX \\ \text{admittance:} \quad & Y^* = G + iB \end{aligned} \tag{5.7}$$

with R the (Ohmian) resistance and X the (blind) reactance. A frequency window around the resonance frequency is swept to record the real (G) and imaginary parts (B) of the resonance curve.

Driving amplitudes. The driving amplitude provided by the Network Analyzer was adjusted in units of dBm. Therefore, throughout this work we refer to driving amplitudes in dBm. This unit is defined via the applied power P or voltage U: $\text{dB} = 10 \cdot \log_{10} P/P_0 = 20 \cdot \log_{10} U/U_0$ where P_0 and U_0 are the respective reference values. Thus, 10 dB corresponds to a change of the power by a factor of 10. In the definition of dBm the reference power is $P_0 = 1$ mW. Most common amplitudes used throughout this work are summarized in Table 5.2. All voltages refer to a 50Ω-matched system.

Table 5.2: Conversion of driving amplitudes.

power P [mW]	rms voltage U_{rms} [V]	dBm
100	2.25	20
1.0	0.225	0
0.10	0.071	-10

5.6.2 Analysis of the Resonance Curves

An ideal resonance curve is Lorentz–shaped (cf. Figure 2.3, Chapter 2.3.2, p. 18). Actually, quartz resonators often display "model-like" resonances because of their high mechanical quality factor $Q \approx 10^5$.

Curve-fitting. Both signals, G and B, are fitted simultaneously to obtain the following parameters:

- At the resonance frequency f the conductance G passes a maximum and the susceptance B crosses the x-axis. f can be determined with an accuracy of about 1 Hz, i.e., a relative resolution in frequency of 10^{-7} is usual. For relative changes in frequency even relative changes of $5 \cdot 10^{-8}$ can be achieved (cf. Chapter 6.2).
- The resonance bandwidth 2Γ is more susceptible to disturbances. Its absolute resolution depends on the quality factor Q of the used quartz. The lower Q, the wider the non-loaded resonance. Thus, the same absolute change in bandwidth $\Delta\Gamma$ results in a lower relative change $\Delta\Gamma/\Gamma$.
- The amplitude a of the resonance.
- A phase shift ϕ that reflects a loss of symmetry of the resonance curves.
- The y–offsets of the resonances O_r and O_i.

Ideally ϕ is zero. However, since the electrical connections to the quartz holder were highly complicated, calibration could not be done at the location of the sample. Allowing for an asymmetry of the resonances with a phase shift ϕ corrects this problem. The resonance frequencies are not affected by the phase shift. Resonance frequency, bandwidth, and amplitude are parameters that are identical for both the real (G) and (B) the imaginary part. The y–offset of the curves depends on the experimental setup and the calibration of the Network Analyzer. Physically, it is a resistance added in parallel. This results in six independent parameters that have to be fitted simultaneously. During this work the simultaneous fit of conductance G and susceptance B of the complex admittance with attention to the phase shift ϕ has been implemented to improve data quality and to improve the signal–to–noise ratio of the frequency determination (cf. Chapter 6.2). The parameters of relevance for analysis are the resonance frequency f, the bandwidth 2Γ, and — to a lesser extent — the amplitude a.

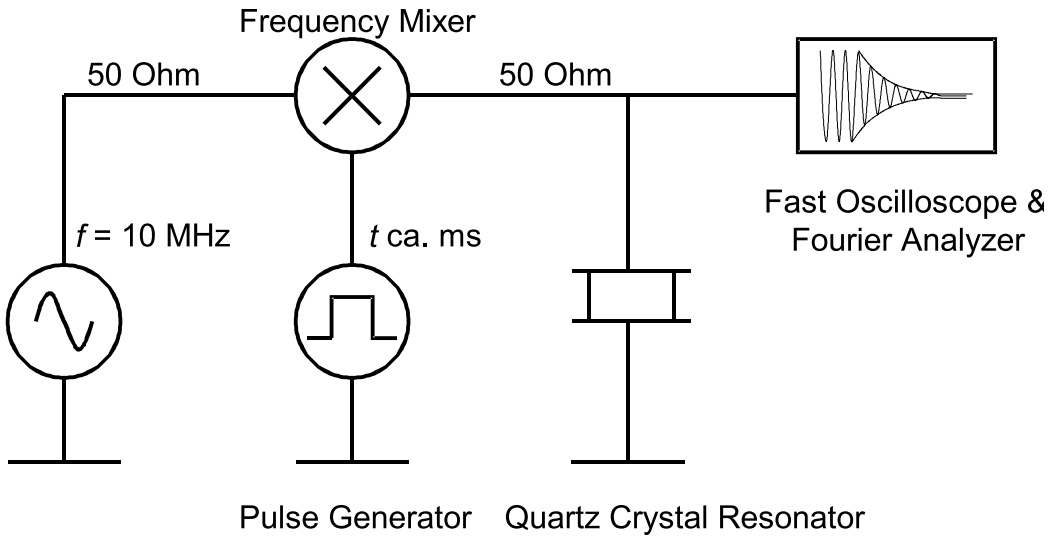

Figure 5.8: Equivalent circuit for the setup used for signal acquisition in the time domain.

5.6.3 Data Acquisition in the Time Domain

Figure 5.8 shows the setup used for monitoring the quartz oscillation in the time domain. It is similar to a circuit used in NMR-experiments (M. Hehn, M. Wilhelm, MPI-P). The intention is to generate a high-frequency pulse to excite the oscillation. After every pulse the free decay of the quartz oscillation can be monitored with a high-frequency dual–channel digital oscilloscope (Model 9410, LeCroy, Heidelberg, Germany). The pulses are generated by mixing the MHz-signal from the NWA with a rectangular millisecond-pulse from a signal generator. Figure 5.7B shows a typical decay signal in the time domain. The oscillation frequency is the eigenfrequency f_0 of the quartz, from the exponentially decaying envelope the damping constant Γ can be determined. The decay time is the inverse of the half-band-half-width of the Lorentz-curve ($\tau = 1/\Gamma$). The advantages of an acquisition in the time domain are the speed (a few milliseconds compared to a frequency scan that takes several seconds), and the possibility to directly observe the real–time movement of the quartz. Thus, if non-linear effects like stick–slip occur at the interface between quartz and approaching sphere, this should be visible in the time-dependent

movement of the quartz. The fast oscilloscope is also able to perform a fast Fourier transform of the time-domain data. The result is the overtone spectrum of the oscillating quartz (cf. Chapter 6.7, Figure 6.8, p. 87).

5.7 Control via Software

A program written in Borland Pascal 7.0 (BP) was used for control of the measurements. Borland Pascal is a Pascal programming language running in an DOS environment. Nevertheless, it was reasonable to use it for this setup because it unifies several advantages:

5.7.1 Programs and Units

The main program generates a menu and controls the access to the different units of the program. They are subdivided by their functions. For every device there is a BP unit. The most important ones are:

- HP network analyzer: data transfer to PC, curve-fitting algorithm.
- PZT flexure stage: drives a pre-chosen approach–retract cycle of the sphere.
- Analog-digital multimeter (PREMA, Mainz, Germany): recording of the values of force transducer, temperature control, capacitive distance determination, etc...

Borland Pascal works in a DOS environment and is stable with respect to intrinsic program breakdowns.

The program coordinates actions of the different devices, triggers them via GPIB and collects and stores the data. Knowledge about the order of data acquisition and device correspondence times can be essential when optimizing the acquisition cycles, e.g., minimizing the acquisition time.

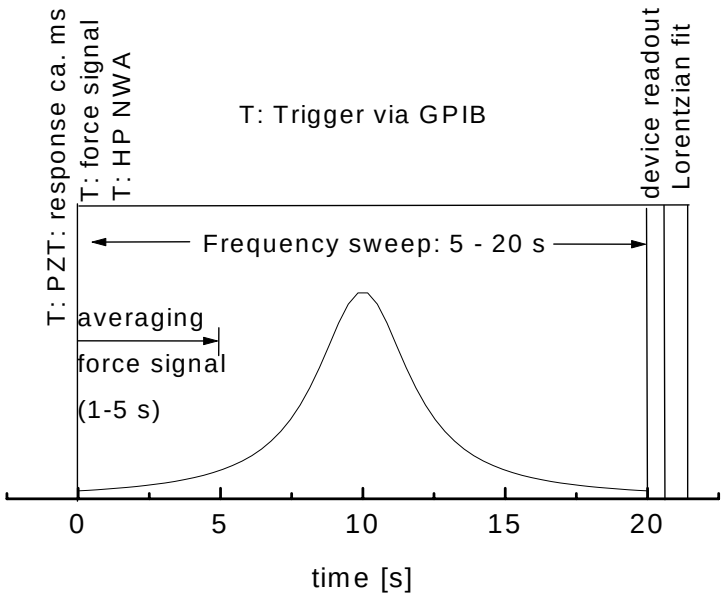

Figure 5.9: Acquisition cycle for a single data point. T: Trigger pulses from the PC for the different devices.

Data acquisition cycles. All the data plots shown in Chapters 6 and 7 consist of curves that show the approach of two surfaces. Our goal was always to get highest possible spatial resolution. Usually, one measurement consists of 1000–4000 data points (resonance curves). The acquisition cycle for one data point is the following (cf. Figure 5.9):

1. Step of the PZT stage (resolution: 1 nm – 1 Å).
2. Trigger pulses for multimeter and force transducer.
3. Acquisition of the resonance curve. One frequency sweep takes between 5 and 20 seconds depending on the chosen integration time (IF-Bandwidth). Note that only during this sweep does the quartz oscillate at a finite amplitude, for all other steps the quartz resonator is off resonance. The off-resonance amplitude $a_{\text{off}} \approx 1$ pm is negligible. This may be important for considerations of wear at the quartz surface.
4. Performance of Lorentz fit: Determination of resonance frequency, bandwidth and amplitude.
5. Device readout.

6. Acquisition of the voltage from the force transducer's amplifier.

The total time for an entire measurement largely depends on the acquisition time of the quartz resonance curve and can vary from 1 hour up to 24 hours. Common measurements ran overnight for a period of 12 hours. As soon as an elastic contact had been reached measurements were stopped to save time. This is appropriate because the focus of a run is the regime close before contact. Here, the surfaces still slide past each other and do not yet stick together.

5.8 The Opposing, Curved Surface

AT-cut quartz crystals are commercially available only in plane-plane geometries. The quartz is a probing device and sample "holder" concurrently, i.e., the top side (ground electrode) is coated with the material to be investigated. This already determines the geometry of one of the surfaces. To be able to calculate interfacial energies at a later stage, the opposing surface has to be chosen either as a plane or as a sphere (Derjaguin approximation, [Isr92c]). A complete plane-parallel approach of two macroscopic planes on a nanometer range scale is practically impossible. The best solution from a practical point of view was to choose spheres as opposing surfaces to the plane quartz substrates. They can be well modeled by use of the Derjaguin approximation.

5.8.1 Different Spherical Surfaces

The search for spherical surfaces that are smooth on an atomic scale resulted in the application of:

- Optical lenses: common glass processing procedures allow manufacturing of spherical surfaces that are highly (optically) polished. The surface roughnesses of high-end products are usually well below $\lambda/10$ of the used light source (common wavelength $\lambda = 632$ nm). Prices range between 30–100 DM/piece.

Table 5.3: Mechanical and physical properties of Ekasin 2000 ball bearings.

Density	3.15 g/cm^3
Vickers hardness	1500HV10
Young's modulus	280–320 GPa
Poisson number	0.26–0.28
Thermal conductivity	35 W/mK
Thermal expansion coefficient	3.5×10^{-6} K^{-1}

- Silicon nitride (Si_3N_4) ball bearings: Ceramic ball bearings have been developed for highly demanding industrial applications such as machine tool spindles. Therefore, they have unique properties (cf. Table 5.3), the price is 2–3 DM/piece.

The ideal properties as well as economic considerations led to the use of silicon nitride ball bearings. The manufacturer (Elektroschmelzwerk Kempten, Germany) gave the specifications in Table 5.3 and 5.4 for Ekasin 2000 ball bearings. They contain more than 95% Si_3N_4, the other components are oxygen (2–4%), iron ($< 1.7\%$), magnesium ($< 1\%$), tungsten ($< 1\%$), aluminum, calcium, and carbon. The best quality available was Grade

Table 5.4: Peak-Roughness and roundness of Ekasin 2000 ball bearings. V_{Dws}: Difference between the largest and the smallest diameter of a sphere, σ_{rms}: rms roughness.

grade	V_{Dws}	σ_{rms}
3+	0.08 μm	0.012 μm
5+	0.13 μm	0.02 μm

5+. Since Grade 3+ was not available in the small charges needed for experiments. The advantages are summarized below:

1. Surface roughness of < 20 nm. Our AFM measurements to confirm these values gave rms roughness values of σ_{rms} less than 3 nm.

2. Silicon nitride is a chemically inert, very hard material. No special care has to be taken to avoid changes in the chemical composition or the geometrical shape.

3. Silicon nitride is also a common material for manufacturing cantilevers (and their tips) used in friction force microscopy (FFM). This makes comparison with results from FFM more facile.

4. The almost perfect roundness makes the issue of sample mounting trivial: no matter in what angle the sphere is actually approached, the interface will always be a flat–spherical contact.

Chapter 6

Characterization of the Setup

With the setup described in Chapter 5, measurements were performed to characterize the effects occurring when a macroscopic sphere approaches the quartz surface. The following topics were investigated:

- Frequency shifts and their origin
- Change in bandwidth at the interfacial contact
- Comparison of frequency shifts on various harmonics
- Nonlinearities

6.1 Data Treatment

6.1.1 Plotting Conventions

Normal force. The resolution of the force transducer was 0.1 μN as determined from the noise level. It was calibrated with small weights (1 mg –10 g, see also Chapter 5.4). While the slope of the calibration curves was highly reproducible, there was an offset that varied between different measurements. One probable explanation is that once the bar was deflected, it did not recover completely (either mechanically or electrically). The

offset of the force was on the order of ($F_{\text{off}} = 1000$ mN) but was not constant between the different measurements. Thus, instead of zeroing the amplifier before every measurement it was compensated for in the data treatment: the force curves were shifted vertically to a zero offset position. Relative changes in forces were not affected by this correction.
For data analysis, the zero value of the force was arbitrarily chosen to be the smallest value of the data curves. Thus, no negative force values occur, although in many data plots attractive interactions are apparent. By convention attractive forces have negative values whereas repulsive interactions have a positive sign.

Hard-wall limit. The common convention in the display of AFM– and SFA–measurements is to plot the data such that the hard wall–limit is on the left side of the layer. We have chosen to display our data according to this convention.

Definition of contact. The "contact" point ($D = 0$) was defined according to the following features:

- the dissipative quartz signal passes through a maximum.
- the normal force passes through a minimum caused by attractive contact.

In many of the measurements these two features coincide and therefore provide an unambigious definition of the point of contact. In some measurements these features were less pronounced or even absent. In these cases the definition is somewhat arbitrary.

6.2 Data Noise and Resolution

Three parameters have been analyzed with respect to the attainable resolution: resonance frequency, bandwidth and normal force. The limits of resolution have different origin for the frequency and the force measurements. They are discussed separately in the following.

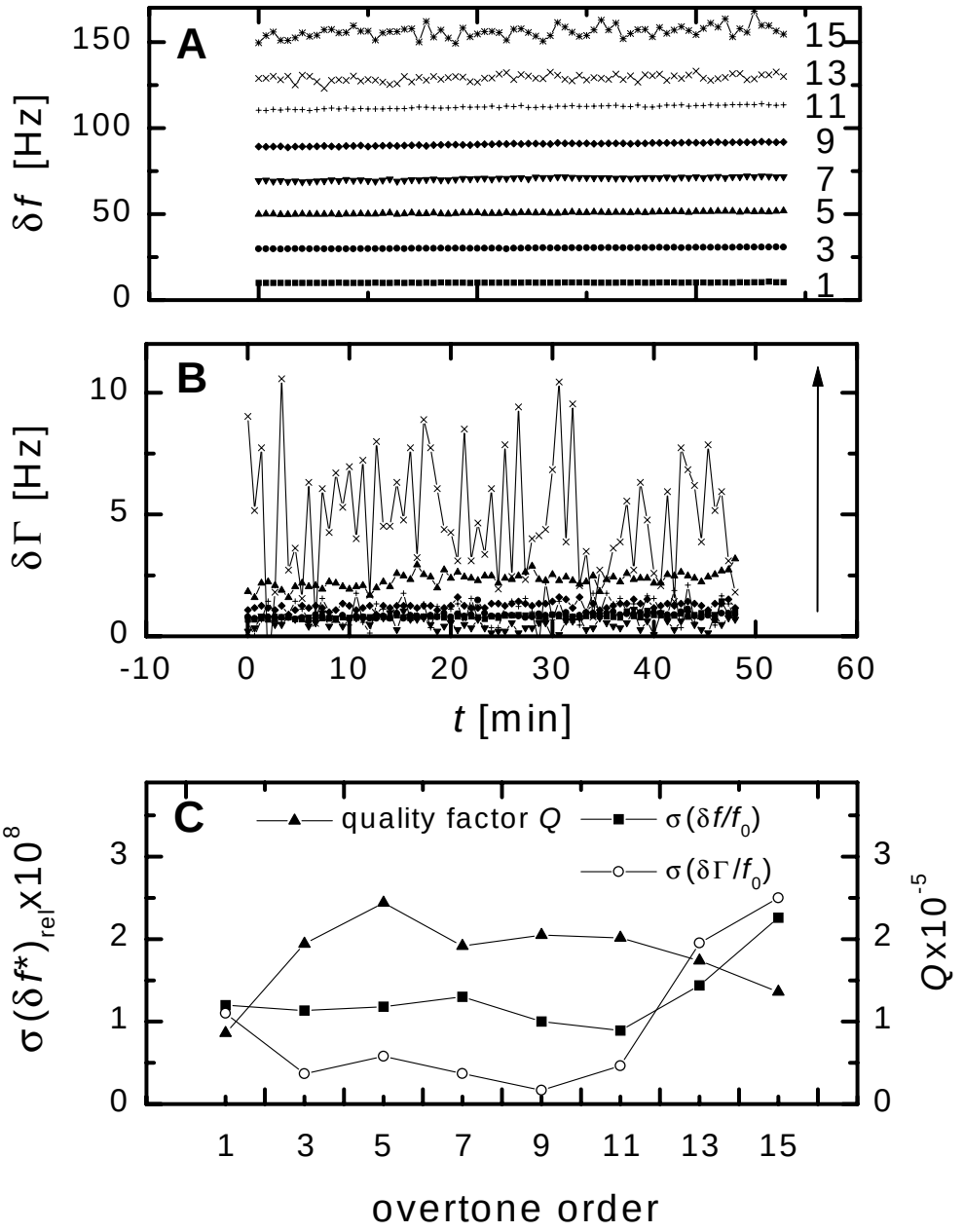

Figure 6.1: Analysis of the data noise in the frequency domain. (A) Frequency shifts for 8 different overtones. The numbers indicate the order of the harmonic. (B) Bandwidth shifts for 7 different overtones. The eighth overtone has been omitted for better display of the lower ones. The arrow indicates increasing overtone order. (C) Standard deviations of the frequency and bandwidth for the different overtones. The quality factors of the different overtones are displayed, as well.

6.2.1 Frequency and Bandwidth

The frequency and bandwidth were determined with a Levenberg-Marquardt algorithm to fit the resonance curves. The measurement on the first eight overtones of a 10 MHz-quartz was carried out at a constant temperature of $T = 24 \pm 0.2\,^{\circ}\mathrm{C}$ to avoid a thermally induced frequency shift. Figure 6.1A and B show the frequency shifts and changes in bandwidth for the first 8 harmonics of a 10 MHz quartz. The baselines were straight without any drift. Table 6.1 shows the standard deviations σ.

Table 6.1: Data obtained from statistical noise analysis of the data in Figure 6.1.

H# ($f \cdot 10^{-7}$)	$\sigma(\delta f)$ [Hz]	$\sigma(\delta\Gamma)$ [Hz]	$\sigma(\delta f/f_0) \cdot 10^8$	$\sigma(\delta\Gamma/f_0) \cdot 10^8$	$Q \times 10^{-5}$
1	0.12	0.11	1.2	1.1	0.86
3	0.34	0.11	1.1	0.37	1.94
5	0.59	0,29	1.2	0.58	2.44
7	0.91	0.26	1.2	0.37	1.91
9	0.9	0.15	1	0.17	2.05
11	0.98	0.51	1	0.46	2.02
13	1.87	2.54	1.4	1.95	1.74
15	3.39	3.75	2.3	2.5	1.36

Since we usually display the normalized values $\delta f/f_0$ and $\delta\Gamma/f_0$, the standard deviations σ for these are given as well (cf. Figure 6.1C). For the first 6 harmonics (10–110 MHz), the maximum noise level for both normalized frequency shift and normalized change in bandwidth, is 1.2×10^{-8}. The first 3–4 harmonics were used primarily for friction measurements. For these a resolution of $6 \cdot 10^{-8}$ in the frequency domain, for both the normalized frequency and bandwidth, could be achieved.

6.2.2 Normal Force

The normal force was detected via a strain gauge (DMS) that changes its electrical resistance when stretched. The resolution of the force measurement was only limited by the

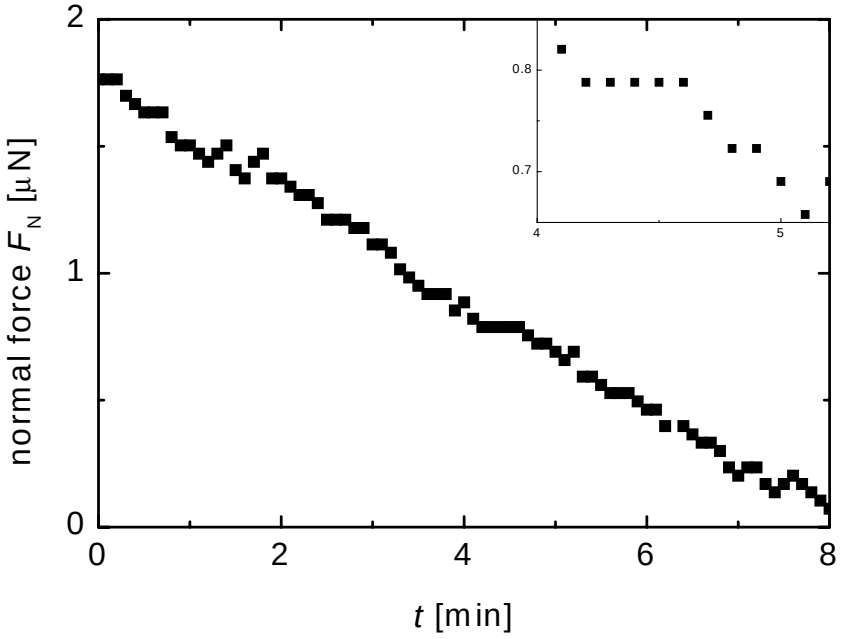

Figure 6.2: Resolution of the normal force measurement. Discrete steps are generated by the digitizing process of the analog force voltage signal. The inlet shows a zoom into a smaller region.

analog-to-digital converter (ADT, PREMA) used for the recording of the output voltage. Figure 6.2 shows a data trace with a small drift. The height of steps of the decaying "staircase" is determined by the resolution of the ADT and amounts to 32.5 nN. A resolution of 0.1 μN can easily be achieved.

6.3 Typical Data for a Gold–Gold Contact

Figure 6.3 shows a typical data curve for a contact of two gold surfaces; the quartz electrode and an optical lens (radius of curvature $R = 3.5$ mm) which was covered by a 200 nm gold layer. The typical surface roughness of the non-annealed gold surfaces was determined by AFM and was $\sigma_{\mathrm{rms}} \approx 3 - 4$ nm. The left-hand side of the plots are the non-contact regime, where the quartz parameters do not change and therefore form a straight baseline. Figure 6.3A shows the entire measurement whereas Figure 6.3B is a zoom into the regime where contact begins ($-20 - +10$ nm). The resolution in travel is 1 Å and both curves are smooth.

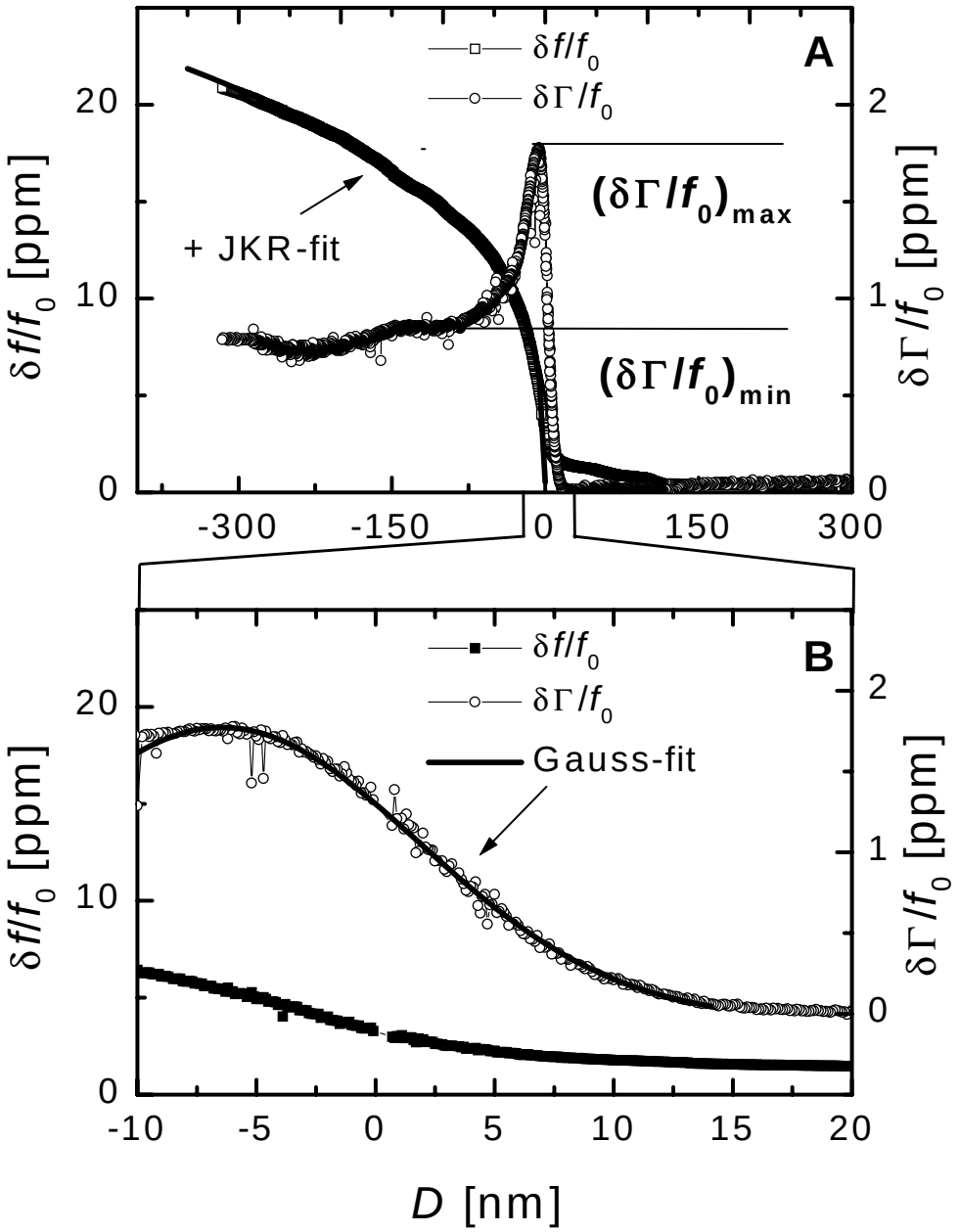

Figure 6.3: Typical measurement for a gold–gold contact. Panel (A) displays the entire measurement (total travel: 800 nm). A JKR-type function was used to fit the frequency shift $\delta f/f_0$ and coincides very well with the data. (B) Zoom into Panel (A) with a travel range of 30 nm. The bandwidth profile is fitted using a Gauss function (cf. Chapter 8.4.5, p. 152). Fit parameters are: width $w = 16.6 \pm 0.3$ nm, center position $x_c = 6.5 \pm 0.1$ nm and height $(\delta\Gamma/f_0)_{\max} = 1.8 \cdot 10^{-6}$. D is the nominal distance as given by the movement of the piezo stage.

On the right-hand sides the surfaces are in intimate contact. The measurement was carried out without a normal force transducer but with a stiff holder instead. As described in Chapter 6.6.5 (p. 89) the "weak" part is the quartz plate (thickness $h_q = 0.4$ mm, spring constant $k = 1.6{\cdot}10^5$) which bends upon normal pressure. Thus, the normal force increases linearly with the position of the piezo drive which is the x-coordinate.

Resonance frequency. The normalized change in frequency $\delta f/f_0$ increases smoothly with increasing load L on the quartz. This is ascribed to an increasing contact area $A_c = \pi r_c^2$ as shown in Chapter 6.7.3 (p. 100, eq. 6.12) where we find that $\delta f/f_0 \sim r_c$. According to JKR theory (cf. Chapter 3.4) the contact radius r_c increases as $r_c \sim L^{1/3}$. It can easily be seen that the frequency shift should scale as

$$\frac{\delta f}{f_0} \sim L^{1/3} \sim d^{1/3} \tag{6.1}$$

A modified allometric function ($f(d) = ax^b + c$) with $a = 3 \cdot 10^{-5} \pm 3 \cdot 10^{-8}, b = 1/3$ and $c = 5 \cdot 10^{-7} \pm 1.5 \cdot 10^{-8}$, fits the data quite well which confirms the model suggested for description of the frequency behavior. Therefore, we assume that in this regime both surfaces are in close elastic contact and do not slide past each other. Throughout all measurements this was reproducible and did not depend on the material combination. Thus, the smoothness of the frequency shifts may be used as a criterion for data quality.

Bandwidth. The normalized change in bandwidth $\delta\Gamma/f_0$ displays a distinct maximum **before** the elastic contact actually started. This was attributed to contact between surface asperities sliding past one another. With increasing overlap of these asperities the friction force increased. The peak had a Gaussian shape and was fitted with a Gauss function. We obtained a width of the Gauss curve of $w = 16$ nm which we believe can be related to the surface roughness of the gold (see AFM-images of gold surfaces on p. 63).

6.4 Smooth, Low-Energy Surfaces

Figure 6.4 shows a measurement of a contact between two fluorocarbon surfaces. The layers were applied to the surfaces in a plasma-polymerization process and were 110 nm

thick. They were highly cross-linked, very smooth (rms–roughness < 10 Å) and had low surface energy ($\gamma = 25$ mN/m) as determined by AFM and contact angle measurements [vOMT+97]. Measurements were carried out on the second (12 MHz) and third harmonic (20 MHz) of a 4 MHz quartz. Figure 6.4 shows the raw data (frequency and bandwidth): The frequency increased as expected for elastic contact, while the bandwidth did *not* display a maximum. Therefore, in Figure 6.4D $\tan\delta = \delta\Gamma/\delta f$ is displayed which is more sensitive to small changes in the dissipative part of the signal. No maximum in $\tan\delta$ was observed either. Figure 6.4A and B show the behavior of the normalized frequency shift and change in bandwidth. Both increase smoothly and, in particular, there is no maximum in $\delta\Gamma/f_0$ observable. This behavior of the friction is ascribed to vanishing lateral forces during interfacial sliding. At least, the forces were below the limit of resolution. For completeness, another magnitude is displayed in Figure 6.4C: the modulus of the complex frequency shift $|\Delta f^*/f_0| = \sqrt{(\delta f/f_0)^2 + (\delta\Gamma/f_0)^2}$. It increases as expected (according to the elastic coupling model and JKR) but does not provide any additional information. The relation between the complex numbers is: $|f^*|e^{i\delta} = f + i\Gamma$. As expected the effect on the higher overtone is always smaller. $\tan\delta$ is an exception but can easily be understood when considering the raw data in Figure 6.4A and B.

6.5 Dependence on Overtone Order

When the resonances of a quartz crystal resonator are measured passively with a NWA it is possible to excite and evaluate up to 20 overtones, depending on the quality of quartz blanks [Wol98]. Their approximate frequencies are at $f_n = n \times f_0$ with $n = 2k + 1$ and f_0 the fundamental frequency.

Figure 6.5 shows a measurement on 6 different harmonics ranging from 10 MHz to 110 MHz while approaching a Silicon Nitride (Si_3N_4) sphere to an amorphous carbon-coated (CN_x) quartz. Figure 6.5C shows the linearly increasing normal force upon contact. Frequencies and bandwidths increase as the sphere is pressed onto the quartz.
The lower panel shows the respective frequency changes for the different overtones at two fixed normal loads ($F_N = 4$ and 40 μN). The elastic coupling model predicts that the shift of the normalized complex frequency should scale with $1/f$. The linear fit in the lower

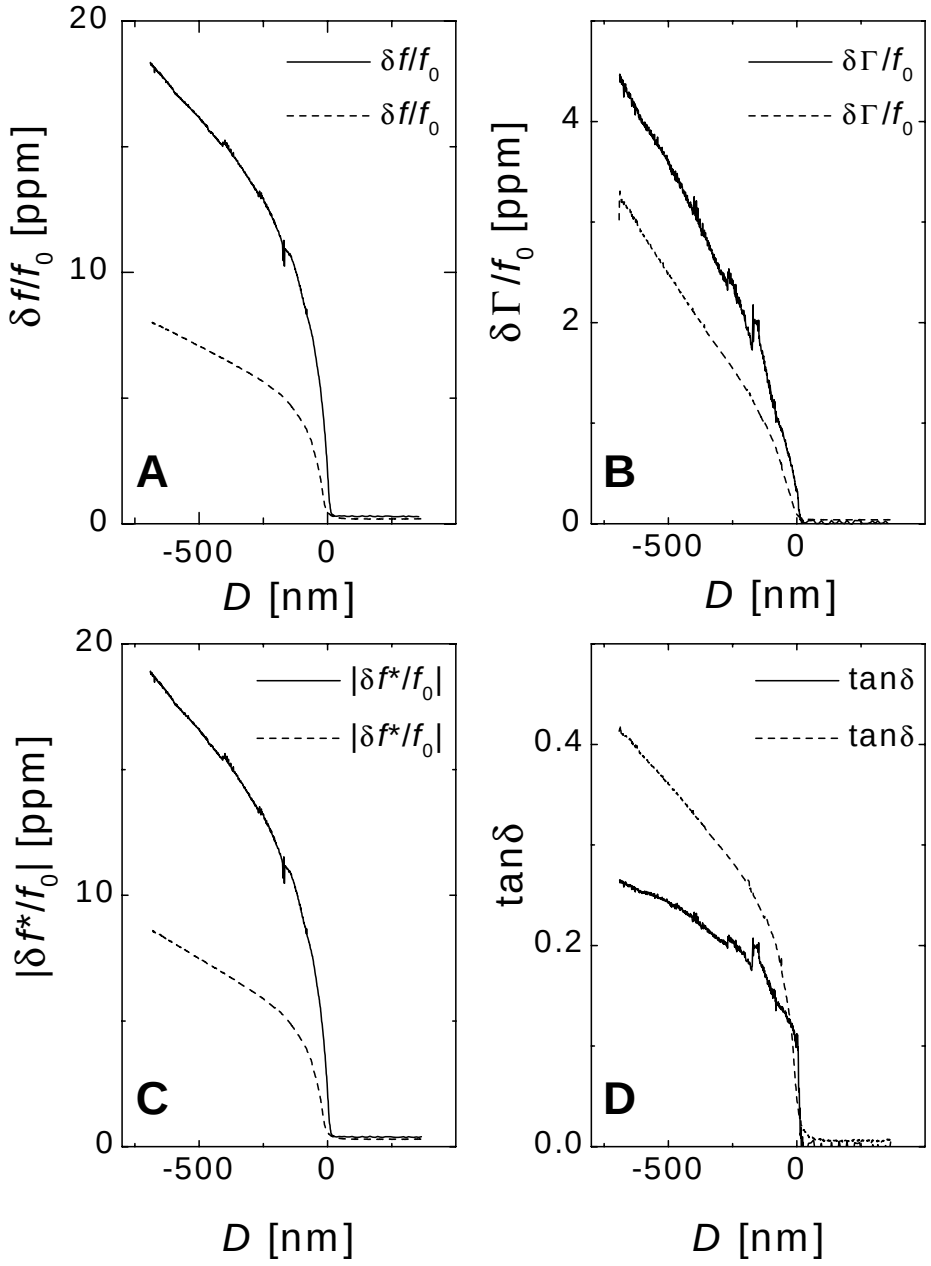

Figure 6.4: Measurement of a fluorocarbon–fluorocarbon contact at 12 MHz (straight lines) and 20 MHz (dashed)(2^{nd} and 3^{rd} harmonic of a 4 MHz quartz). Total travel: 1100 nm. Resolution around contact: 1 nm. (A): normalized frequency shift ($\delta f/f_0$); (B): normalized change in bandwidth ($\delta\Gamma/f_0$); (C): Modulus of the complex frequency shift ($|\delta f^*/f_0|$); (D): $\tan\delta = \delta\Gamma/\delta f$. D is the nominal distance as given by the movement of the piezo stage.

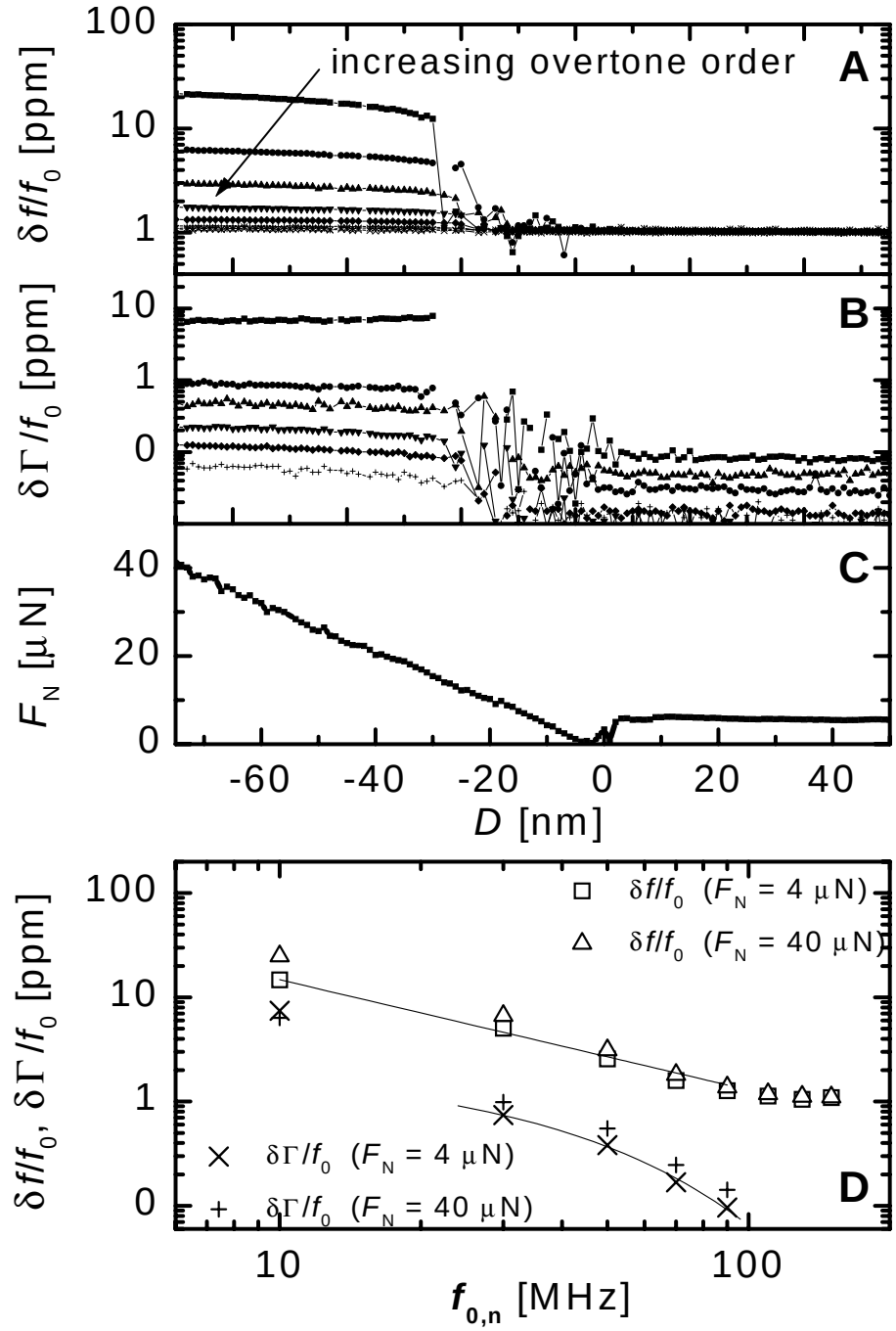

Figure 6.5: Dependence of the normalized frequency shift on the frequency (overtone order). (A): Normalized frequency shifts; (B): Changes in bandwidth; (C): Normal force. x-range: $-50 - +80$ nm. Panel (D) displays the magnitude of the frequency and bandwidth changes at two applied normal forces ($F_N = 4$ and 40 μN) for the different overtones. D is the nominal distance as given by the movement of the piezo stage.

Table 6.2: Maximum oscillation amplitudes and surface speeds of the different overtones.

Harmonic	Max. Amplitude [nm]	Maximum Speed [m/sec]
1	240	7
3	80	15
5	60	19
7	34	15
9	28	16
11	23	16
13	17	13.5

panel indicates that this behavior is obeyed for $\delta f/f_0$ for the first 6 harmonics. However, at higher overtones there are deviations from this scaling behavior: The frequency shift is higher whereas the change in bandwidth is lower than the law predicts. A final conclusion for the deviation from the predicted behavior cannot be drawn. Lower harmonics appear to be more sensitive to the surface coupling. This is supported by the fact that a maximum in bandwidth occurs for the first harmonic. This maximum is far less pronounced for the higher ones.

Table 6.2 shows the calculated maximum amplitudes and surface speeds of the quartz at its different overtones (eq. 6.17, p. 101). The amplitude decreases with overtone order due to the varying quality factors of the different harmonics. The speed increases with overtone order, mainly from the first to the third harmonic, also due to the strongly increasing quality factor, which is an expected behavior (cf. Chapter 6.7.4, p. 100). For this quartz, however, quality factors of the harmonics increase with increasing overtone order.

6.6 Nonlinearities

Frictional sliding at an interface is usually accompanied by non-linear effects originating from stick-slip events for example. Therefore, the following tests have been carried out to

probe the nonlinear responses.

6.6.1 Drive Level Dependence

The oscillating amplitude of the quartz can be changed by varying the level of the excitation voltage. Figure 6.6 shows two measurements carried out on a fluorocarbon–fluorocarbon contact. (A): Modulus $|f^*/f_0|$ of the complex frequency change; (B): $\tan\delta$; (C): Lorentz-Amplitude of the resonance curves. One run was carried out at a driving amplitude of 0 dBm, the other one at 20 dBm, that is, the power being a factor of 100 larger. None of the quartz signals shows a significant difference due to the change in drive-level. With nonlinearities present, one would expect large differences. Only the Lorentz amplitude is larger for the higher drive-level. It changes drastically when the "point of contact" is reached.

6.6.2 Anharmonic Sidebands

Figure 6.8B displays the first harmonic of a 10 MHz quartz and the anharmonic sidebands in its vicinity. From bottom to top the surfaces are moved into contact. Besides a decrease of the amplitude of the main harmonic one does not find any changes in the parasitic resonances. The different normal modes of a three-dimensional circular plate can also be calculated theoretically [Bot82] although it is extremely complex to do so. Figure 6.7 shows the relative phase and charges on the surface for different modes occurring. Their frequencies can be calculated via:

$$f_{nmk} = \frac{nc}{2h_q} + \frac{ch_q B_{mk}^2}{4n(\pi A_e)^2} = f_{n00} + const. \cdot B_{mk}^2 \tag{6.2}$$

with n = 1, 3, 5,... the order of the harmonic, m = 0, 1, 2, 3,... the order of the Bessel function B_m, c the velocity of sound in the quartz crystal, h_q its thickness, and A_e the vibrating area (area of the small electrode). The index m indicates the number of occurring nodal lines across the diameter and the index k the number of circular nodal lines (cf. Figure 6.7). Although the spectrum of the anharmonic sidebands has been calculated we do not attempt a quantitative comparison with theory here. The main point is that

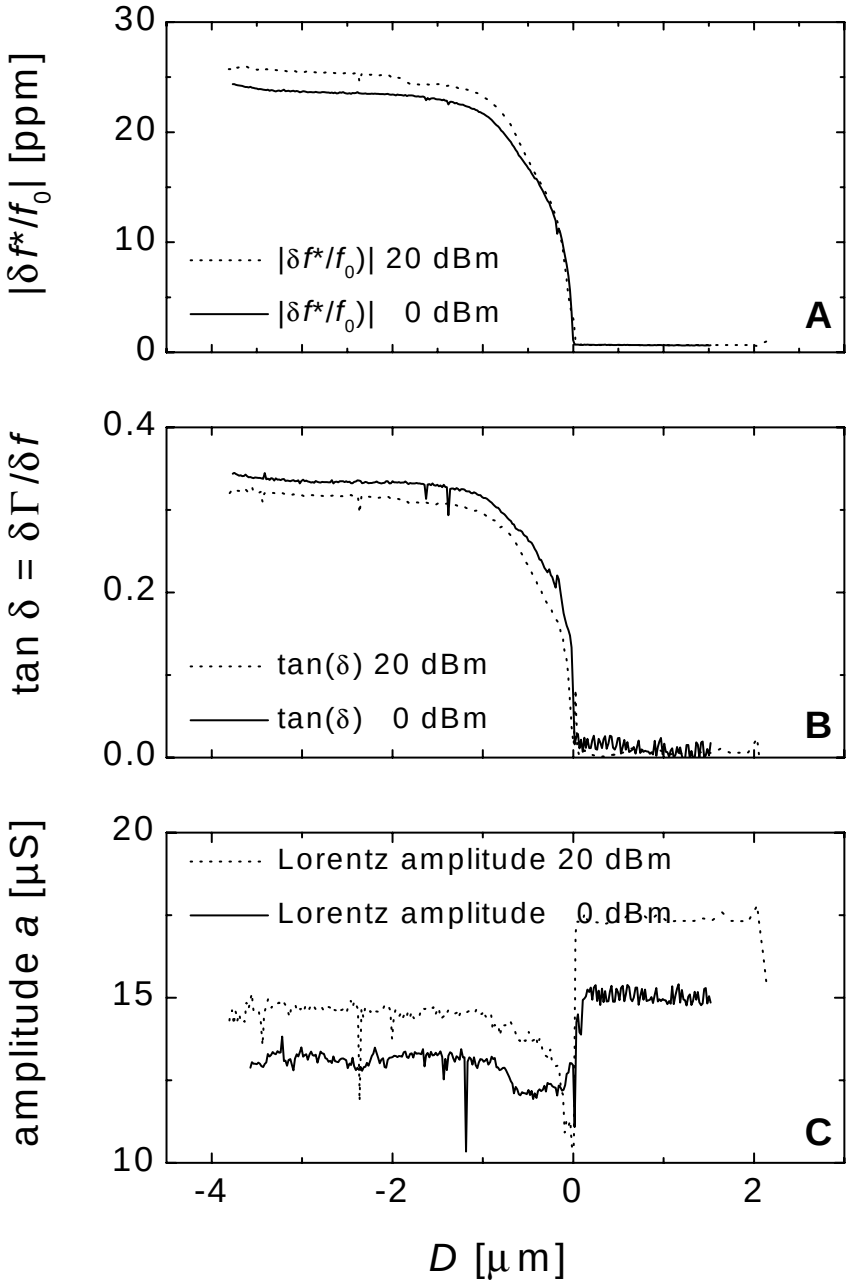

Figure 6.6: Drive-level dependence: Comparison of two measurements at 0 dBm and 20 dBm, respectively. (A): Modulus $|f^*/f_0|$ of the complex frequency change; (B): $\tan\delta$; (C): Lorentz-Amplitude of the resonance curves.

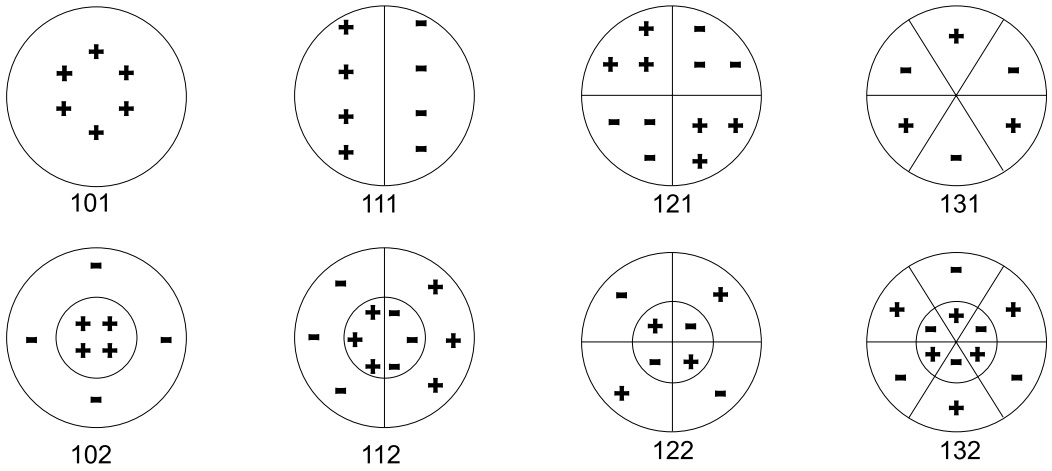

Figure 6.7: Relative phase and charge on the surface of a thickness-shear plate vibration of different modes nmk (from [Bot82]).

---

the mode pattern is largely maintained upon contact. Apparently, the contact is a weak disturbance.

6.6.3 Fourier Amplitudes from Time Domain Experiments

The goal of experiments in the time–domain was to observe non-linearities like stick-slip events directly in the time-dependent movement of the quartz, that is, in the traces from the fast oscilloscope monitoring the free decay of the quartz oscillation after excitation with a radio-frequency–pulse. However, no evidence of such kind of events could be found. The oscillations are not disturbed in any way but rather keep their sinusoidal shape as for the unperturbed movement. Only little irregularities superimposed onto the peaks of the sinusoidals could be observed when bringing the surfaces barely into contact. Fourier transformation of the time-domain trace shows that higher Fourier components are present. Figure 6.8A shows the Fourier–spectrum obtained from experiments in the time-domain (cf. Chapter 5.6.3, p. 67). A comparison of the Fourier spectrum for the non-loaded quartz and the quartz in contact with the opposing surface is shown. Astonishingly, one observes not only the odd harmonics but also the even ones. Fourier components that

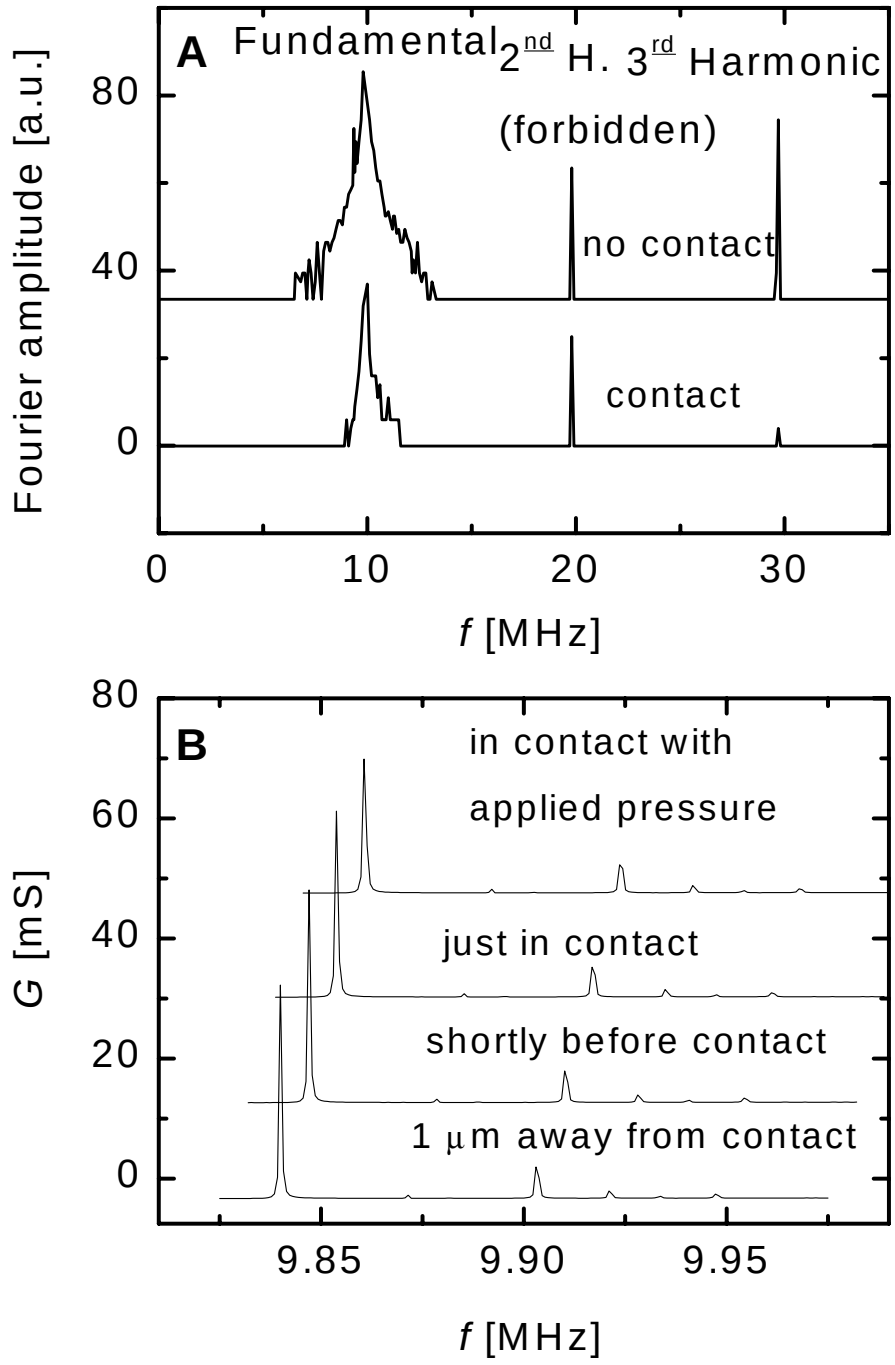

Figure 6.8: (A): Fourier amplitudes of the fundamental oscillation obtained from time–domain experiments. (B): Anharmonic sidebands in the vicinity of the first harmonic (101) of a 10 MHz quartz (from left to right) nmk = 101, 111, 102, 121, 112, and 103 respectively.

depend on the even powers of the driving amplitude cannot be excited electrically. Normal forces, on the other hand, do not change sign when the direction of the lateral force is reversed. We therefore associate the second harmonic amplitude with periodic normal force components. Nonlinear stress-strain relations can lead to a vertical movement of the quartz surface proportional to the square of the lateral speed.

When the sphere makes contact with the quartz plate the amplitude of motion decreases by about 15 dB. As a consequence, the amplitudes of the harmonics decrease as well. For example the third harmonic decreases by 37 dB, where 45 dB would have been expected for a strictly cubic effect. The second harmonic, on the other hand, decreases by only 5 dB, that is, it decreases less than the fundamental (15 dB). After normalizing the 2^{nd} harmonic amplitude to the fundamental it even increases from -22 dB to -11 dB. Apparently, periodic vertical forces pushing the sphere away from the quartz are present. The occurrence of such kind of normal forces could be explained with the asperities: To move two asperities past one another (at least) one asperity has to be moved out of the way. This can happen either by elastic or plastic deformation of the surface or by a vertical movement. The latter is probably the reason for the induction of movements perpendicular to the quartz surface.

6.6.4 Nonlinearities of the Unloaded Quartz Resonator

In time–domain experiments we always compared the unloaded situation (quartz and sphere not in contact) with the loaded situation (surfaces in contact). For the unloaded situation we could observe a non-linear behavior of the quartzes depending on the driving amplitude applied to the quartzes: For driving amplitudes larger than 0 dBm (P = 1 mW) there was a strong non-linear response of the unloaded quartz: The shape of the sinusoidal oscillation changed in such a way that the peaks of the oscillation were "cut-off". At driving amplitudes < 0 dBm the oscillation was always sinusoidal. Therefore, all following experiments have been carried out at a driving amplitude of -10 dBm (P = 0.1 mW).

6.6.5 Bending of a Circular Quartz Plate

When we press on the center of the quartz plate with a force F it will bend by a distance x, and an effective spring constant can be calculated via [LL75]

$$k = \frac{F}{x} = \frac{4\pi h_{\mathrm{q}}^3 E_{\mathrm{q}}}{3(1-\sigma^2)R^2} \tag{6.3}$$

where $E_{\mathrm{q}} \approx 86$ GPa is the Young's modulus of the quartz plate; $\nu \approx 0.11$ the Poisson number[1]; h_{q} the thickness of the plate; and R = 6.5 mm the radius of the rim of the holder. For some of the initial experiments we used 4 MHz quartzes with a thickness $h_{\mathrm{q}} = 0.4$ mm and for all following experiments, especially for those on perfluoropolyether lubricants, we used 10 MHz quartzes with a thickness $h_{\mathrm{q}} = 0.18$ mm. For their effective spring constants we obtained: $k(10\ \mathrm{MHz}) = 1.5 \cdot 10^4$ N/m and $k(4\ \mathrm{MHz}) = 1.6 \cdot 10^5$ N/m, respectively. For experiments with the 400 μm-thick quartzes we used a stiff holder for the approaching surface, that is, the quartz plate was the weakest part and bended. For experiments with the 10 MHz quartzes the spheres were mounted on a force transducer with a spring constant $k_F = 8.6 \cdot 10^3$ N/m (cf. Chapter 5.4.1, p. 54). Since the quartzes' spring constant is only a factor of two larger, both components will bend. For typical maximum forces of $F_N \approx 100$ μN, the thin quartzes would bend almost 7 nm, whereas the thicker ones only 0.6 nm.

6.6.6 Pressure Dependence of Resonance Frequencies

We had to consider whether the observed frequency increase in our experiments results from an applied static stress onto the quartz. Therefore, we carried out a measurement to check the dependence of the quartz frequency on the applied normal pressure.

Figure 6.9 shows the setup used for this measurement: A 4 MHz quartz resonator (diameter 14 mm, thickness 0.4 mm, area $A \approx 1.5 \cdot 10^{-4}\mathrm{m}^2$) was mounted at the bottom of a glass column (radius $r = 11$ mm). While following the second (12 MHz), third (20 MHz) and fifth harmonic (35 MHz), the column was filled with increasing water levels of known volumes (V = 20 ml, 120 ml, 220 ml, and 320 ml). The corresponding pressures were

[1] The equation assumes an isotropic medium. We have used $E_{\mathrm{q}} \approx c_{11}$ and $\nu \approx 1/2(c_{12}+c_{13})/c_{11}$ with the numerical values from [Bot82].

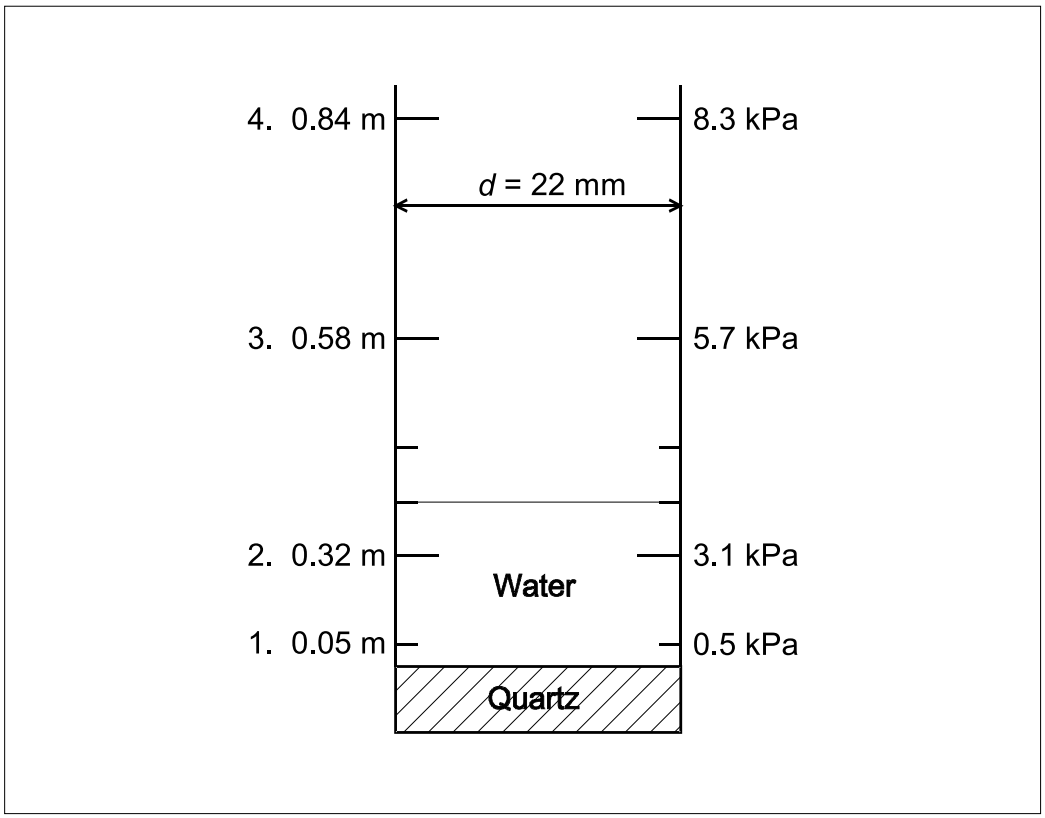

Figure 6.9: Setup for measuring the pressure dependence of the resonance frequency. The column was filled with Milli-Q (18.5 MΩ) water, at different water levels.

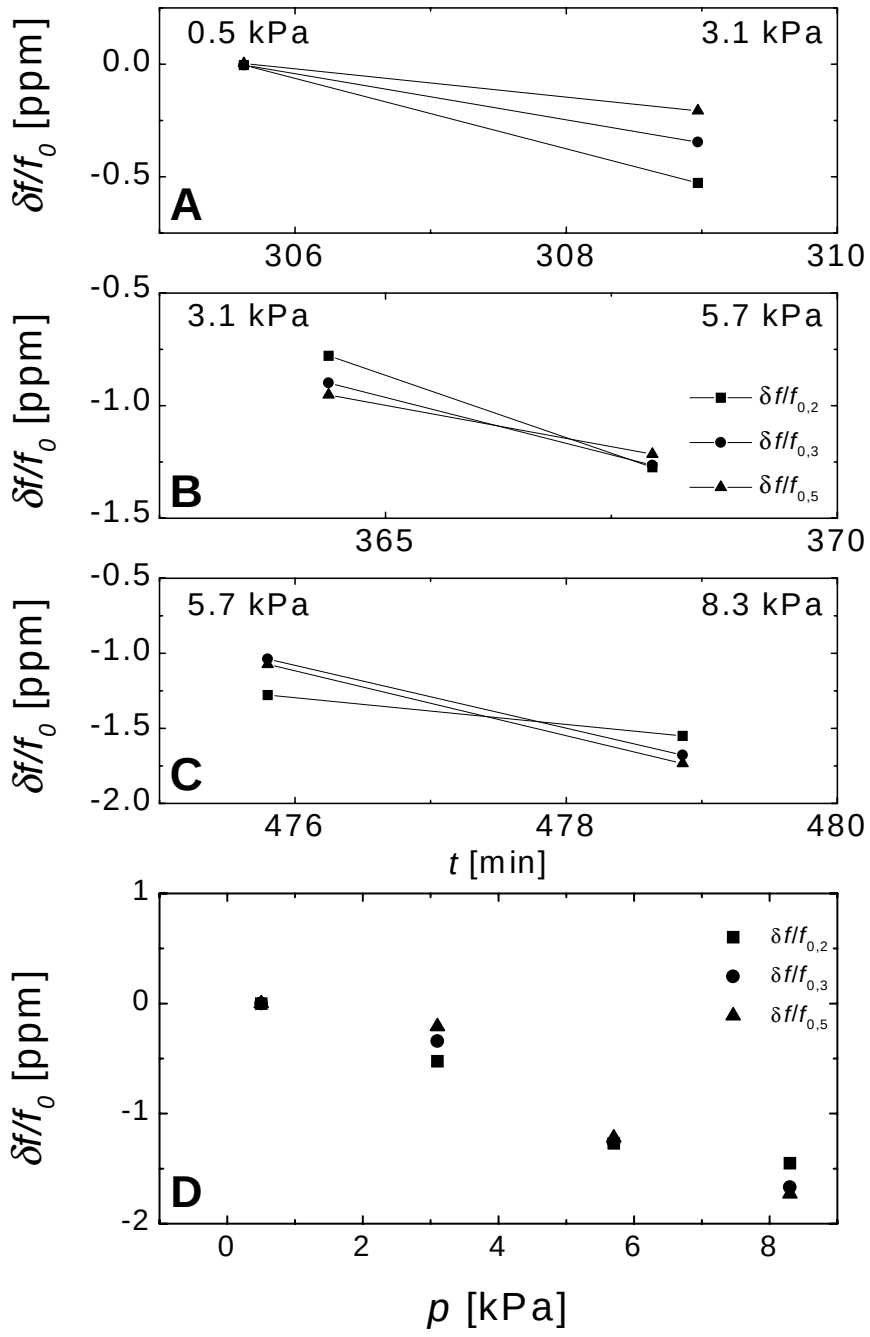

Figure 6.10: Variation of the resonance frequency for the 2nd (12 MHz), 3rd (20 MHz) and 5th harmonic (35 MHz) of a 4 MHz quartz.

calculated using $p = \rho \cdot h = \rho \cdot V/(\pi r^2)$ with the density of water $\rho \approx 1000$ kg/m^3; and h the height of the water column. Figure 6.10A-C shows the pressure change of the 12 MHz, 20 MHz and 35 MHz overtones of a 4 MHz quartz. For all harmonics the *increasing* pressure steps cause the frequency to *decrease*. Figure 6.10D displays the change of the frequencies depending on the applied normal pressures (0.5, 3.1, 5.7, and 8.3 kPa). The frequency was recorded continuously between the different pressure steps and a slight decreasing drift of the frequency was observed.

Both observations confirmed measurements by Heusler and co-workers who also find a decreasing frequency with an increasing normal pressure [HGJP88]. Heusler and co-workers used 10 MHz quartzes (thickness $d = 0.17$ mm). The stiffness of the quartz plate scales with d^{-3}. Therefore, we expect the effects in our experiment to be a factor $(0.4/0.17)^3 \approx 13$ weaker than the ones observed by Heusler with the thin quartz plates.

We conclude from these observations that the increase in frequency observed in the friction experiment was not caused by a bending of the quartz but must be due to other effects. In the following we present a model that explains the observed increase in frequency (cf. Chapter 6.7.3).

6.7 Quartz Crystals for Tribological Investigations

6.7.1 Linear Modeling

Throughout this work we only apply linear models: The forces depend linearly on the displacements $F(x) = \partial V(x)/\partial x \sim x$. That means that the potential function $V(x)$ depends quadratically on the displacement x. This assumption is justified by our experimental findings: In time-domain experiments we always observe harmonic oscillations of the quartzes, no matter how close to contact we operate and independent of the type of layers under investigation. To express this in terms of friction, only viscous Stokes behavior could be observed in our experiments (that is, the friction forces scaled linearly with the velocity $v = \partial x/\partial t$).

This is somewhat surprising because boundary layer friction is an inherently nonlinear phenomenon. Stick-slip is the most prominent example, where one observes spikes instead of harmonic oscillations.

So far we do not have a conclusive explanation for this seeming contradiction between the expected nonlinear and the observed linear behavior. Two explanations are proposed:

(A) The surfaces always stay in a *steady-sliding* regime because of the high frequency.

The prerequisite for the occurrence of stick-slip behavior is – as self-evident as it might sound – a sticking between the materials. In order to be able to stick together, the two surfaces must be in rest relative to each other for a certain time t_{res}, that has to be longer than a surface-specific characteristic time τ_c for stick-slip to occur: "A system needs a certain time τ_c during 'stop' to nucleate the pinned state [Per98]." For polymer surfaces, this critical time is presumably closely related to molecular relaxation times that also determine whether the lubricant layer acts fluid- or solid-like.

For the quartz resonator experiments we have to consider what "stop" really means: The peak velocity is about 1 m/s, that is, five orders of magnitude larger than the largest critical velocity found so far (typically $v_c \approx 1 - 10$ μm/s,[YCI93a]). On the other hand, the quartz has zero speed in the turning points of the oscillation. In the following, we quantitatively estimate the resting time.

As the condition for resting we chose:

$$\begin{aligned} |v(t)| &= |v_{max} \sin \omega t_{\mathrm{res}}| < v_c \\ &\Rightarrow \sin \omega t_{\mathrm{res}} \approx \omega t_{\mathrm{res}} < \frac{v_c}{v_{\max}} \\ &\Rightarrow t_{\mathrm{res}} < \omega^{-1} \frac{v_c}{v_{\max}} \approx 1.6 \cdot 10^{-13}\ s. \end{aligned} \tag{6.4}$$

This is not only shorter than any relaxation time occurring in polymers but also very short compared to relaxation times of smaller molecules. Possibly, it is too short to establish a sticking contact.

(B) The investigated surfaces actually are in a *fluid state*.

For a boundary lubrication situation (films thinner than 4 monolayers) a solidifi-

cation of the fluid lubricant layers has been found, hence, viscous behavior is not expected. But let us have a closer look at the systems that have mainly been investigated:

(a) Perfluoropolyethers are especially designed for lubrication purposes under extreme conditions (high strain rates, high velocities) and have to be effective also when applied as a very thin film. They have to maintain their fluidity even under these conditions. Numerous studies have confirmed that their liquid bulk behavior is conserved down to monolayer coverage ($h = 25$ Å). Only when the actual film thickness decreases below this limit, a liquid-solid phase transition can occur. This actually is the regime where we also observe an increasing friction.

(b) High-energy metal surfaces are certainly model-candidates for non-linear behavior: Their (hard) surface asperities are not protected, impact must occur and their high-surface energies lead to strong van der Waals adhesion which increases the adhesion contribution to friction forces. Although these surfaces have been plasma-cleaned before the experiments, these were carried out in environmental conditions. Thus, contaminating particles (water, grease) from the surrounding atmosphere are adsorbed and form a lubricating layer. Water, in particular, can decrease the friction between surfaces by an order of magnitude and exhibit the same coefficient of friction as bulk ice. This layer then would also exhibit fluid properties and this could explain why we could not find nonlinear behavior for these surfaces. The same argument could apply for the bare amorphous carbon surfaces.

(c) Plasma-polymerized fluorocarbon surfaces are very hydrophobic (low-energetic) like the perfluoropolyether film. Adsorption of water is not expected. But in this case the friction forces are below the limit of detection of the quartz method. If no friction occurs, it is unlikely to observe stick-slip behavior but rather to move in a steady-sliding regime.

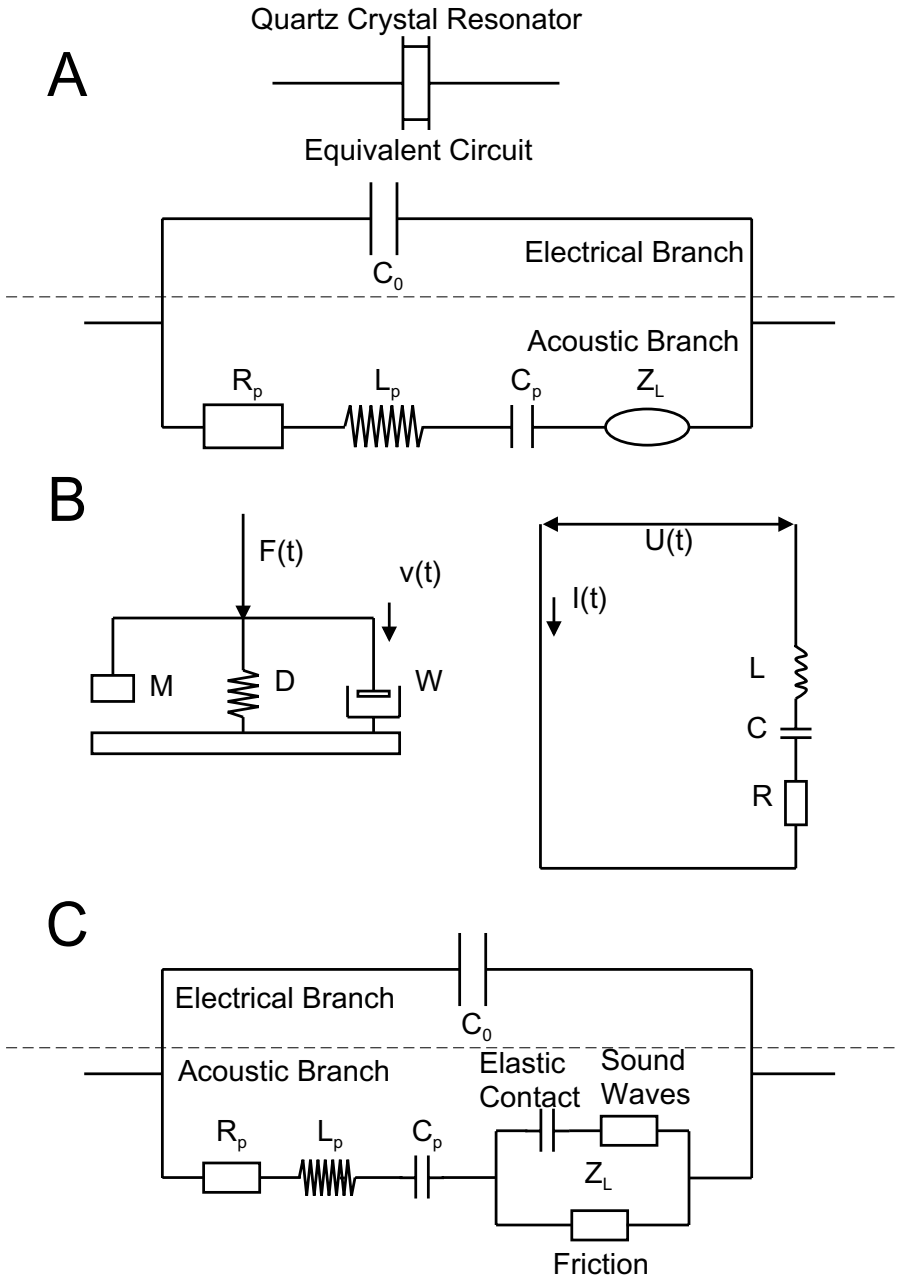

Figure 6.11: (A) Butterworth–van Dyke equivalent circuit for a Quartz Crystal Resonator. (B) Electro-mechanical Analogy (C) Extended equivalent circuit for friction experiments.

6.7.2 Equivalent Circuits – Mechanical Impedances

Figure 6.11A shows the equivalent circuit commonly used to describe the electrical properties of a quartz resonator, the Butterworth-van Dyke circuit (van Dyke, 1923). The capacitance C_0 in parallel corresponds to the electric capacitance across the electrodes and is not of importance in this context. Figure 6.11B shows the electro-mechanical analogy that connects electrical and mechanical waves. The force F is the equivalent of the voltage U, the speed of particle displacement $v = \dot{u}$ corresponds to the current I, the mass M corresponds to an inductive element $i\omega L$, the compliance D ($= 1/\kappa$, with $\kappa_q = G_q/h_q$ the stiffness of the quartz plate, G_q and h_q its shear modulus and thickness, respectively) to a capacitive element $i\omega C$, and the friction resistance W to a resistive element R. All elements have the dimension of stress/(velocity$\times$area) and are the acoustic analogues of the electric impedances which have the dimension of voltage/current. In acoustics the area is usually incorporated into the definition of the impedance, whereas it is not for electrical circuits. The parallel acoustic network transforms into a serial electric network because in a parallel acoustic network the stresses ("voltages") are additive rather than the displacements ("currents").

6.7.3 Modeling of the Frequency Behavior

In the following we present a model that is able to explain why the frequency in our experiments *increases*. This model is based on the assumption that sound waves emanate from the quartz into the sphere. The functional dependence can be modeled when taking into account the JKR-like increase in contact area when increasing the normal load.
In a mechanical spring–mass system the frequency depends on the mass m and the spring constant k as $\omega = \sqrt{k/m}$. On an intuitive basis this is the explanation for the frequency decrease observed in quartz crystal microbalance experiments. In our friction experiments the mass coverage of the quartz does not change. In particular, it does not decrease as would be expected when naively applying the picture from Quartz Crystal Microbalances to the friction experiments. Another reason for an increasing frequency could be an increased stiffness k of the quartz–sphere system as compared to the bare quartz.

Frequency Shifts

A resonance is described by its frequency f and bandwidth Γ (see Chapter 2.3.2). Materials brought onto the quartz surface couple to the mechanical resonances which results in a change in both frequency (δf) and bandwidth ($\delta\Gamma$). δf is a measure of the elastic coupling to the quartz resonator and $\delta\Gamma$ reflects dissipative phenomena occurring in the material (visco-elastic measurements) or at the interface between quartz and sample (tribological measurements).
Once the load impedance Z_q is known, the complex frequency shift of the quartz resonance $\delta f^*/f_0$ can be expressed as:

$$\frac{\delta f^*}{f_0} = \frac{\delta f}{f_0} + i\frac{\delta\Gamma}{f_0} = \frac{i}{\pi}\frac{Z_L^*}{Z_q} \tag{6.5}$$

with $Z_q = 8.8 \times 10^6$ kg/sm^2 the acoustic impedance of AT-cut quartz, f_0 the resonance frequency of the unloaded quartz, $\delta f/f_0$ and $\delta\Gamma/f_0$ the real and imaginary part of the normalized frequency shift. In the derivation of equation 6.5 it was assumed that Z_L is much smaller than the other elements of the circuit. This implies that the disturbance (or normalized frequency shift $\delta f^*/f_0$) is small. The analogue to the load impedance in our friction experiments is not obvious. For a very thin film one has $Z_L \approx i\omega m_f$ with m_f the mass per unit area of the film. Thus, a small "added mass" leads to a frequency decrease. A similar situation has been reported by Krim et al. who report a slight frequency increase when pressing with an STM-tip onto a shear quartz resonator [KDD93]. The authors postulate that the increased frequency was due to the increased stiffness of the complete system. However, they do not explain this by a model with the impedance defined by a term such as $\kappa/(i\omega)$. Here, we show that a small sphere touching the quartz surface represents a disturbance of this kind.

It is possible to estimate the order of magnitude of the occurring effects by using a rather crude wave picture. Figure 6.12 shows the setup developed in our laboratory and the situation between the quartz surface and the sphere. The contact radius r_c is assumed to be much smaller than the wavelength of sound ($\lambda \ll r_c$). All vertical movements are much smaller than the wavelength of sound. In our setup, the contact radius cannot be determined experimentally. Therefore, we estimate it by application of the Johnson–Kendall–Roberts (JKR) theory [JKR71] (cf. Chapter 3.4) for an elastic point contact.

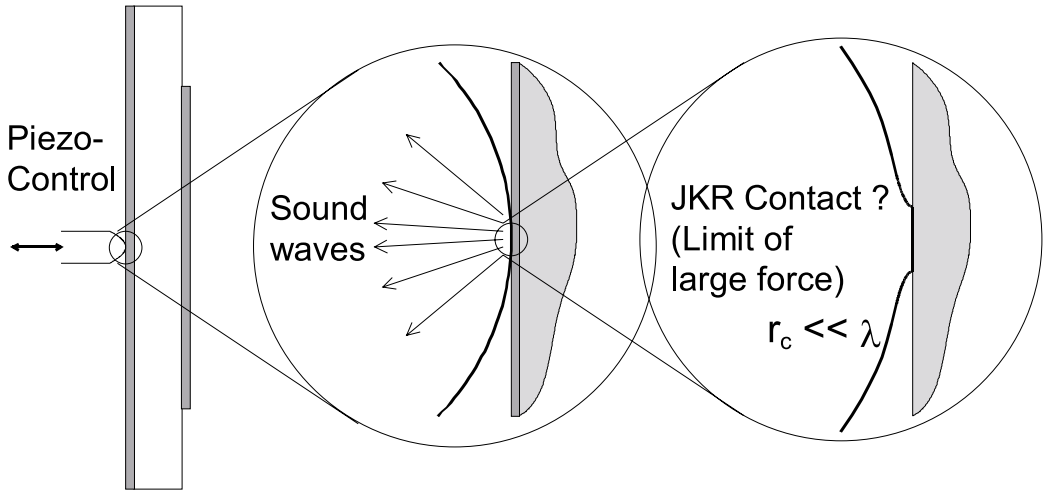

Figure 6.12: Sketch of the "point contact model" illustrating the geometry. Provided that the contact radius is smaller than the wavelength of sound, the wave field inside the sphere may be approximated as spherical.

We find r_c to be in the range of a few micrometers. (This estimation is supported by the calculation in Chapter 7.) This contact radius is much less than the wavelength of sound in the silicon nitride spheres used in our experiments: From Table 5.3, (p. 71) we extract the following parameters for the spheres:
Young's modulus E = 300 GPa; Poisson number $\mu = 0.27$; and density $\rho = 3150$ kg/m^3. We confine ourselves to transverse shear waves and therefore use the shear modulus $G = E/(1+2\mu) = 120$ GPa. The velocity of the shear waves in the quartz is obtained from $c_t = \sqrt{G/\rho} \approx 6200$ m/s. This leads to a wavelength of $\lambda_1 = c_t/\nu = 610$ μm for a frequency of $\nu = 10$ MHz. For higher harmonics of the order $n = 1, 3, 5, \ldots$ 2k+1 one obtains wavelengths $\lambda_n = \lambda_1/n$. The corresponding longitudinal waves are a factor of $\sqrt{1.54} = 1.24$ longer.
Two basic assumptions have to be made for the estimation:

- From the point of contact a spherical wave propagates into the sphere.
- The oscillation is a pure shear motion, thus, we only have to account for the elastic shear modulus G of the sphere.

Under these premises the deformation of the sphere may be approximated as

$$\begin{aligned} u(r) &\approx \quad u_0 \tfrac{r_c}{r} e^{-ikr} \quad \text{for } r > r_c \\ u(r) &\approx \qquad u_0 \qquad \text{for } r < r_c \end{aligned} \tag{6.6}$$

where u is the displacement, r is the radial coordinate originating at the point of contact, $k = 2\pi/\lambda$ is the wavenumber, r_c is the contact radius, and u_0 is the amplitude of oscillation. The complex mechanical load impedance is defined as

$$Z_L^* = \frac{\sigma^*}{\partial u/\partial t} \tag{6.7}$$

and is by definition normalized to the area A, σ is the shear stress. Outside the contact area ($r > r_c$) the stress can be expressed as

$$\sigma^* \;\sim\; G\nabla u \;\sim G\; u_0\; r_c\; (-\tfrac{1}{r^2} - \tfrac{ik}{r}) \quad \text{for } (r \;>\; r_c) \tag{6.8}$$

where G is the shear modulus.[2] All numerical factors have been dropped. For $r < r_c$ we assume that the stress is constant everywhere[3] and equal to the stress at $r = r_c$. Evaluated according to equation 6.8, this leads to

$$\sigma^* \;\sim\; \tfrac{Gu_0}{r_c}(-1 - kr_c) \quad \text{for } r \;<\; r_c. \tag{6.9}$$

At this point we have to account for the fact that the acoustic impedance by definition is normalized to the area of the wave. To stay consistent with this convention we include a factor r_c^2/r_e^2 into the impedance (where r_e^2 is the actively oscillating area of the quartz which — because of energy trapping — coincides fairly well with the area of the electrode, $r_e = 2.5$ mm). The load impedance in this case becomes (cf. equation 6.7):

$$Z_L^* = \frac{r_c^2}{r_e^2} \cdot \frac{\sigma^*}{\partial u/\partial t} \tag{6.10}$$

[2]Although G, in general, is also a complex quantity, in this case the imaginary part (loss modulus G'') is very low compared to the elastic part. Therefore we omit G'' in the following.

[3]This does not adequately represent the real situation in the contact area (cf. Chapter 3.4).

Inserting equation 6.9 into 6.10 we obtain

$$Z_L^* \sim \frac{1}{r_e^2} \cdot \frac{Gr_c}{-i\omega}(-1 - ikr_c) \tag{6.11}$$

Inserting equation 6.11 into equation 6.5 one finds for the resulting complex frequency shift [LJ99]:

$$\frac{\delta f^*}{f_0} = \frac{\delta f}{f_0} + i\frac{\delta \Gamma}{f_0} = \frac{i}{\pi}\frac{Z_L^*}{Z_q} = \frac{Gr_c(1 + ikr_c)}{\pi Z_q r_e^2 \omega} \sim \frac{\kappa}{\pi Z_q r_e^2 \omega}(1 + ikr_c) \tag{6.12}$$

6.7.4 Oscillation Amplitude and Surface Velocity for Different Overtones

The time dependence of the displacement of the oscillator surface is described by

$$u(t) = u_0 \; e^{i\omega t} \tag{6.13}$$

where u_0 is the maximum displacement from the equilibrium position. Derivation with respect to time gives the speed:

$$\dot{u}(t) = i\omega \; u_0 \; e^{i\omega t} \tag{6.14}$$

The applied electrical voltage U_{el} causes a shear strain $\frac{du(z)}{dz} = d_{26} \cdot \frac{U_{\mathrm{el}}}{d}$ and an off-resonance surface displacement of

$$a_{\mathrm{off}} = \frac{1}{2} d_{26} \cdot U_{\mathrm{el}} \tag{6.15}$$

with $d_{\mathrm{piezo}} = d_{26} = 3.2 \cdot 10^{-12}$ m/V the relevant piezoelectric coefficient. The off-resonance amplitude for common voltages (0.1 V) is in the range of $a_{\mathrm{off}} = 0.3$ pm. In resonance the amplitude is amplified by the quality factor of the resonance $Q = f/2\Gamma$ [Bot82]. However, this Q–factor does not directly translate to the displacement at the surface, but rather to the shear strain in the nodes of the standing wave $\frac{du(z)}{dz}|_{\max}$ (cf. Figure 6.13A). The displacement at the surface u_0 is given by

$$u_0 = \frac{1}{n}\frac{d}{\pi} \cdot \frac{du(z)}{dz}|_{\max} = \frac{1}{n\pi} \; Q \cdot d_{26} \cdot U_{\mathrm{el}} \tag{6.16}$$

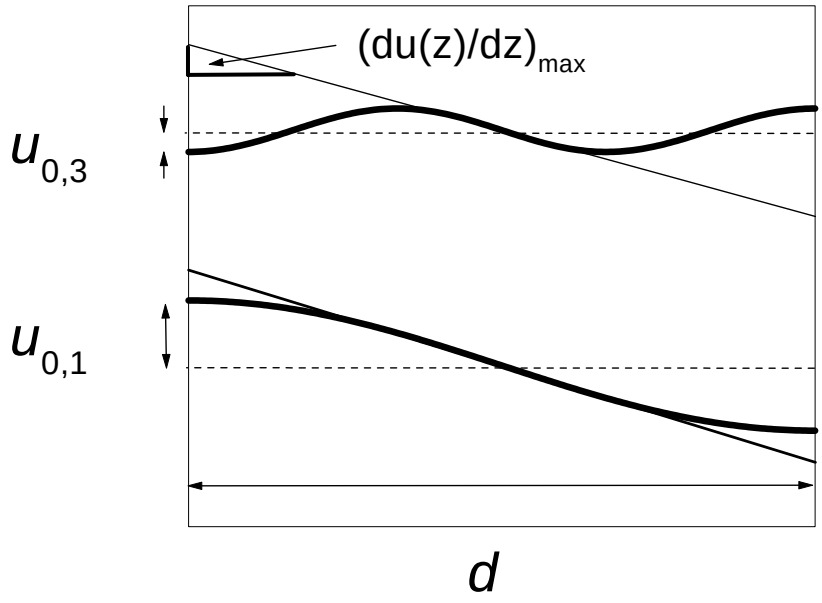

Figure 6.13: Standing waves inside a quartz plate: 1^{st} (bottom) and 3^{rd} harmonic (top). $\frac{du(z)}{dz}|_{\max} = \frac{2\pi}{\lambda}u_0 = \pi u_0/d$.

---

where n is the number of nodal planes which is equal to the overtone order. Thus, the resonance amplitude at the shear quartz surface is amplified by a factor of Q/π compared to the off-resonance amplitude.

Resonances of the used quartzes have quality factors of $Q \approx 10^5$. Therefore, typical amplitudes in resonance are about 10 nm.

Combined with eq. 6.13 and 6.14, eq. 6.15 becomes:

$$\begin{aligned} u(t) = u_0 e^{i\omega t} &= \frac{1}{n\pi} d_{26} \cdot U_{\text{el}}\ Q\ e^{i\omega t} \\ \dot{u}(t) = \dot{u}_0 e^{i\omega t} &= \frac{1}{n\pi} i\omega \underbrace{d_{26} \cdot U_{\text{el}}}_{2a_{\text{off}}} Q\ e^{i\omega t} = i2f_0 d_{26} U_{\text{el}} Q\ e^{i\omega t} \end{aligned} \tag{6.17}$$

The amplitude of the oscillation decreases with $1/n$, whereas the surface velocity is independent of the overtone order.

6.7.5 Calculation of Rheological Parameters

In this section we relate the measured bandwidth parameter $\delta\Gamma/f_0$ to the rheological parameters such as strain, shear rate, shear stress, lateral forces, and viscosity. With the experimental values for frequency shift and bandwidth, the latter quantities can be estimated.

Mechanical strain. The mechanical strain ϵ in a shear experiment is defined by:

$$\epsilon = \delta u/h \tag{6.18}$$

with δu the difference between the lateral displacement at the top and the bottom of the film and h the film thickness.

A typical shear amplitude of the lateral motion of the quartz resonator was $u_0 \sim 10$ nm. A typical film thickness in our experiments was $h \approx 10$ Å. Assuming that the top of the film is at rest (that is, $\delta u \approx u_0$), one finds a shear strain of $\epsilon \sim 10$. In bulk rheology a rule of thumb is that for a strain larger than 1% non-linear response can be observed [Fer80].

Shear rate. The shear rate is defined by:

$$\dot{\gamma} = \frac{\delta \dot{u}}{h} = \frac{i\omega \delta u}{h} = i\omega\epsilon \tag{6.19}$$

with $\omega = 2\pi f$ and $\dot{u} = v$ the shear velocity. For quartzes a typical magnitude of shear rate is $\dot{\gamma} \approx 10^9$ s^{-1}. Common shear rates in SFA experiments are from $10^{-2} - 10^4$ s^{-1}.

Mechanical impedance and shear stress. The load impedance Z_L in our quartz experiment can be expressed by:

$$Z_L = \frac{\sigma}{\dot{u}} = \pi Z_q \frac{A_e}{A_c} \cdot \frac{\delta f^*}{f_0} \approx 1.73 \cdot 10^{14} \text{ kg/sm}^2 \tag{6.20}$$

where $A_e = \pi r_e^2$ and $A_c = \pi r_c^2$ are the oscillating area of the electrode and the contact area, respectively; Z_q is the acoustic impedance of AT-cut quartz and σ is the stress

averaged over the contact area A_c. Eq. 6.20 is to be understood in the complex sense. The real and the imaginary part denote the components of the stress which are in phase and out of phase with the velocity. Because the phase is defined relative to the velocity, the in-phase component dissipates energy while the energy in the out-of-phase component is recovered during each oscillation cycle.

The modulus of the average shear stress is given by

$$|\sigma| = |\dot{u}|\pi Z_q \frac{r_e^2}{r_c^2} \cdot \frac{|\delta f^*|}{f_0} = |\dot{u}|\pi Z_q \frac{r_e^2}{r_c^2} \frac{\sqrt{\delta f^2 + \delta\Gamma^2}}{f_0} \tag{6.21}$$

Using an amplitude of motion of $u = 10$ nm, a frequency of $f_0 = 10$ MHz, a contact radius of $r_c = 1\mu$m, and an electrode radius of $r_e = 2.5$ mm one arrives at

$$|\sigma| = 1.73 \cdot 10^{14} \cdot \frac{|\delta f|}{f_0} \text{ Pa} \tag{6.22}$$

Here and in the following all values are the peak values of the oscillation cycle and at the peak of the resonance. With typical values of $|\delta f|/f_0$ in the range of 10^{-6} one sees that the typical shear stress is of the order $\sigma \approx 200$ MPa.

Lateral force. Within this simple model the modulus of the lateral force is

$$|F_p| = \sigma \cdot r_c^2 = \dot{u}_{0,\mathrm{q}} \pi^2 Z_q r_e^2 \frac{|\delta f|}{f_0} \tag{6.23}$$

Note that the contact area does *not* enter the calculation of the force. Since the contact area is often known with poor accuracy, the lateral force is a more meaningful quantity than the lateral stress. With the same numbers as used above one finds $|F_p| \approx 6 \cdot 10^{-4}$ N. We now make use of the fact that the phase angle of $Z_L^* = \sigma/\dot{u}$ is known. The reactive and the dissipative components can be separated.

The dissipative, in-phase part of the lateral force is

$$|F_{\mathrm{p,d}}| = \dot{u}_0 \pi^2 Z_q r_e^2 \frac{\delta\Gamma}{f_0} \tag{6.24}$$

The dissipated power is

$$\begin{aligned} P &= \frac{1}{T}\int_0^T F_{\mathrm{p,d}} \dot{u}_0 (\cos\omega t)^2 dt = \frac{1}{2}\pi^2 Z_q r_e^2 \frac{\delta\Gamma}{f_0} \dot{u}_0^2 \\ &= \frac{1}{2}\pi^2 Z_q r_e^2 \frac{\delta\Gamma}{f_0} 4 f_0^2 d_{26}^2 Q^2 U_{el}^2 = \frac{1}{2} F_{\mathrm{p,d}} \dot{u}_0 = \frac{1}{2} Z_q \pi^2 r_e^2 u_0^2 Q^2 \frac{\delta\Gamma}{f_0} \end{aligned} \tag{6.25}$$

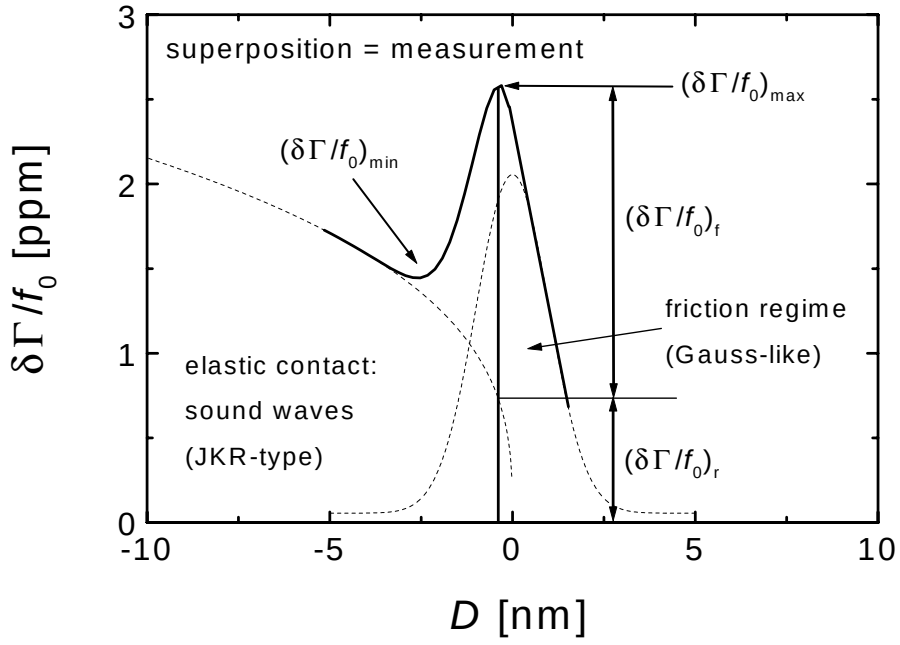

Figure 6.14: Graphical representation of the separation of the two different dissipation channels in the measurement: The elastic contact follows a JKR-type behavior whereas the friction profile has a Gaussian form.

Note that the dependence of the dissipated power on the bandwidth is somewhat subtle because Q in turn also depends on $\delta\Gamma$ via

$$Q = \frac{f}{2(\Gamma + \delta\Gamma)} \tag{6.26}$$

Only when $\delta\Gamma \ll \Gamma$ is fulfilled, is the dissipated power proportional to $\delta\Gamma$.

Importantly, the dissipated power has two separate contributions, namely the friction at the interface and soundwaves radiated into the sphere. This is expressed by the two distinct resistive elements in the equivalent circuit in Figure 6.11C (p. 95).

There is no a priori way to separate the two channels of dissipation. However, one can make assumptions about the amount of radiated energy. This can be either done with the model from section 6.7.3 or, more phenomenologically, by extrapolating the line from high normal forces. Under high force a tight contact is made and there is no sliding friction. If the dependence of radiated energy on vertical force is smooth, which should be fulfilled, such an approximation should yield at least an estimate. Figure 6.14 illustrates the procedure: The functional form of the elastic contact regime is JKR-like and the friction

regime has a Gaussian shape following the height distribution of the surface asperities. The convolution of both results in the idealized functional form of the measured data curves. Interestingly, both phenomena depend on the contact area: The friction behavior depends on the effective contact area that in turn depends directly on the number of overlapping surface asperities. The irradiation of sound depends on the elastically coupled contact area which follows a JKR-behavior.

Thus, for a correct evaluation one should subtract the elastic part from the data curves to obtain the pure friction part. Unfortunately, it is often difficult to measure far enough into the elastic coupling regime to determine the elastic curve.

In Figure 6.14 we also marked the maximum $(\delta\Gamma)_{\max}$ and local minimum $(\delta\Gamma)_{\min}$ that we will refer to for the quantitative data evaluation in Chapter 8.2. The maximum could already be affected by the elastic coupling. The minimum is very close to the value of the pure elastic curve. Thus, relating both parameters one can approximately subtract the elastic coupling.

The power dissipated through friction is

$$P_f = \frac{1}{2} Z_q \pi^2 r_e^2 \dot{u}^2 \frac{\delta\Gamma_f}{f_0} \tag{6.27}$$

while the radiated power is

$$P_r = \frac{1}{2} Z_q \pi^2 r_e^2 \dot{u}^2 \frac{\delta\Gamma_r}{f_0} \tag{6.28}$$

With the separation of radiative and frictional dissipation one can determine the sliding speed, that is, the difference between the speed of the quartz surface and the sphere.

The flow of energy in an acoustic wave is given by

$$P_r = \frac{1}{2} Z_s \dot{u}_s^2 A_c \tag{6.29}$$

with Z_s the acoustic impedance of the medium, u_s the amplitude of the wave and A the cross-sectional area. Equating P_r in eqs. 6.28 and 6.29 one arrives at

$$Z_s \dot{u}_s^2 \pi r_c^2 = Z_q \pi^2 r_e^2 \underbrace{(\dot{u}_0)^2}_{=:\ 4 f_0^2 d_{26}^2 U_{e1}^2 Q^2} \cdot \frac{\delta\Gamma_r}{f_0} \Rightarrow \dot{u}_s = \dot{u}_0 \left[\frac{Z_q}{Z_s} \frac{r_e^2}{r_c^2} \pi \frac{\delta\Gamma_r}{f_0} \right]^{1/2} \tag{6.30}$$

Again, the amplitude $\dot{u}_0$ depends on $\delta\Gamma$ through the quality factor Q.
With eq. 6.30 the speed of sliding $\Delta\dot{u}$ is

$$\Delta\dot{u} = \dot{u}_0 \left(1 - \left[\frac{Z_q}{Z_s}\frac{r_e^2}{r_c^2}\pi\frac{\delta\Gamma_r}{f_0}\right]^{1/2}\right) \tag{6.31}$$

Friction coefficient. Note that it is not possible to use the lateral force and the normal force to derive a friction coefficient μ in the Amontons sense. This would imply that the friction force is independent of velocity, while our experiments show that the friction force scales linearly with sliding speed. We observe friction in the Stokes sense.

Viscosity. One may, however, use F_p and $\Delta\dot{u}$ to infer an "effective viscosity" of a lubricant confined to the space between the quartz and the sphere. This necessarily requires assumptions on both the contact area and the thickness of lubricant layer h_l. For example, one could calculate the contact area from the JKR theory and assume that the thickness of the lubricating film is the same as before contact. Clearly, these will always be rather inaccurate values. Still, one could estimate an "effective viscosity" as

$$\eta^* = \frac{\sigma^*}{\Delta\dot{u}} \cdot h_l \approx h_l \pi Z_q \frac{r_e^2}{r_c^2}\frac{|\delta f^*|}{f_0}\left(1 - \left[\frac{Z_q}{Z_s}\frac{r_e^2}{r_c^2}\pi\frac{\delta\Gamma_r}{f_0}\right]^{1/2}\right)^{-1} \tag{6.32}$$

This equation may be simplified, when the contact is just barely made. Then the sphere is at rest and $\Delta\dot{u} \approx \dot{u}_0$. In this case one has

$$\eta^* \approx h_l \pi Z_q \frac{r_e^2}{r_c^2}\frac{\delta|f^*|}{f_0} \tag{6.33}$$

Here we shortly summarize the different parameters, their experimental relevance and how they can be influenced.

1. *Constant.* $\pi^2 \cdot r_e^2 \cdot Z_q = \pi^2 \cdot (2.5\text{ mm})^2 \cdot 8.8 \cdot 10^6\text{ kg/m}^2\text{s} = 543\text{ kg/s}$ is a constant numerical factor for all quartzes.

2. *Off-resonance amplitude.* $a_{\text{off}} = \frac{1}{2}d_{26} \cdot U_{\text{el}}$ is constant during the measurement because we do not change the excitation voltage. For easier comparison of different experiments this voltage was always held at the same value ($U = 0.071\text{ V} \mathrel{\hat{=}} P = -10\text{ dBm}$) unless stated otherwise.

3. The *lateral forces* are independent of frequency and the overtone order. On the other hand, we saw that the amplitude decreases inversely to the overtone order.

4. The *quality factor* $Q = f/2\Gamma$ can vary significantly $(10^4 - 10^6)$ between different quartzes, between the different overtones, and different amounts of normal force. For a comparison of the friction curves from different samples and quartzes multiplication of the change in bandwidth $\delta\Gamma/f_0$ with either Q or the speed $\dot{u}$ could facilitate comparison.

5. *Change in resonance bandwidth.* The lateral force is proportional to the change in resonance bandwidth $\delta\Gamma/f_0$ as long as $\delta\Gamma \ll \Gamma$. For higher damping, the situation becomes more complicated.

6.8 Experimental Problems

6.8.1 Amplitude Distribution and Energy Trapping

Sauerbrey [Sau64b] investigated the dependence of the amplitude distribution on the geometrical quartz parameters such as the thickness of the quartz plate h_q, thickness of the electrodes h_e, diameter of the electrodes and the overtone order. Figure 6.15A shows the distribution of the amplitude across the area of the quartz plate for an 0.4 mm-thick (4 MHz) quartz plate with facets and an 0.17 mm-thick (10 MHz) without such. Generally speaking, the shear amplitude has a maximum in the middle of the electrode and the quartz is only oscillating in the electrically excited area (electrode). From the edges of the electrode to the edge of the quartz the amplitude decays exponentially. This phenomenon is called *energy trapping*. The edges of the quartz are not oscillating, thus, the holder for electrical contacting does not disturb the resonance properties at all. Energy trapping becomes more effective with a) decreasing quartz plate thickness b) overtone order and c) thicker electrodes. Figure 6.15B shows the amplitude distribution of a 0.4 mm-thick (4 MHz) quartz plate without facets. Here the amplitude distribution oscillates along the area of the electrode. Particularly important for the friction measurements is a vanishing vertical component of the movement to keep the distance between the surfaces constant.

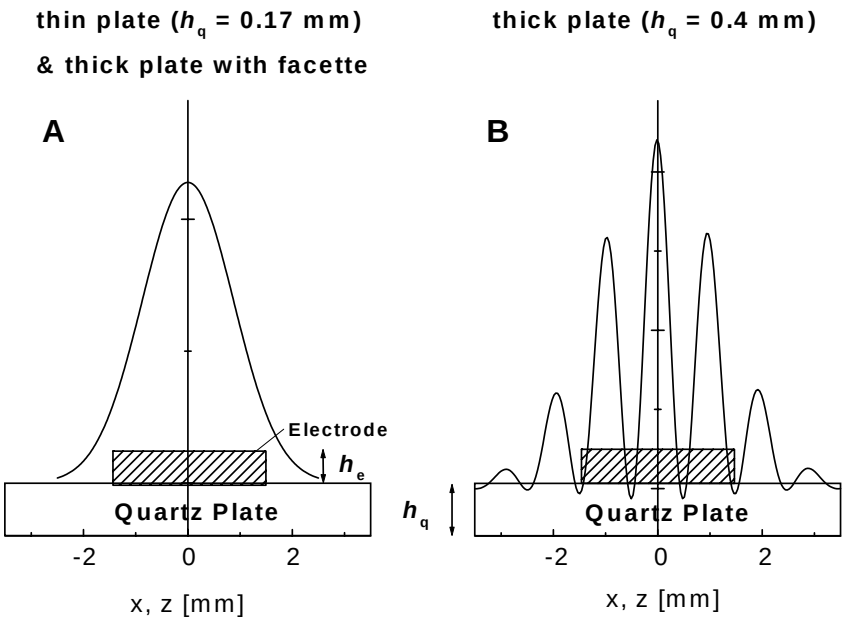

Figure 6.15: Amplitude distribution along quartz plates (from [Sau64b]).

Sauerbrey argues, that a vertical component of the movement may be present if the energy trapping is poor (Figure 6.15B). Figure 6.16 shows a measurement carried out with an 0.4 mm-thick (4MHz) quartz plate without facets. Clearly, there are oscillations in the frequency and the bandwidth superimposed onto the regular elastic coupling behavior. Presumably, the quartz plate's oscillation couples to the 13 mm-diam holder and vibration energy is emitted periodically into it depending on the fulfillment of geometrical resonance conditions.

6.8.2 Long-Range Normal Force Drift and its Correction

In many experiments we observed an *apparent* long-range interaction in the normal force. In this section we show that this is probably an artifact produced by the force transducer. Further, we show that a correction of the long-range force data is possible and that the short-range normal force data seems to be reliable.

Figure 6.17 shows a typical measurement on a lubed CN_x surface. The lubricant thickness

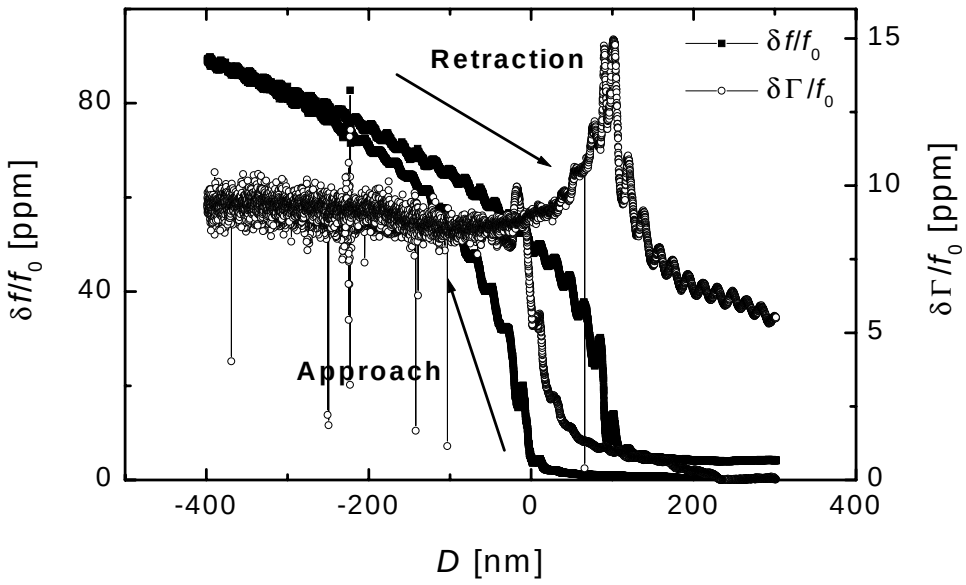

Figure 6.16: Measurement with an 0.4 mm quartz plate without facets. Recorded was the first resonance at 4 MHz. Oscillations are caused by coupling of the resonance to the holder. At higher overtones this could be avoided because energy trapping is better. However, the overtones are not as sensitive to the friction forces.

is 4 Å on top of a 50 Å amorphous CN_x layer. Panel A displays the normal force and dissipative quartz signal $\delta\Gamma/f_0$ over a total z-travel range of 200 nm. The normal force appears to increase from a $D = 100$ nm surface separation and close before contact amounts to $F_N \approx 70$ μN. After contact is established it has a constant slope as expected for pressing onto a rigid surface. The quartz damping remains constant at a zero value until contact with the surface starts.

Figure 6.17B is an enlargement of Figure 6.17A with a z-range of 10 nm around the contact. Both signals, normal force and resonance bandwidth, (both operate independently from the piezo performance and from each other) change continuously when the surfaces approach. Also, they show a reasonable coincidence: As the (normal) attraction of the surfaces increases ($D = -1.4 - 0$ nm), the friction force does the same. At surface separations above 25 nm, that is, above the separation range expected for van der Waals forces and direct contact between the Si_3N_4-sphere and the lubricant film, the quartz signal was equal to zero (within the scatter), which indicates that the surfaces do not interact above this separation.

Discussion of long-range behavior. The following behavior can be extracted: The surfaces start attracting at a separation of 140 nm with a force of 1–2 μN. Shortly before contact this force has increased to a value of about 73 μN. The different parts of the curves appear to scale linearly with distance D. A van der Waals interaction (which would be the possible, attractive interaction to expect) should rather exhibit a D^{-2} behavior for a sphere–flat contact. However, the forces that seem to act, were much too high for a van der Waals interaction. (The estimation of the Hamaker constant results in $A_H \approx 10^{-17}$ J.) Furthermore, it was not possible to fit the data with this functional dependence. Other reasons for *apparent*, attractive forces could be:

- electric (patch) charges [BCP92] on the surfaces that lead to an electrostatic interaction force.
- a liquid lubricant meniscus could form between the sphere and the carbon surface (cf. Chapter 8), however, the total amount of lubricant is not enough to form a meniscus that would connect the surfaces at a separation of more than 10 nm.

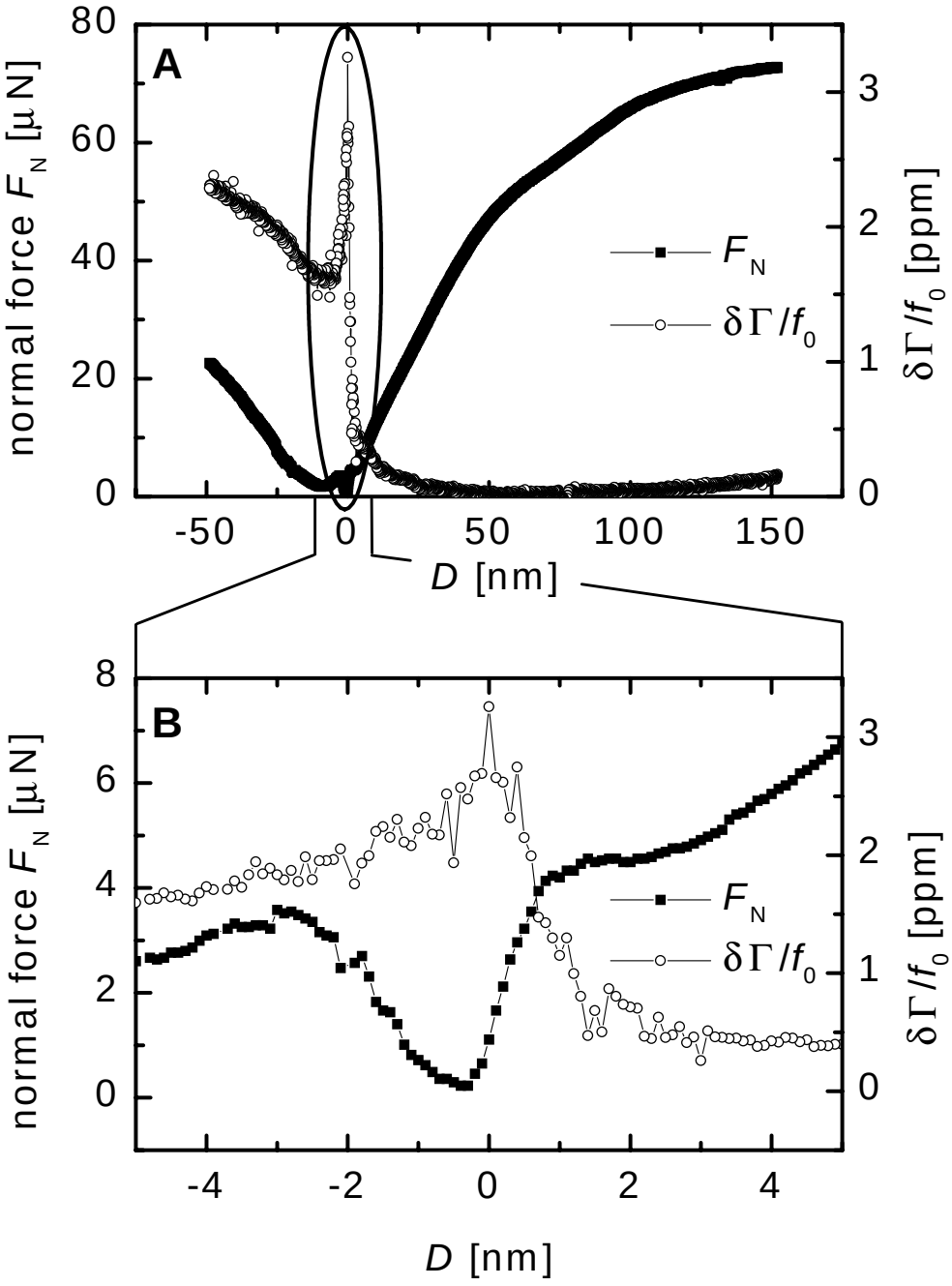

Figure 6.17: 50 Å CN_x surface with a 4 Å lubricant layer. (A) Entire measurement with a total travel range of 200 nm. (B) Zoom into (A) with a travel range of 10 nm. Resolution of the piezo steps is 1 Å.

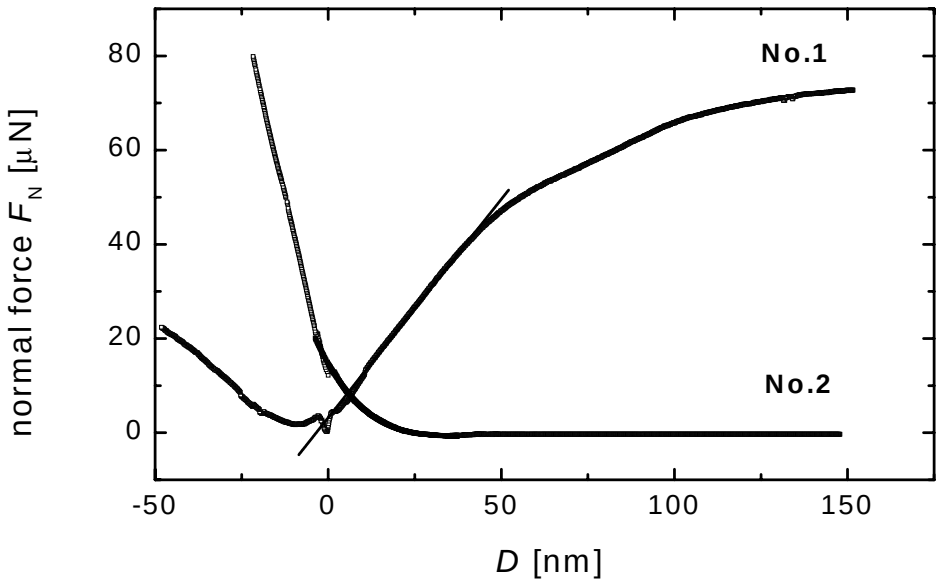

Figure 6.18: Two subsequent measurements on a 4 Å ZDOL4000 layer on a CN_x surface. The long-range behavior at $D > 0$ nm changes from attraction to zero interaction on the second approach. First and third order polynomials were used to fit the force vs. D curves at $D = -40 - -5$ nm. Fits are drawn into the plot.

- Thermal drift causing thermal expansion of the components, may occur, especially during long experiment times.

We will not ascribe the long-range behavior to any kind of interactions between the surfaces but rather treat it as an experimental artifact. In order to analyze the short-range interaction, we give an example of how data were treated in order to subtract the long- from the short-range behavior of the normal force. Figure 6.18 compares the first cycle on the 4 Å lubricant layer on CN_x with the second one. The shape of the long-range behavior changes from first strongly "attractive" to zero interaction. The repulsive behavior observed during the second approach can even be regarded as a short-range behavior ($D < 10$ nm). Without taking into account for this behavior we fitted the long-range behavior with first ("attractive" part) and third ("repulsive" part) order polynomials to get a good approximation of the long-range behavior. Fit curves are also drawn into the plot and describe the data fairly well. These were subtracted from the

measured normal force data and we obtain the curves shown in Figure 6.19. No other calculation was performed. Afterwards, the curves were *not* shifted further, neither in vertical nor in horizontal direction.

Short-range interactions. The resulting curves for the short-range regime superimpose astonishingly well if one takes into account the large difference between the long-range behavior in the different measurements.

The first measurement was performed on the 1^{st} harmonic (10 MHz), the second one on the 3^{rd} harmonic (30 MHz). Figure 6.19B shows the normalized frequency shifts $\delta f/f_0$ of both harmonics. From the shape of the curve and its smoothness one can conclude that no anomalies in the sample (for example dust particles) have occurred during the measurements. Figure 6.19C shows the corresponding change in bandwidth. For both frequencies the increased damping of the quartz coincides with the onset of the short-range normal force interaction. However, the 30 MHz data do not display a distinct maximum. We conclude that the lateral forces occur only within the range of the short-range normal forces which in this case are attractive for $D < 14$ Å and repulsive when elastic contact has been established.

From the discussion above we conclude, that the most probable reason for the occurrence of the long-range behavior of the force transducer is a thermal drift. Thus, on a long-range ($\hat{=}$ long time) scale, the normal force signal definitely is unreliable. On the other hand, it could be shown, that this artifact can easily be subtracted from the data curves and that the resulting short-range behavior can be well monitored by means of the used force transducer.

6.8.3 Distortion of Resonances

In Chapter 6.3, we reported that the quality of the resonance curves of the quartzes was not affected by the contact with the sphere, that is, they had still Lorentzian shape, and were not phase-shifted compared to the non-contact case. This was also an argument against the occurrence of nonlinear phenomena.

However, this statement was qualified for the narrow regime just before elastic contact starts, that is, where interfacial sliding and friction events take place.

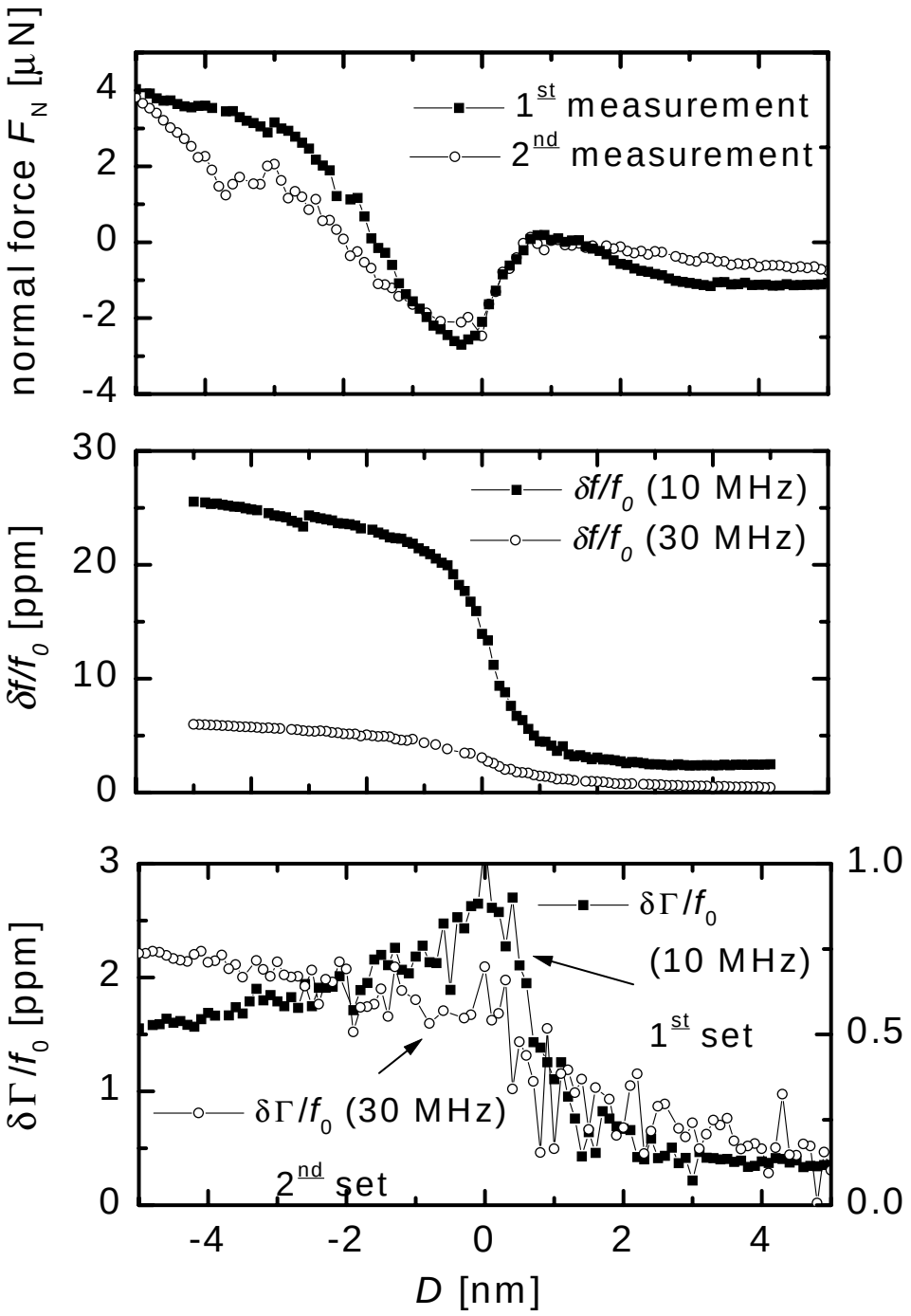

Figure 6.19: Comparison of the corrected normal forces and the original quartz data for two subsequent measurements on the same sample. (A): normal forces after correction; (B): Change in bandwidth and (C) frequency for 10 MHz and 30 MHz resonances, respectively.

During the course of our measurements on ZDOL lubricant films this effect became much greater. Figure 6.20A shows a typical resonance curve recorded in contact with a 25 Å PFPE film. The disturbances appear to be very regular and look like beating, a phenomenon that occurs when two oscillations with slightly different frequencies are superimposed. The characteristic frequencies in the example shown are the modulation frequency $f_{\mathrm{mod}} = 150$ Hz and a beating frequency of $f_{\mathrm{b}} = 3$ kHz. The occurrence of such resonance curves inhibited accurate fits. This in turn resulted in very noisy frequency and bandwidth data. Figure 6.20B-C displays the normal force, the resonance frequency, and the bandwidth data. The noise in the regime close to contact is due to distorted resonances as shown in Figure 6.20A.

However, it was possible to overcome this problem by choosing a smaller "IF-Bandwidth" on the network analyzer. The effect of this is to increase the sweep time for the recording of one resonance (by a factor 4) while keeping the number of data points constant at 201. For every data point the averaging time also increases by a factor 4. Of course, this also affects the total acquisition time, and it was already stated that the measuring time for a complete scan should preferably be minimized in order to avoid thermal drifts. However, the bad data quality obtained with shorter averaging periods forced us to use longer times. The cause of this effect could not be identified and it is not possible to determine whether it is a mechanical or an electrical effect.

6.8.4 Varying the Approach Speed

The aim of our measurements was to gain insight into molecular processes. Consequently, the resolution in surface separation and the steps performed to approach the surfaces were chosen to be as small as possible. The lower limit in resolution of the PZT stage is 1 Å as shown in Chapter 6. However, this could not always be achieved because of the sample structure (rough or thick lubricant coating) and thermal drifts. (Sometimes the contact point was not reached in a measurement although the pre-positioning had already placed the surfaces less than 100 nm apart from each other.) Also for some of the measurements, it was appropriate to choose less resolution in order to observe a larger travel range or to survey the general behavior of a surface.

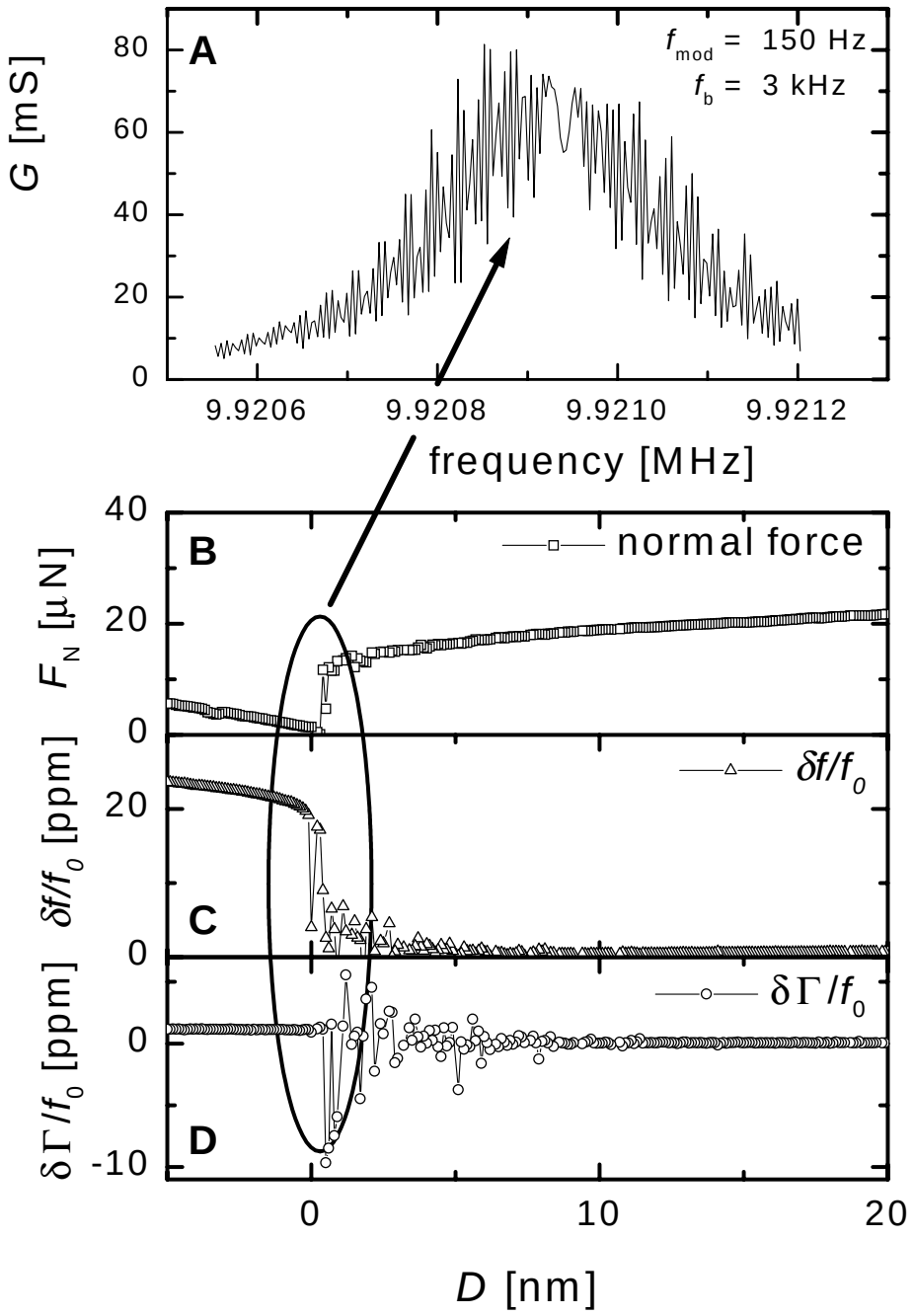

Figure 6.20: Distorted resonance (A) and its effect on the data noise. (B) Normal force; (C) Resonance frequency; (D) Resonance Bandwidth. The data was recorded on a 25 Å PFPE film on CN_x.

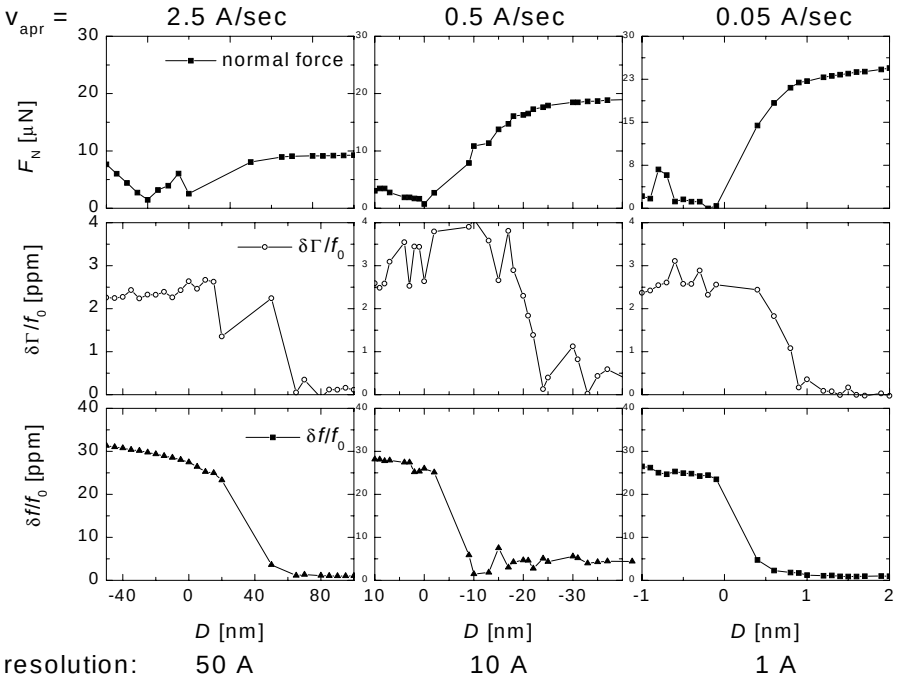

Figure 6.21: Dependence of several parameters on the approaching speed.

An example of three subsequent measurements carried out on the same sample but at different approaching speeds shows artifacts that are produced by varying the approaching speed v_{apr} (Figure 6.21). No other parameter was changed.

The frequency and the bandwidth change in the same way for all of the three measurements. The normalized change in frequency amounts to $\delta f/f_0 \approx 30$ ppm and the one in bandwidth is $\delta\Gamma/f_0 \approx 2.5$ ppm in elastic contact. However, the onset of the changes of the quartz parameters seems to depend strongly on v_{apr}:

The bandwidth begins changing at the same surface separation as the normal forces for all data sets. However, the frequency always starts changing later than the bandwidth. It appears as if the added stiffness to the quartz does not become effective until the dissipative signal has already gone through its maximum value.

Table 6.3 gives the parameters that apparently vary when changing the speed of approach. It is significant that the height of the force step decreases by a factor 3 with increasing approach speed v_{apr} of a factor 50. Although we know that the surface properties change with the number of contacts, from the previous experiments one should expect a decreasing force step instead of an increasing one. An explanation could be the mechanical inertia of

Table 6.3: Varying parameters for different approaching velocities.

No.	7	8	9
resolution [Å]	50	10	1
v_{apr} [Å/s]	2.5	0.5	0.05
ΔF_N [μN]	8	20	25
ΔD [nm]	60	20	0.8

the force transducer which prevents it from exactly following the force profile when being moved too fast.

Also, the interaction range seems to increase by a factor of 60 with increasing v_{apr}. A reason for this could be the increasing instability of the mechanical setup when moving the surface at a higher speed.

From these results it is appropriate to conclude that any increase of the approach speed produces experimental artifacts in the magnitude of the forces as well as the width of the interaction range. We did not investigate this issue in further detail but rather attempted to drive the measurements as slowly as possible to the detriment of the other experimental constraints that should be followed (for example, thermal drifts that do not allow extention of the measurement time to any desired length).

Chapter 7

Friction Properties of Perfluoropolyether Coated Amorphous Carbon Surfaces

7.1 Introduction

An application where "nanotribology" becomes important is the lubrication of hard-disks in the storage disks in the computer industry. Because the head–disk distance is only a few nanometers the lubricating layer must be molecularly thin. Typical shear rates for the lubricant film in disk–drives are in the order of $\dot{\gamma} = 10^9$ s^{-1} [JB95], which is in the range of the ones occurring in the quartz resonator experiment. This method provides several experimental conditions that are similar to those occurring in a real disk drive, above all, the high surface speed of the quartzes (1 m/s) when oscillating and the high frequencies accessible. No other described method (SFA or AFM) is able to perform such rapid movements.

The lubricant is a key component in magnetic disk technology. Its role is to minimize friction between head and disk and to protect the medium from wear caused by direct head-to-disk contact [Bhu96]. The perfluoropolyethers (PFPEs), which have been used as magnetic disk lubricants, are liquid oligomers fulfilling such technological requirements as chemical inertness, oxidative resistance, thermal stability, low surface tension, relatively

high molecular weight, low vapor pressure, good viscosity index and good lubricity. The substrate is amorphous carbon which is mechanically very robust. A review on hard-disk and lubrication technology is presented in [JMM+96].
With the instrumentation described in Chapter 5 we were able to look at mainly two types of interactions:

1. The normal forces between two surfaces upon approach and separation. These results should be comparable to measurements with the surface forces apparatus because geometries and conditions are quite similar.

2. Lateral forces occurring at the interface between quartz and sphere, which can be probed by means of the change in the quartz resonator signal.

It is expected that correlations between lateral and normal forces will provide insight into the control of the lubricating properties of the polymer layer.

7.1.1 Materials and Sample Preparation

Quartzes

The quartz blanks (Quarztechnik Daun, Germany) used for friction experiments have fundamental frequencies of 10 MHz, and (allowed) higher harmonics situated at 30, 50, 70, and 90 MHz. Their diameter was 14 mm, and the thickness 0.18 mm. For a more comprehensive characterization we refer to Chapter 5.5.4, p.60.

Amorphous Carbon

The amorphous carbon (a-C) layers were sputtered on top of one of the gold electrodes of the quartz. Two different types of carbon have been used for experiments. By adding the respective gas during sputtering the carbon can either be nitrogenated (a-C:N, CN_x) or hydrogenated (a-C:H, CH_x).
In general, these diamond-like carbon coatings have several properties that make them

very suitable as wear-protective coatings in the disk-drive application. However, their structure and properties strongly depend on the sputtering method and conditions. Therefore, values reported in literature vary.

They contain mixed amorphous and graphitic (micro-)crystalline phases of carbon where the crystal phases are sparsely distributed in the amorphous matrix [SWCJ97]. The random structure consists mostly of carbon atoms which are bonded to one another with either fourfold (sp^3 hybridization, diamond) or threefold coordination (sp^2, graphite). Hydrogen in the films partially passivates dangling carbon bonds within the films and has also the effect of substituting for carbon–carbon bonds, leading to a reduction in the three-dimensional rigidity of the structure [JMM+96].

The amorphous carbon films have a density of $\rho = 1.8 - 2.3$ g/cm^3 and are very hard (Young's modulus $E = 100 - 250$ GPa [RAvV+94], Hardness H = Load/Area = 18 − 32 GPa [KWN97]). They are usually very smooth (0.25 nm rms roughness on silicon wafers) [CLCB96] and "replicate the substrate topography, giving rise to a surface roughness equal to or better than the original substrates" [LCC+94]. The surface roughness strongly influences the disk performance where life time, loss of bits and error rate are acceptable below an rms roughness of $\sigma_{\text{rms}} = 5$ nm. For greater surface roughness these properties deteriorate dramatically [JMM+96]. Comparative studies of the macroscopic friction coefficient resulted in $\mu = 0.23$ for CN_x- and $\mu = 0.39$ for CH_x-surfaces. The setup used for determination of these values was a scratch tester with a 3.2 mm-diam pin ruby Al_2O_3–ball. The testing speed was $v = 1$ m/s and the applied load in the gram-range. The surface roughness of the substrate was $\sigma_{\text{rms}} = 0.3$ nm [WBM+95]. Mate [Mat92] used friction force microscopy to determine friction coefficients of non-lubricated and lubricated (25 Å ZDOL) CH_x-surfaces vs. a tungsten tip at typical sliding velocities of 300 nm/s. He finds friction coefficients of $\mu = 0.5$ for the non-lubricated surface and $\mu = 0.2$ for the lubricated surface.

Perfluoropolyether (PFPE)

Perfluoropolyethers have been developed in the late 1960s by D. Sianesi and coworkers in Milan (Italy). They are fluids that have the structure of polyethers and maintain an elastohydrodynamic state due to their high compressibility and their viscosity–temperature

characteristics [SZFB71]. The perfluoropolyethers used in this work were derivatives of the Fomblin Z backbone [TLWC98]:

$$X - CF_2 - O - (CF_2 - O-)_p - (CF_2CF_2 - O-)_q - CF_2 - X$$

where the backbone can be terminated with a variety of functionalities (X). In the case of Fomblin Z, termination of the polymer with functional end-groups occurs at both ends of the polymer. During this study we only used the hydroxyl–terminated Fomblin-Z derivative ($X = CH_2OH$) (ZDOL) that was obtained from Ausimont USA, Inc. The polydisperse polymer ZDOL4000 had the average molecular weight $M_w = 3800$ kg/mol. The ratio p/q is commonly called the C_1:C_2-ratio and was $C_1/C_2 = 1.08$. The higher this ratio the stiffer the chains, i.e., the higher the glass transition temperature.

The perfluoropolyether lubricant ZDOL4000 was applied to the carbon-overcoated disk from solutions of the PFPE in perfluorohexane using a dip-coat method [GLCR95]. The applied PFPE thickness was controlled by adjusting the pull rate. All film thickness measurements were carried out using FTIR-spectroscopy (Nicolet Model 5100). The peak height of the major infrared absorption band at 1280 cm^{-1} was calibrated to the lubricant thickness via ellipsometry and XPS (X-Ray Photoelectron Spectroscopy) [AY83]. All thickness values have been verified with the frequency shift between non-coated and coated quartzes and confirm the FTIR results.

Results from molecular orbital calculations on the Fomblin Z polymer yield a diameter of the PFPE molecule in the order of 7–8 Å and a length of approximately 1400 Å for $M_w = 4000$ g/mol. With increasing molecular weight the glass transition temperature and the viscosity increase. A decrease in the C_1:C_2–ratio makes the chain stiffer and less susceptible to deformation.

Dynamic bulk properties. Marchionni and coworkers investigated the molecular weight dependence of rheological and thermal properties of perfluoropolyethers [MAP88, MARP91]. For non-terminated linear Fomblin Z the authors report the following dependence of the glass transition temperature T_g on the number molecular weight M_n:

$$T_g = 142.1 - 1.49 \times 10^4 / M_n \tag{7.1}$$

Thus, for a molecular weight of $M_n = 3581$ g/mol the authors measured a glass transition temperature $T_g = 137.1$ K = –136 °C. The respective density and viscosity of the bulk

sample of same molecular weight at room temperature (T = 293 K) was $\rho = 1828.8$ kg/m^3, and $\eta = 53.4$ mPas [MAP88]. Further, the same author states in another report that "the perfuoropolyethers are Newtonian, i.e., their viscosity is usually independent of shear rate, within wide limits of shear rate. In the same paper, Marchionni et al. determine the temperature dependence of the shear viscosity of samples of different molecular weight. A sample of $M_n = 5130$ g/mol has viscosities of $\eta \approx 50$ mPas at room temperature (T = 298 K) and $\eta \approx 180$ mPas for T = 258 K [MAP92]. For these samples the C_1:C_2–ratio was p/q = 0.69. For similar derivatives having a stiffer backbone with p/q = 1.15 the same authors report of an increased glass transition temperature of $T_g = 147.5$ K = 125.6°C [MARP91]. In any case, even if we apply the temperature–frequency superposition principle for the quartz method that probes at MHz-frequencies, and thus, 40 K below room temperature, we are still far above the bulk glass transition of the lubricant. Therefore, at MHz-frequencies they should still exhibit liquid properties in the bulk.

7.1.2 Properties of Thin PFPE Films and Interaction with Amorphous Carbon Substrates

Figure 7.1A shows the dependence of several thermodynamic quantities on the applied film thickness of non-functionalized PFPE lubricant, Fomblin Z03, ($M_w = 4000$ g/mol) in contact with a CH_x-surface. They were obtained from evaporation experiments [TW99] and contact angle measurements [TWP98]. The thickness dependence of the free energy coupled with the measured temperature dependence of the evaporation are used to determine both the film entropy, and the attractive potential energy of the solid-liquid interfacial interactions.

The polar and dispersive surface energies of CH_x were determined to $\gamma^p = 13 - 14$ mJ/m^2 and $\gamma^d = 40$ mJ/m^2 by contact angle measurements using the sessile drop method. For the determination of the dispersive component non-polar organic solvents were used (hexadecane, heptane) [TLWC98]. Figure 7.1B shows the dependence of the dispersive component of the free surface energy γ^d on the layer thickness of ZDOL on both, CH_x and CN_x. The bulk value for both surfaces is identical (15.7 mJ/m^2). Qualitatively, this can be understood in terms of surface coverage: As the amount of the low-surface-energy lubricant

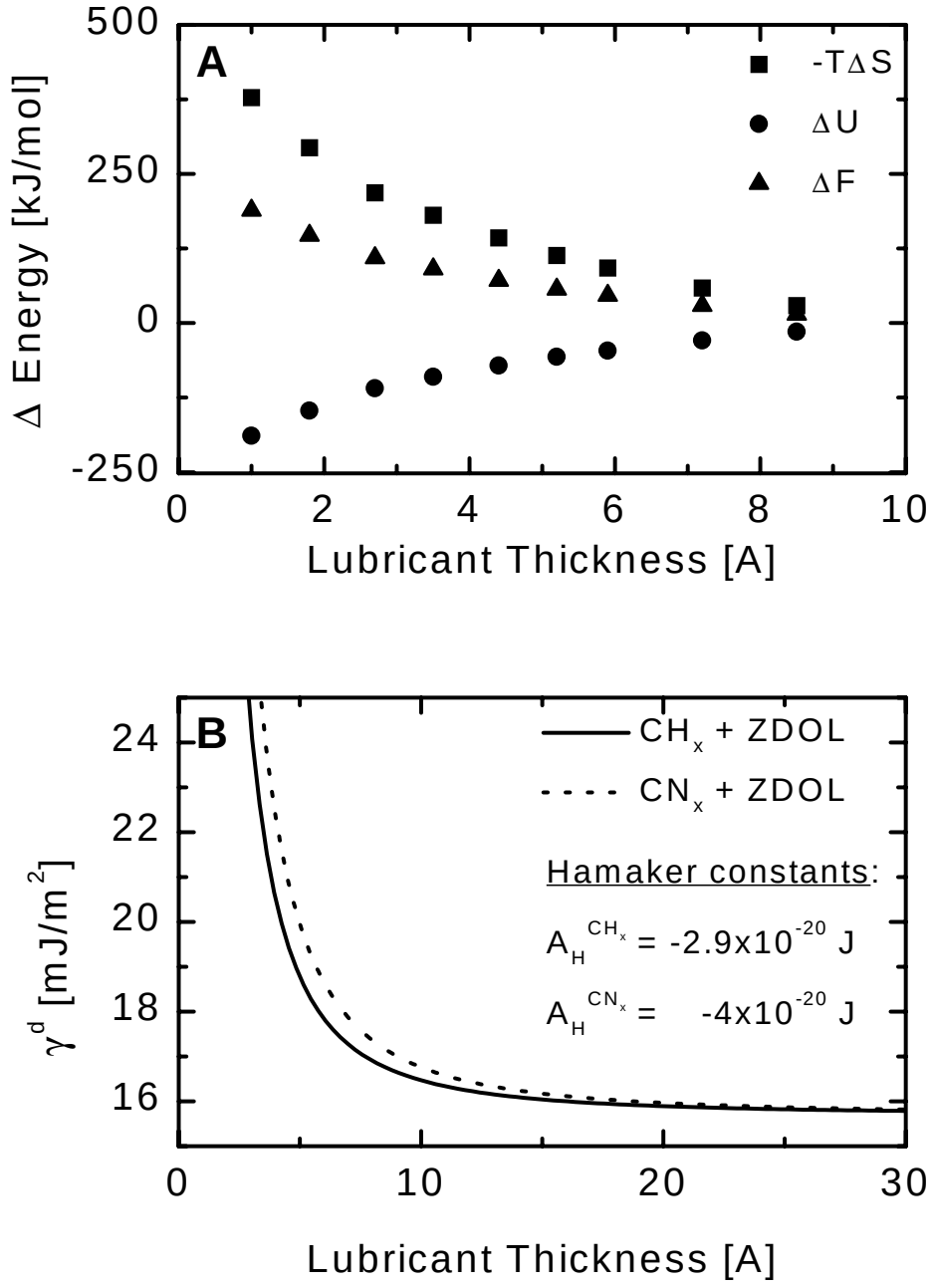

Figure 7.1: Dependence of thermodynamic quantities on lubricant thickness. (A) The entropy S and the internal energy U of the film decreases with decreasing film thickness, the Helmholtz free energy F increases with decreasing film thickness (from [TW99]). (B) Dependence of the dispersive surface energy γ^d on film thickness for ZDOL films on CH_x and CN_x surfaces. The respective Hamaker constants A_H for the respective interaction with the substrates are given [TWP98].

that is applied to the high-energy carbon surface increases, the dispersive surface energy decreases. Complete physical coverage can be defined at the point where the underlying carbon surface no longer contributes to the measured dispersive energy, i.e., where γ^d reaches the asymptotic limit. From Figure 7.1B the authors estimate that complete coverage of the surface by ZDOL occurs at $h_0 = 14 \pm 1$ Å for CH_x and $h_0 = 21 \pm 2$ Å for CN_x. From the analysis of the functional form of the free energy change ΔF^d with thickness the authors conclude that the solid-liquid van der Waals interactions are thermoneutral (not repulsive and not attractive) for ZDOL on CH_x, but are repulsive for ZDOL on CN_x. The polar components of the free surface energy are $\gamma^p \approx 10$ mJ/m^2 for CH_x and $\gamma^p = 15$ mJ/m^2 for CN_x. Interestingly, γ^p "oscillates" for a layer thickness < 40 Å on CH_x which the authors attribute to the different nature of the interaction of ZDOL with CN_x and CH_x [TWP98].

The differing interaction with the various carbon surfaces can be understood when regarding the active surface sites of both. On the CN_x-surfaces nitrogenated species compose the active sites, in particular, surface imine ($> C = N-$) appears to be an important functionality. On CH_x-surfaces the main functionality are hydrogen atoms. From ab-initio quantum chemical calculations the same authors find that the imine nitrogen atoms have excess negative charges, thus, are basic in a Lewis sense. The fluorine atom, as well as the hydroxyl and ether oxygens in the ZDOL backbone are negatively charged. Thus, the hydroxyl-endgroups (acidic) are (strongly) attracted by both types of surfaces. However, the interaction of the ZDOL backbone with the imine sites on CN_x is repulsive whereas it is neutral for CH_x.

Surface characterization. AFM images of CN_x surfaces are shown in Figure 7.2: (A) for a bare surface, (B) for a 18 Å and (C) for a 30 Å lubricant layer on top. Rms surface roughness of the bare surface is $\sigma_{rms} = 18$ Å, for the 6 Å lubricated surface it is $\sigma_{rms} = 13.1$ Å, and for the 30 Å lubricant film it decreases to $\sigma_{rms} = 10$ Å. The surface structure of the lubricant layers (Figure 7.2B and C) is similar and resembles images of the non-lubricated amorphous carbon overcoat (CN_x) (Figure 7.2A). Therefore, we assume that the AFM tip is pushed through the liquid lubricant layer (tapping mode) and that the imaged surface profile is still that of the underlying substrate. Investigations of force–distance curves from Mate et al. support this assumption [Mat92]. Nevertheless, it is

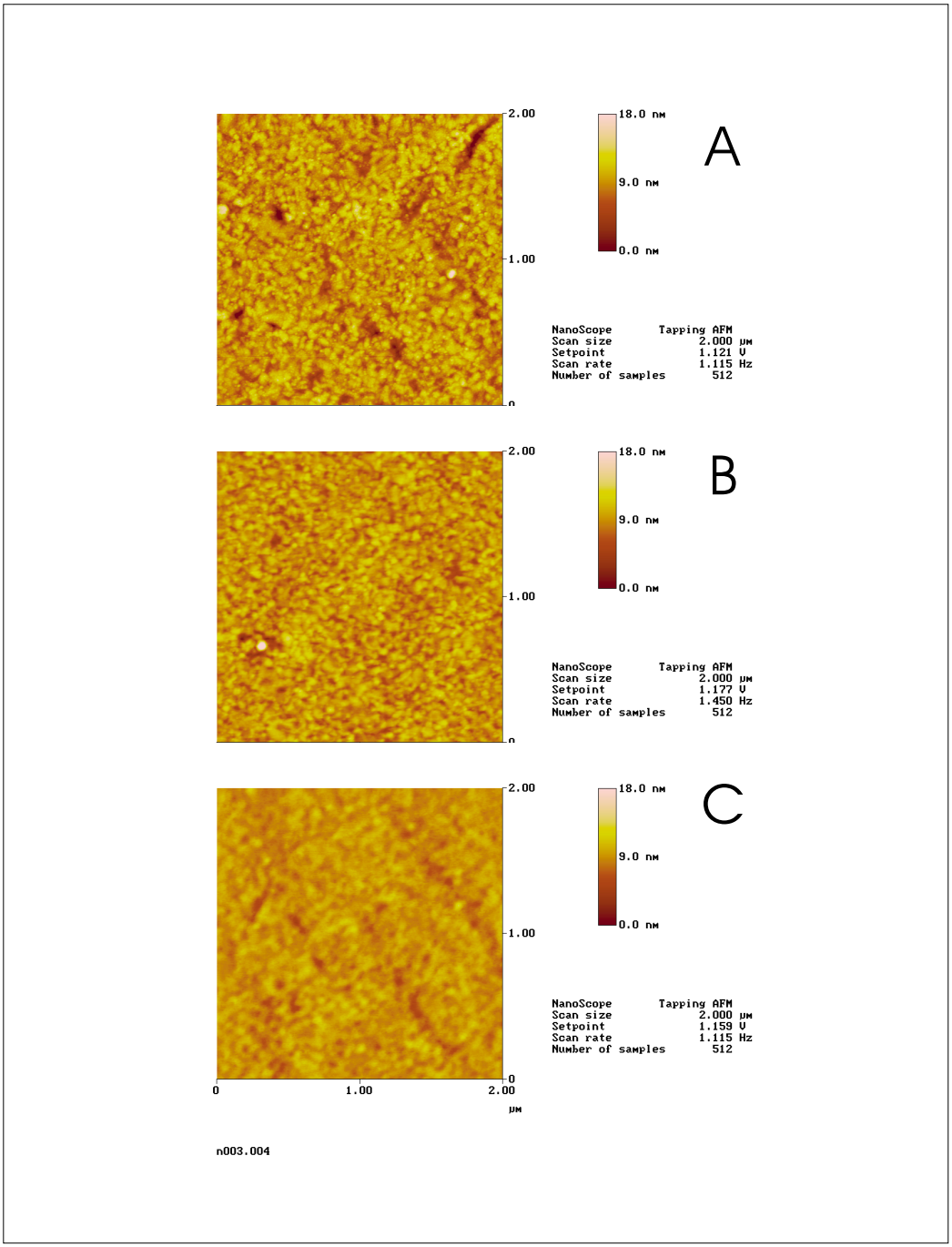

Figure 7.2: AFM (Tapping mode) images of (A) a bare CN_x surface ($\sigma_{\rm rms} = 18$ Å) (B) coated with a 6 Å ($\sigma_{\rm rms} = 13$ Å) and (C) a 30 Å lubricant layer ($\sigma_{\rm rms} = 9$ Å). The (apparent) surface roughness $\sigma_{\rm rms}$ decreases with increasing lubricant layer thickness.

interesting to note that the surface roughness seems to decrease with increasing lubricant thickness. This would support the assumption that the liquid lubricant first fills up the holes in the surface.

7.1.3 Experimental Conditions

The silicon nitride sphere (radius $2.3813 \pm 2 \times 10^{-4}$ mm) was plasma-cleaned before the start of any experiment and then exposed to normal environmental conditions ($T = 25\,^{\circ}C$, relative humidity 45%). No special care was taken to reduce the relative humidity. Usually, it should be controlled for surface forces measurements because the formation of a water layer on the surface is highly likely. First, a layer of polar water molecules can drastically change the surface energy. Second, the formation of a water meniscus due to capillary forces is expected. Both affect the measured friction forces compared to the surface without a water layer [PM97]. In this study we were only using perfluoropolyether lubricants with low surface energies ($\gamma \approx 20 - 30$ mN/m). The contact angle of water is $\theta_{H_2O} \approx 105^{\circ}$ and the surface was thus not wetted by water even though the experiment was carried out in a humid atmosphere.[1] Since water contact angles on the carbon surface amount to $\theta_{H_2O} \approx 30 - 40^{\circ}$, in an ideal situation water will not wet the carbon layer either. Influences of the humidity on surface properties were only reported for a relative humidity higher than 80% [XFTT98]. The average humidity in all of our experiments was 40–50%. Based on the discussion above, we conclude that the observed effects were not caused by water layers on the surface. This argument is supported by investigations of Binggeli and coworkers [BM95] who found that "the water capillary formation around the tip is greatly suppressed ... on the hydrophobic surface of silicon oxide covered with a perfluoropolyether lubricant."

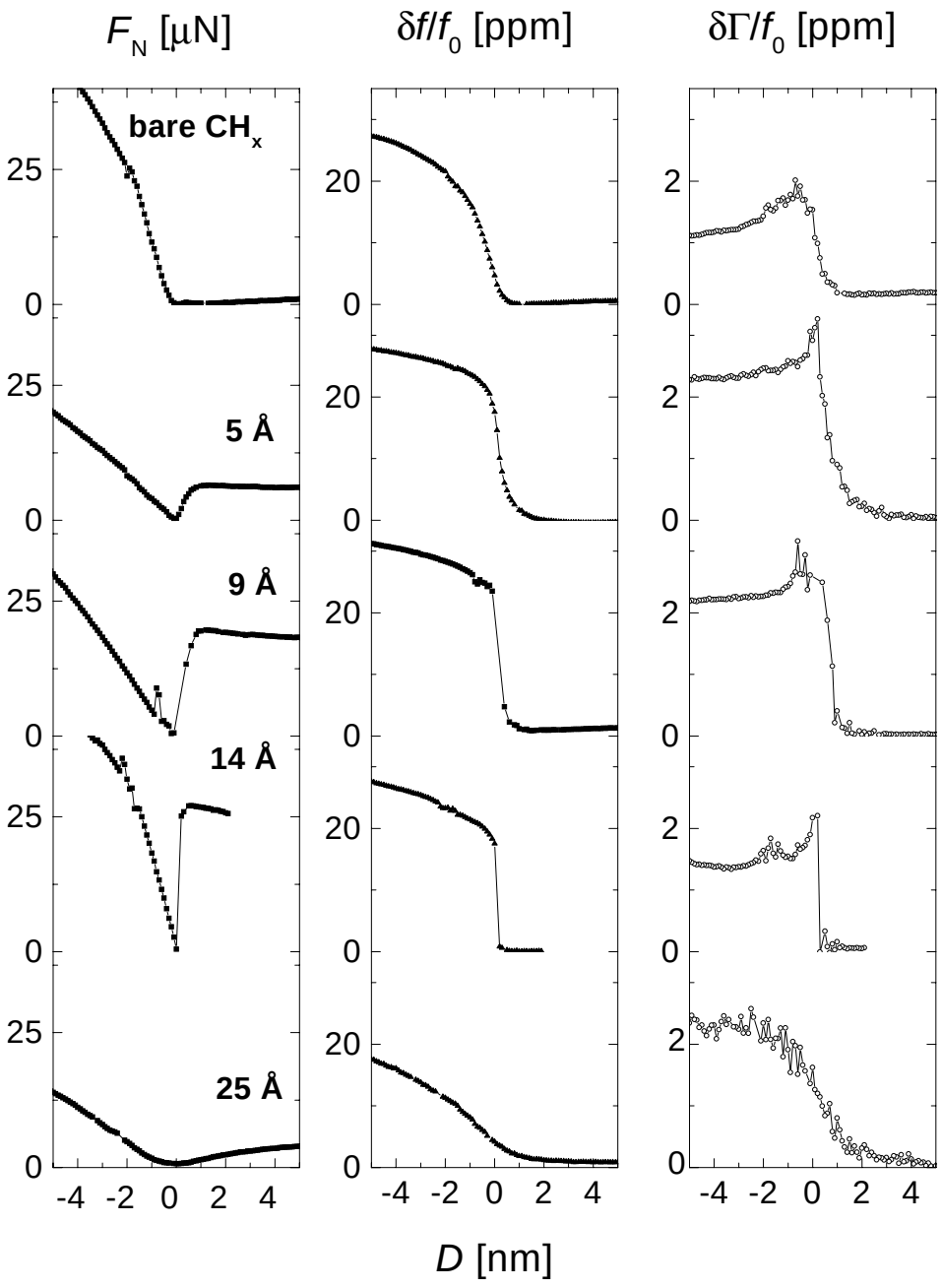

Figure 7.3: Dependence on lubricant (ZDOL 4000) layer thickness on CH_x surfaces. Columns (from left to right): normal force F_N in μN; and change in dissipative quartz signal $\delta\Gamma/f_0$ [ppm], normalized frequency change $\delta f/f_0$ [ppm]. Rows (top to bottom): Increasing lubricant thickness: bare CH_x surface, 5 Å ZDOL 4000, 9 Å, 14 Å, and 25 Å. The x-scale for all plots is the same: $D = -5 - +15$ nm (relative to the contact point). The y-scale for each panel in a column is the same: F_N =0–80 μN, $\delta\Gamma/f_0 = 0 - 3.5$ ppm, and $\delta f/f_0 = 0 - 35$ ppm.

7.2 Effect of Varying Thickness of the Lubricant Layer

7.2.1 CH_x Substrate

In Figure 7.3 we compare measurements on surfaces with 4 different lubricant thicknesses on CH_x to a measurement on a bare CH_x surface.

Normal Forces

The first column shows the normal force exerted on the quartz during approach. For all data sets the baseline on the left side of the plots is straight and flat: The force equals zero up to the point where interaction starts. On the right-hand side elastic contact is reached and the force increases linearly with the traveled distance. The slope of the curves is within the same order of magnitude because of the elastic response of the spring constant of the force transducer. For the bare as well as for the 25 Å layer the transition from non-contact to the contact regime is very smooth. Intermediate film thicknesses all display a force step that can be attributed to an attractive force acting between the surfaces. This attractive force increases with increasing film thickness.

Frequency Shifts

Normalized frequency shifts are displayed in the 2^{nd} column. All these curves are very smooth in the contact regime and show the expected asymptotic behavior which is attributed to the increasing contact radius (JKR, cf. Chapter 3.26). Before contact the base lines are also flat and smooth. A jump to higher values occurs at the same point where the force drops for the attractive cases. The frequency curves give no further insight into the dissipative behavior of interest. Nevertheless, they represent a good control of environmental and surface conditions during the measurement because the resonance frequency is very sensitive to changes in temperature, pressure, and surface coverage.

[1] This is valid for a complete film, i.e., "bulk" coverage, for thinner films holes in the film can be found and water from the atmosphere can actually promote a partial dewetting of the surface.

Dissipative Signal

The 3^{rd} column displays the normalized change in the bandwidth of the quartz resonances $\delta\Gamma/f_0$. Like the other signals it is very smooth in the non-contact as well as in the elastic–contact regimes. In contrast to the frequency shifts it does not continue to increase when firm contact is established but rather maintains a constant value that is higher than that before contact. In-between these extreme cases, in the region where contact is just barely reached, the signal becomes noisier and exhibits a maximum.

7.2.2 CN_x Substrate

Figure 7.4 shows measurements on a bare CN_x surface (top row) compared to 4 different ZDOL layers with varying thickness (top to bottom: 4, 8, 11 and 25 Å). All plots have the same x-scale ($D = -5 - +5$ nm relative to contact) except the one for the bare surface ($D = -50 - +50$ nm). The y-scales for each panel in a column are the same: Normal force $F_N = 0 - 40$ μN; normalized frequency shift $\delta f/f_0 = 0 - 30$ ppm and normalized change in bandwidth $\delta\Gamma/f_0 = 0 - 3$ ppm.
The baselines for all signals are flat and smooth, indicating the absence of contaminating dust particles between the surface and appropriate temperature stability during approach.

Normal force. Drift subtraction of the baseline was performed for only the 11 Å sample. The interaction between the bare surfaces is purely repulsive, whereas there is notable attraction on a short scale for the surfaces covered with lubricant films. Here, this behavior is not as pronounced and regular as for the measurements on CH_x surfaces (Figure 7.3, p. 128).

Frequency shift. The resonance frequencies of the quartzes show a smooth variation behavior simultaneous to the other signal changes.

Dissipative signal. The bandwidth parameter passes a maximum for all samples except for the 25 Å. This indicates that lubrication for that sample is complete whereas for the

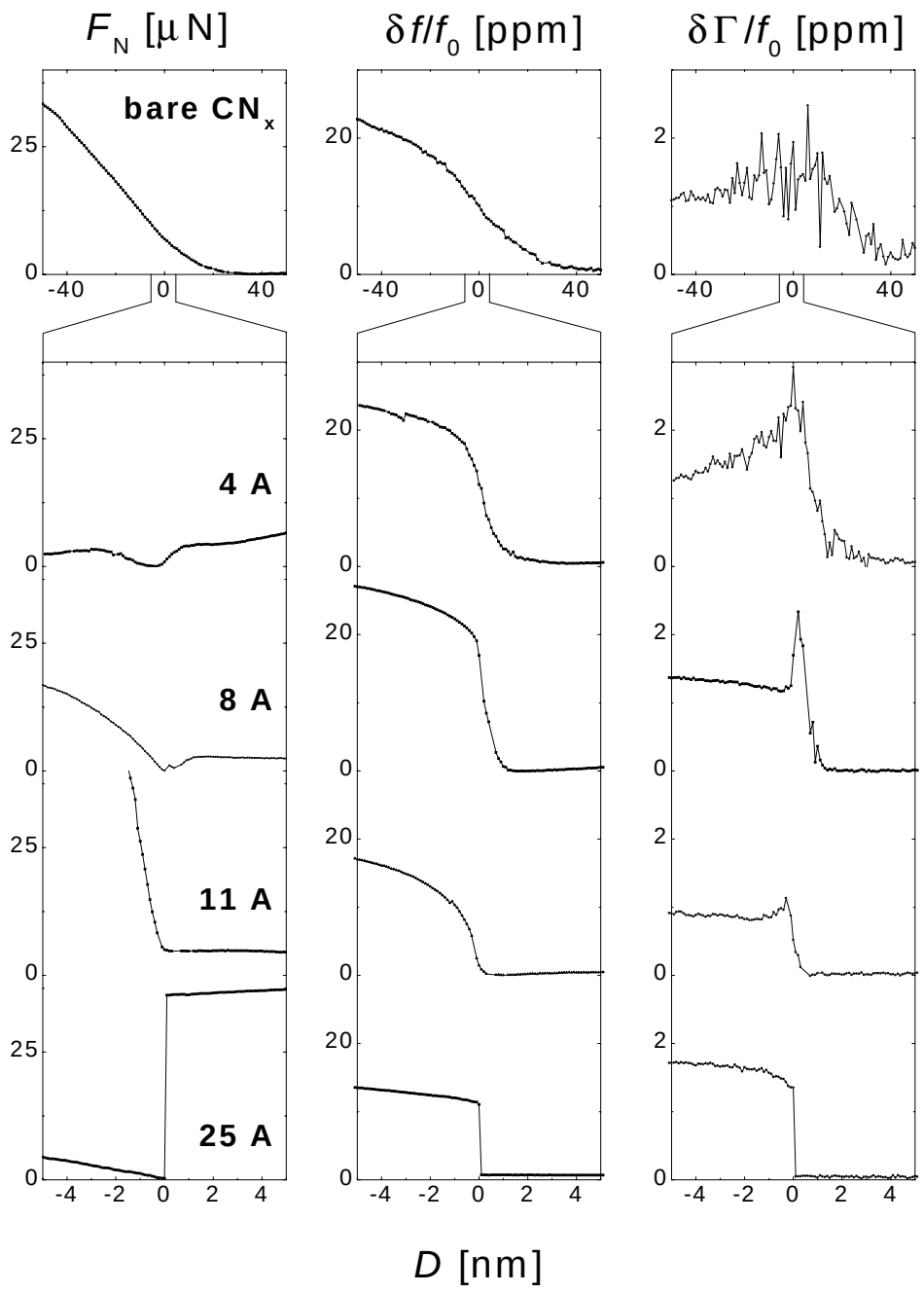

Figure 7.4: Dependence on lubricant layer thickness on CN_x surfaces. Columns (from left to right): normal force F_N in μN; normalized frequency change $\delta f/f_0$ [ppm] and change in dissipative quartz signal $\delta\Gamma/f_0$ [ppm]. Rows (top to bottom): Increasing lubricant thickness: bare CN_x surface, 4 Å, 8 Å, 11 Å, 25 Å ZDOL 4000. The x-scale for all lubricated samples ranges from -5−+15 nm, for the bare CN_x surface it is -50−+50 nm. The y-scales for the columns are: $F_N = 0 - 40$ μN, $\delta f/f_0 = 0 - 30$ ppm, and $\delta\Gamma/f_0 = 0 - 3$ ppm.

thinner layers there is still considerable dissipation occurring. Note that for all curves of intermediate film thickness (4–11 Å), the maximum in bandwidth occurs before a significant increase in frequency and simultaneously to the beginning of the short range attraction between the samples. Extracted parameters for all measurements are given in Table 8.2.

7.3 Attraction and Adhesion

Figure 7.5 shows an approach–retraction cycle carried out on a 25 Å-coated CN_x surface. While approaching the surface over a range of 98 nm (t = 80 min) the changes in the baselines of force and frequency indicate a thermal drift during the course of the measurement. Suddenly the sphere jumps into contact because of an attractive force $F_{\mathrm{attr}} = 22\ \mu$N between the surfaces. After establishing contact the sphere is "pressed" onto the sample for another 7 minutes before retracting the sphere. This is indicated by the linear slope of the force–distance curve. On separation, the force initially follows the exact same slope. Retraction until rupture of the contact takes another 10 minutes (25 nm) before the sphere jumps apart revealing an adhesive force of $F_{\mathrm{adh}} = 37\ \mu$N. After that, the force returns to the baseline measured before contact, which indicates that no hysteresis or plastic deformation of the force transducer has occurred.

This approach–retract cycle resembles the ones obtained from AFM force–distance scans (cf. Figure 4.5, Chapter 4.4, p. 42). There is an "attractive hysteresis" observable. Presumably, this is due to liquid meniscus formation between the surfaces.

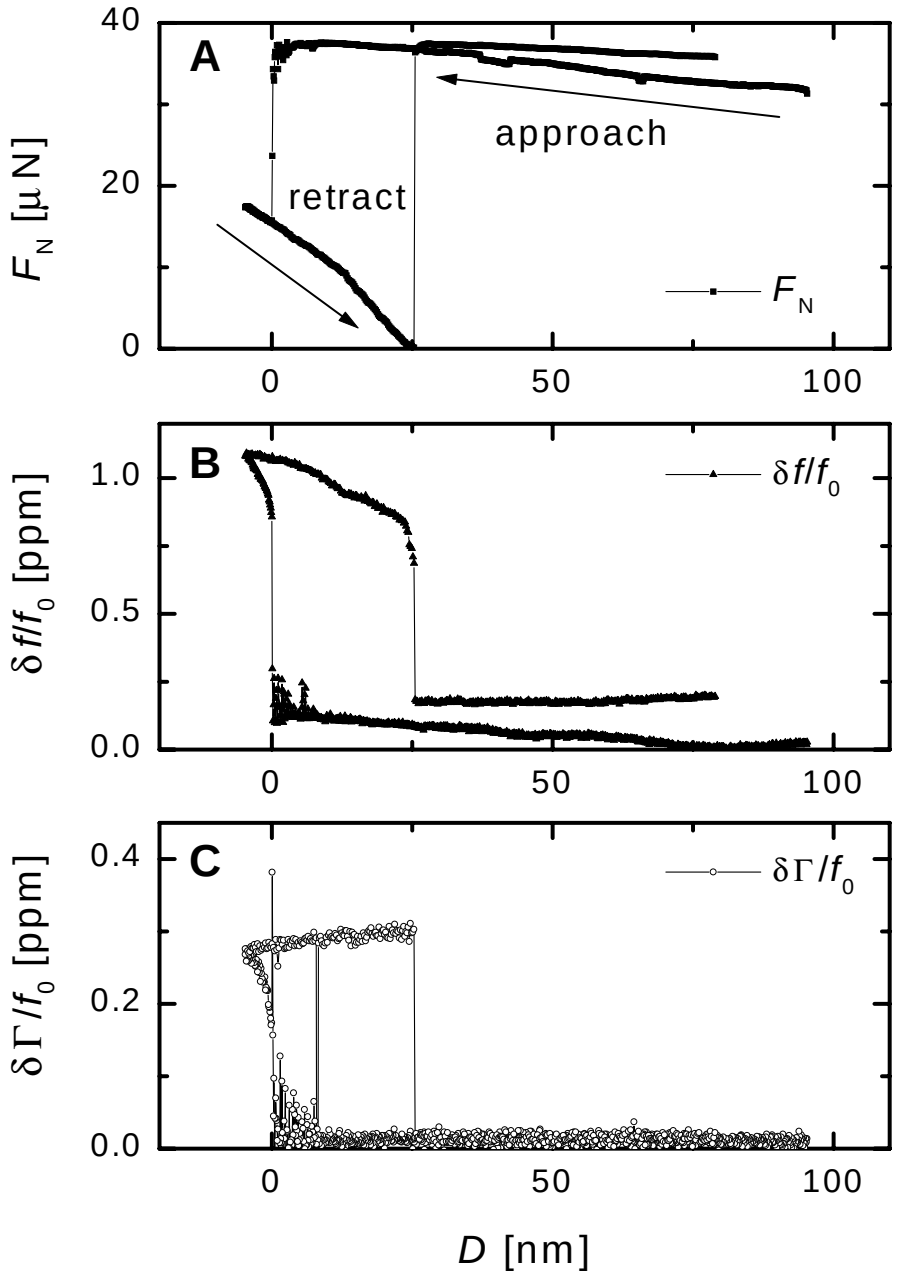

Figure 7.5: Approach–retract cycle on a 25 Å ZDOL layer on CN_x. The surfaces jump into contact because of an attractive force of $F_{\mathrm{attr}} = 22\ \mu$N and detach while retracting at a distance $D = 25$ nm from the first contact point. The adhesive force at this point amounts to $F_{\mathrm{adh}} = 37\ \mu$N. (A) normal force F_N, (B) normalized frequency shift $\delta f/f_0$, (C) normalized change in bandwidth $\delta\Gamma/f_0$.

Chapter 8

Discussion of Results on PFPE Films

8.1 Introduction

In Chapter 6 it was shown that with the quartz method one is able to distinguish between high- and low-energy surfaces. The change in bandwidth passes through a maximum when high friction occurs but does not for low-friction contacts. However, this was only a qualitative statement about these two extremes, and we would like to determine whether it is also possible to distinguish quantitatively between surfaces with varying friction.
The instrumentation was developed to investigate thin surface layers such as monomolecular films. As seen in Chapter 7, a system with lubricating properties already at monolayer coverage of the underlying substrate is the group of perfluoropolyethers used for hard-disk lubrication. Their properties have already been characterized extensively, and therefore it is possible to compare our results with the information obtained from other methods such as Friction Force Microscopy (FFM) and Surface Forces Apparatus (SFA).
In the following, the results from Chapter 7 are discussed by summarizing and comparing the parameters extracted from our measurements. We will also compare the significance of different parameters that could be considered as characterizing the friction forces.

The main experimental problems were discussed in Chapter 6.8. These were thermal drifts, noisy data in the region close to contact, and contamination of the surfaces. In particular, the superposition of these different "disturbances" made their conceptual isolation more difficult.

8.2 Variations in Friction with Lubricant Thickness

The occurrence of friction at the quartz surface is accompanied by a distinct maximum in $\delta\Gamma/f_0$ or $\tan\delta = \delta\Gamma/\delta f$ that does not occur for a low-friction interface. Thus, this maximum should also contain information about the magnitude of friction occurring. There is a need to quantify the properties of these maxima: We will start with the raw data and consider ways to relate them to friction forces. Tables 8.1 and 8.2 summarize the extracted parameters from Figures 7.3 (p.128) and 7.4 (p.131) for measurements on CH_x and CN_x surfaces.

Table 8.1: Varying bandwidth and measurement parameters for different lubricant thickness on CH_x-surfaces.

thickness [Å]	0 (bare)	5	9	14	25
$(\delta\Gamma/f_0)_{\max}$ [ppm]	1.9 ± 0.1	3.1 ± 0.1	2.93 ± 0.3	2.2 ± 0.1	2.34 ± 0.11
$(\delta\Gamma/f_0)_{\min}$ [ppm]	1.03 ± 0.02	2.3 ± 0.02	2.15 ± 0.02	1.34 ± 0.02	2.32 ± 0.02
$\Delta(\delta\Gamma/f_0)$ [ppm]	0.87 ± 0.03	0.80 ± 0.03	0.78 ± 0.32	0.86 ± 0.12	0.02 ± 0.13
$\delta\Gamma_{\text{ratio}}$	1.84 ± 0.14	1.35 ± 0.05	1.36 ± 0.16	1.64 ± 0.1	1.01 ± 0.06
Q $\times 10^{-4}$	6.6 ± 0.4	11.5 ± 1.5	8.5 ± 1.0	6.0 ± 0.4	3.7 ± 0.1
Amplitude a [nm]	15.5 ± 0.1	27 ± 4	20 ± 2	14.4 ± 0.8	8.7 ± 1.1
Speed v [m/s]	0.96 ± 0.06	1.7 ± 0.25	1.26 ± 0.12	0.9 ± 0.05	0.54 ± 0.01
$(\delta\Gamma)_{\max} \cdot v$	1.82 ± 0.22	5.27 ± 0.97	3.69 ± 0.77	1.98 ± 0.21	1.26 ± 0.08
$(\delta\Gamma)_{\text{ratio}} \cdot v$	1.77 ± 0.25	2.30 ± 0.43	1.71 ± 0.39	1.48 ± 0.17	0.54 ± 0.05
r_c [μm]	0.5 ± 0.3	0.5 ± 0.3	0.6 ± 0.2	1.0 ± 0.3	0.02 ± 0.02
resolution [Å]	1	1	1	1	1
time/step [min]	0.33 ± 0.02	0.35 ± 0.02	0.34 ± 0.02	0.34 ± 0.02	0.05 ± 0.01
data points/curve	168	354	442	320	350
total time [min]	55	124	150	109	17.5
ΔF [μN]	—	6 ± 0.5	18.9 ± 1.0	26.5 ± 0.5	4 ± 1

Both tables contain the following parameters (from top to bottom):

- The maximum value of the resonance bandwidth $(\delta\Gamma/f_0)_{\max}$,

Table 8.2: Varying bandwidth and measurement parameters for different lubricant thickness on CN_x surface.

Layer [Å]	0 (bare)	4	8	11	25
$(\delta\Gamma/f_0)_{\max}$ [ppm]	1.77 ± 0.40	2.32 ± 0.20	1.93 ± 0.20	1.13 ± 0.20	1.60 ± 0.02
$(\delta\Gamma/f_0)_{\min}$ [ppm]	0.80 ± 0.10	1.31 ± 0.03	1.17 ± 0.03	0.82 ± 0.02	1.59 ± 0.02
$\Delta(\delta\Gamma/f_0)$ [ppm]	0.97 ± 0.50	1.01 ± 0.23	0.76 ± 0.22	0.31 ± 0.22	0.01 ± 0.04
$(\delta\Gamma)_{\text{ratio}}$	2.21 ± 0.89	1.77 ± 0.20	1.65 ± 0.22	1.38 ± 0.28	1.01 ± 0.02
$Q \times 10^{-4}$	2.68 ± 0.1	3.6 ± 0.2	9.42 ± 0.01	6.2 ± 0.3	8.2 ± 0.02
Amplitude a [nm]	8.7 ± 0.2	8.5 ± 0.3	21.4 ± 0.01	14 ± 0.5	18.6 ± 0.1
Speed v [m/s]	0.54 ± 0.02	0.53 ± 0.02	1.33 ± 0.01	0.88 ± 0.04	1.16 ± 0.01
$(\delta\Gamma/f_0)_{\max} \cdot v$	0.96 ± 0.21	1.23 ± 0.16	2.57 ± 0.28	0.99 ± 0.23	1.86 ± 0.04
$(\delta\Gamma)_{\text{ratio}} \cdot v$	1.19 ± 0.55	0.94 ± 0.14	2.19 ± 0.32	1.21 ± 0.32	1.17 ± 0.04
r_c [μm]	0.05 ± 0.03	1.0 ± 0.1	4.9 ± 0.1	1.0 ± 0.3	0.5 ± 0.3
resolution [Å]	10	1	1	1	1
time/step [min]	0.1 ± 0.02	0.13 ± 0.02	0.3 ± 0.02	0.33 ± 0.02	0.07 ± 0.01
data points/curve	310	100	224	310	102
total time [min]	93	13	67	102	7
ΔF [μN]	—	3.9 ± 0.1	2.7 ± 0.3	—	36 ± 0.3

- the minimum value of the resonance bandwidth *in* elastic contact $(\delta\Gamma/f_0)_{\min}$,
- the difference $\Delta(\delta\Gamma) = (\delta\Gamma/f_0)_{\max} - (\delta\Gamma/f_0)_{\min}$,
- the ratio $\Gamma_{\text{ratio}} = (\delta\Gamma)_{\max}/(\delta\Gamma)_{\min}$,
- the quality factor Q,
- the calculated resonance amplitude a,
- the calculated surface speed v,
- the product $(\delta\Gamma/f_0)_{\max} \cdot v$,
- the product $(\delta\Gamma)_{\text{ratio}} \cdot v$,

- the calculated contact radius (JKR) r_c,
- the step width of approach,
- the time between every single step of the piezo stage,
- the (displayed) data points per curve,
- the total acquisition time for the (displayed) measurement,
- and the height of the force step (if observed).

Absolute height of the maximum $(\delta\Gamma/f_0)_{\max}$**.** In all measurements, except those for the 25 Å films, there is a distinct maximum in the change in bandwidth $\delta\Gamma/f_0$. $(\delta\Gamma/f_0)_{\max}$ is displayed in Figure 8.1A. For intermediate film thickness (4–14 Å) a decrease of friction with increasing film thickness was observed. However, the bare surfaces have a lower bandwidth maximum than the lubricated ones and the surfaces with a (25 Å) thick film had a larger maximum value than surfaces with thinner layers in each case, CH_x and CN_x. For the 25 Å-films, there is no distinct maximum in bandwidth observable, therefore these values are not comparable to those of curves which display a maximum. Presumably, the transition from viscous sliding to the elastic coupling (at high normal loads) for these films is very smooth as opposed to the thinner films, where the transition from the friction to the elastic–coupling regime is accompanied by a decrease in dissipation. We can also assume that for the thicker films a compression will occur.
The bare surfaces display a low bandwidth maximum compared to the lubricated surfaces. A possible explanation could be the "contamination" of the surfaces by a water layer that can only be avoided in vacuum. This water layer also lubricates the surface (cf. Chapter 4, p. 39)[BDI98, Bhu95].

Relative height of the maximum. The absolute value of the height of the maximum was not recognizable for surfaces with very low friction because there was no distinct maximum. From the shape of the bandwidth curve of the bulk-like samples (25 Å), which did not decrease after the maximum, we concluded that a better measure for the friction was the ratio of the maximum in bandwidth and the following minimum in contact,

$\Gamma_{rat} = \Gamma_{max}/\Gamma_{min}$, which is displayed in Figure 8.1B for the different films.
The bare surface now exhibits the highest value whereas the 25 Å films have the lowest. A decreasing friction for increasing film thickness could be observed for the entire set of CN_x samples. For CH_x, however, the intermediate film thicknesses showed an increase in friction with increasing film thickness. The order of magnitude of Γ_{rat} was the same for CN_x and CH_x surfaces.

Scaling with surface speed. As shown in Chapter 6.7, the lateral force F_p acting at the interface can be related to the change in resonance bandwidth (eq. 6.23, p. 103):

$$F_p \sim \frac{\delta\Gamma}{f_0} \cdot \dot{u} \tag{8.1}$$

Moreover, we have observed that the lateral force F_p was proportional to the surface speed $\dot{u} = v$. Each of the lubricant films was prepared on a different quartz sample. For comparison one can account for the differing resonance properties by multiplying $(\delta\Gamma/f_0)_{max}$ with the surface speed $v = \dot{u}$. Data obtained from this calculation are displayed in Figure 8.1C. For CN_x this product does not show a reasonable trend but rather remains constant. For CH_x the product with the surface speed v decreases smoothly. This would mean that the lateral forces decrease with increasing lubricant thickness. However, we believe that this is mainly due to the scaling with v because it also decreases in this set of quartzes.

8.3 Attractive Forces

8.3.1 Force Steps and Attractive Minima

In some experiments the otherwise smooth data curves display a discontinuity in all recorded signals simultaneously, that is, in the normal force, resonance frequency, and bandwidth of the quartz. Without any exceptions the normal force in this point jumps into contact. This assumption is supported by the fact that for other samples or other data cycles we observe a distinct attractive minimum in the normal force. Although the

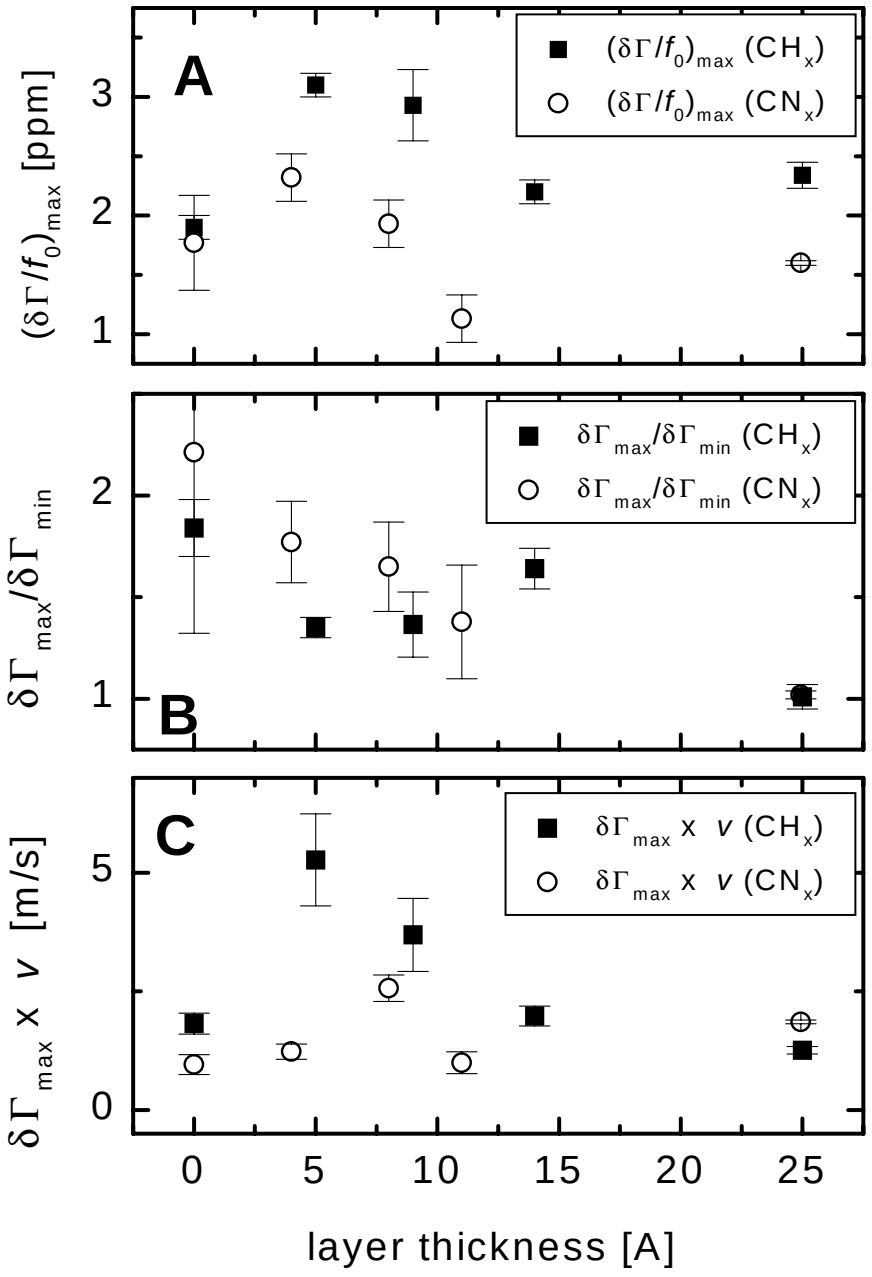

Figure 8.1: Comparison of friction force related quartz parameters for varying film thickness on CH_x and CN_x; (A): absolute maximum value of the change in bandwidth $(\delta\Gamma/f_0)_{max}$; (B): relative to the minimum value in contact $\Gamma_{rat} = \delta\Gamma_{max}/\delta\Gamma_{min}$; (C): multiplied by surface speed $\Gamma_{rat} \times v$.

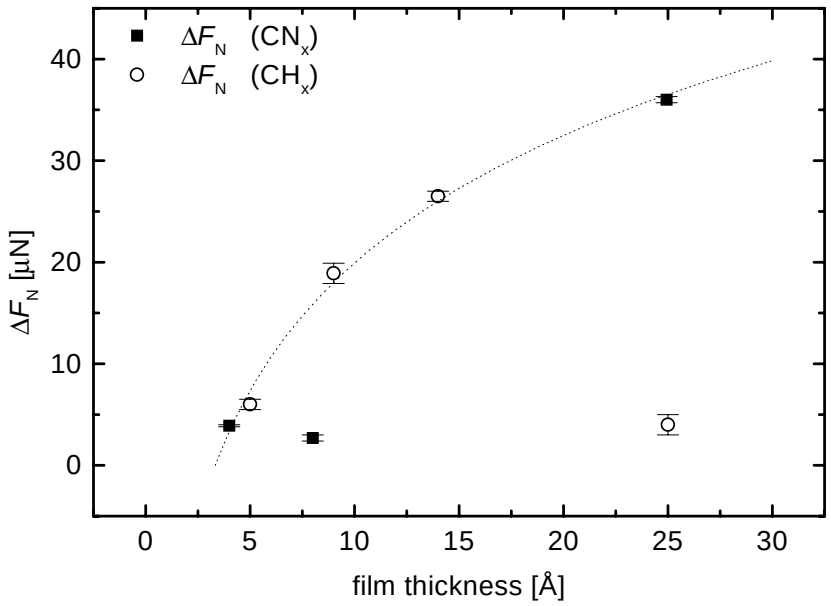

Figure 8.2: Force-steps during approach of the surfaces for CH_x and CN_x surfaces. The line is only a guide-to-the-eye. The increase of the attractive forces with layer thickness could indicate a (lubricant) meniscus formation.

---

normal force is not the focus of our measurements we summarize its behavior for different samples in order to provide an explanation.

Correction of the measured distance due to deflection of the cantilever. If we do not confine ourselves to the special case of van der Waals forces no specific force law need to be assumed. Instead we estimate the distance x of the surfaces just before a jump into contact occurs: Maximum measured force steps were in the range of $F_{\max} = 40\ \mu$N. Using the spring constant k from the previous calibration (cf. Chapter 5.4.1, p.54), we obtain: $x = F/k = 40 \cdot 10^{-6}$ N/(8620N/m) = 4.6 nm. Thus, the surfaces jump into contact over a maximum distance of 4.6 nm. Figure 8.2 shows a summary of the height of different force steps and attractive minima that occurred during approach of the surfaces depending on the lubricant layer thickness. Since the relation between jump distance and force step is linear the smallest observed jumps of $F_{\max} = 10\ \mu$N can be identified with a jump distance of 1 nm. Smaller force steps could not be observed. For smaller (attractive) normal forces the signal changes rather smoothly when approaching contact. In this case,

we have to correct all the recorded distance values by the deflection of the force transducer caused by the attractive force in this point. Figure 8.3 shows this correction for a 4 Å film and a 25 Å film on CN_x.

Estimation of Hamaker constant for short-range interaction Figure 8.2 shows a summary of the height of different force steps that occurred during approach of the surfaces in dependence on the lubricant layer thickness. In order to estimate whether the attractive forces could arise from vdW attraction we do a rough calculation of the Hamaker constant from the measured parameters: $F/R = -A_H/6D^2 \Rightarrow A_H = -6D^2F/R$, with $R = 2.3813$ mm. For the exerted force we take the depth of the potential well (-2.9 ± 0.2 μN), and for the distance of the surfaces we use 15±2 Å which is the width of the decreasing part of the potential. Inserting these values we obtain a Hamaker constant of $A_H = 1.64 \pm 0.61 \times 10^{-20}$ J. The order of magnitude coincides well with Hamaker constants reported for fluorocarbon systems which range from $2.6 - 3.0 \times 10^{-20}$ J [Dru96]. Using these literature values for calculating the distance at which the measured force should occur we obtain a value of $\approx$ 20 Å. The definition of the contact point is always somewhat arbitrary in our experiments since the surface separation cannot be determined explicitly and errors for the determination of the surface separation can easily be within 100% of the measured value. At least, with this estimation we are able to conclude that the normal forces acting between the thinly (4 Å) coated CN_x surface could have their origin in van der Waals interactions.

8.3.2 Calculated van der Waals Forces

In Table 8.3 we give several calculated Hamaker constants from literature [Ber97, TWP98] that may be important for our experiments:

The values given in Table 8.3 refer to clean surfaces. However, high-energy surfaces are covered with contaminant layers if not stored under UHV conditions. In practice, a carbon surface is not clean because its high surface energy immediately attracts contaminant layers. This is reflected in the friction coefficient that increases by a factor of almost 3 in air compared to Argon atmosphere [Bhu95]. In our experiments we did not take any

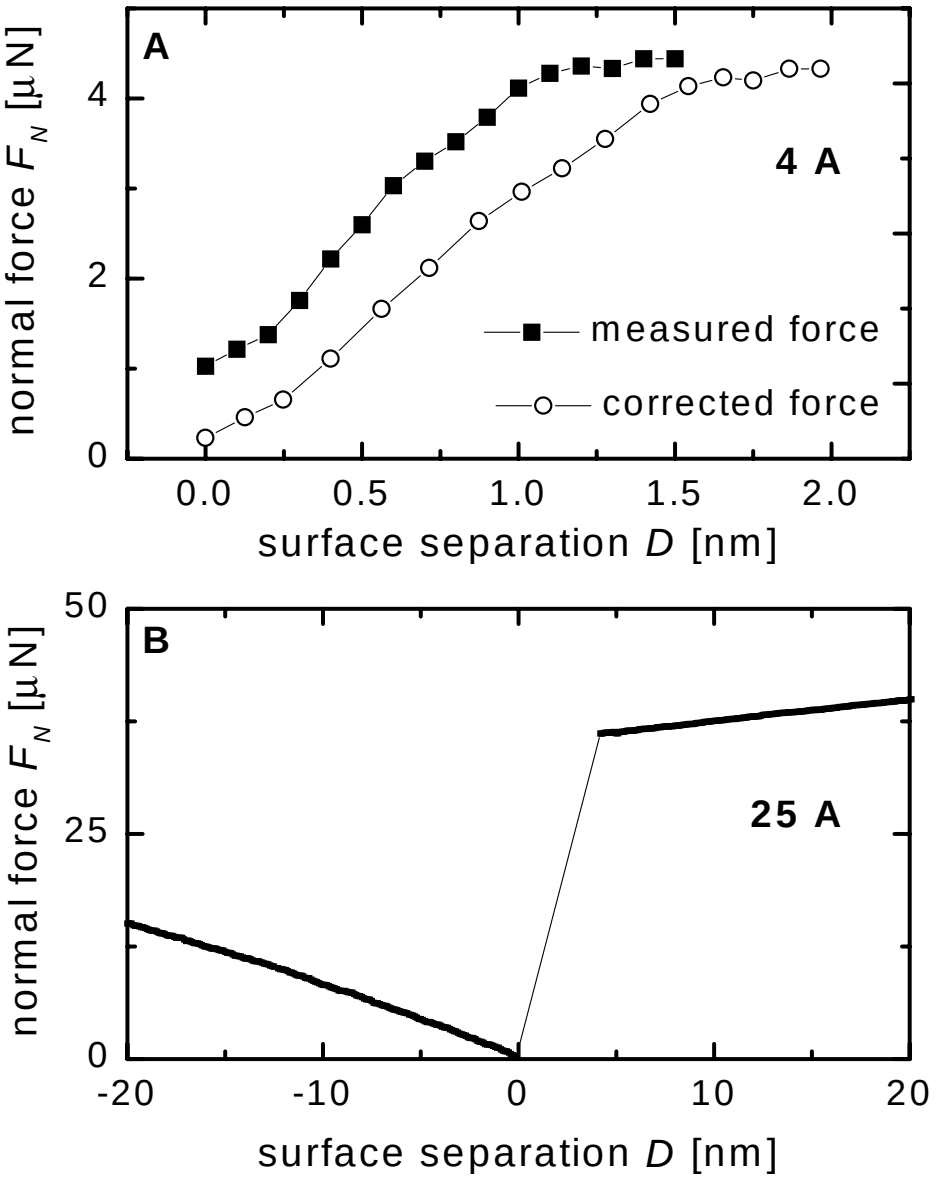

Figure 8.3: Correction of the recorded distance by the deflection of the force transducer for a (A) 4 Å and (B) a 25 Å ZDOL film on CN_x.

Table 8.3: Calculated Hamaker constants (unit: 10^{-20} J) from literature (diagonal elements,[Ber97, TWP98]). Off-diagonal elements have been calculated via combining rules [Isr92c].

Material	Si_3N_4	ZDOL	a-Carbon
Si_3N_4	16.5		
ZDOL	9.4	5.3	
a-Carbon	13.7	7.7	11.3

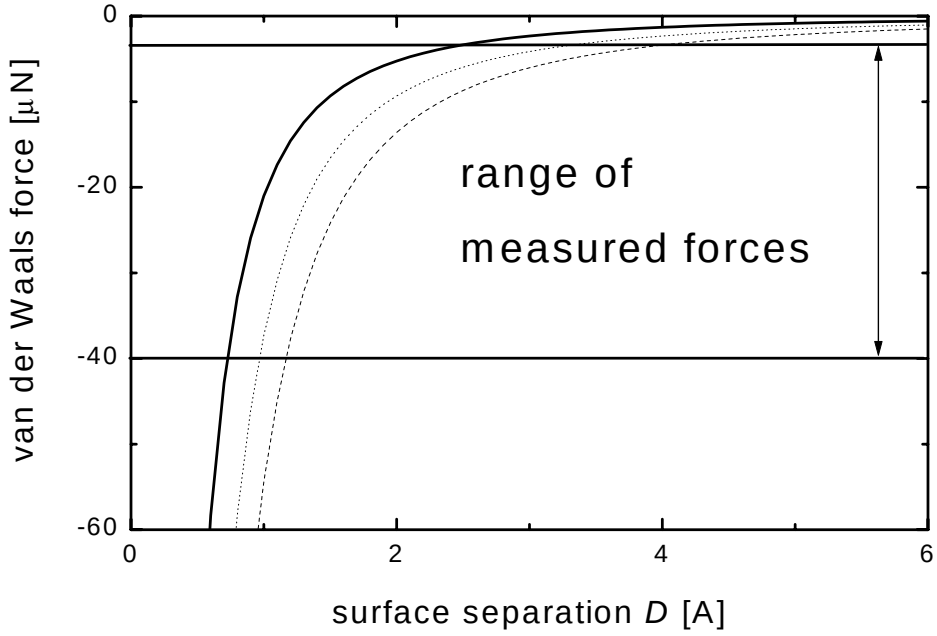

Figure 8.4: Calculated attractive van der Waals forces occurring in our system. Straight: ZDOL–ZDOL interaction (short-range). Dash: Interaction of Si_3N_4 and amorphous carbon (long-range and bare surfaces). Dot: Situation at the beginning of the experiments: ZDOL–Si_3N_4 interaction.

special precautions for clean environmental conditions.

Surface energies for lubricant-coated carbon films have been experimentally determined by Tyndall et al. [TLWC98] Figure 8.4 displays the theoretical force laws for the situations occurring in our experiments: For bare surfaces the interfacial energy between Si_3N_4 and amorphous carbon is $\gamma_{SC} = 65$ mJ/m^2, if both surfaces are completely covered with lubricant it amounts to $\gamma_{ZZ} = 14.8$ mJ/m^2. The situation at the beginning of our experiments is an intermediate one where one surface is covered with lubricant and the other one is a plasma-cleaned silicon nitride sphere ($\gamma_{ZS} = 45$ mJ/m^2). The horizontal lines mark the range of measured forces ($-4 - -40$ μN). From this we infer that the maximum range of the normal forces that were observed could only be $D_{max} = 4$ Å if their origin is a van der Waals interaction. For the starting situation the normal force range is 3 Å and 2 Å for two completely lubed surfaces, respectively. Also, we can see that forces higher than 5-10 μN are not very likely to originate from van der Waals interaction.

Thus, we conclude that the smooth transitions in the normal forces may be explained by a van der Waals attraction, but that the higher force steps must be due to some other reason. The attractive forces seem to increase with increasing layer thickness. This cannot originate from the vdW forces, neither from a water meniscus. However, Mate et al. found similar results for varying film thickness of the same lubricant system [MN91]. He points out three reasons for these forces assuming the formation of a lubricant meniscus:

1. The capillary or Laplace pressure acting over the area where the meniscus contacts the tip,
2. The force due to surface tension acting around the annulus of the meniscus, and
3. The force due to polymer bridging the gap between the two surfaces.

8.3.3 Estimation of Laplace Pressure

Capillary forces and adhesion. Adhesion is very sensitive to small amounts of water on the surfaces. The formation of a water meniscus due to capillary condensation causes additional attractive forces that can exceed the magnitude of the forces of interests. Cap-

illary condensation occurs because the vapor pressure of a liquid increases when the radius r_K of the curved liquid surface decreases. This is described by the Kelvin equation:

$$r_K = \frac{\gamma V}{RT \ln p/p_s} \tag{8.2}$$

The contribution of capillary condensation to the adhesive forces can be calculated considering the Laplace pressure P in the liquid [Ada76]:

$$P \approx \gamma_L / r \tag{8.3}$$

The Laplace pressure contribution to the adhesion force becomes:

$$F \approx 4\pi R \gamma_L \cos\theta \tag{8.4}$$

Calculation. A water layer on the PFPE-surface is not expected because it is hydrophobic. However, a meniscus could be formed by the lubricant molecules themselves. This assumption is enforced by reported bridging effects observed for similar experimental situations (PEO-PS-PEO-Triblock-Copolymer in SFA) [DT92]. Therefore, we estimate the force that would be exerted by such a Laplace pressure using equation 8.4; with $\gamma_L = 25$ mN/m (surface energy of ZDOL), $\theta = 0$ (contact angle of ZDOL on carbon surface) and $R = 2.3813$ mm (radius of the Si_3N_4 sphere) we arrive at a force of $F \approx 0.75$ mN $= 750\mu$N. Compared to the forces that have occurred in our measurements (< 50 μN) this is too high by a factor of 15.

Mate [HIGM89] also argues that — referring to SFA experiments of Homola et al. — at separations greater than 15 Å the bridging forces are negligible. Further, the contact angle between liquid and tip is small, and the force due to surface tension is much smaller than the force from capillary pressure when the capillary radius r is much smaller than the tip radius. Thus, the capillary pressure can be approximated by [MLN89]:

$$F_{\text{attr}} \approx -2\pi\gamma R[1 + \cos\theta + h/r] \tag{8.5}$$

with h the film thickness. This explains an increase of the attractive force with film thickness. However, one has also to account for the film thickness dependence of the surface energy [TWP98]:

$$\begin{aligned}\gamma &= \frac{F}{2} = \frac{(F^d + F^p)}{2} = \frac{(F^d_{\text{bulk}} + F^p + \Delta F^d(h))}{2} \\ &= 0.5 \cdot [25.7\text{mN/m} - \frac{1}{12\pi}\frac{A^*_H}{h^2}]\end{aligned} \tag{8.6}$$

with $A^*_H = -2.9 - -4.0 \times 10^{-20}$ J. This explains the asymptotic behavior of the force steps when reaching a bulk value. The capillary forces dominate the entire range of film thicknesses (eq. 8.5), therefore, the attractive force increases with film thickness. However, for thin films the thickness dependence of the surface energy (eq. 8.6) appears to influence the asymptotic behavior of the attractive forces. A more detailed calculation and discussion is not attempted because of the lack of systematic data to check this behavior.

The most probable explanation for the attractive forces is the formation of a lubricant meniscus because of bridging of the molecules. This is valid at least for the thick films. For the thinner films (< 10 Å), the order of magnitude of the forces could also suggest the presence of van der Waals forces. This would be supported by the fact that for thin films, the lubricant molecules are lying flatter on the surface in order to completely wet it. Energetically, a dangling tail that could "catch" another surface is not as favorable as for thicker films.

8.4 Miscellaneous

8.4.1 Shear Viscosity of the Lubricant Layers

If the liquid in the gap is Newtonian, that is, if its viscosity η is independent of the shear rate, the effective viscosity η_{eff} is related to the shear stress σ by:

$$\sigma = \frac{F_p}{A} = \frac{\eta_{\text{eff}}}{D} \cdot v = \eta_{\text{eff}} \cdot \dot{\gamma} \tag{8.7}$$

with D the film thickness; and $\dot{\gamma} = v/D$ the shear rate. When calculated for molecularly thin liquid layers this often results in astonishingly high values (for example 2000 Pas for a 1 nm–thick hexadecane film [YCI93b] or 10^4 Pas for perfluoropolyether films of the same thickness [RG99]).

The shear viscosity of the lubricant films can be calculated using equation 6.33 from Chapter 6.7.5:

$$\eta = 1.73 \cdot 10^{-2} \cdot D[\text{Å}] \cdot \frac{\delta\Gamma}{f_0} \text{ [ppm]} \tag{8.8}$$

The frequency-dependent viscosity $\eta(\omega)$ is closely related to the loss modulus $G''(\omega)$:

$$G''(\omega) = \omega \cdot \eta(\omega) = 6.28 \cdot 10^7 \cdot \eta(\omega) \tag{8.9}$$

Figure 8.5 shows the calculated shear viscosity for the different lubricant films. The right y-axis displays the values of the loss modulus G''. For the calculation of the viscosity we used the values of the resonance bandwidth at its maximum $(\delta\Gamma/f_0)_{\max}$ for every film. Thus, this maximum is used as a "point of reference" where maximum dissipation occurs. For liquid molecular films this dissipation is directly related to their shear properties, that is their viscosity. It can be seen that calculated values range between 0.16 and 1 Pa·s. The bulk viscosity of PFPEs of molecular weight M_w = 4000 g/mol and C1:C2-ratio p/q = 0.69 was determined to 53.4 mPas (T = 293 K) [MAP88]. The glass transition temperature of this sample was T_g = 137.1 K = –136°C. Since the C_1:C_2-ratio of our samples was p/q = 1.08 the viscosity at room temperature is expected to be slightly larger.
Moreover, the quartzes probe the viscoelastic properties at an equivalent temperature of approximately 40 K below room temperature because MHz–frequencies are used. A lower temperature also leads to an increase in viscosity. Accounting for these facts the order of magnitude of the calculated viscosity values seems to be comparable to bulk values.
In Figure 8.5 the film thickness increases from left to right, and the shear viscosity increases with increasing film thickness $\eta = 0.16 - 1$ Pas.

This can be compared with results obtained by Hahm and coworkers [HB97] on non-functionalized Fomblin-Z03 at high shear rates of up to $\dot{\gamma} = 10^7$ s^{-1}. They obtain absolute values of the viscosity measured on 50 nm-thick films (C1:C2-ratio p/q $\sim$ 2/3) of $\eta = 0.05$

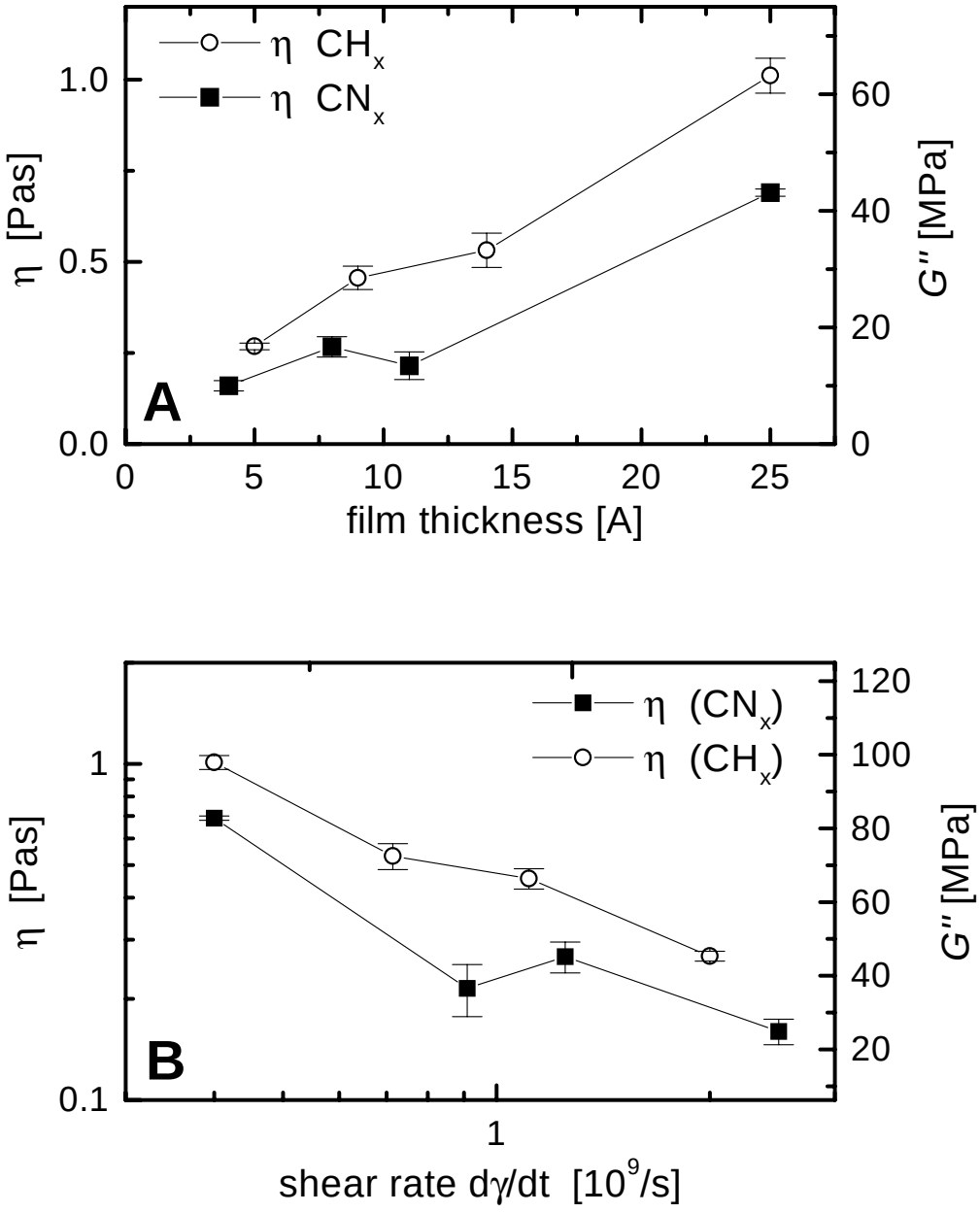

Figure 8.5: Apparent effective shear viscosity of the different lubricant layers on CN_x and CH_x surfaces.

Pas ($\hat{=}$ bulk value) that are not dependent on the shear rate between $\dot{\gamma} = 10^4 - 10^7$. The authors also report that the lubricant displayed "Newtonian behavior at all shear rates" and that "no shear thinning was observed". Moreover, they found out that the lubricant is capable of sustaining extremely high tensile stresses, on the order of 1 MPa. Shear rates in the quartz experiments are in the range of $\gamma \approx 10^9$ s^{-1}. Therefore, a slight increase in viscosity compared to Hahm's experiments could be expected. Shear measurements carried out with an SFA at lubricant film thickness comparable to ours but much lower shear rates $\dot{\gamma} < 10^2$ gave values of the shear viscosity of $\eta = 10^4$ Pas. However, these experiments also showed that η decreases considerably for higher shear rates [RG99], although it is expected that the viscosity will reach a certain plateau value.

Conclusion. For the calculation of the viscosity we implicitly assumed that the thickness of the layer between the two (hard) surfaces did not change upon approach of the surfaces, hence, that the lubricant was *not* squeezed out. Most probably, this does not describe the real situation because the lubricants' steady-state behavior is liquid–like. In particular, for thicker films a "squeezing–out" would be expected. We conclude that the order of magnitude of the calculated shear viscosity is reasonable, but that the effect of film thickness on viscosity is not.

8.4.2 Dissipated Power

The dissipated power can be calculated via (eq. 6.25, p. 103):

$$P = \frac{1}{T}\int_0^T F_{\mathrm{p,d}}\dot{u}_0 \cos^2 \omega t dt = \frac{1}{2}F_{\mathrm{p,d}}\dot{u}_0 = \frac{1}{2}Z_q\pi^2 r_e^2 u_0^2 Q^2 \frac{\delta\Gamma}{f_0} \tag{8.10}$$

for an amplitude of $u_0 = 10$ nm, we obtain

$$P = \frac{1}{2}Z_q\pi^2 r_e^2 u_0^2 Q^2 \frac{\delta\Gamma}{f_0} \approx 8.6 \cdot 10^{-15} \cdot \frac{\delta\Gamma}{f_0}\ \mathrm{W} \tag{8.11}$$

Thus, in our measurements the dissipated power is on the order of $10^{-20} - 10^{-19}$ W. The energy dissipation per cycle (10^{-7} s) is around 10^{-27} J.

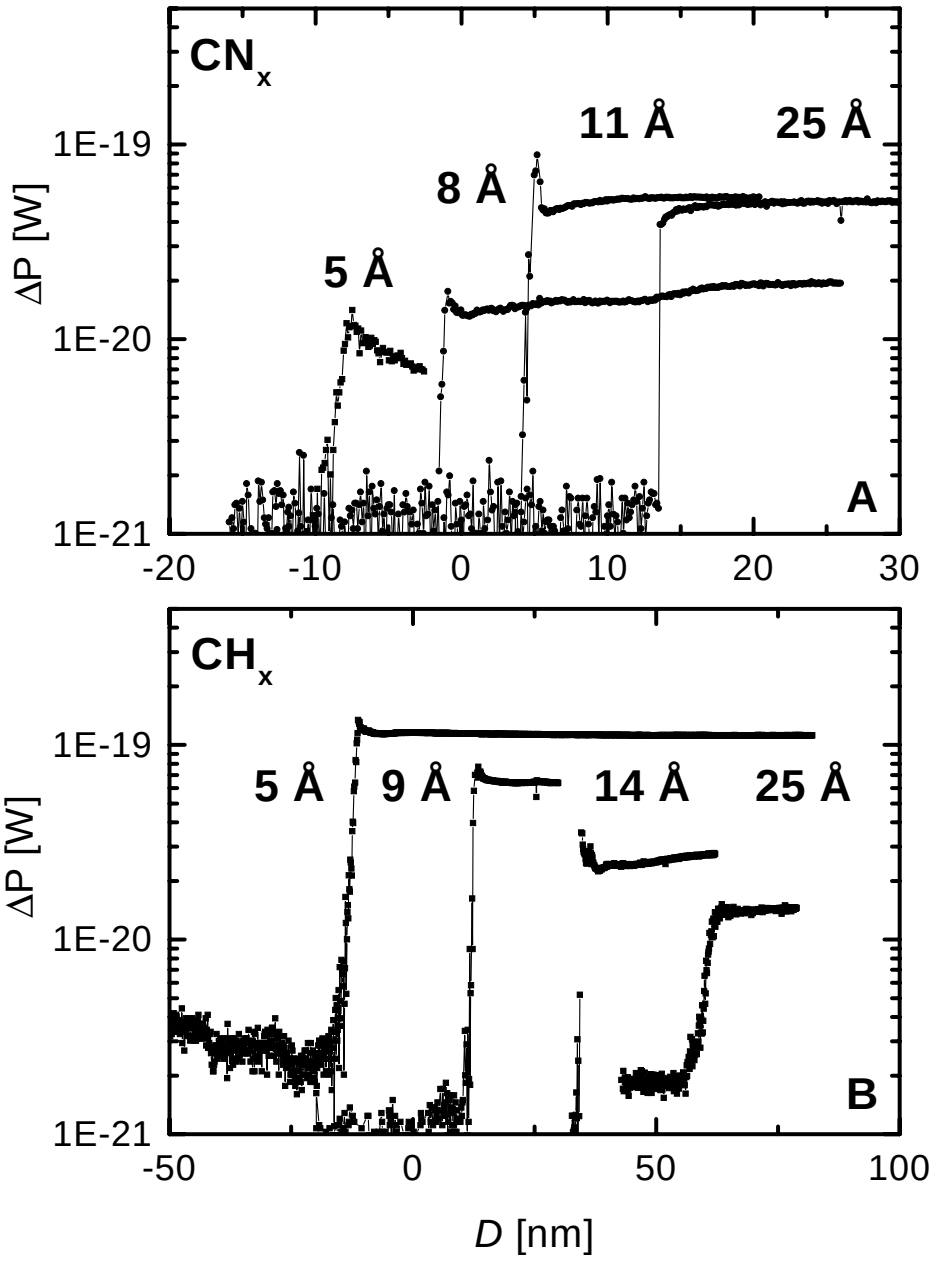

Figure 8.6: Dissipated power for the different films on CN_x and CH_x.

Figure 8.6 shows the dissipated power for all measurements on CN_x and CH_x substrates. For increasing film thickness on CH_x (Fig. 8.6B) the energy loss is diminished: the lubricant becomes more effective when reaching the bulk limit. On the other hand, results for the CN_x surfaces (Fig. 8.6A), seem to show a trend towards higher power dissipation for thicker films.

We suspect the behavior to be strongly dependent on the (implicit) scaling with the quality factor Q of each quartz resonator.

8.4.3 Stability of the Lubricant Layers

The conditions in the quartz experiment are characterized by high frequencies, speeds, shear rates and strains. This leads to high exerted shear stresses in the contact zone. Thus, it could readily be expected that within the course of the experiment the lubricant layer will be squeezed out of the surface gap or that the lubricant molecules are just ruptured. This would result in an increased friction with increasing number of experiments in the gap.

However, there seems to be reproducibility of the results that have been measured at the same spot of the surface, i.e., the magnitude of lateral forces does not change. This is valid for the bulk case ($h > h_{\mathrm{monolayer}} = 25$ Å): A surface that is completely covered by a lubricant film remains lubricated although subjected to extreme experimental conditions. If a chain transfer from the quartz to the sphere is assumed this process would leave holes in the lubricant film. Thus, friction would increase with increasing number of contacts. We do not observe this.

There could be two explanation for this apparent stability:

- The molecules are *not* torn away from the surface, i.e., although occurring stresses are very high, the combination of surface attachment and ability to absorb and transform friction energy to molecular motion inhibits the rupture of the surface bonds.

- The molecules are (i) squeezed out and (ii) transferred to the non-coated sphere but the combination of lateral mobility (diffusion constant $D \approx 5{\cdot}10^{11}\mathrm{m}^2/\mathrm{s}$, [WWM+96])

and tendency to equilibrate the surface energy leads to a re-wetting by wandering of molecules from the surrounding layer into the uncovered surface spot.

Regarding the results the second explanation is more probable.

8.4.4 Differing Data Quality between CH_x and CN_x

The amount of data collected for the CN_x surfaces was approximately a factor of four higher than that for the CH_x surfaces. However, data quality was much higher for the CH_x surfaces. On CN_x the data was generally a lot noisier when coming close to contact. From the different thickness at which the films reach bulk properties on the various underlayers we can already derive that the interaction varies: Generally speaking, the interaction between ZDOL backbones and CN_x is more repulsive than with CH_x. Therefore, the chains do not lie as "flat" on the CN_x surface as they do on the CH_x surface. A bridging of the molecules from the sample surface to the sphere is highly likely to happen, in particular, for the CN_x surfaces.

8.4.5 Friction Surface Profiles

In order to obtain an objective measure for the height of the friction maximum before surface contact the functional form of these profiles has to be analyzed. In Chapter 6.3 it was already mentioned that the width of these profiles appears to be closely related to the surface roughness of the samples, i.e. the height distribution of the overlapping asperities. For most engineering surfaces one can assume a Gaussian distribution of the asperity heights [Per98, Bhu95]:

$$\Phi(x) = \Phi_0 + (\frac{2}{\pi w^2})^{1/2} e^{-\frac{2(x-x_c)}{w^2}} \tag{8.12}$$

$\Phi(x)$ the asperity height distribution, x_c and Φ_0 the x- and Φ-offsets, and w the full-width at half-maximum (FWHM). It is common to fit histograms from FFM and AFM images with Gauss functions and this can be justified by AFM measurements [HGH99, HGW+95]. Haugstad et al. analyze their FFM images with histograms of the friction force: The

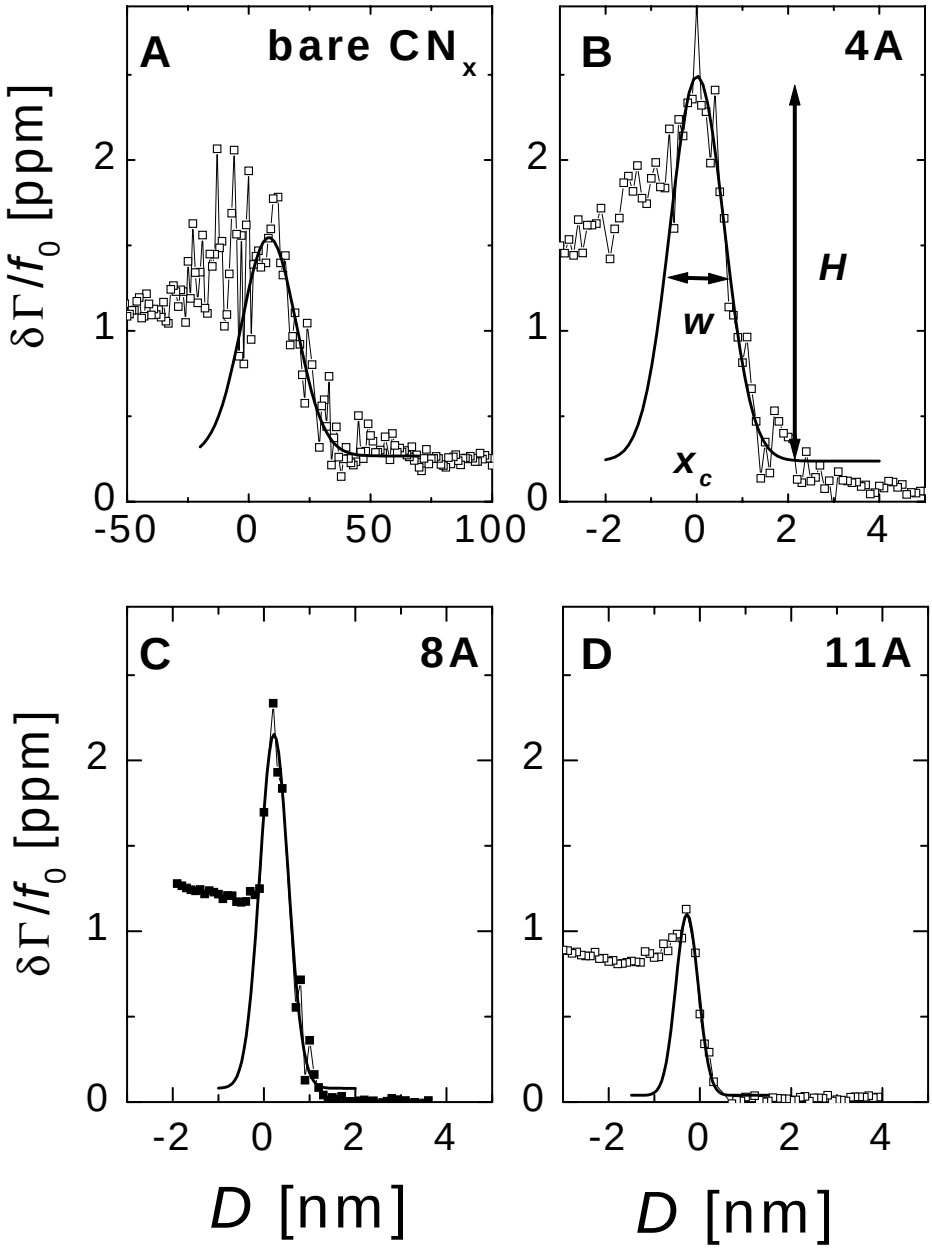

Figure 8.7: Gaussian fits of the friction profiles of CN_x surfaces with varying lubricant thickness. Fit parameters are the y-offset y_0 , the x-center position x_c, the width w, and the area A or the height H. A comparison of the parameters is given in Table 8.4.

Table 8.4: Parameters from Gauss fits of the "friction" surface profiles of ZDOL 4000 on CN_x. h: film thickness, y_0: offset, x_c: center position, w: full-width at half maximum (FWHM), A: area, H: height.

h [Å]	$y_0 \times 10^{-6}$	x_c [Å]	w [Å]	A [Å]	$H \times 10^6$
0	(-1.43± 8.08)	(3.0±2.2)	740±1180	(2740±11800)	2.954
4	(0.238±0.049)	-9×10^{-2}	11.9±0.8	(33.7±2.2)	2.25
8	(8.07±6.83)10^{-2}	(-2.2 ± 0.2)	6.2±0.5	16.2±1.5	2.07
11	(3.96±6.07)10^{-2}	2.8±0.3	4.9±0.7	6.56±1.03	1.06

number of points with the same lateral force level are counted and plotted against the force level. The same analysis can be carried out for topographic AFM-images. Figure 8.8 shows the histograms of the AFM-images shown in Figure 7.2 (p. 126) acquired on differently coated CN_x–surfaces (bare, 6 Å, 30 Å PFPE). The width of the distribution of the asperity heights decreases significantly with increasing lubricant layer thickness. This confirms our findings: Figure 8.7 shows the fitted friction profiles from our quartz measurements for different lubricant thickness on CN_x. The Gauss distribution fits the friction profile well.

Discussion. For the lubricant-covered surfaces there is a clear trend towards a *decrease* in the width of the friction interaction profiles with *increasing* lubricant layer thickness. This could be intuitively explained with the fact that the lubricant "fills the surface holes" in order to form a "flat" cushion between the sliding surfaces. At thicknesses above 25 Å the film forms a soft, homogeneous surface. This would explain why the AFM image of a thick lubricant layer is more "fuzzy" than that of a thin layer. Figure 8.8 shows the histograms of the AFM-images taken on CN_x–surfaces with varying lubricant thickness (cf. Figure 7.2, p. 126). The profile form can be fitted with a Gauss function. The FWHM from these fits is compared to the rms-roughness values (σ_{rms}) obtained from the common AFM-imaging procedure. Theoretically, they are related via $w = 2 \cdot \sigma_{\mathrm{rms}}$. This is roughly fulfilled. Both values decrease with increasing lubricant film thickness. Thus, the *apparent* roughness is decreased by a liquid lubricant film. (Since the images were taken in tapping mode one cannot be sure that the tip did not penetrate the lubricant film. If this was the case the conclusion would be that a lubricant layer partly inhibits

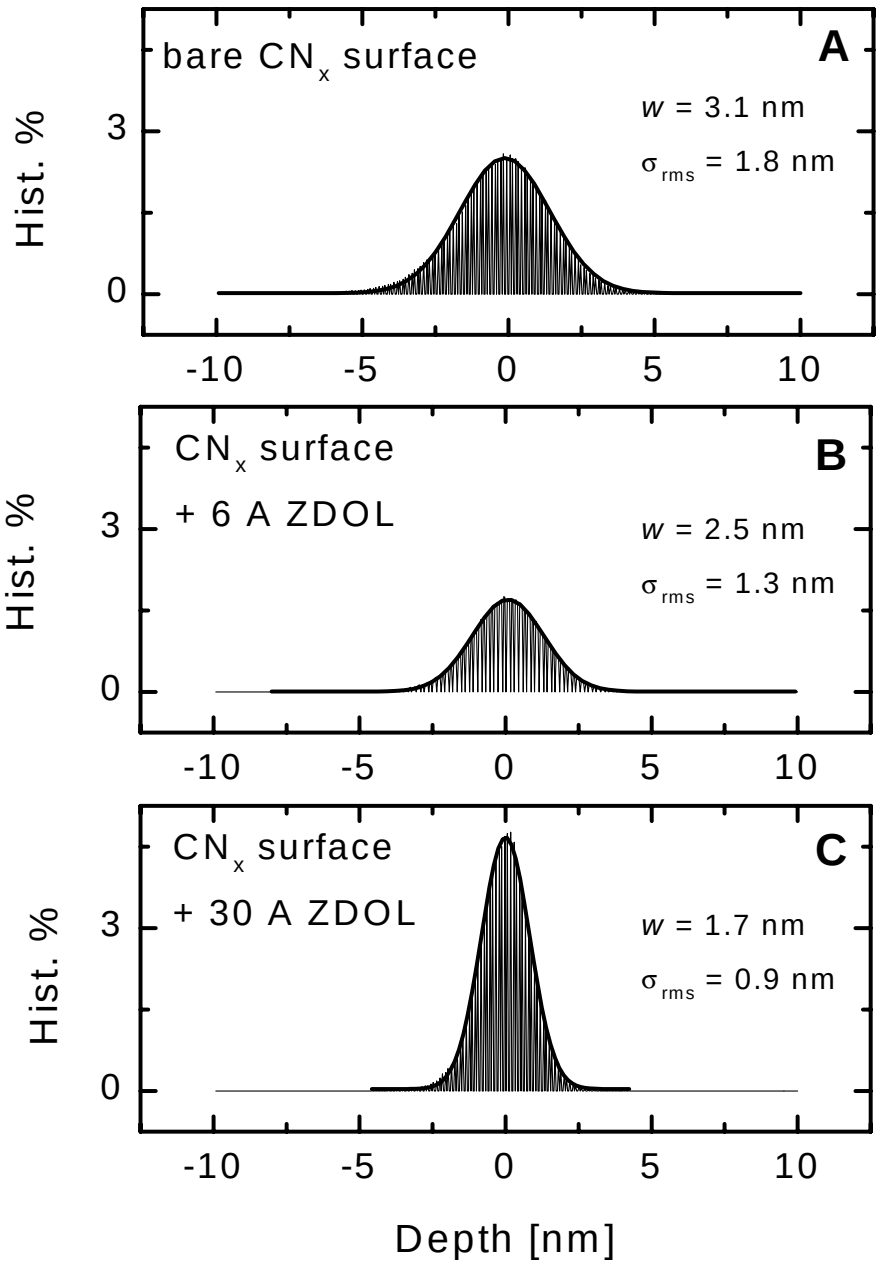

Figure 8.8: Histogram of the AFM images shown in Figure 7.2. Plotted are the counts obtained per surface height level (depth = x-axis). (A): bare CN_x–surface, (B): CN_x–surface coated with a 6 Å ZDOL4000 layer, (C): CN_x–surface coated with a 30 Å ZDOL4000 layer. w is the full width of the Gauss curve and decreases for increasing lubricant film thickness. The rms surface roughness (σ_{rms}) obtained from AFM measurements is given, as well.

the movement of the cantilever-tip.)

With regard to the form of the friction profile two distinct classes of behavior are found. For lubricant covered surfaces the width of the friction profile correlates with the width of the asperity height distribution. In particular, both quantities decrease with increasing thickness of the lubricant layer. The friction profile found for the bare CN_x surface, on the other hand, does not fit into this picture. This applies only to the bare CN_x surface, not to the bare CH_x surface (cf. Figure 7.3). At this point we can only speculate about the potential reasons for this astonishing behavior. The CN_x also differs from the other data traces in the fact that the onset of the repulsive normal force and the maximum of friction do not coincide. Possibly, intermittent contact has differing consequences for bare CN_x surfaces than for other surfaces. The CH_x is less polar than the CN_x surface and interactions with another surface could be influenced by surface (patch) charges [BCP92]. Also, because of their polarity it is more likely that contamination with charged or polar molecules occurs.

Chapter 9

Solvent–Induced Glass Transition in Thin Polymer Brushes

9.1 Introduction

Polymers confined to thin films frequently have a structure and dynamics different from the bulk [San92, Bin94]. There are a number of different sources for these anomalies such as geometrical constraints, enthalpic interaction with the substrate, and enrichment of chain ends or impurities at the interface. A shift of the glass temperature T_g in thin films has been reported by a number of researchers. Early indications of a decrease of T_g in thin films were reported by Reiter, who found that polystyrene films dewet silicon wafers at temperatures, where one would expect them to be immobile [Rei93]. Keddie and Jones have ellipsometrically investigated the thermal expansion of spincast polystyrene (PS) films on silicon wafers as a function of temperature [KJC94]. They find a glass step which they use to derive the glass transition temperature T_g. A decrease of T_g of up to 25 °C is observed for thin films. Wallace et al., on the other hand, find an increase of T_g for the same system using X-ray reflectometry [WvZW95]. Apparently, the precise conditions at the substrate surface have a large influence and have to be characterized with care. DeMaggio et al. have used positronium lifetime spectroscopy to probe the internal free volume in thin polystyrene films on silicon wafers [DFG97]. They also find a decrease of T_g. Additionally, the authors report on a decreased thermal expansivity above T_g for

the same samples. Monte Carlo simulations on polymers close to a free surface [MT91] and a solid wall [BB95] show that the dynamics is faster than in the bulk at the free interface, whereas it is slowed down close to the substrate. For a polymer melt confined between two solid walls, a strongly anisotropic mobility was found [BB96]. Adopting the view that the glass transition is correlated to the free volume inside the film, one would conclude that the chains in films with decreased T_g are arranged such that they fill space less well than they do in the bulk. The free volume inside a polymer sample is affected not only by temperature, but also by the addition of low molecular weight additives [Fer80]. The effect of plasticizers on the polymer dynamics is fairly well described by a decrease of the glass temperature T_g. This implies that at a constant temperature, the glass transition can also be driven by solvent. By gradually adding plasticizers to a polymeric material, its internal free volume is increased until at a certain solvent volume fraction ϕ_g the glass temperature T_g is lowered to room temperature and the material becomes soft. Conversely, if solvent is withdrawn from a polymer solution, the polymer will rigidify at about the same solvent content ϕ_g. The solvent chemical potential corresponding to ϕ_g we call μ_g, and the corresponding solvent activity a_g, where activity and chemical potential are related by $\mu = k_B T ln(a)$. We use the activity rather than the chemical potential to display the data, because the activity $a = p/p_{sat}$ (p the vapor pressure and p_{sat} the saturation vapor pressure) is closer to intuition and to the experimental procedure. There is an analogy between the temperature-driven glass transition and the solvent-driven glass transition. In the same way as entropy is frozen in when a polymer melt is cooled to below T_g, the solvent is trapped in the polymer matrix when it is dried to below a_g. Below the glass transition, the rigidity of the matrix opposes its collapse. Free sites remain inside the polymer, which attract solvent molecules and therefore induce an excess solvent content. Provided that drying is performed slow enough, this excess solvent uptake is not a kinetic phenomenon caused by slow solvent transport, but an intrinsic property of the glassy polymer. The sorption curve $\phi_S(a)$ of polymeric glass formers displays a characteristic kink at the glass transition activity a_g [LS93, Ber80, VV91]. In order to emphasize the analogy with differential scanning calorimetry (DSC), we differentiate the sorption curve with respect to solvent activity a. We call the derivative $c_\pi = d\phi_S/da$ "osmotic capacity". It is the analogue of the heat capacity in DSC. In particular, it displays the glass step. Micro-weighing a polymeric film in solvent vapor therefore is a way to probe the film's

glass transition. We report on the solvent-induced glass transition of polystyrene brushes. The term brush in this context is used for a dense layer of linear polymer chains which have been covalently bound to the substrate at one end [HTL92, SC96, GM94]. The reason for employing brushes rather than spin-cast films is simply that brushes cannot dewet the substrates, whereas spin-cast films frequently do. The brushes were grown on the surfaces of quartz resonators by the "grafting from" technique [PR98b, PR98a]. The resonators are operated as quartz crystal microbalances [Sau57, Sau59]. They are mounted inside a vacuum chamber. When toluene vapor is admitted to the chamber the brushes swell. The mass of the brush/solvent system is monitored during slow drying ramps. The (de-)sorption curves display a characteristic kink, which is analyzed as a function of drying speed, history, substrate properties, and - most importantly - brush thickness.

9.2 Theoretical Background

For polymer melts above the glass transition sorption is usually described by the Flory-Huggins law [Flo53]:

$$\mu_{int}^{FH} = k_B T \left[\ln(1 - \phi_P) + \phi_P + \chi \phi_P^2 \right] \tag{9.1}$$

where ϕ_P is the polymer volume fraction and χ is the polymer-solvent interaction parameter. In diffusion equilibrium the solvent chemical potential in the film is equal to the chemical potential in the vapor phase given by

$$\mu_{ext} = k_B T \ln(a) = k_B T \ln p/p_{sat} \tag{9.2}$$

with a the activity, p the solvent vapor pressure, and p_{sat} the saturation vapor pressure. The Flory-Huggins law predicts a smooth dependence of solvent content on vapor pressure with a positive curvature everywhere. Close to a solvent volume fraction $\phi_S = 0$ the solvent content depends almost linearly on vapor pressure. This regime is sometimes called Henry sorption. A slight caveat to be mentioned is the fact that the χ parameter often depends on concentration in this regime [BI89, NHUF84].

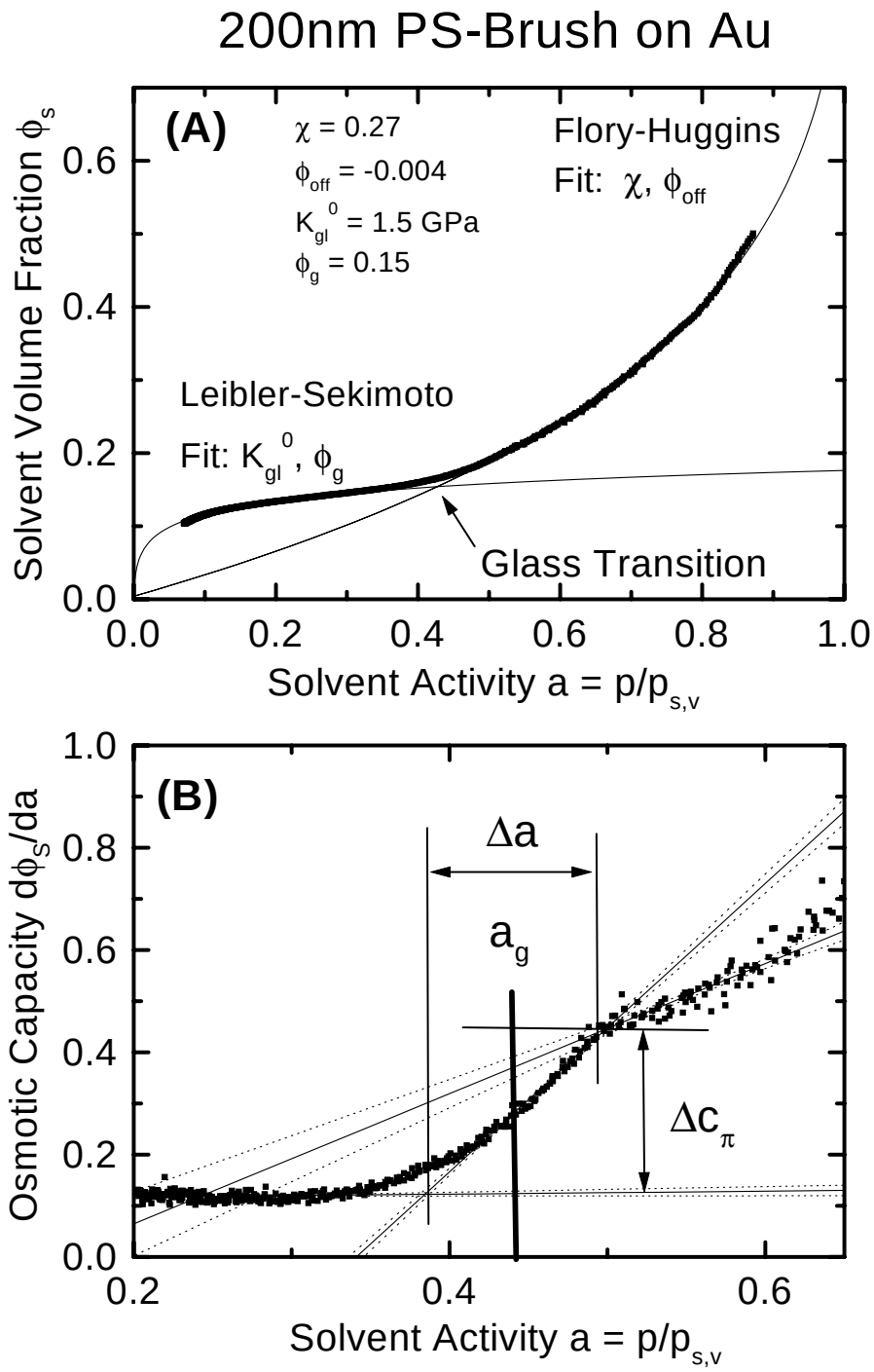

Figure 9.1: (A): Typical sorption curve. The lines are fits to equations 9.1 in the highly-swollen regime and 9.3 in the glass regime. Fit parameters are given in the figure. (B): Osmotic capacity which is the first derivative of the sorption curve from (A). The straight lines indicate the idealized glass transition.

Below the glass transition one finds an excess solvent uptake and a negative curvature of the sorption curve (Figure 9.1). It is sometimes explained as "Langmuir hole filling" or "dual mode sorption" [Ber80]. According to this view, the glassy polymer matrix does not collapse in the same way as a polymer melt. Some free sites remain which are populated by solvent molecules following Langmuir statistics. The dual mode picture suggests that the sorption has two separate components in parallel which are the one obeying the Flory-Huggins law and a second one obeying the Langmuir isotherm. The sorption/desorption curve has a kink at the point where the solvent induced plastification is just sufficient to lower T_g to ambient temperature.

Leibler and Sekimoto have put forward an alternative explanation to the excess solvent uptake which relies on internal stress rather than voids [LS93]. They assume that the polymer-solvent system is incompressible and all loss of solvent is followed by matrix contraction. Below the glass transition, matrix contraction is opposed by its stiffness which is parametrized by an elastic modulus $K_{gl}(\phi_S)$. The resulting internal stress enters the free energy as an elastic contribution. Assuming that $K_{gl}(\phi_S)$ is zero above the glass transition and a constant K_{gl}^0 below the glass transition, Leibler and Sekimoto find

$$\begin{aligned} \mu_{int}(\phi_P, T) &= \mu_{int}^{FH}(\phi_P, T) + \mu_{int}^{LS}(\phi_P, T) \\ &= k_B T \left[\ln(1-\phi_P) + \phi_P + \chi\phi_P^2\right] - \nu_1 K_{gl}^0 \ln\left(\frac{\phi_P}{\phi_{P,g}(T)}\right) \end{aligned} \qquad (9.3)$$

where ν_1 is the solvent molecular volume and $\phi_{P,g}$ is the polymer volume fraction at the glass transition. Since the matrix collapse is achieved by local rearrangements of chains, the numerical value of K_{gl}^0 should be of the same order of magnitude as the macroscopic shear modulus, which is indeed the case. Equation 9.3 reproduces the excess solvent uptake close to the glass transition quite well. It is a convenient function for fitting. However, the interpretation is somewhat unclear. Presumably, both internal stress and voids contribute to the excess solvent uptake. It is not certain that the fit parameter K_{gl}^0 can be straightforwardly interpreted as a local elastic modulus.

In view of the conceptual difficulties connected to a thermodynamically rigorous explanation, we seek a description which avoids specific assumptions about the origin of the excess sorption as much as possible. We do not want to make a statement with regard to the microscopic origin of the excess solvent content, but rather use the excess solvent

to probe the glass transition as a function of external parameters like film thickness and drying speed. We take the view that the solvent chemical potential μ can be regarded as an intrinsic variable of state, which drives the glass transition in essentially the same way as temperature. On microscopic grounds, this point of view certainly is a simplification. Rössler et al. have probed the dynamics of the PS/toluene system with NMR [RSS85]. Taking the dephasing time T_2 as a criterion for the glass transition, they can identify two separate glass transitions for the PS/toluene system, which they attribute to the two components. Apparently, the components retain some of their dynamical identity even in the mixture. We believe that the glass transition observed in the sorption curve should be ascribed to the polystyrene component.

A conceptual difference between the solvent-driven and the temperature-driven glass transition is the possibility of annealing the sample in vacuum at high temperatures. In this way, virtually all solvent is removed. There is no way of withdrawing all entropy from a sample in the temperature-driven glass transition, which would be the equivalent process to "annealing". Interestingly, high temperature annealing of the brushes has a very profound effect on their sorption behavior (see Chapter 9.5).

Treating the solvent chemical potential μ as an intrinsic variable of state, the solvent-induced glass transition is of pseudo-second order in the Ehrenfest sense. The second derivative of the grand canonical potential Ξ with respect to solvent chemical potential has a step at the glass transition. For the grand canonic potential Ξ we write

$$\Xi = \Xi_0 + \mu N_S \tag{9.4}$$

where Ξ_0 contains all contributions independent of solvent content, and N_s is the number of solvent molecules inside the film. The number of solvent molecules N_s is related to the solvent volume fraction ϕ_S by

$$\phi_S = \frac{N_S V_S}{N_S V_S + N_P V_P} \tag{9.5}$$

where V_S and V_P are the molar volumes of solvent and polymer, and N_P is the number of polymer segments. We have assumed that the volume of mixing is zero. With equations 9.3–9.5 the derivative $d\phi_S/da$ becomes

$$c_\pi = \frac{d\phi_S}{da} = \frac{d\phi_S}{dN_S}\frac{dN_S}{d\mu}\frac{d\mu}{da} = \left(\frac{d\phi_S}{dN_S}\frac{d\mu}{da}\right)\frac{d^2\Xi}{d\mu^2} \tag{9.6}$$

We call the derivative $d\phi_S/da$ "osmotic capacity" c_π. Some authors use the osmotic modulus $K_\pi = \phi_S dp/d\phi_S$ for a thermodynamic description rather than $d\phi_S/da$. We prefer to use the capacity in order to emphasize the analogy to the differential scanning calorimetry. Apart from the prefactor in brackets, the osmotic capacity is the second derivative of the grand canonical potential with respect to solvent chemical potential. It corresponds to the heat capacity which is a second derivative of the free energy with respect to temperature. Because the prefactor is a smooth function of the activity a, the step in the second derivative $d^2\Xi/d\mu^2$ translates into a similar step in the osmotic capacity c_π. From the step in the osmotic capacity the glass transition activity a_g can be derived in the same way as T_g is determined from the specific heat in calorimetry.

9.3 Materials

The synthesis of the polymer brush followed the "grafting from" approach, which is detail described in references [PR98a] and [PR98b]. The first step is the formation of a self-assembled monolayer of an initiator for free radical polymerization at the substrate surface. As substrates we mainly used bare gold. In order to investigate the influence of the substrate, we also performed experiments on SiO_x layers evaporated onto the gold electrode. The SiO_x surface is rougher than the gold surface and is known to have a porous structure. Also, SiO_x has an oxidic surface, which may affect the physical contacts between polymer chains and the substrate. Generally speaking, the results obtained on gold and SiO_x surfaces are similar. However, the data quality and reproducibility was better on gold substrates. We assume that the reason for this could be the somewhat fragile structure of the SiO_x layer. Thermally evaporated SiO_x layers contain voids which may condense with time. Within the accuracy of our data, we see no differences between the different substrates. The linker chemistry is based on thiols for the gold surface and on monochlorosilyl moieties for the SiO_x surface. The initiators are derivatives of AIBN. After preparation of the self-assembled monolayer of initiator the polymerization is started in a solution of styrene monomer in toluene. The brush thickness is adjusted by the polymerization time and the monomer concentration. After polymerization, the samples are rinsed with solvent and undergo Soxhlet extraction with toluene for 15 hours to remove

physisorbed polymer. The molecular weight of a given sample is a priori unknown. A lower limit on the molecular weight can be derived from reference experiments where the grafted material was cleaved off the surface after brush formation and investigated with size exclusion chromatography. From these investigations we conclude that the molecular weight is above $M_w \sim 100$ kg/mol with a polydispersity in the range of $M_w/M_n \sim 1.5$. Polymer brushes are quite peculiar systems, whose behavior differs in several different ways from bulk polymers [HTL92, SC96, GM94]. However, these anomalies are of minor interest in this context. Most of the anomalous behavior is observed when the brushes are swollen in solvent or bulk polymer. Most importantly, chain stretching is observed in this case, which profoundly affects the physical properties of the substrate–brush–bulk system. Here, we work with collapsed brushes. Chain stretching in the collapsed state is only present for the thick samples ($d \sim 200$ nm). Also, the physical properties underlying the glass transition are believed to occur on a local scale as evidenced by the fact that T_g is largely independent of molecular weight. Prucker et al. have carried out a systematic comparison of spin-cast films and brushes with respect to their thermal glass transitions and did not find a significant difference [PCB+98]. We therefore believe that the terminal attachment has a minor influence on the glass transition. The prime advantage of covalent attachment is the fact that it prevents dewetting. Dewetting proved to be a serious problem for sorption experiments on spin–cast films. The thickness of the brushes was independently measured at different spots with ellipsometry [AB87]. There was a slight lateral variation of thickness over the quartz plate of up to 15 % of the average thickness. This is the horizontal error bar in Figure 9.7.

9.4 Experimental and Data Analysis

Details of the experimental setup have been described previously [BGA+98]. All samples were annealed in a vacuum oven at 110 °C for 12 hours prior to experiment. The AT-cut quartz blanks were mounted with alligator clamps. The temperature was kept constant at T = 25.8 ± 0.3 °C during the whole experiment.

The resonator frequency was determined by impedance analysis [DJ96]. We determined the resonance frequency by fitting a Lorentzian to the spectrum of the real conductance

(cf. Chapter 5.6.2, p.65). The bandwidth of the resonance is also automatically obtained. In some investigations we used a reference quartz in parallel to monitor pressure– or temperature–induced frequency drifts. Temperature–frequency coupling was completely negligible. We did observe a slight dependence of frequency on hydrostatic pressure as reported in the literature (cf. Chapter 6.6.6, p.89, [HGJP88]). The magnitude of the effect never exceeded 1% of the film mass and has been neglected. There were no significant differences between the values of the solvent content as determined from the different harmonics. We mostly used the 4^{th} harmonic at 28 MHz.

For soft layers, one can in principle deduce viscoelastic information on the layers from the bandwidth and a comparison of the frequency shift on the different harmonics [DJ96, WSJ97]. We indeed observe a substantial increase in bandwidth $\delta\Gamma$ (cf. Figure 9.3) for highly swollen films. This softening is caused by the glass transition. However, this is the MHz glass transition which occurs at a much higher solvent concentration than the DC glass transition. Alig and coworkers have obtained similar information with a technique based on ultrasonic reflectometry [ALST97]. The solvent-driven glass transition shifts with the frequency of the experiment in the same way as the temperature-driven transition. Therefore we do not discuss the bandwidth in the following and confine ourselves to the shifts in frequency, i.e. the film mass. The kink in the film mass is connected to the low frequency glass transition. (cf. Figures 9.2 and 9.3).

For highly swollen films, softening introduces an elastic correction to the apparent mass as determined by application of the Sauerbrey equation. There is a scheme to measure this effect and correct for it relying on the comparison of the frequency shifts on different overtones [DJ96]. We only found small elastic effects for very highly swollen brushes and neglect them in the following.

Another potential source of artifacts are stresses due to a lateral expansion of the polymer film. Elastic energy stored in the quartz may shift its resonance frequency due to small non–linearities. Heusler et al. have measured the frequency shift induced by a difference in hydrostatic pressure between the two sides [HGJP88]. They find a parabolic dependence with a shift $\delta f \sim$ 100 Hz for a pressure difference of about 10 kbar. An order of magnitude estimation using the yield stress of polystyrene and the equations of elastic beams shows

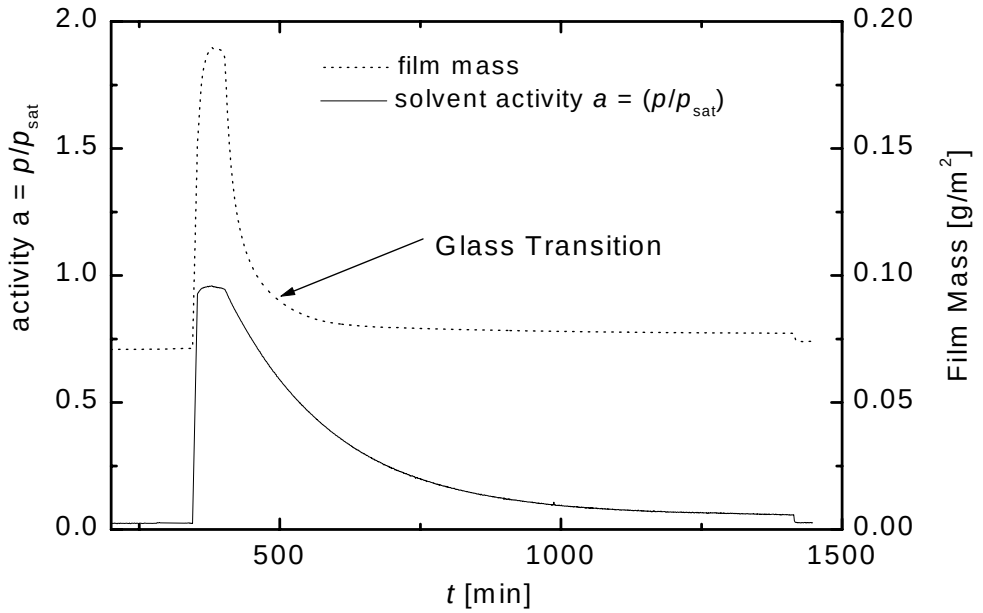

Figure 9.2: Typical raw data recorded on a 35 nm PS-brush. The straight curve shows a decreasing pressure ramp (activity = normalized pressure). The dotted line displays the response of the film mass to the vapor pressure. The glass transition is at the point where the curve has a kink because of the changing sorption behavior.

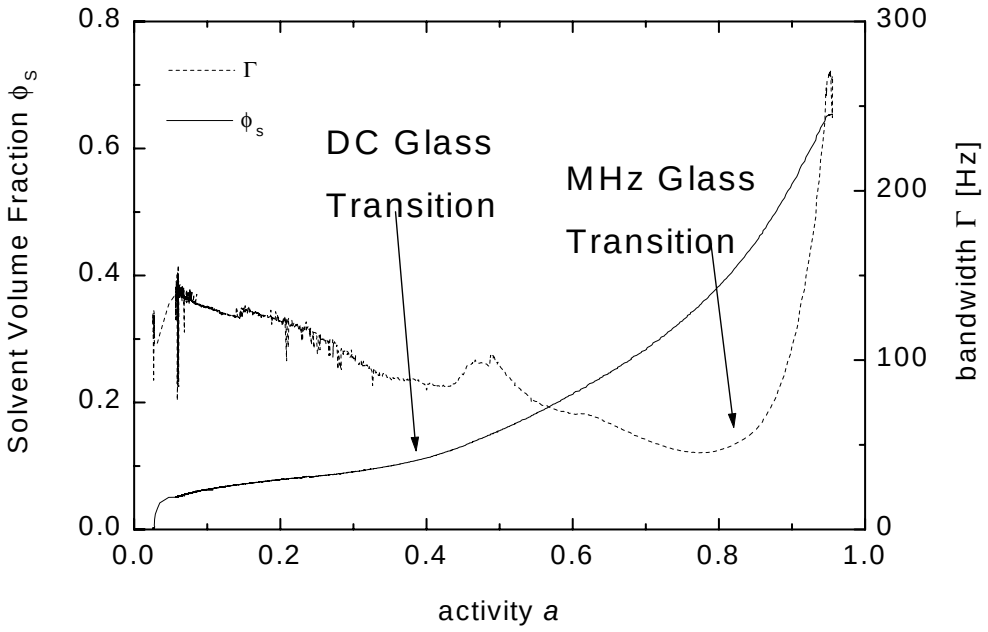

Figure 9.3: Low and high frequency glass transition for a 35 nm PS-brush. The straight curve is obtained from combining the curves from Figure 9.2 by eliminating the time dependence. The high frequency glass transition occurs at high vapor pressures compared to the DC glass transition. This is expected because of the temperature–frequency superposition principle.

that this effect is negligible here. After mounting the samples, the chamber was first evacuated to about 10^{-2} Torr. Subsequently, vapor was admitted. The pressure was adjusted to about 26 Torr, which corresponds to an activity of about 0.85. The saturation vapor pressure of toluene at 26 °C is 31 Torr [Lid95]. We used MKS Baratron Type 128 pressure sensors which work on a capacative principle and therefore are suitable for many kinds of gases. The estimated error of the activity is about 0.01. After a steady-state of film mass had been reached, the solvent vapor was withdrawn through a needle valve. The resulting pressure ramp has the shape of a single exponential decay (Figure 9.2). A typical time constant was three hours. This pumping speed was chosen slow enough to ensure that an approximate diffusion equilibrium was maintained throughout the whole experiment.

We worked with decreasing rather than increasing pressure ramps for two reasons. Firstly, the condition that pumping has to be slow compared to the diffusion time is more easily fulfilled with decreasing ramps. In the initial phase, when pumping is fast, the diffusion is fast. Diffusion slows down as the film dries. At the same time the speed of evacuation slows down as well. Secondly, it turned out that the glass steps were more easily observed on drying then on swelling. This is exemplified by the data set comparing swelling and drying shown in 9.4. Upon swelling, there is an overshoot in the osmotic capacity $d\phi_S/da$. Presumably, this is connected to a fundamental difference between drying and swelling. During swelling large concentration gradients can build up inside the film because diffusion is faster for the parts already swollen than for the parts still dry. The swelling kinetics can be rather complex. For drying, the phenomenology is simpler, because there is no solvent reservoir. The scheme of analysis used here can only be applied to data taken during drying.

The plasticizing effect of solvent is frequently described by writing

$$T_g = T_{g,2} - k\omega_S \tag{9.7}$$

with $T_{g,2}$ the glass temperature of the pure polymer, ω_S the solvent weight fraction and k a constant. For the PS/toluene system the constant k is about 500 °C [Fer80, Cho80]. In accordance with the literature, T_g is lowered to room temperature at a solvent volume fraction of about $\omega_S = 0.14$. The frequency shifts were converted to a mass per unit area

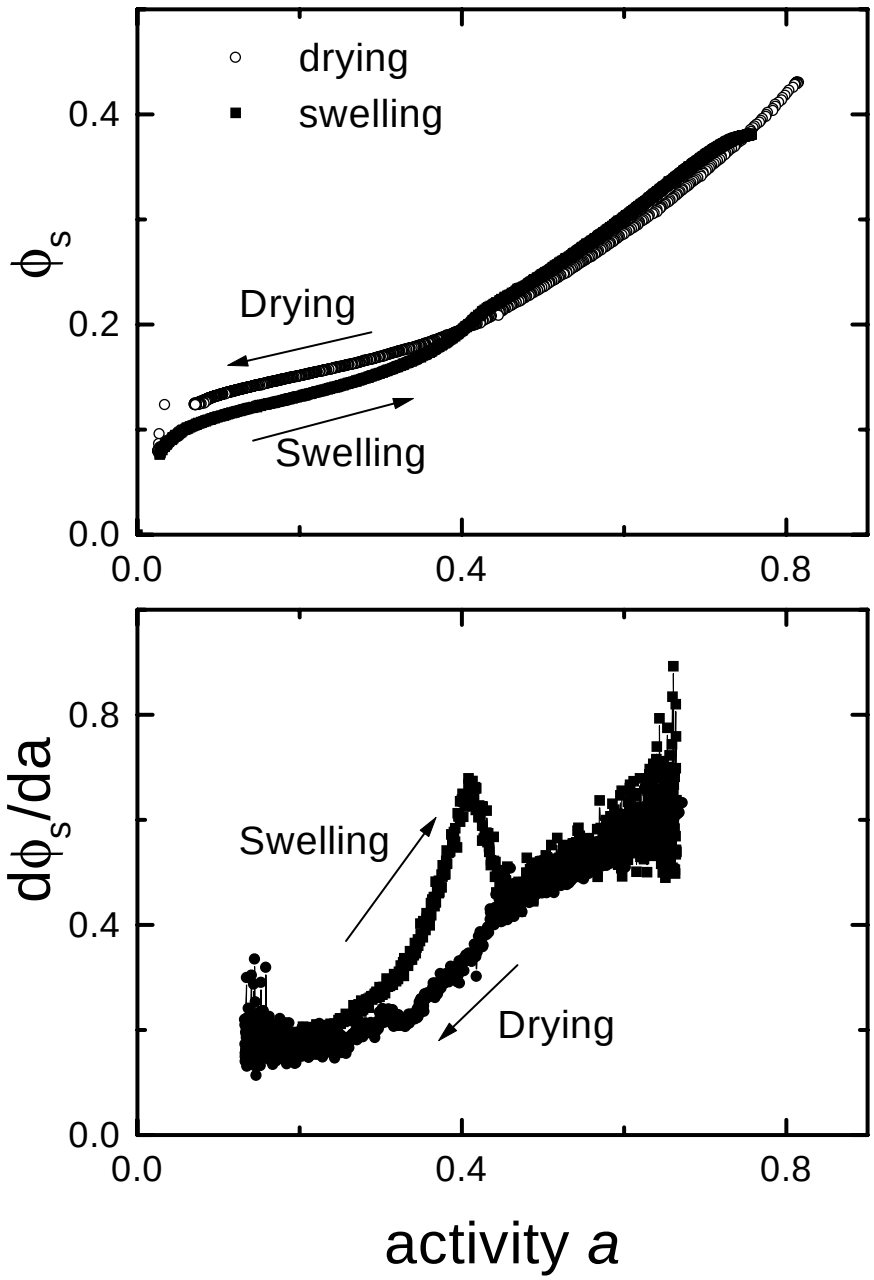

Figure 9.4: Comparison between the swelling and the drying of a 80 nm thick Polystyrene brush. (A) Volume fraction ϕ_s of solvent in the film and (B) Derivatives $d\phi_s/da$.

δm with the Sauerbrey equation [Sau59] with $Z_q = 8.8 \cdot 10^6$ kgm^{-2}s^{-1} the impedance of AT-cut quartz, f_0 the fundamental frequency, δf the frequency shift and f the frequency of the harmonic used for measurement. It is known that the Sauerbrey equation is in practice only accurate within some percent [WSJ97]. This error cancels, when the solvent mass is normalized to the film mass to obtain the solvent mass fraction ω_S. The solvent volume fraction ϕ_S was derived according to equation 9.5. The osmotic capacity was analyzed in the same way as it is usually done for DSC-data. Figure 9.1 shows a typical data set and illustrates how the parameters are derived. We manually set limits between three regions (dotted vertical lines) and fit straight lines to the data sets in the different regions. These straight lines represent the idealized glass step. The center of the step is the glass activity a_g, the width of the transition is Δa. The magnitude of the step Δc_π is determined by extrapolating the lines from below a_g and above a_g to a_g and reading their difference (Figure 9.1B). Finally, we obtain the solvent volume fraction at the glass transition $\phi_g(a_g)$ from the sorption curve $\phi_S(a)$.

9.5 Results and Discussion

9.5.1 Influence of Pumping Speed

Sorption experiments on glass formers in the bulk are very time consuming because the diffusion equilibrium is approached only very slowly. However, the diffusion time scale $t_D = d^2/D$ goes with the square of the film thickness d. For a film thickness in the range of 100 nm t_D is in the order of a few minutes and "quasi-stationary" drying experiments become feasible. The term "quasi-stationary" here implies that diffusion equilibrium is largely maintained. Diffusion equilibrium does not, however, imply thermodynamic equilibrium. There may be intrinsic mechanical relaxations on the time scale of weeks and months even for very thin films. These relaxations are not governed by the solvent transport dynamics, but rather by a reorganization of the local structure.

The fact that the drying dynamics is governed by intrinsic dynamics rather than transport dynamics is evidenced by an increase of the glass transition chemical potential μ_g with increasing drying speed. Fig. 9.5B shows sorption data obtained on a 120 nm brush taken

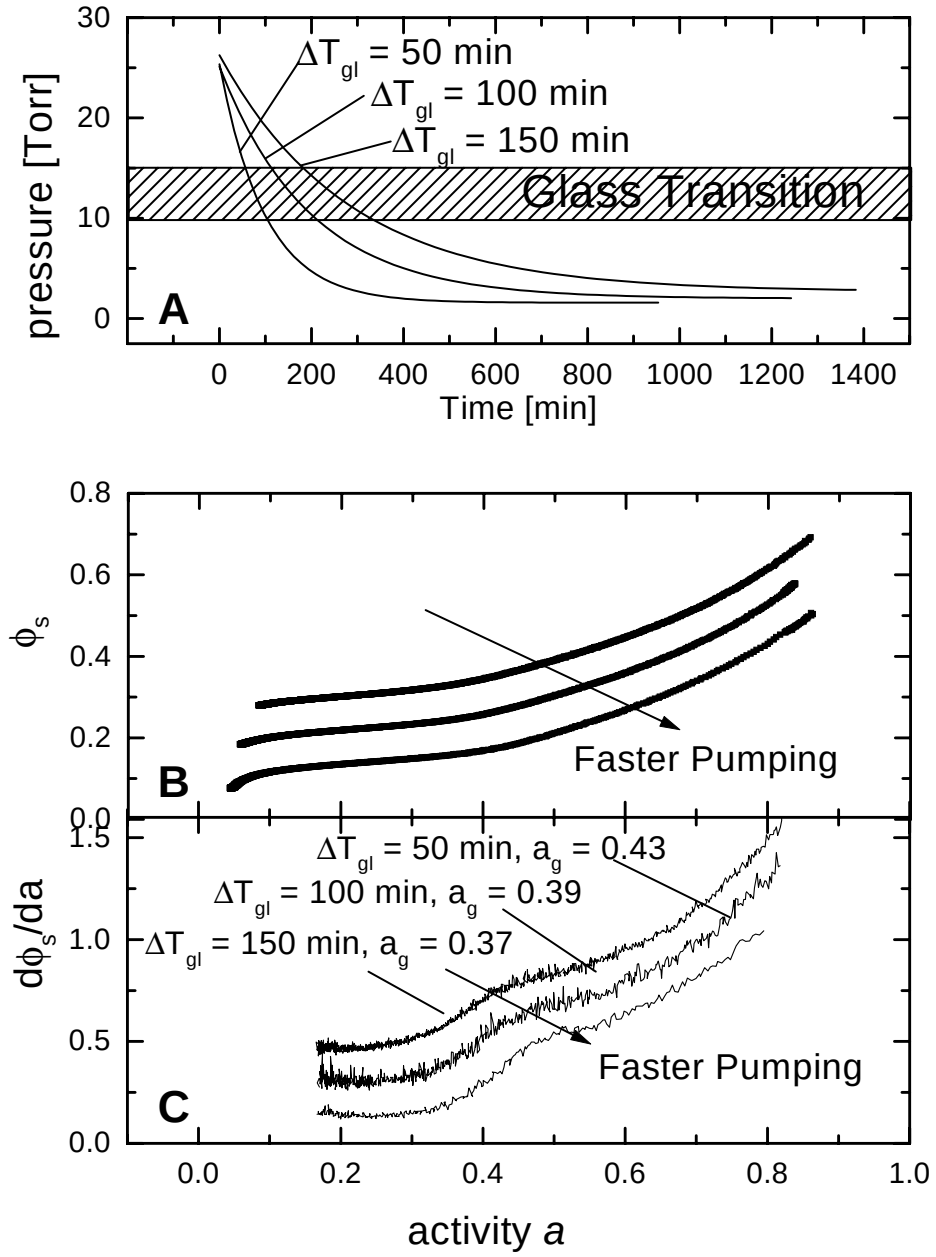

Figure 9.5: (A) Solvent vapor pressure vs. time for three different drying speeds (B) Sorption curves and (C) osmotic capacity for a 120-nm polystyrene brush on SiO_x at different drying speeds. The glass transition activity a_g increases with increasing drying speed.

at different pumping speeds. The evolution of pressure with time closely follows a single exponential decay (Fig. 9.5a) with the time constants t = 100, 200, and 300 min. The effect of drying speed is most critical when the film crosses the glass transition, which happens at about p = 12 Torr. In the range between 15 and 10 Torr the pressure ramp is fairly linear. It takes ΔT_{gl} = 50, 100, and 150 min to cross the range from 15 to 10 Torr for the three different pumping speeds. This time ΔT_{gl} has to be compared to the characteristic time for diffusion t_D. We have determined this time in separate pressure step experiments to be less than 10 min for all samples. This is in accordance with an estimate of t_D from the diffusion constants given in reference [GK91]. The comparison shows that the experimental time scale is longer than the diffusion time scale. Especially for thinner films, the difference is some orders of magnitude. Figure 9.5b shows the sorption curves and their derivatives. The glass transition clearly shifts to lower activities for slower pumping. This shift is not caused by a deviation from diffusion equilibrium. If this was the case, the solvent chemical potential in the vapor phase would be less than the chemical potential inside the film. In the case of insufficient equilibration during fast pumping the apparent glass activity would be lowered. The opposite is observed, proving that the shift of a_g with pumping speed is an intrinsic phenomenon. A shift of T_g with cooling speed is well known from calorimetric experiments. If the glass transition region is crossed quickly, the material is trapped in a state less dense and less relaxed than for slow cooling. Our findings appear to correspond to this phenomenon. When the drying occurs quickly the polymer matrix is trapped in a less dense state than the one found when drying is performed slowly. Because the solvent diffusivity strongly depends on the density of the matrix fast drying should advantageously affect the removal of residual solvent in later stages of drying. Small amounts of volatile organic components in packaging materials are a very critical issue for environmental reasons. Traces of residual solvent are very hard to remove from glassy films. Following the above considerations, the glassy film may have a somewhat open architecture, if it was dried quickly enough. Rapid drying in early phases of the process will therefore be beneficial for the removal or residual solvent in the final state of drying.

9.5.2 Influence of Thickness

Figure 9.6 shows the sorption curves and the osmotic capacities obtained for brushes with different thicknesses on gold. The data have been vertically displaced for clarity. The osmotic capacity $d\phi_S/da$ displays the glass step more clearly than the sorption curves $d\phi_S(a)$ themselves. The fact that the osmotic capacity above T_g is not a constant but increases with solvent content is caused by the functional form of the Flory-Huggins law (eq. 9.1, p. 159). The sorption curve in the melt regime is curved upward, which results in an increase in osmotic capacity. The derived fit parameters are given in Figure 9.7. The open squares are the fit parameters determined for each measurement. The error bars are derived from the fitting of the straight lines to the various sections of the data set (cf. Figure 9.1B). The full dots are the averages from the different measurements. The error bars on the full dots are either the averaged errors from the individual data points divided by $N^{1/2}$ (N the number of measurements) or the standard deviation from the different measurements, which ever is larger. The height of the glass step Δc_p decreases with decreasing thickness. Also, the glass step shifts to lower activities a_g and - with the exception of the 12 nm sample - to a lower solvent content ϕ_g. The 12 nm sample appears to be somewhat exceptional because it has an increased ϕ_g and also a substantially larger width of the glass transition Δa.

Generally, our findings are in line with the previous observations on the temperature-driven glass transition [KJC94, DFG97]. A connection between the solvent content at the glass transition ϕ_g and the glass transition temperature T_g is made by equation 9.7. For polystyrene the constant k is about 500°C [Fer80, Cho80]. With this value a decrease in ϕ_g of 2% translates into a decrease in T_g of about 10°C. The orders of magnitude of the observed effects therefore roughly agree. In accordance with the majority of the previous experiments, thin films appear to contain more free volume than thick films. Presumably, they are packed less densely than the bulk material. The variation of the fit parameters with thickness appears to be rather continuous. From our data we cannot determine a characteristic thickness for the occurrence of thin film anomalies.

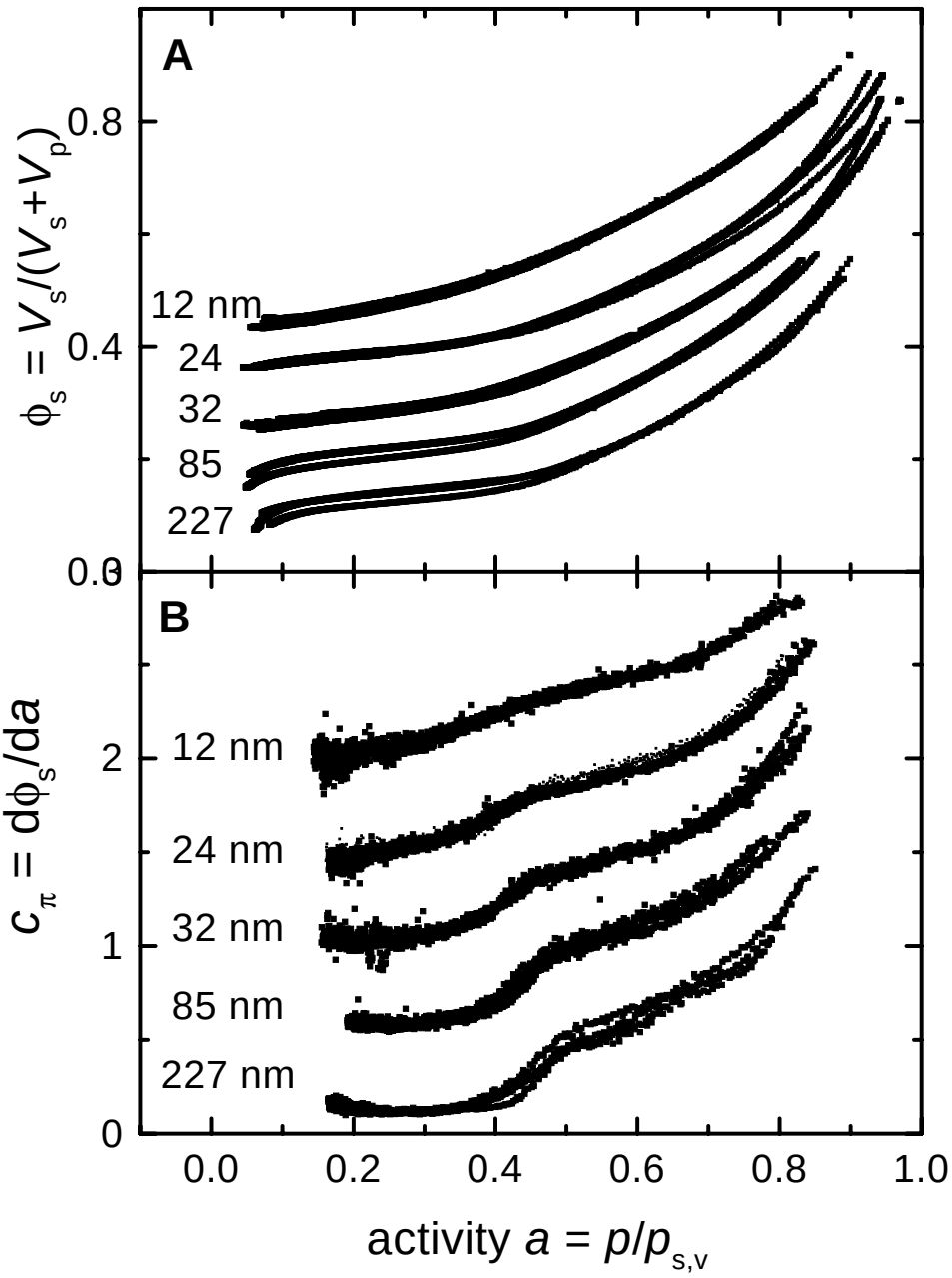

Figure 9.6: (A) Sorption curves and (B) osmotic capacities for polystyrene brushes on gold. Data sets for different thicknesses have been vertically displaced for clarity. All samples have been measured three times to show the reproducibility.

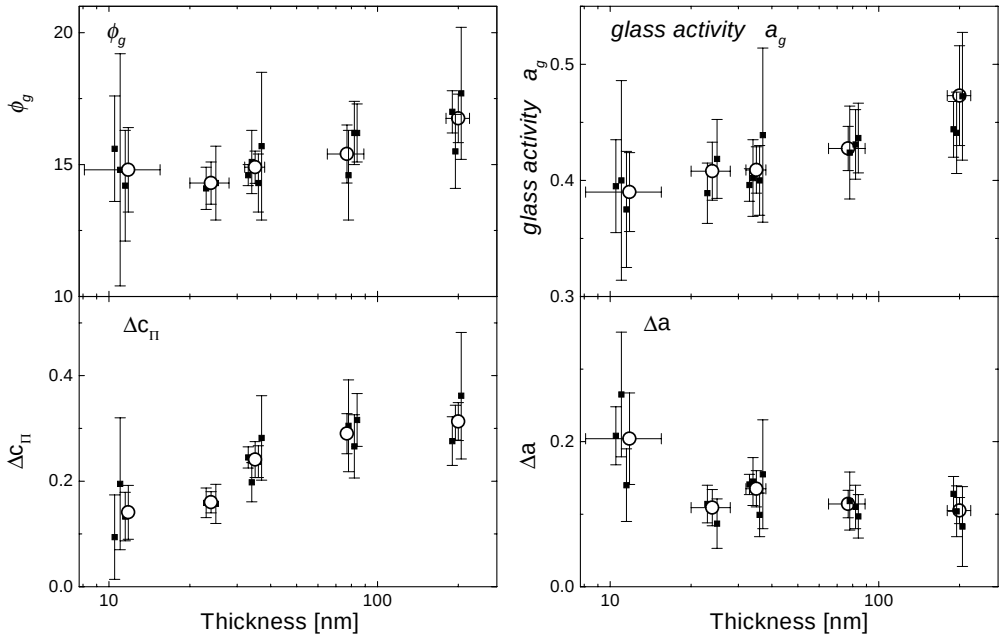

Figure 9.7: Drying measurements of polystyrene brushes on gold surfaces. Summary of the extracted parameters from Figure 9.6.

9.5.3 Influence of History

Given that a true equilibrium is never reached in the glassy state, it is not surprising to find effects of history on drying as well. In Figure 9.8 we show sorption data on the 200 nm sample obtained with repeated wet/dry cycles without high temperature annealing between different runs. In this case the sorption curves were not displaced vertically for clarity. There is an irreversible accumulation of solvent in the film. The same effect could not be induced by just keeping the films in the wet state for long times. Evidently, the wet state reached after swelling freshly annealed brushes in solvent vapor for several hours is not a true equilibrium state. Repeated cycling through the dry and the wet state causes an internal reorganization of the polymeric material which would take much longer without these swelling and drying steps. It seems doubtful whether the situation reached after repeated cycling is closer to a thermodynamic equilibrium than the freshly annealed state. If the dynamics of solvent inflow is more efficient than the dynamics of solvent removal, solvent will accumulate in the film for purely kinetic reasons. The fact that equilibrium is practically unachievable for surface bound polymers even in the

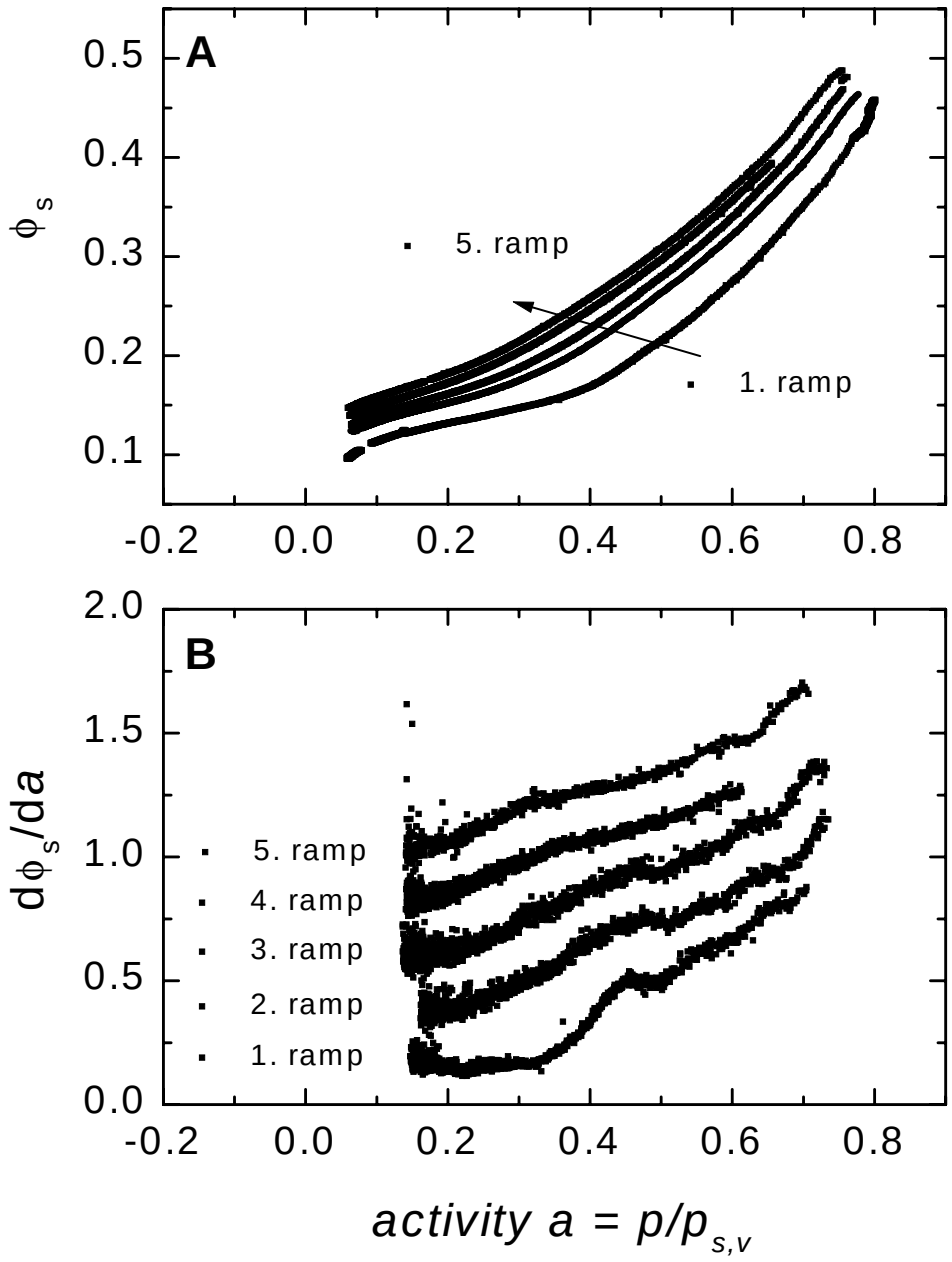

Figure 9.8: Repeated drying ramps on a 200 nm polystyrene brush *without* high-temperature annealing between the different runs: (A): sorption curves (B): derivatives (osmotic capacity). In this case the sorption curves were *not* displaced vertically for clarity. There is an irreversible accumulation of solvent in the film. The glass transition gradually disappears.

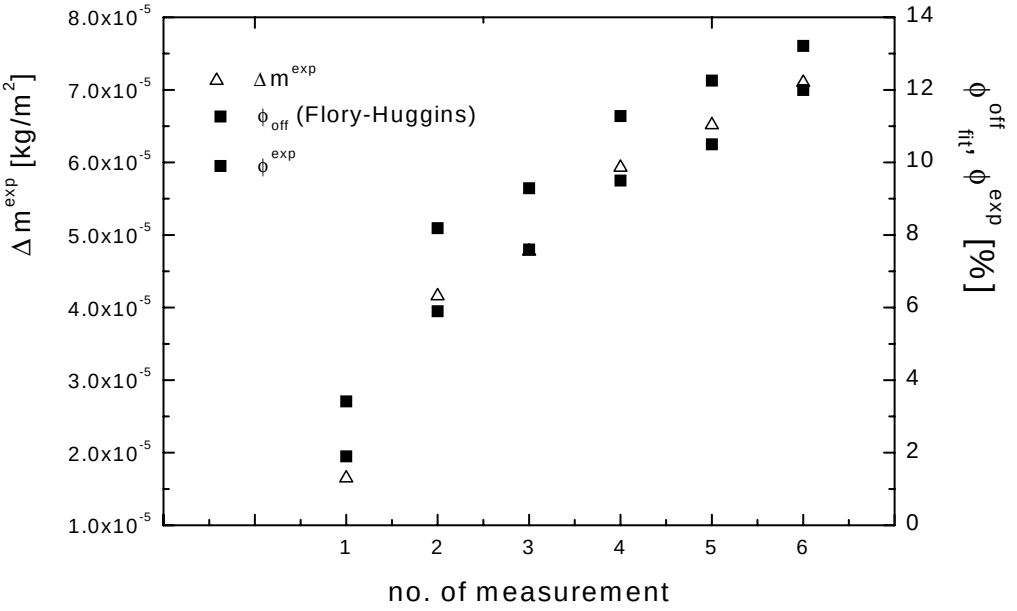

Figure 9.9: Comparison of the theoretical offset parameter with the measured mass increase.

---

presence of substantial amounts of solvent has been reported previously by Granick and coworkers [HG92, HGS94]. This group was interested in the properties of physisorbed polymers and concluded that the conditions of preparation were by far the most important factor determining the properties of the polymer layers. The dynamics of reorganizations appeared to exceedingly slow down due to the attachment of the chains to the substrate. Presumably, the situation is similar here. Figure 9.10 shows the derived fit parameters for the repeated dry/wet cycles. Interestingly, the glass transition activity a_g depends much more on history than the critical solvent volume fraction ϕ_g. There seems to be a certain amount of immobile solvent inside the film which affects the glass transition although it does not take part in the solvent transport. Figure 9.9 shows a comparison between the χ-offset parameter obtained from the Flory-Huggins (FH) fits with a modified FH function that includes a remaining solvent part instead of a change in slope during sorption — like suggested theoretically.

All data in this work have been fitted with an offset parameter ϕ^{off} in the Flory-Huggins function. This accorded best to the data. Also, it reflects the trend of the mass of solvent remaining in the polymer matrix after swelling quite well. However, it is constantly

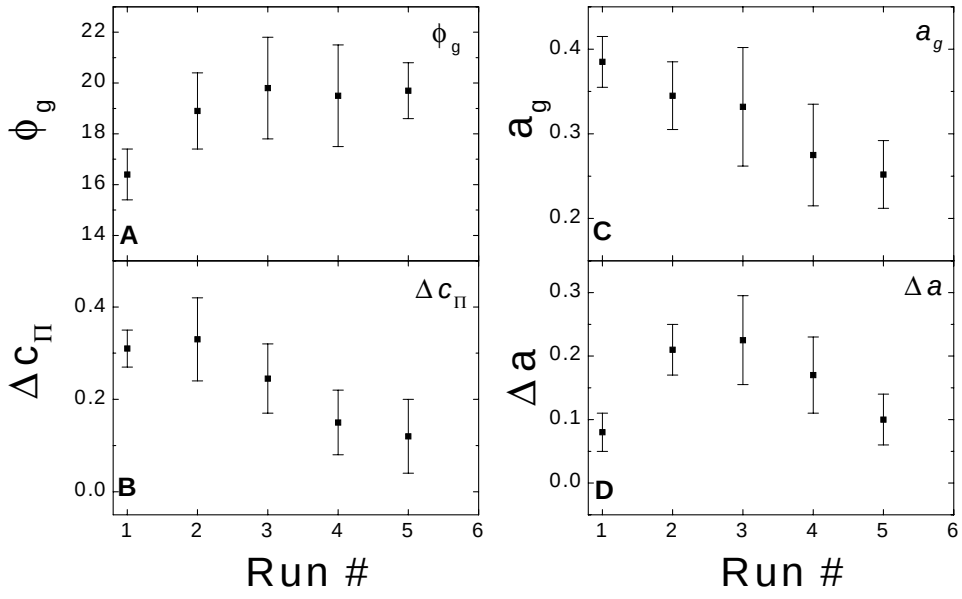

Figure 9.10: Change of the curve parameters with subsequent swelling. (A) The solvent content at the glass transition ϕ_g increases. (B), (C) and (D): The osmotic capacity c_π the glass activity a_g as well as the width of the transition a_g decrease.

$\approx 1.5\%$ below the actual remaining solvent mass Δm^{exp} determined after each measurement. To explain this, we think about at what point of time during the experiment both parameters were determined: The offset parameter ϕ_{fit}^{off} from the FH-fit is determined while the brush is swollen, i.e., it represents the excess mass uptake in the FH–regime. The measured mass uptake Δm^{exp}, however, contains an additional part that could presumably be explained by the "Langmuir-hole-filling". This would mean that the solvent content ϕ_g in the glassy state cannot "escape" from the glassy polymer matrix because the diffusion time scale has increased by several orders of magnitude.

9.6 Conclusions

We have investigated the solvent induced glass transition in polystyrene polymer brushes on gold as function of thickness, drying speed, and sample history. For thin films, the glass transition is less pronounced than for thick ones. Also, it is shifted towards lower solvent activities, which indicates that the chains are packed less densely. In analogy to the temperature-driven glass transition the glass transition activity a_g increases when drying is performed fast. The glass transition is most pronounced directly after the samples have been vacuum annealed at elevated temperatures. After repeated wet/dry cycles, solvent irreversibly accumulates in the film and the glass transition gradually disappears. The width of the glass transitions found widens with decreasing film thickness. Also, the height of the glass steps diminishes. This coincides with results obtained by Cho et al. who measured the glass transition of thin polyisoprene layers confined between mica sheets simultaneously probing their mechanical and dielectric response in an SFA. The authors report that "the slow normal mode distribution is much broader and the terminal relaxation time is much longer for chains in thin layers. These dielectric features are attributed to spatial constraints on global chain motion in the thin layers and also to adsorption of chains on mica surfaces when the layer thickness is comparable to the unperturbed chain dimension." [CWG99]. Transferred to the sorption experiments, we could conclude that the cooperative motion of the polystyrene-brush chains is influenced by both surfaces: the free surface and the interface with the solid substrate, which could broaden the relaxation time spectrum observed for thinner films.

Chapter 10

Conclusions

10.1 Summary

In this work we used quartz crystal resonators for dynamical measurements on very thin polymer films. It was divided in two different parts:

- Development of a setup to measure friction at the quartz resonator surface.
- Investigation of thin film anomalies in the solvent-induced glass transition in polymer brushes.

In the following the results obtained from these investigations are summarized.

10.1.1 Friction Experiments

The setup for the measurement of friction forces has been developed during this thesis. Its potential was tested with measurements on molecular lubricant films.

1. With the quartz resonator method described in this thesis it is possible to probe the friction forces occurring at the quartz surface. This could be shown by the comparison of surfaces that are known to exhibit high (gold) and low friction forces (plasma-polymerized fluorocarbon). The quartz surface moves at frequencies in the

MHz-range and at velocities of about $v = 1$ m/s. A spatial resolution of 1 Å perpendicular to the surface can reproducibly be achieved.

2. When tight contact between the quartz resonator and the opposing surface is reached the frequency increases. This effect has been modeled by the assumption that sound waves are launched into the sphere. The functional form of the frequency increase follows an usual force JKR-behavior for the increasing contact area quite well. We assume that in this regime the surfaces stick together rather than sliding past each other. The frequency shift is proportional to the contact radius.

3. Before sticking contact a sliding friction regime could be identified which is characterized by the resonance bandwidth of the quartz passing through a maximum. Here the surfaces are in a steady–sliding condition.

4. The sliding friction appeared to be linear in velocity for all cases. One mostly finds liquid-like behavior.

5. The setup was tested on a molecular model–lubricant system. The results obtained from this study coincide well with those from literature obtained with other methods.

   (a) CH_x exhibits higher friction than CN_x.

   (b) The friction decreases with increasing lubricant thickness.

   (c) Above these bulk values there is no friction, or it is below the detection limit of the quartz method, i.e. the lubricant "works". This means that under conditions similar to those occurring in a real disk-drive ($v = 1$m/s, $f \approx 10^6$, shear rate $\dot{\gamma} \approx 10^9$ s^{-1}, strains $\epsilon \approx 10$) the lubricant maintains its liquid properties. AFM–results from Mate support this, while general investigations on ultrathin polymer films with the SFA finds a solidification for such a confined geometry (boundary lubrication).

   (d) In particular, this means that the lubricant molecules are neither removed (squeezed out) from in between the surfaces nor destroyed by he extreme conditions applied.

   (e) The order of magnitude of the measured shear viscosity agrees with values reported in literature.

(f) The normal forces probably occur due to bridging effects of the lubricant (molecules). They do *not* correlate well to the measured friction. The friction is not adhesion-controlled.

6. The surface roughness and the distribution of the height of the surface asperities presumably reflects in the form (Gaussian) of the maximum in bandwidth before contact. The width of the maximum is probably closely related to the (combined) roughness of the surfaces in contact.

10.1.2 Osmotic Glass Transition in Thin Films

We have investigated the solvent induced glass transition in polystyrene polymer brushes on gold as function of thickness, drying speed, and sample history. First, it could be shown that the sorption of solvent molecules in thin polymer brushes induces a glass transition that is similar to the temperature-induced glass transition. Their sorption behavior can be described by the Flory-Huggins (FH) theory for the highly swollen regime and a modified FH-law for the glass regime (Leibler–Sekimoto). The sorption curves $\phi_s(a)$ display a kink at the glass transition. Further, we modified the FH-law by an experimental solvent offset parameter that accounts for solvent that remains in the polymer matrix after drying. Generally, this function fitted the data better than the common use of a second FH-interaction parameter χ_2. In spite of the fact that the data were well-described by these models we decided for a model-independent data evaluation: The data enabled to derive the sorption curves ϕ_s with respect to the solvent activity a. In analogy to the thermal glass transition we call this derivative the osmotic capacity c_π. It shows a step at the glass transition. For decreasing film thickness the glass transition is shifted to lower transition activities a_g and the solvent content ϕ_g, that is needed to plastify the polymer matrix, decreases as well. When putting forward the analogy to the temperature–induced glass transition in thin polymer films, our results coincide well with experimental findings of a decreased glass transition temperature T_g because of a confined geometry.
Additionally, we find that the glass step becomes less pronounced (the step height Δc_π decreases, the width of the transition Δa increases) for decreasing film thickness.
The same behavior is found if a brush is subjected to several subsequent "dry-wet" cycles.

The glass transition is most pronounced directly after the samples have been vacuum annealed at elevated temperatures. After repeated wet/dry cycles, solvent irreversibly accumulates in the film and the glass transition gradually disappears.

10.2 Perspectives

10.2.1 Electrical Measurements

The electrode of the quartz which comes into contact with the sphere is gold-coated and grounded and, hence, provides an electrical contact. If the Si_3N_4 sphere would be coated with gold and electrically contacted different measurements would be possible.

10.2.2 Measurement of Interfacial Distance

As shown in Chapter 6 a capacitive sensor has already been used to control the distance between the surfaces and determine the contact point qualitatively. However, within these test measurements a quantitative evaluation was not possible because of the unknown electrical parameters of the used electrical circuit. With a circuit designed especially for this purpose one could determine the distance directly and the point of contact would be clearly defined by the onset of conductivity. However, analysis becomes more difficult for lubricant layers with unknown dielectric constants.

10.2.3 Dielectric Measurements

Another possibility would be to implement a dielectric measurement by applying an oscillating electrical field to the confined layer. The same has been done for a Surface Forces Apparatus [CWG99]. The authors were able to relate mechanical and dielectric measurements and to observe effects due to confinement of the layers between the surfaces.

10.2.4 Measurement of Contact Area

Usually the contact area is determined using optical interferometry (SFA or JKR-measurements). In the quartz setup there is no access for a light beam since the Si_3N_4 spheres are not transparent and the top electrode is not accessible. For light access from the bottom there are two problems: (i) the quartz is transparent but the gold electrode is not. (ii) The quartz holder is closed.
However, another possibilty to determine the contact area is to measure the electrical resisitance of the point contact [KKM96]. For circular contact spots the electrical resistance R reads as follows:

$$R(r_c) = \rho/2r_c \tag{10.1}$$

with r_c the contact radius; and ρ the specific volume resistance. Thus, if contact is established the capacitive measurements are not possible because of an electrical short-cut between the surfaces. However, this is an ideal prerequisite for electrical resistance measurements.

10.3 Measurements in Vacuum or in a Liquid

For measurements of interfacial forces the clean surfaces are an absolute prerequisite. In particular, the formation of water layers has been reported to cause effects that often are much larger than the ones of interest. Environmental conditions that fulfill this requirement can only be provided by a vacuum environment or by measurements in liquids. We have also performed test measurements in water. However, the viscosity of the liquid damps the quartz oscillation. With the increased damping the relative changes of the resonance bandwidth become smaller. This disadvantage might be outweighed by the well defined environment.

10.4 Surface Preparation

The aim of constructing the quartz setup was to create a high-frequency and high-velocity access to nanotribology. However, the surfaces used are not atomically flat. This requirement for measurements on a nanoscopic level could be fulfilled by different measures:
The quartz surface could be covered with thin mica sheets. Tests to glue mica onto the quartz surfaces have already been carried out. The main problem here was that the additional layer (mica + glue) ($\approx 3 - 5\mu$m) increased the quartz damping such that the resulting S/N-ratio did not allow friction–sensitive measurements. However, a careful preparation and a "hard" glue (with low viscosity) could make these measurements possible.

10.4.1 Spheres

The Si_3N_4 spheres were the smoothest round surfaces available. Another possibility for macroscopic spheres would be the use of "glass droplets" that should be very smooth because glass is "a frozen liquid". Also, one could try to combine the quartz resonator method with the AFM. Although we could not observe resolvable effects during our preliminary experiments (cf. Chapter 6) Krim and coworkers reported such effects in experiments with STM (Scanning Tunneling Microscopy) tips. A reason for the lack of an effect could have been the small contact area: As we derive in Chapter 6.7 the magnitude of the effects depends on the ratio of the contact area to the electrode area (A_c/A_e). To increase the effect one would have to either increase the contact area (e.g., by using latex microspheres glued to the AFM-cantilever) or to decrease the electrode area.

Bibliography

[AB87] R.M.A. Azzam and N.M. Bashara. *Ellipsometry and Polarized Light*. Elsevier, Amsterdam, 1987.

[Ada76] A.W. Adamson. *Physical Chemistry of Surfaces*. Wiley, New York, 3rd edition, 1976.

[AHM+89] S. Alexander, L. Hellemans, O. Marti, J. Schneir, V. Elings, P. K. Hansma, M. Longmire, and J. Gurley. An atomic-resolution atomic-force microscope implemented using an optical-lever. *Journal of Applied Physics*, 65(1):164–167, 1989.

[ALST97] I. Alig, D. Lellinger, J. Sulimma, and S. Tadjbakhsch. Ultrasonic shear wave reflection method for measurements of the viscoelastic properties of polymer films. *Review of Scientific Instruments*, 68(3):1536–1542, 1997.

[AY83] V. Au-Yeung. FTIR determination of fluorocarbon lubricant film thicknesses on magnetic disk media. *IEEE Transactions on Magnetics*, 19(5):1662–1664, 1983.

[BB95] J. Baschnagel and K. Binder. On the influence of hard walls on structural-properties in polymer glass simulation. *Macromolecules*, 28(20):6808–6818, 1995.

[BB96] J. Baschnagel and K. Binder. Dynamics of glassy polymer melts in confined geometry: A monte carlo simulation. *Journal De Physique I*, 6(10):1271–1294, 1996.

[BCP92] N. A. Burnham, R. J. Colton, and H. M. Pollock. Work-function anisotropies as an origin of long-range surface forces. *Physical Review Letters*, 69(1):144–147, 1992.

[BDI98] A. Berman, C. Drummond, and J.N. Israelachvili. Amonontons' law at the molecular level. *Trib. Lett.*, 4:95–101, 1998.

[Ber80] A.R. Berens. Gravimetric and volumetric study of the sorption of gases and vapors in poly(vinyl chloride) powders. *Polymer Engineering and Science*, 20(1):95–101, 1980.

[Ber97] L. Bergström. Hamaker constants of inorganic materials. *Advances in Colloid and Interface Science*, 70:125–169, 1997.

[BGA+98] C. Bouchard, B. Guerrier, C. Allain, A. Laschitsch, A. C. Saby, and D. Johannsmann. Drying of glassy polymer varnishes: A quartz resonator study. *Journal of Applied Polymer Science*, 69(11):2235–2246, 1998.

[BHP94] T. Baumberger, F. Heslot, and B. Perrin. Crossover from creep to inertial motion in friction dynamics. *Nature*, 367:544–546, 1994.

[Bhu95] B. Bhushan. *Handbook of Micro/Nanotribology*. CRC Press, London, 1995.

[Bhu96] B. Bhushan. Chapter 8. In *Tribology and Mechanics of Magnetic Storage Devices*. Springer, Berlin, 2nd edition, 1996.

[BI89] J. Brandrup and E.H. Immergut. *Polymer Handbook*. Wiley, New York, 3rd edition, 1989.

[BIL95] B. Bhushan, J.N. Israelachvili, and U. Landman. Nanotribology: Friction, wear and lubrication at the atomic scale. *Nature*, 374:607–616, 1995.

[Bin94] K. Binder. Phase-transitions in polymer blends and block-copolymer melts — some recent developments. In *Theories and Mechanism of Phase Transitions, Heterophase Polymerizations, Homopolymerization, Addition Polymerization*, volume 112 of *Advances in Polymer Science*, pages 181–299. 1994.

[BM95] M. Binggeli and C.M. Mate. Influence of water vapor on nanotribology studied by friction force microscopy. *Journal of Vacuum Science and Technology B*, 13(3):1312–1315, 1995.

[Bot82] V.E. Bottom. *Introduction to Quartz Crystal Unit Design*. Van Nostrand - Reinhold, New York, 1982.

[BQG86] G. Binnig, C. F. Quate, and C. Gerber. Atomic force microscope. *Physical Review Letters*, 56(9):930–933, 1986.

[BSS+93] H.-J. Butt, P. Siedle, K. Seifert, K. Fendler, T. Seeger, E. Bamberg, A. L. Weisenhorn, K. Goldie, and A. Engel. Scan speed limit in atomic force microscopy. *Journal of Microscopy-Oxford*, 169:75–84, 1993.

[BT73] F.P. Bowden and D. Tabor. *Friction: An Introduction to Tribology*. Anchor Press/Doubleday, Garden City, 1973.

[Bun99] Andreas Bund. *Die Quarzmikrowaage in Rheologie und Elektrochemie: Fortschritte in der Signalauswertung durch Netzwerkanalyse*. PhD thesis, Universitaet des Saarlandes, 1999.

[CHI91] Y.I. Chen, C.A. Helm, and J.N. Israelachvili. Molecular mechanisms associated with adhesion and contact angle hysteresis of monolayer surfaces. *J. Chem. Phys.*, 95:10736–10747, 1991.

[Cho80] T.S. Chow. Molecular interpretation of the glass transition temperature of polymer-diluent systems. *Macromolecules*, 13:362–364, 1980.

[CLCB96] E.C. Cutiongco, D. Li, Y.-W. Chung, and C.S. Bhatia. Tribological behavior of amorphous carbon nitride overcaots fo magnetic thin-film rigid disks. *Journal of Tribology*, 118:543–548, 1996.

[CWG99] Y. K. Cho, H. Watanabe, and S. Granick. Dielectric response of polymer films confined between mica surfaces. *Journal of Chemical Physics*, 110(19):9688–9696, 1999.

[Der34] B.V. Derjaguin. *Kolloid Zeits.*, 69:155–164, 1934.

[DFG97] G.B. DeMaggio, W.E. Frieze, and D.W. Gidley. Interface and surface effects on the glass transition in thin polystyrene films. *Physical Review Letters*, 78(8):1524–1527, 1997.

[DG96] A.L. Demirel and S. Granick. Glasslike transition of a confined simple fluid. *Phys. Rev. Lett.*, 77(11):2261–2264, 1996.

[DJ96] A. Domack and D. Johannsmann. Plastification during sorption of polymeric thin films: A quartz resonator study. *Journal of Applied Physics*, 80(5):2599–2604, 1996.

[DK96a] C. Daly and J. Krim. Friction and damping of Xe/Ag(111). *Surface Science*, 368:49–54, 1996.

[DK96b] C. Daly and J. Krim. Sliding friction of solid Xenon monolayers and bilayers on Ag(111). *Phys. Rev. Lett.*, 76(5):803–806, 1996.

[DMT75] B. V. Derjaguin, V. M. Muller, and Y. P. Toporov. Effect of contact deformations on adhesion of particles. *Journal of Colloid and Interface Science*, 53(2):314–326, 1975.

[Dow79] D. Dowson. *History of Tribology*. Longman, London, 1979.

[DT92] L. Dai and C. Toprakcioglu. End-adsorbed triblock copolymer chains at the liquid-solid interface: Bridging effects in a good solvent. *Macromolecules*, 25:6000–6006, 1992.

[Fer80] J.D. Ferry. *Viscoelastic Properties of Polymers*. Wiley, New York, 1980.

[Flo53] P.J. Flory. *Principles of Polymer Chemistry*. Cornell University Press, New York, 1953.

[GK91] T.P. Gall and E.J. Kramer. Diffusion of deuterated toluene in polystyrene. *Polymer*, 32(2):265–271, 1991.

[GLCR95] C. Gao, Y. C. Lee, J. Chao, and M. Russak. Dip-coating of ultra-thin liquid lubricant and its control for thin-film magnetic hard disks. *Ieee Transactions On Magnetics*, 31(6):2982–2984, 1995.

[GM94] Gary S. Grest and M. Murat. In K. Binder, editor, *Monte Carlo and Molecular Dynamics Simulations in Polymer Science*. Clarendon Press, Oxford, 1994.

[GMIH90] M.L. Gee, P.M. McGuiggan, J.N. Israelachvili, and A.M. Homola. Liquid to solidlike transitions of molecularly thin films under shear. *J. Chem. Phys.*, 93(3):1895–1906, 1990.

[Gra91] S. Granick. Motions and relaxations of confined liquids. *Science*, 253:1374–1379, 1991.

[Gra99] S. Granick. Soft matter in a tight spot. *Physics Today*, 7:26–31, 1999.

[HA97] T.R. Hicks and P.D. Atherton. *The NanoPositioning Book*. Queensgate Instruments Ltd., Waterside Park, UK, 1 edition, 1997.

[HB97] C. D. Hahm and B. Bhushan. High shear rate viscosity measurements of perfluoropolyether lubricants for magnetic thin-film rigid disks. *Journal of Applied Physics*, 81(8):5384–5386, 1997.

[Her81] H. Hertz. *J. Reine Angew. Math.*, 92:156–171, 1881.

[HG92] H. W. Hu and S. Granick. Viscoelastic dynamics of confined polymer melts. *Science*, 258(5086):1339–1342, 1992.

[HGH99] J. A. Hammerschmidt, W. L. Gladfelter, and G. Haugstad. Probing polymer viscoelastic relaxations with temperature- controlled friction force microscopy. *Macromolecules*, 32(10):3360–3367, 1999.

[HGJP88] K.E. Heusler, A. Grzegorzewski, L. Jckel, and J. Pietrucha. Measurement of mass and surface stress at one electrode of a quartz oscillator. *Ber. Bunsenges. Phys. Chem.*, 92:1218–1225, 1988.

[HGS94] H.-W. Hu, S. Grannick, and K.S. Schweizer. Static and dynamical structure of confined polymer films. *Journal of Non-Crystalline Solids*, 172-174:721–728, 1994.

[HGW+95] G. Haugstad, W. L. Gladfelter, E. B. Weberg, R. T. Weberg, and R. R. Jones. Probing molecular relaxation on polymer surfaces with friction force microscopy. *Langmuir*, 11(9):3473–3482, 1995.

[HH80] P. Horowitz and W. Hill. *The Art of Electronics*. Cambridge University Press, London, 1980.

[HIGM89] A.M. Homola, J.N. Israelachvili, M.L. Gee, and P.M. McGuiggan. Measurements of and relation between the adhesion and friction of two surfaces separated by thin liquid and polymer films. *J. Tribol.*, 111:675–682, 1989.

[HTL92] A. Halperin, M. Tirrell, and T. P. Lodge. Tethered chains in polymer microstructures. *Advances in Polymer Science*, 100:31–71, 1992.

[IA78] J.N. Israelachvili and G.E. Adams. Measurement of forces between two mica surfaces in aqueous electrolyte solutions in the range 0-100 nm. *J. Chem. Soc. Faraday Trans. I*, 74:975–1001, 1978.

[ICY94] J.N. Israelachvili, Y.-L. Chen, and H. Yoshizawa. Relationship between adhesion and friction forces. *J. Adhesion Sci. Technol.*, 8(11):1231–1249, 1994.

[Isr72] J.N. Israelachvili. The calculation of van der waals dispersion forces between macroscopic bodies. *Proc. R. Soc. Lond. A*, 331:39–55, 1972.

[Isr87] J.N. Israelachvili. Direct measurements of forces between surfaces in liquids at the molecular level. In *Proc. Natl. Acad. Sci. USA*, volume 84, pages 4722–4724, 1987.

[Isr92a] J. N. Israelachvili. Adhesion forces between surfaces in liquids and condensable vapors. *Surface Science Reports*, 14(3):109–159, 1992.

[Isr92b] J.N. Israelachvili. *J. Vac. Sci. Tech.*, 10:2961, 1992.

[Isr92c] J.N. Israelachvili. *Intermolecular and Surface Forces*. Academic Press, London, 2 edition, 1992.

[Isr99] J.N. Israelachvili. *Homepage Surface Forces Laboratory*. Internet, http://www.chemengr.ucsb.edu/ sfalab/mark-II.html, 1999.

[IT72] J.N. Israelachvili and D. Tabor. The measurement of van der waals dispersion forces in the range 1.5 to 130 nm. *Proc. R. Soc. Lond. A*, 331:19–38, 1972.

[Jae86] J. Jaeckle. Models of the glass transition. *Rep. Prog. Phys.*, 49:171–231, 1986.

[JB95] U. Jonsson and B. Bhushan. Measurement of rheological properties of ultrathin lubricant films at very high-shear rates and near-ambient pressure. *Journal of Applied Physics*, 78(5):3107–3114, 1995.

[JKR71] K.L. Johnson, K. Kendall, and A.D. Roberts. Surface energy and the contact of elastic solids. *Proc. R. Soc. Lond. A*, 324:301–313, 1971.

[JMM+96] K.E. Johnson, C.M. Mate, J.A. Merz, R.L. White, and A.W. Wu. Thin-film media — current and future technology. *IBM J. Res. Develop.*, 40(5):511–532, 1996.

[Joh91] D. Johannsmann. *Einsatz von Quarz-Resonatoren und Ellipsometrie zur viskoelastischen Charakterisierung von dünnen Schichten und Adsorbaten*. PhD thesis, Universitt Mainz, 1991.

[Joh99] D. Johannsmann. Viscoelastic analysis of organic thin films on quartz resonators. *Macromol. Chem. Phys.*, 200(3):501–516, 1999.

[Kan90] K. K. Kanazawa. The physical description of films coating quartz resonators. *Thin Solid Films*, 187(2):L7–L10, 1990.

[Kan97] K. K. Kanazawa. Mechanical behaviour of films on the quartz microbalance. *Faraday Discussions*, (107):77–90, 1997.

[KC91] J. Krim and R. Chiarello. Sliding friction measurements of molecularly thin films. *J. Vac. Sci. Technol. A*, 9(4):2566–2569, 1991.

[KDD93] J. Krim, J. Dayo, and C. Daly. Combined scanning tunneling microscope and quartz microbalance study of molecularly thin water layers. In *STM/AFM*, Natick, MA, 1993. Plenum Press.

[KJC94] J.L. Keddie, R.A.L. Jones, and R.A. Cory. Size-dependent depression of the glass transition temperature in polymer films. *Europhysics Letters*, 27(1):59–64, 1994.

[KKM96] W. Konchits, YE. Kirpichenko, and N.K. Myshkin. Micromechanics and electrical conductivity of point contacts in boundary lubrication. 29(5):365–371, 1996.

[KM93] K. K. Kanazawa and O. R. Melroy. The quartz resonator - electrochemical applications. *Ibm Journal of Research and Development*, 37(2):157–171, 1993.

[KSC91] J. Krim, D.H. Solina, and R. Chiarello. Nanotribology of a Kr monolayer: A quartz-crystal microbalance study of atomic-scale friction. *Phys. Rev. Lett.*, 66(2):181–184, 1991.

[KW88] J. Krim and A. Widom. Damping of a crystal oscillator by an adsorbed monolayer and its relation to interfacial viscosity. *Phys. Rev. B*, 38(17):12184–12188, 1988.

[KWN97] P. Kodali, K.C. Walter, and M. Nastasi. Investigation of mechanical and tribological properties of amorphous diamond-like carbon coatings. *Tribology International*, 30(8):591–598, 1997.

[LBH+99] A. Laschitsch, C. Bouchard, J. Habicht, M. Schimmel, J. Rühe, and D. Johannsmann. Thickness dependence of the solvent-induced glass transition in polymer brushes. *Macromolecules*, 32(4):1244–1251, 1999.

[LCC+94] D. Li, E. Cutiongco, Y.-W. Chung, M.-S. Wong, and W.D. Sproul. Composition, structure and tribological properties of amorphous carbon nitride coatings. *Surface Coatings Technology*, 68/69:611–615, 1994.

[Lid95] D.R. Lide. *Handbook of Chemistry and Physics*. CRC Press, 76th edition, 1995.

[LJ99] A. Laschitsch and D. Johannsmann. High frequency tribological investigations on quartz resonator surfaces. *Journal of Applied Physics*, 85(7):3759–3765, 1999.

[LL75] L.D. Landau and E.M. Lifshitz. *Theory of Elasticity*, volume 7 of *Lehrbuch der theoretischen Physik*. Pergamon, New York, 1975.

[LS93] L. Leibler and K. Sekimoto. On the sorption of gases and liquids in glassy polymers. *Macromolecules*, 26:6937–6939, 1993.

[MA88] G. Meyer and N. M. Amer. Novel optical approach to atomic force microscopy. *Applied Physics Letters*, 53(12):1045–1047, 1988.

[MAP88] G. Marchionni, G. Ajroldi, and G. Pezzin. Molecular weight dependence of some rheological and thermal properties of perfluoropolyethers. *Eur.Polym.J.*, 24(12):1211–1216, 1988.

[MAP92] G. Marchionni, G. Ajroldi, and G. Pezzin. Viscosity of perfluoropolyether lubricants: Influence of structure, chain dimensions and molecular interactions. *Rheology and Tribology of Engine Oils*, (922289):87–96, 1992.

[MARP91] G. Marchionni, G. Ajroldi, M.C. Righetti, and G. Pezzin. Perfluoropolyethers: Critical molecular weight and molecular weight dependence of glass transition temperature. *Polymer Communications*, 32(3):71, 1991.

[Mat92] C.M. Mate. Atomic-force-microscopy study of polymer lubricants on silicon surfaces. *Phys. Rev. Lett.*, 68(22):3323–3326, 1992.

[Mau92] Daniel Maugis. Adhesion of spheres: The jkr-dmt transition using a dugdale model. *Journal of Colloid and Interface Science*, 150(1):243–269, 1992.

[MLN89] C. M. Mate, M. R. Lorenz, and V. J. Novotny. Atomic force microscopy of polymeric liquid-films. *Journal of Chemical Physics*, 90(12):7550–7555, 1989.

[MMEC87] C. M. Mate, G.M. McClelland, R. Erlandsson, and S. Chiang. Atomic-scale friction of a tungsten tip on a graphite surface. *Phys. Rev. Lett.*, 59(17):1942–1945, 1987.

[MN91] C. Mathew Mate and V.J. Novotny. Molecular conformation and disjoining pressure of polymeric liquid films. *J. Chem. Phys.*, 94(12):8420–8427, 1991.

[MT91] K.F. Mansfield and D.N. Theodorou. Molecular dynamics simulation of a glassy polymer surface. *Macromolecules*, 24:6283–6294, 1991.

[NHUF84] I. Noda, Y. Higo, N. Ueno, and T. Fujimoto. Semidilute region for linear polymers in good solvents. *Macromolecules*, 17:1055–1059, 1984.

[NVL97] A. Noy, D.V. Vezenov, and C.M. Lieber. Chemical force microscopy. *Annu. Rev. Mater. Sci.*, 27:381–421, 1997.

[OCS96] D. F. Ogletree, R. W. Carpick, and M. Salmeron. Calibration of frictional forces in atomic force microscopy. *Review of Scientific Instruments*, 67(9):3298–3306, 1996.

[OW69] D.K. Owens and R.C. Wendt. Estimation of the surface free energy of polymers. *J. Appl. Pol. Sc.*, 13:1741–1747, 1969.

[PBH90] C. B. Prater, H.-J. Butt, and P. K. Hansma. Atomic force microscopy. *Nature*, 345(6278):839–840, 1990.

[PCB+98] O. Prucker, S. Christian, H. Bock, J. Ruhe, C. W. Frank, and W. Knoll. On the glass transition in ultrathin polymer films of different molecular architecture. *Macromolecular Chemistry and Physics*, 199(7):1435–1444, 1998.

[Per98] B.N.J. Persson. *Sliding Friction - Physical Principles and Applications*. Nanoscience and Technology. Springer, Heidelberg, 1 edition, 1998.

[PM97] R.D. Piner and C.A. Mirkin. Effect of water on lateral force microscopy in air. *Langmuir*, 13:6864–6868, 1997.

[PR98a] O. Prucker and J. Ruhe. Mechanism of radical chain polymerizations initiated by azo compounds covalently bound to the surface of spherical particles. *Macromolecules*, 31(3):602–613, 1998.

[PR98b] O. Prucker and J. Ruhe. Synthesis of poly(styrene) monolayers attached to high surface area silica gels through self-assembled monolayers of azo initiators. *Macromolecules*, 31(3):592–601, 1998.

[RAvV+94] F. Rossi, B. Andre, A. van Veen, P.E. Mijnardens, H. Schut, F. Labohm, H. Dunlop, M.P. Delplancke, and K. Hubbard. Physical properties of a-c:n films produced by ion beam assisted deposition. *J. Mater. Res.*, 9(9):2440–2449, 1994.

[Rei93] G. Reiter. Mobility of polymers in films thinner than their unperturbed size. *Europhysics Letters*, 23(8):579–584, 1993.

[RG99] M. Ruths and S. Granick. Tribology of confined fomblin-z perfluoropolalkyl ethers: Role of chain-end chemical functionality. *J. Phys. Chem. B*, accepted, 1999.

[RKK90] C. E. Reed, K. K. Kanazawa, and J. H. Kaufman. Physical description of a viscoelastically loaded at-cut quartz resonator. *Journal of Applied Physics*, 68(5):1993–2001, 1990.

[Rob91] M.O. Robbins. Critical velocity of stick-slip motion. *Science*, 253:916, 1991.

[RSHA97] U. Rabe, V. Scherer, S. Hirsekorn, and W. Arnold. Nanomechanical surface characterization by atomic force acoustic microscopy. *Journal of Vacuum Science and Technology B*, 15(4):1506–1511, 1997.

[RSS85] E. Roessler, H. Sillescu, and H.W. Spiess. Deuteron N.M.R. in relation to the glass transition in polymers. *Polymer*, 26:203–207, 1985.

[San92] I.C. Sanchez. *Physics of Polymer Surfaces and Interfaces*. Butterworth, London, 1992.

[Sau57] G. Sauerbrey. Waegung duenner Schichten mit Schwingquarzen. *Phys. Verhandl.*, 8:113, 1957.

[Sau59] G. Sauerbrey. Verwendung von Schwingquarzen zur Waegung duenner Schichten und zur Mikrowaegung. *Z. Phys.*, 155:206–222, 1959.

[Sau64a] G. Sauerbrey. Amplitudenverteilung und elektrische ersatzdaten von schwingquarzplatten (at-schnitt). *Arch. Elektrotech. Uebertrag.*, 18(10):624–628, 1964.

[Sau64b] G. Sauerbrey. Einfluss der Elektrodenmasse auf die Schwingungsfiguren duenner Schwingquarzplatten. *Arch. Elektrotech. Uebertragung*, 18(10):617–624, 1964.

[SBRA97] V. Scherer, B. Bhushan, U. Rabe, and W. Arnold. Local elasticity and lubrication measurements using atomic force and friction force microscopy at ultrasonic frequencies. *IEEE Transactions On Magnetics*, 33(5):4077–4079, 1997.

[SC96] I. Szleifer and M. A. Carignano. Tethered polymer layers. In *Advances in Chemical Physics, Vol XCIV*, volume 94 of *Advances in Chemical Physics*, pages 165–260. 1996.

[Sch93] P. Schwarzenberger. *Beschreibung und Anwendung der Quarzresonatormethode zur Bestimmung des komplexen Schermoduls von viskoelastischen Stoffen auch unter hydrostatischem Druck.* PhD thesis, Universitt Ulm, 1993.

[Stu98] H. Sturm. SFM experiments probing micro-mechanical properties on polymer surfaces using harmonically modulated friction techniques (i): Principles of operation. *Macromolecular Symposia*, (August), 1998.

[SWCJ97] J.M. Sivertsen, G. Wang, G-L. Chen, and J.H. Judy. Evaluation of amorphous diamond-like carbon-nitrogen films as wear protective coatings on thin film media and thin film head sliders. *IEEE Transactions on Magnetics*, 33(1):926–931, 1997.

[SZFB71] D. Sianesi, V. Zamboni, R. Fontanelli, and M. Binaghi. Perfluoropolyethers: Their physical properties and behavior at high and low temperatures. *Wear*, 18:85–100, 1971.

[Tab82] D. Tabor. *The Role of Surface and Intermolecular Forces in Thin Film Lubrication.* Microscopic Aspects of Adhesion and Lubrication. Societe de Chimie Physique, Paris, 1982.

[TLWC98] G.W. Tyndall, P.B. Leezenberg, R.J. Waltman, and J. Castenada. Interfacial interactions of perfluoropolyether lubricants with magnetic recording media. *J. Trib. Lett.*, 4:103–108, 1998.

[TR90] P.A. Thompson and M.O. Robbins. Origin of stick-slip motion in boundary lubrication. *Science*, 250:792–794, 1990.

[TW99] G.W. Tyndall and R.J. Waltman. Thermodynamics of confined perfluoropolyether films: The evaporation kinetics of non-functionalized Fomblin Z03 from CH_x surfaces. *submitted*, 1999.

[TWP98] G. W. Tyndall, R. J. Waltman, and D. J. Pocker. Concerning the interactions between Zdol perfluoropolyether lubricant and an amorphous-nitrogenated carbon surface. *Langmuir*, 14(26), 1998.

[vAG90a] J. van Alsten and S. Granick. The origin of static friction in ultrathin liquid films. *Langmuir*, 6:876–880, 1990.

[vAG90b] J. van Alsten and S. Granick. Shear rheology in a confined geometry: Polysiloxane melts. *Macromolecules*, 23:4856–4862, 1990.

[vOMT+97] M.T. van Os, B. Menges, R.B. Timmons, W. Knoll, and R. Foerch. In *13th Int. Symp. on Plasma Chem.*, volume 3, page 1298, Beijing, China, 1997.

[VV91] J.S. Vrentas and C.M. Vrentas. Sorption in glassy polymers. *Macromolecules*, 24:2404–2412, 1991.

[WBM+95] R.L. White, S.S. Bhatia, S.W. Meeks, M.C. Friedenberg, and C.M. Mate. RF-sputtered amorphous CN_x for contact recording applications. *ASME/STLE Transactions*, 1995.

[Wie94] R. Wiesendanger. *Scanning Probe Microscopy and Spectroscopy.* University Press, Cambridge, 1994.

[Wol98] O. Wolff. *Bestimmung des viskoelastischen Verhaltens duenner und ultraduenner Polymerfilme mithilfe von Schwingquarzen.* PhD thesis, Ruprecht-Karls-Universitaet, 1998.

[WSJ97] O. Wolff, E. Seydel, and D. Johannsmann. Viscoelastic properties of thin films studied with quartz crystal resonators. *Faraday Discussions*, (107):91–104, 1997.

[WvZW95] W.E. Wallace, J.H. van Zanten, and W.L. Wu. Influence of an impenetrable interface on a polymer glass-transition temperature. *Phys. Rev. E*, 52(4):3329–3332, 1995.

[WWM+96] R.-H. Wang, R.L. White, S.W. Meeks, B.G. Min, A. Kellock, A.M. Homola, and D. Yoon. The interaction of perfluoro-polyether lubricant with hydrogenated carbon. *IEEE Transactions on Magnetics*, 32(5):3777–3779, 1996.

[XFTT98] C. Xu, Curt W. Frank, W.T. Tang, and C. Terrill. End group effects on adhesion of perfuoropolyether lubricants to solid substrates. *J. Adhesion*, 67:195–215, 1998.

[YCI93a] H. Yoshizawa, Y.-L. Chen, and J.N. Israelachvili. Recent advantages in molecular level understanding of adhesion, friction and lubrication. *Wear*, 168:161–166, 1993.

[YCI93b] H. Yoshizawa, Y.L. Chen, and J. Israelachvili. Fundamental mechanisms of interfacial friction. 1. Relation between adhesion and friction. *J. Phys. Chem.*, 97:4128–4140, 1993.

[YI93] H. Yoshizawa and J.N. Israelachvili. Fundamental mechanisms of interfacial friction. 2. Stick-slip friction of spherical and chain molecules. *J. Phys. Chem.*, 97:11300–11313, 1993.

List of Figures

2.1 Left-handed quartz crystal 14

2.2 Shear deformation of an AT-cut quartz plate 17

2.3 Typical resonance curves 18

4.1 Cobblestone model 33

4.2 Stick-slip motion 34

4.3 Friction phase diagram 37

4.4 AFM working principle 40

4.5 Force–distance curve 42

4.6 Surface Forces Apparatus 45

5.1 Sketch of the quartz resonator setup. 50

5.2 Sketch of the force transducer 53

5.3 Calibration of the force transducer 56

5.4 Drawing of the quartz holder 59

5.5 Shape of electrodes 61

5.6 Annealing of gold electrodes 63

5.7 Quartz signals in f– and t–domain 64

5.8 Equivalent Circuit for t–domain experiments 67

5.9 Acquisition Cycle 69

6.1 Data noise 75

6.2 Resolution of normal force 77

6.3 Friction measurement on a gold–gold contact 78

6.4 Measurement of a fluorocarbon contact . . . 81
6.5 Dependence on overtone order . . . 82
6.6 Drive-level dependence . . . 85
6.7 Plate vibration modes . . . 86
6.8 Fourier amplitudes and anharmonic sidebands . . . 87
6.9 Setup for measuring the pressure dependence . . . 90
6.10 Pressure dependence . . . 91
6.11 Equivalent Circuits . . . 95
6.12 Point contact model . . . 98
6.13 Standing waves in a quartz plate . . . 101
6.14 Separation of dissipative channels . . . 104
6.15 Amplitude distribution . . . 108
6.16 Oscillation due to coupling to the holder . . . 109
6.17 Measurement on a 4 Å lubricant layer on CN_x . . . 111
6.18 Varying long-range forces on the same surface . . . 112
6.19 Comparison of the corrected short-range behavior . . . 114
6.20 Distorted resonances . . . 116
6.21 Dependence on the approaching speed . . . 117

7.1 Film-Thickness dependence of thermodynamic quantities . . . 124
7.2 Surface roughness of lubricant layers . . . 126
7.3 Film thickness dependence of the friction on CH_x surfaces. . . . 128
7.4 Measurements for different lubricant thickness on CN_x . . . 131
7.5 Approach–separation cycle . . . 133

8.1 All extracted friction parameters for varying lubricant thickness . . . 139
8.2 Force-steps for different layer thickness . . . 140
8.3 Distance correction . . . 142
8.4 Simulation of vdW forces . . . 143
8.5 Effective shear viscosity . . . 148

8.6 Dissipated power 150
8.7 Gaussian friction profiles 153
8.8 AFM-histograms of lubricant coated CN_x–surfaces 155

9.1 Typical sorption curves and derivatives 160
9.2 Raw data: pressure ramp and mass response 166
9.3 Low and high frequency glass transition 167
9.4 Drying–swelling asymmetry 169
9.5 Influence of drying speed 171
9.6 Sorption curves for different film thickness 174
9.7 Film-thickness dependence of the different parameters 175
9.8 Repeated drying ramps 176
9.9 Offset parameter for FH-fit 177
9.10 Parameters for subsequent swelling 178

List of Tables

2.1 AT-Quartz Properties 16

5.1 Specifications of capacitors 51

5.2 Amplitude Conversion 65

5.3 Mechanical properties of Ekasin 2000 71

5.4 Roughness of Si_3N_4spheres 71

6.1 Data from noise analysis 76

6.2 Amplitude and speed at different overtones 83

6.3 Varying the approaching speed 118

8.1 Friction Parameters for CH_x 135

8.2 Friction Parameters for CN_x 136

8.3 Hamaker constants 143

8.4 Gauss fit parameters for friction profiles 154

Acknowledgements

First I would like to thank my advisor Priv.-Doz. Dr. Diethelm Johannsmann for his inspiring and motivating spirit that made me enjoy to "learn science". Further, for his trust and his ability to leave me space to develop own ideas and having a helping mind whenever needed.

I would like to acknowledge Prof. Dr. Wolfgang Knoll for the opportunity of working under the best possible conditions and the chance to experience his vision of a world-wide cross-linked scientific community.

I want to thank Prof. Dr. Hans-Jürgen Butt for being the second referee of this thesis and the useful hints during his lectures and in his script.

I greatly benefited from discussions with Dr. George W. Tyndall and want to thank him for his patience to explain me lubrication concepts and never being tired to critically discuss "strange" data.

For the "asylum" during the writing of this thesis I would like to thank Dr. Marina Ruths. Her comprehensive expertise in surface forces, friction and lubrication gave strong impulses for the interpretation of data. Also, I want to thank her for proof-reading the early draft that more resembled a raw collection of ideas.

Volker Scheumann for lots of useful discussion on every question concerning AFM techniques and applications.

I would also like to acknowledge the main "supplier" of the polymer brushes and that he made them grow on gold: Dr. Jörg Habicht and his helping hand Iris Homann.

All the technical problems during this work would never have been solved without the help of the electronics and mechanics workshops. Standing in for all I would like to thank Achim Gerstenberg and Dirk Richter for their immediate help and their excellent work.

Whenever there was a problem with the computers, I was always glad that I could count on Andreas Scheller for help.

Without the good atmosphere in the entire Knoll group this work would not have been possible.

And I want to thank my parents for endless support.